DEDICATED

TO

MY WIFE AND PARENTS

"τά πάντα κόποις κτῶνται"

ELECTRON OPTICAL AND RELATED DESIGN CONSIDERATIONS FOR MICRO-X-RAY SOURCES

A THESIS FOR THE DEGREE OF DOCTOR OF PHILOSOPHY

BY

Stelios Christofides

Abstract

The purpose of the work described in this dissertation is to investigate the design considerations associated with multi-purpose micro-x-ray sources, with special emphasis on the electron optical requirements of micro sources for micro-x-ray fluorescence equipment in Forensic Science.

The x-ray resolution that can be achieved by a micro-x-ray source, the appropriate x-ray target geometry, the maximum power density such an x-ray target can withstand without damage and the power dissipation in such a target are briefly discussed. Micro-radiographs obtained from an experimental single lens micro-x-ray source were used to estimate the x-ray resolution that can be achieved in practice. Experiments have also been performed to investigate the maximum power that a thin target can withstand under the heating effects of the incident electron beam. It is shown that for the electron spot sizes usually associated with Forensic micro-x-ray sources, water cooling of the target is not advantageous.

Previously described electron optical columns employing conventional magnetic lenses have many disadvantages compared to those with single polepiece lenses. The optimum use of a single polepiece lens as an objective lens for the probe forming system of a micro-x-ray source has been investigated and new form of highly saturated single polepiece and asymmetric lenses have been developed.

It is shown that objective lenses of this type are also well suited as objective lenses in high resolution electron microscopes intended for analytical purposes. Experimental forms of these lenses have been constructed and tested in an electron optical bench.

Finally in order to test these ideas in practice, an experimental micro-x-ray source, was constructed. This was used for microradiography and for preliminary investigations in micro-x-ray fluorescence analysis.

Key words : magnetic lenses, micro-x-ray source, power dissipation, x-ray target, x-ray fluorescence analysis.

II Contents

III Acknowledgements

I am most grateful to my supervisor, Professor T. Mulvey, for his help and advice throughout this work.

I also like to acknowledge the staff of the Physics Workshop, for constructing the lenses and associated accessories described in the thesis and Mr R. Keen (TEM, Physics Department) for his technical assistance.

My thanks are due to my colleagues, Miss Al-Hilly, Miss Al-Khashab, and Dr. Nasr, for their time and energy over consultations and opinions.

I would particularly like to acknowledge the generosity of the Science Research Council, in providing the financial support that enabled me to undertake this research.

Finally, I am very grateful to my parents and wife, for their patience and encouragment throughout this work. Particularly, I like to thank my wife for reproducing the photographs and microradiographs of this work.

IV List of symbols

Unless otherwise stated in the text, the following symbols are in S.I. units as used throughout the text.

A	Cross-sectional area of electron spot
a	Radius of sphere
B	Magnetic flux density
B_{coil}	Magnetic flux density at any point due to the coil of a lens
B_{fe}	Magnetic flux density in the polepiece ($B_{fe} = B_z$ on the axis)
B_{iron}	Magnetic flux density at any point due to the magnetisation of the iron
B_{max}	Peak value of the axial magnetic flux density distribution
B_o	Maximum axial magnetic flux density at the surface of a sphere
B_{pf}	Poleface magnetic flux density
B_{pp}	Maximum magnetic flux density in the polepiece
B_{total}	Total magnetic flux density at any point ($B_{total} = B_{coil} + B_{iron}$)
B_z	Axial magnetic flux density
b	Distance between specimen and x-ray target
C	Capacitance of the insulating layer formed on the x-ray target.
C_c	Chromatic aberration coefficient
C_s	Spherical aberration coefficient
D_{in}	Diameter of lens bore
D_m	Mean diameter of coil ($D_m = (D_1 + D_2)/2$)
D_{out}	Outer diameter of lens polepiece

D_{in}/D_{out}	Lens bore ratio ((inner/outer) polepiece diameters)
D_1	Inner diameter of coil
D_2	Outer diameter of coil
d	Electron spot diameter
d_f	Fresnel diffraction fringe width
d_g	Gaussian electron spot diameter
d_h	Effective halfwidth of the axial magnetic flux density distribution
d_{hc}	Halfwidth of the axial magnetic flux density distribution of the lens coil
d_{hs}	Halfwidth of the spherical field
d_{min}	Minimum disc of confusion
d_o	Diameter of electron source
d_s	Electron spot diameter due to spherical aberration
dZ	Distance between target and focal planes
F_{obj}	Objective focal length
f	Frequency of the electron beam modulation
G	Geometrical scaling factor giving a poleface flux density B_{pf} = 2 Tesla
H	Magnetic field strength
I	Electron beam current striking the x-ray target
I_c	Current supplied to the lens coil
I_t	X-ray target current
$\bar{I}$	Attenuated x-ray intensity
$\bar{I}_o$	Primary x-ray intensity
ℓ	X-ray target thickness
ℓ_i	Thickness of insulating layer formed on the x-ray target
NI	Lens excitation
NI_A	Lens excitation giving a poleface flux density B_{pf}

NI_G	Lens excitation for a particular geometrical scaling factor G
$NI/V_r^{\frac{1}{2}}$	Lens excitation parameter
n	Geometrical scaling factor
P_i	Improvement factor (ratio of power density of a rotating target with respect to the power of the target being stationary)
p	Power retention factor
R	Electron spot radius
R_c	Resistance of coil windings
R_i	Resistance of the insulating layer formed on the x-ray target
r_o	Radius of lens aperture (or radius of lens bore if no aperture is used)
S	Thickness of coil
S_x	X-ray source size for d = 0
S'_x	X-ray source size for d > 0
t_o	Thickness of x-ray attenuation filter
V	X-ray target velocity
V_o	Electron accelerating voltage
V_r	Relativistically corrected electron accelerating voltage
W	Maximum power input in an x-ray target
W_c	Power dissipated in the lens coil
X	External diameter of lens
x_o	Maximum electron penetration in the x-ray target
Y	Distance between lens polepiece and electron source
Z_f	Working distance
Z_p	Distance of the peak of the axial magnetic flux density distribution from the lens polepiece tip

Z_t	Distance of the x-ray target from the lens polepiece
α	Semi-angle of the electron beam
α_s	X-ray exit semi-angle from the x-ray target
β	Electron gun brigthness
δ_o	Spatial resolution
ε	Permitivity of the insulating layer formed on the x-ray target
ε_o	Permitivity of free space
λ	Wavelength
μ/ρ	Mass absorption coefficient of x-ray attenuation filter
μ	Permeability of the magnetic material
μ_o	Permeability of free space
ρ	Density
ρ_i	Resistivity of the insulating layer formed on the x-ray target
σ	Current density in the lens coil
τ	Phase shift

V List of figures

VI List of tables

1 Introduction

1.1 The micro-x-ray source and its applications

Any source of x-rays whose source size is in the micrometer region, can be termed a micro-x-ray source. This includes sources of x-rays ranging from cyclotrons and linear particle accelerators to radioactive isotopes (see appendix A). More frequently a micro-x-ray source is referred to as a generator of x-rays by a focused electron beam striking an x-ray target.

Micro-x-ray sources are employed in a large range of applications. These can be divided in three major groups :

a) X-ray microchemical analysis

b) X-ray microradiography

c) Calibration x-ray sources

X-ray microchemical analysis has its own large range of sub-divisions, identified by the method of x-ray production and by the method in which the x-rays are used for microchemical analysis. Emission x-ray fluorescence analysis is the most commonly used method. Appendix A describes briefly the principles of x-ray fluorescence analysis and the various methods of primary x-ray production, with reference to a large selection of published literature.

X-ray microradiography is usually performed using micro-x-ray sources employing a focused electron beam to generate x-rays in a thin x-ray target. Calibration x-ray sources are usually micro-x-ray sources which also employ a focused electron beam for x-ray generation. This method of x-ray production can be identified as the projection x-ray microscope, which can also be used to perform microchemical analysis.

Cosslett and Nixon (1953), Cosslett (1954), Nixon and Baez (1956), can be regarded as the pioneers of the x-ray projection microscope, although many other workers in the field of x-ray

microscopy helped to develop and used the projection x-ray microscope during the 1950's and early 1960's.

Figure 1.1 a), shows the main features of the projection x-ray microscope as used for microradiography. It consists essentially of an electron probe forming system composed of an electron gun which produces a beam of electrons, which is focused by magnetic lenses onto a thin x-ray target, which usually also acts as a vacuum seal. X-rays generated by the electron beam in the x-ray target, which are transmitted through the target, are used to irradiate a specimen situated above the target; thus a magnified x-ray shadow image is formed on a photographic plate some distance above the specimen.

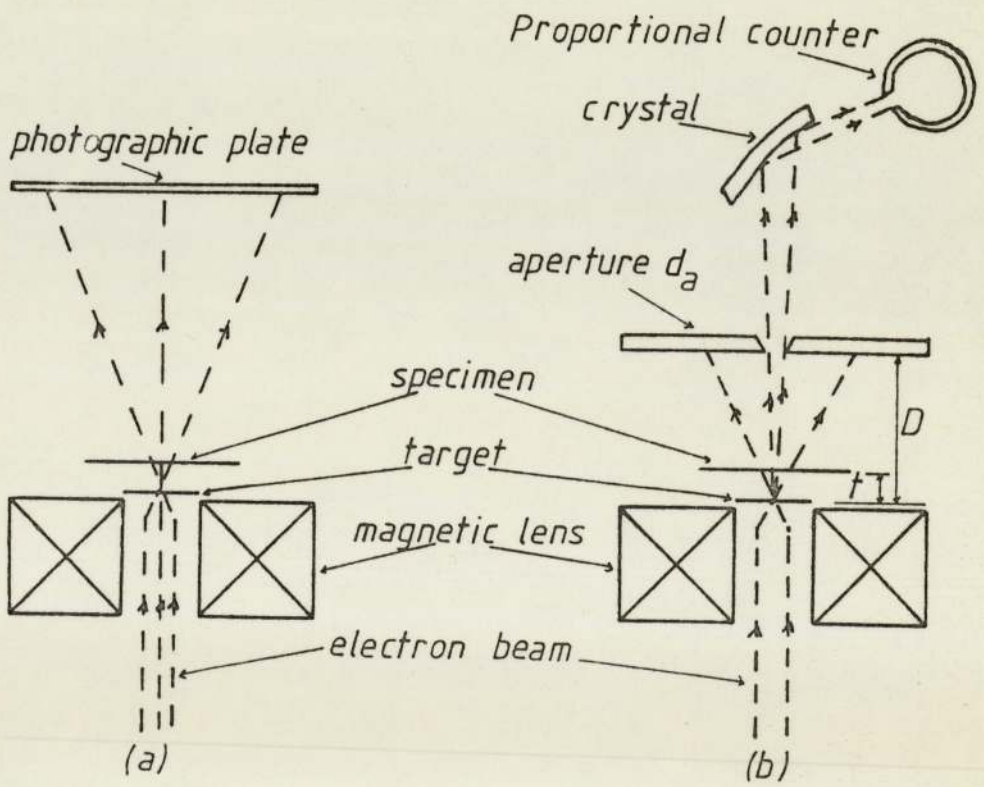

Figure 1.1 Schematic representation of the x-ray projection microscope. a) microradiography mode, b) absorption microchemical analysis mode.

The resolution of the x-ray projection microscope is mainly set by the electron spot size formed on the x-ray target. A practical

resolution which can readily be achieved, is of the order of 0.1 μm. The practical limitations of the projection x-ray microscope are set primarily by the spherical aberration inherent in the final magnetic (objective) lens, the spread of the electron beam in the x-ray target and the rate of energy dissipation in the x-ray target.

The spherical aberration inherent in the objective lens has the effect of spreading the electron beam in the Gaussian image plane into a disc of diameter d_s, given by :

$$d_s = 2C_s\alpha^3 \quad \text{- 1.1}$$

where

C_s is the spherical aberration coefficient

α is the semi-angle of the electron beam.

In effect a physical aperture must be used to limit α according to the radius of the electron spot required to strike the x-ray target. Consequently the electron beam current arriving at the target is limited with the effect of reducing the x-ray intensity produced within the target. Consequently, for an x-ray resolution below 0.1 μm, the exposure time runs into hours and therefore it renders the projection x-ray microscope inconvenient.

In microradiography low electron accelerating voltages are usually used and therefore the penetration and scattering of electrons in the target take place within the electron spot size. The target thickness should always be thick enough to absorb all the electrons striking it, so as to avoid additional x-ray scattering occurring within the target material. Since the target is also used as a vacuum seal, the thickness of the target is limited by its mechanical strength to withstand the necessary vacuum presure. A target thickness of 0.1 μm for a 0.1 μm electron spot presents no experimental difficulties.

For spot sizes less than around 1 μm, the power input to the

target is limited by the emissive power of the probe forming system rather than the energy dissipation in the target.

A final limitation of the projection x-ray microscope is Fresnel diffraction, which introduces a limit of resolution given by :

$$d_f = (b\lambda)^{\frac{1}{2}} \text{ - } 1.2$$

where

b is the distance between the specimen and the x-ray target

λ is the x-ray wavelength.

For a 0.2 nm wavelength, to achieve a resolution of 0.1 μm, the specimen must be placed 50 μm from the target. At short distances of this magnitude the area of the specimen that can be magnified on a photographic plate is limited by the cone angle which is set by the bore of the second polepiece of the objective magnetic lens.

Figure 1.1 b), shows a schematic representation of the projection x-ray microscope used as a source of x-rays for absorption microchemical analysis (Long and Cosslett, 1957; Long, 1958). The probe forming system is the same as used for microradiography. For absorption microanalysis, the specimen distance t, the aperture distance D and the aperture diameter d_a, determine the area of specimen to be analysed. This area will eventually be limited by the smallest x-ray source size that can be produced in the x-ray target. For example if t is 0.5 mm, d_a is 100 μm and D is 15 mm above the target, then x-rays will be transmitted through a specimen area of 3 μm in diameter provided that the x-ray source size is smaller than 3 μm in diameter. In the system used by Long (1958), x-ray source sizes down to 1 μm in diameter could readily be achieved. A crystal analyser and a counter, set above this aperture may then be used to record the intensity of selected x-ray wavelengths. The high loading of the target (approximately 100 Kw/mm^2), the small

x-ray source size and the target to specimen distance (1 μm and 0.5 mm respectively), combine to produce a high flux through the specimen and a high primary magnification in the aperture plane. It is thus possible to determine directly the transmission of precisely located areas in the specimen without using very small apertures.

This technique of absorption microanalysis is very useful in determining the amount of an element present in a given area of the specimen. Measurements on calcium content in a 10 μm^2 area of a gypsum sample carried out by Long (1958) on his original instrument yielded values as low as 0.5×10^{-9} grammes.

The set up shown in figure 1.1 b) can be modified slightly for x-ray fluorescence microanalysis, by placing a small aperture below the specimen and using the proportional counter directly, at an angle to the primary x-ray beam, above the specimen. With such an arrangement Long and Cosslett (1957) found that the minimum detectable masses are 7×10^{-9} grammes for a 500 μm aperture and 7×10^{-11} grammes for a 50 μm aperture, from a calcium specimen using a copper target at 10 KV and 7 μA. The 500 μm aperture was placed at 8 mm from the target and the 50 μm aperture was placed at 0.8 mm from the target ensuring that the x-ray intensity was the same for both apertures. As can be seen from the above figures this increased the sensitivity of the technique by a factor of 100.

The specimen areas analysed by the techniques of absorption and fluorescence microanalysis may be reduced to that of the source size (1 - 2 μm), either by moving the specimen closer to the target or if sufficient x-ray intensity is available by reducing the diameter of the apertures. Count rates of up to 2000 counts per minute were recorded in the above investigations. If the apertures are reduced in size then the count rate will be reduced drastically and thus the analysis time will increase proportionally, rendering

the technique inefficient.

Nicholson (1971) constructed a micro-x-ray fluorescence analyser, specifically designed for analysing biological specimens. He used as the basis of his analyser the electron gun and magnetic lenses of the prototype of the first A.E.I. electron probe micro-analyser, described by Mulvey (1960).

The x-rays from a thin foil transmission target were collimated by a double aperture (trap) as shown in figure 1.2 and as previously used by Long and Rockert (1963). The second aperture of the trap system is always bigger than the first one and is present to cut off the scattered x-rays from the first aperture, thus restricting the scattered x-rays from striking the specimen.

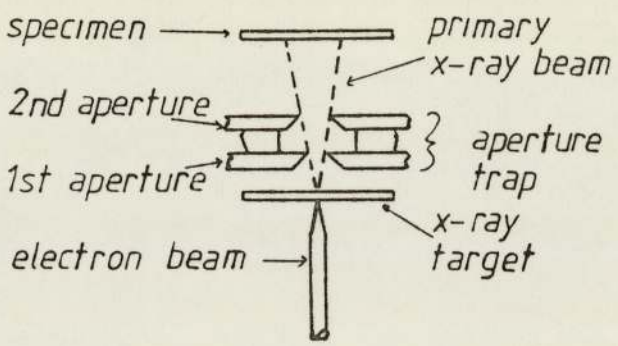

Figure 1.2 Schematic representation of the aperture trap used to collimate an x-ray beam.

The fluorescent x-rays from the specimen were detected by a proportional counter which was calibrated to monitor the particular energy of the x-rays emitted by the element of interest present in the specimen. Using a titanium target with an x-ray trap of 100 μm in diameter and the proportional counter monitoring 6.6 kev, he managed to detect sulphur down to a mass fraction of 60 ppm or a mass of 6×10^{-11} grammes. The counting time was 20 seconds and the electron accelerating voltage was 25 KV.

These results were very encouraging and he concluded that the detection limit can be improved to the region of 10 ppm, if the

probe forming system of the analyser was redesigned so as to provide smaller x-ray source sizes with increased x-ray intensities available for analysis. These improvements would allow smaller trap apertures to be used without a substantial reduction in the x-ray intensity at the specimen.

More recently the considerable research effort devoted to x-ray optics, stimulated particularly by the advances in x-ray astronomy, has resulted in the development of a wide range of x-ray optical components such as mirrors, diffraction gratings, telescopes and microscopes (Gursky and Zehnpfennig, 1966; Zehnpfennig 1966; Dijkstra and Lantwaard 1975; Franks 1977).

The projection x-ray microscope or the micro-x-ray source as it is referred to today (and from henceforth in this work), can provide an efficient and convenient means of using and evaluating x-ray optical components. It may, for example, obviate the need for complex collimation systems when assessing the performance of x-ray telescopes and microscopes.

X-ray microscopes (constructed from x-ray optical components) are widely used in Laser Fusion work (Boyle and Ahlstrom, 1978) where they are used to study the x-rays emitted from the imploding fusion microsphere targets. This helps to understand the symmetry and complexity of the implosion of these fusion microspheres. X-ray microradiography is also used in Laser Fusion work, to screen and study the defects in the walls of the microspheres (Halpern , et al, 1977; Henderson, et al, 1977; Whitman, et al, 1979; Whitman and Day, 1980; Singleton, et al 1979).

From the puplished literature cited above on the more recent advances in x-ray optics it is evident that a micro-x-ray source with an x-ray source size in the region of 0.1 μm is essential for testing and calibrating x-ray optical components. Photographic exposure times associated with tests of such x-ray optical

components usually are of the order of 30 minutes. Therefore an increase in the x-ray flux of the micro-x-ray source is also desirable to reduce exposure times. Such a micro-x-ray source will also be useful for studying the defects of fusion microsphere targets in Laser Fusion.

1.1.1 Micro-x-ray fluorescence analysis in Forensic Science

An important application of x-ray fluorescence analysis is in the field of Forensic Science, where non-destructive analysis of small samples (10 - 50 μm diameter) for the determination of trace elements is essential. The preservation of such small samples taken from the scene of a crime is important because these samples may be required as evidence in a subsequent court hearing.

A difficulty which is often faced by the Forensic Scientist in non-destructive analysis (Montecalvo, 1977) is due to the increasing necessity for analysing a large number of smaller and smaller samples (i.e glass splinters smaller than 60 μg in weight), mainly for qualitative screening purposes. These samples are often too small for conventional x-ray fluorescence analysis (minimum sample size of around 1 mm in diameter). In addition small samples can be observed in a Scanning Electron Microscope (SEM), but the characteristic x-ray spectrum from trace elements cannot be displayed due to the large bremstruhlung background produced by the incident electron beam, which substantially reduces the signal to background ratio (Keeley and Christofides, 1979; Christofides, 1977; Howden, et al, 1977; Dudley, et al, 1980; Reeve and Keener, 1976; West, 1975). For this reason trace elements such as 30 ppm of magnesium in glass samples cannot be detected in the SEM. Furthermore the standard methods of preparing SEM specimens by polishing and coating with metal, destroy the value of the specimen as legal exhibit in evidence in a court room.

A micro-x-ray source can readily provide x-ray source sizes smaller than the samples the Forensic Scientist needs to analyse. A micro-x-ray source interfaced to a solid state detector and a multi-channel analyser, may well prove to be a useful instrument for the Forensic Scientist.

A necessary requirement of a micro-x-ray source in this mode of micro-x-ray analysis is that a large solid angle must be available around the specimen when this is placed closed to the x-ray target. This is essential for the optimum positioning of the solid state detector close to the specimen. A high x-ray flux exciting the specimen is also desirable in order to reduce the analysis time for each specimen.

The requirements of x-ray Astronomy, Laser Fusion and Forensic Science, are only three examples of modern science where a micro-x-ray source can be of tremendous value in assisting research and development. A high intensity micro-x-ray source with very good spatial resolution may find application in other fields such as the Welding Industry, Biology, Medicine, Agriculture, Enviromental Studies, Geology, Metallurgy and so many other fields where x-rays are used.

1.2 Limitations of the micro-x-ray source and aims of this work

The purpose of the work described in this thesis was to investigate the design parameters associated with such a multi-purpose micro-x-ray source, with special emphasis on the electron optical requirements.

It is evident from the above paragraphs that a micro-x-ray source must have the following properties in order to fulfil the requirements of its modern applications :

a) X-ray source size varying from 0.1 to 2 μm in diameter.

b) A primary x-ray excitation intensity capable of producing

sufficient fluorescence intensity from a specimen to utilise fully the x-ray detector.

c) A large solid angle must be available in the region of the x-ray target to allow easy access to the target, manipulation of the x-ray collimation apertures and for the optimum positioning of the x-ray detector.

1.2.1 X-ray source size

The limitations imposed on the x-ray source size are due to the way electrons penetrate the x-ray target. Electrons penetrating the target are scattered in all directions thereby increasing the dimensions of the effective x-ray source size, as shown schematically in figure 1.3. Several authors in the field of electron microprobe analysis have derived theoretical and empirical equations giving the electron penetration and x-ray source size in solid targets (Bethe, 1930; Duncumb,1960; Reed, 1965; Cosslett and Thomas, 1964). Beaman and Isasi (1972) summarise most of the work on electron penetration and x-ray source size in a review article on electron microprobe analysis.

Electron penetration in the x-ray target increases roughly as the square of the electron beam energy and inversely as the density of the target material. The x-ray source size depends on the electron spot size and the electron scattering in the target. Further as stressed by Reed (1965), the effective x-ray source size also depend on the secondary fluorescence, that is , the x-ray intensity generated by the continuous spectrum created by the incident electron beam and also by characteristic radiation if the target contains many elements.

Since x-rays penetrate deeper into the target than electrons, the effective x-ray source size is always larger than the effective electron source size as shown in figure 1.3. The minimum x-ray

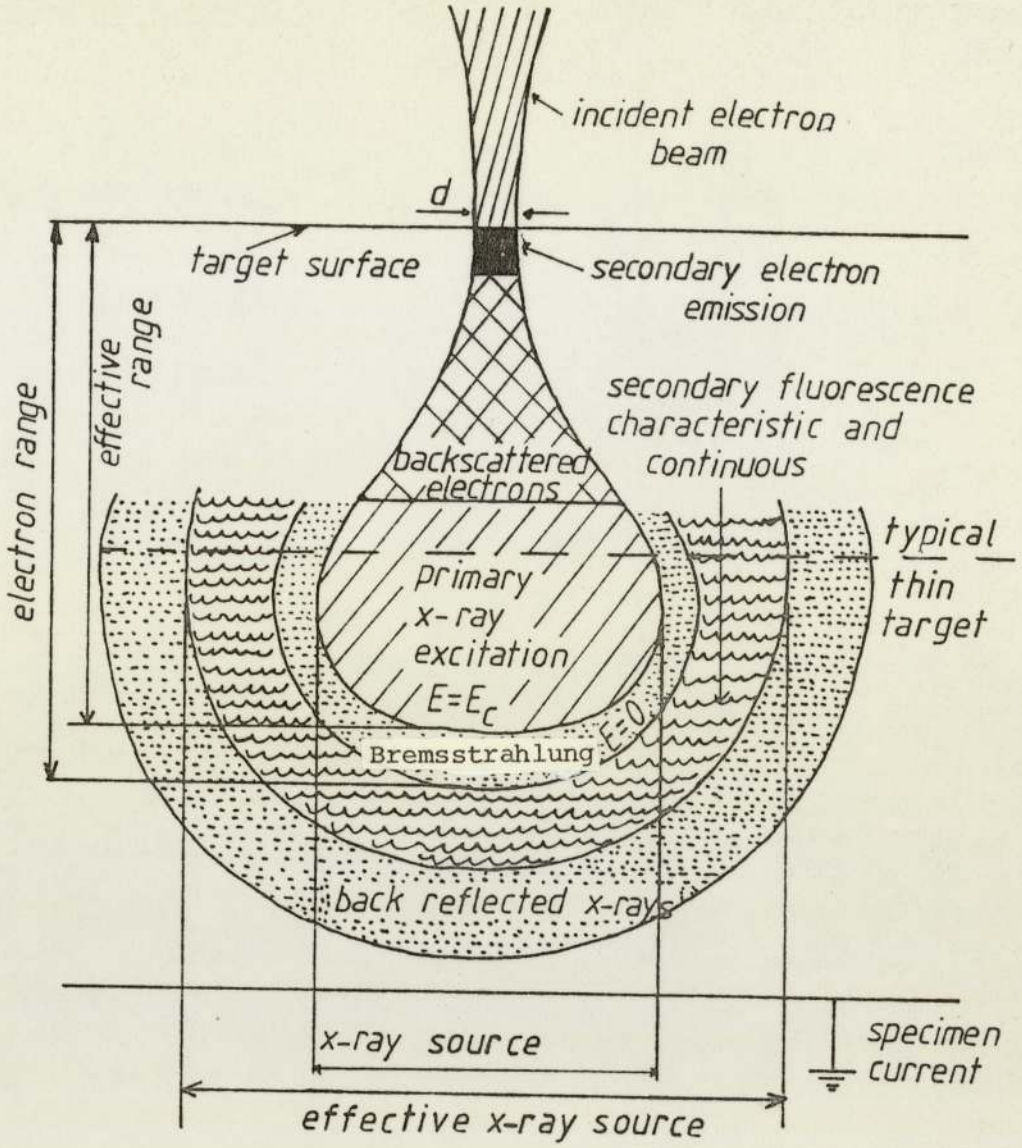

Figure 1.3 Schematic representation of the electron penetration and x-ray production in an x-ray target (Beaman and Isasi, 1972).

source size therefore occurs when the electron spot size d is small compared with the x-ray source size.

Figure 1.4 shows the variation of the effective x-ray source size S_x (for d = 0) as a function of the relativistically corrected accelerating voltage V_r for a copper target. It should be borne in mind that this curve is a first approximation only, since the detailed arrangement of the target and the x-ray detector can modify slightly the effective x-ray source size.

For a finite electron source size d a useful approximation for

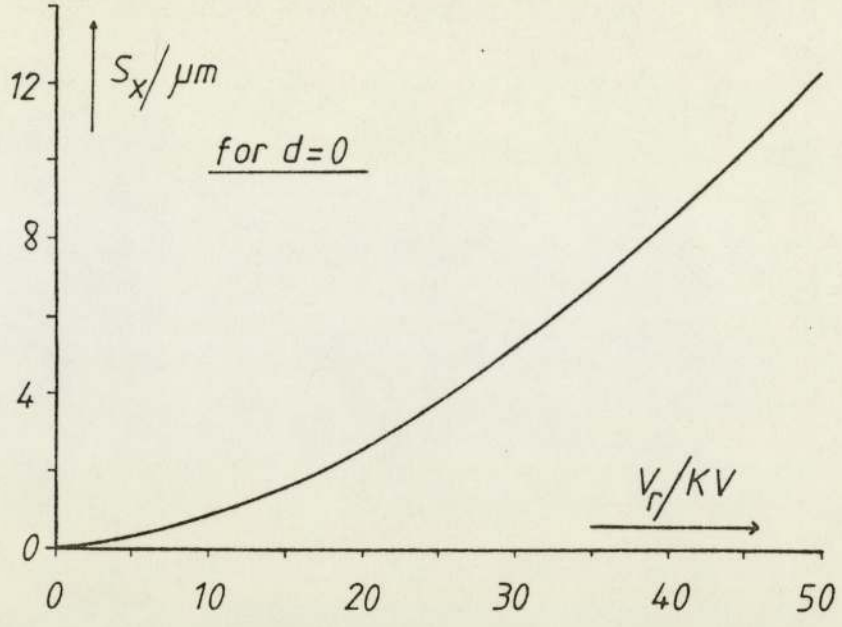

Figure 1.4 The effective x-ray source size as a function of the electron accelerating voltage V_r (for d = 0).

the effective x-ray source size is given by :

$$S'_x = \sqrt{S_x^2 + d^2} \quad \text{- -} \quad 1.3$$

For a thin target the effective x-ray source size will be reduced. This can be seen from figure 1.3 since the effective volume of x-ray generation will be reduced.

Simple experiments were carried out by the author to investigate experimentally the effective x-ray source size at different electron accelerating voltages from a copper x-ray transmission target. The results are discussed in chapter 4.

1.2.2 X-ray target geometry

The x-ray intensity produced in the target depend on the electron beam current the probe forming system can deliver in an electron spot of given diameter on the x-ray target; it also depends on the thermal properties of the target material.

The energy of the electron beam when striking the x-ray target is dissipated in the target mainly in the form of heat. In order

to estimate how much power the target can withstand without damage, it is necessary to estimate the power that the probe forming system can provide the target. This power depends on the electron gun brightness (β), the electron accelerating voltage (V_o), the spherical aberration coefficient (C_s) of the final (objective) magnetic electron lens and the diameter of the electron spot size (d_g) on the x-ray target.

Vine and Einstein (1964), using the Archard model (1961) of electron penetration, have derived expessions for the power input in an electron spot on the x-ray target. They also derived expressions for the maximum power a target can sustain, assuming that the target is a semi-infinite block of uniform material having thermal properties independent of temperature.

Figure 1.5 summarises Vine and Einstein's results for a semi-infinite copper target. In this figure it is assumed that the spherical aberration coefficient (C_s) of the objective lens is 1 mm (which can readily be achieved in modern magnetic lenses, as will be seen later in the next chapter) and that the electron gun brightness (β) is $2.5 \times V_o$ (A $cm^{-2} sr^{-1}$). Appropriate average values were assumed for the thermal properties of copper and that the melting point of copper is reached by a temperature of 1000 ^{o}C above ambient temperature, in the centre of the electron focal spot.

Figure 1.5 shows the limits of power density input to the semi-infinite copper target for a number of electron accelerating voltages (V_o). These limits are set by the performance of the probe forming system and by the melting temperature of copper.

From the curves showing the limits imposed by the melting point of copper (dashed lines) can be seen that for a given electron spot size, the power density required to raise the temperature of copper by 1000 ^{o}C, increases with increasing electron accelerating voltage. This is due to the increasing electron penetration and electron

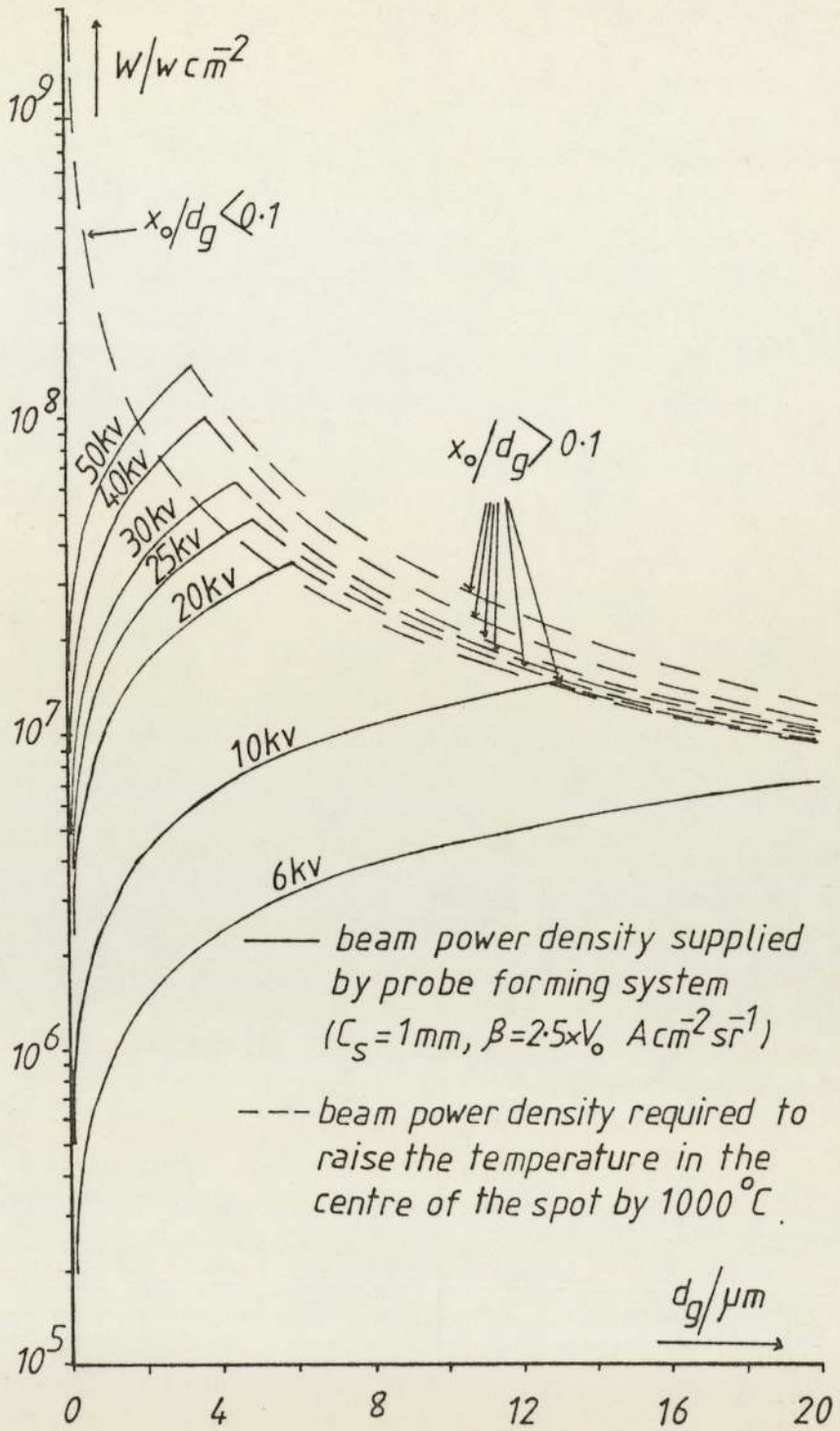

Figure 1.5 The limits of power density in electron spots of given diameter on a semi-infinite copper target, imposed by the probe forming system and by the melting point of copper, assuming that C_s = 1 mm and $\beta = 2.5 \times V_o$ (A cm^{-2}sr^{-1}), where V_o is in volts.

scattering in the target with increasing electron accelerating voltage. This has the effect of spreading the beam power in a larger volume in the target as the electron accelerating voltage increases. This phenomenon holds true only for cases in which $x_o/d_g \rangle 0.1$, where x_o is the depth of electron penetration. For cases in which $x_o/d_g \langle 0.1$, the curves converge into one curve. This curve represents the cases for which the electron penetration in the target is negligible compared with the electron spot diameter.

The limits set by the performance of the probe forming system (solid lines) in figure 1.5, can be exceeded by improving the performance of the probe forming system of the micro-x-ray source, either by improving the spherical aberration of the objective lens or by improving the electron gun brightness (β).

Practical x-ray targets are of finite size and therefore the results of Vine and Einstein indicate an upper limit only for the power density a target can sustain before suffering any damage.

In practice it may be possible to increase the power density a finite target can sustain by rotating or cooling the finite x-ray target. Oosterkamp (1948) has studied rotating and cooled x-ray targets extensively. Unfortunately Oosterkamp was interested in applications in which large electron spot diameters are used. As a result he made the assumption that the electron penetration in the x-ray target is negligible compared with the electron beam diameter d (i.e. $x_o/d_g \leqslant 0.1$). In the region of interest in the present work (spot diameters from 0.1 to 2 μm) this assumption breaks down. Nevertheless Oosterkamp's work on rotating x-ray targets can be used to show to a first approximation the improvement in power density a rotating target can sustain over a stationary target.

The improvement factor P_i (ratio of power density of a rotating target with respect to a stationary target) is shown as a function of the product VR in figure 1.6, where V is the velocity of the

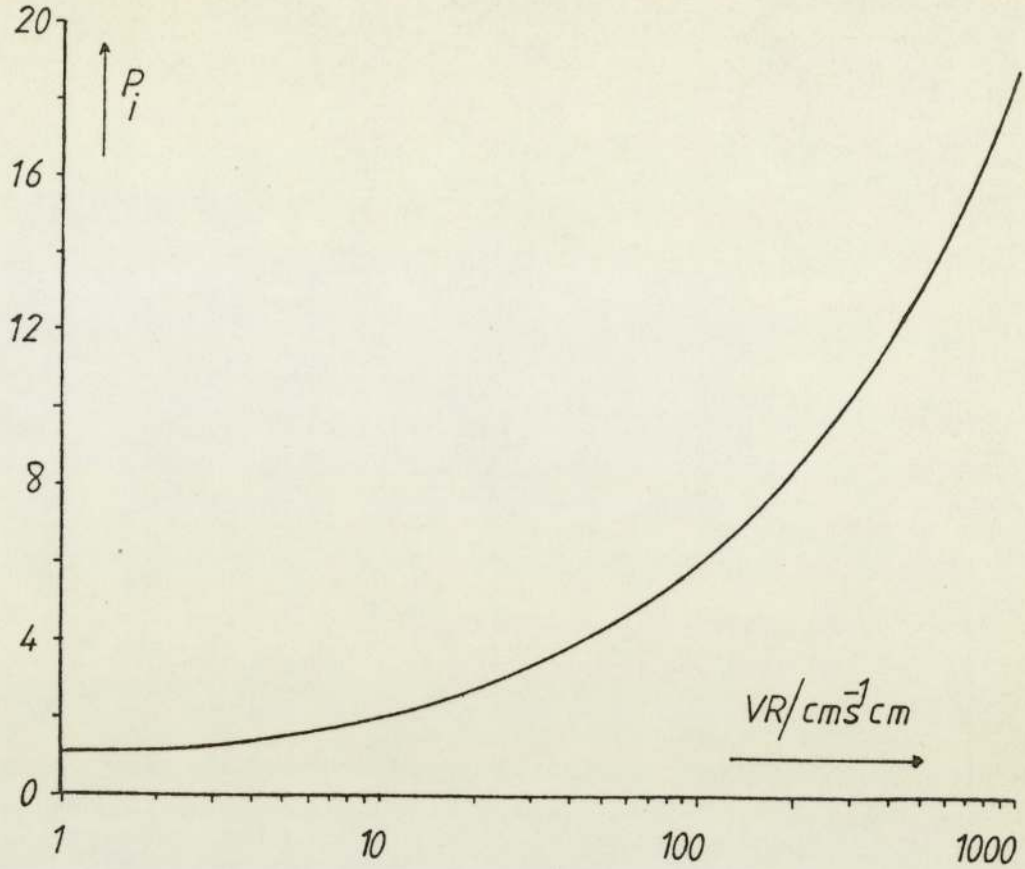

Figure 1.6 The variation of the improvement factor P_i as a function of the product VR.

rotating target and R is the radius of the electron spot. To achieve an improvement by a factor of six for an electron spot of 2 μm in diameter, a target velocity of 10^6 cm s^{-1} is required. For the same target velocity an improvement of 13.3 is achieved for a spot diameter of 20 μm. In practice such a velocity is difficult if not impossible to achieve. For moderate velocities which can be achieved in practice, the improvement is so small that a rotating target for use with the electron spot sizes of interest in the present work, will be more of a disadvantage than an advantage. For applications where electron spot sizes in the region of 1 mm radius are used, a rotating target can improve the maximum power density by 8.4, when the target velocity is 2000 cm s^{-1}. Such a velocity can easily be obtained in a mechanical system. A point at the periphery of a disc of say 15 cm in diameter, moves with this

velocity, if the disc makes approximately 2500 revolutions per minute.

In cases where there is not enough room to accommodate a bulky target, one is forced to use targets of finite dimensions. In these cases, one is trying to simulate a semi-infinite target by removing the heat ariving at the finite boundaries of the target. The removal of heat is usually carried out by a liquid cooling agent flowing along the finite boundaries of the target. For reflection targets, where the x-rays are collected from the same target side as the striking electrons, the cooling is carried out by a cooling agent on the opposite surface from the one exposed to the electron beam. For transmission x-ray targets, where the x-rays are collected from the opposite surface than that exposed to the electrons, cooling can be carried out at the circumference.

According to Oosterkamp (1948), a cooling water flow of 8 m s^{-1} can dissipate a maximum amount of heat flux from the cooled surface of the target equal to 2400 watts cm^{-2}. This heat flux raises the temperature of the cooling water just below its boiling point.

Oosterkamp's work on the cooling of reflection x-ray targets cannot be used in the present work since he only considered cases for which the electron penetration in the target is negligible compared with the electron spot diameter d (i.e. $x_o/d_g \ll 0.1$).

Cosslett (1952) has derived an expession for the heat dissipation in thin foil targets assuming that the heat flow within the target is in a purely radial direction. He made the assumption that the electron spot diameter is larger than the thickness (ℓ) of the target ($d \ggg \ell$). Because of this assumption Cosslett's work cannot be applied to the present work since the electron spot sizes of interest in the present work are much smaller than the electron penetration in the target and for targets with a thickness less than the spot diameter, electrons will be transmitted through the target.

In order to solve the problem of finite targets applicable to the present work, an electron diffusion model such as the Archard model (1961), must be used to predict the heat flux arriving at the finite boundaries of the target. The use of such a model will involve complicated computational procedures and it will not be considered in the present work, but the computations required to solve the above problem are discussed in more detail in chapter 6.

A transmission x-ray target, where the usuful x-rays are collected from the opposite surface than the one exposed to the electron beam, will be of a suitable geometry for the present work. In practice such a target need to be held in place by a holder. Heat arriving at the radial boundary of the target may well be conducted away by this holder and in some cases, especially when the target seals the vacuum and one of its surfaces is exposed in air, water cooling may not be required for a small range of electron spot sizes formed on the x-ray target.

Simple experiments were carried out in vacuum on a thin disc transmission x-ray copper target which was held in the correct position by a holder. The object of these experiments was to determine experimentally the range of electron spot sizes for which cooling of the target is not necessary. These experiments and the experimental results are discussed in chapter 4.

1.2.3 The probe forming system

At low electron accelerating voltages and electron spot sizes in the region of 0.1 to 2 μm in diameter, the power input to the x-ray target is limited by the power that the probe forming system can deliver to the x-ray target, as shown in figure 1.5. The power that the probe forming system can deliver to the x-ray target can be increased by reducing the aberrations of the objective lens of the probe forming system or by increasing the electron gun brightness.

Mulvey (1967) discusses the electron optical problems that have to be solved in order to obtain maximum intensity in the smallest possible electron probe, bearing in mind the special applications of probes of different diameter.

Consider the probe forming system shown in figure 1.7; a two-stage demagnifying system with an electron source, an intermediate (condenser) lens and a final (objective) lens.

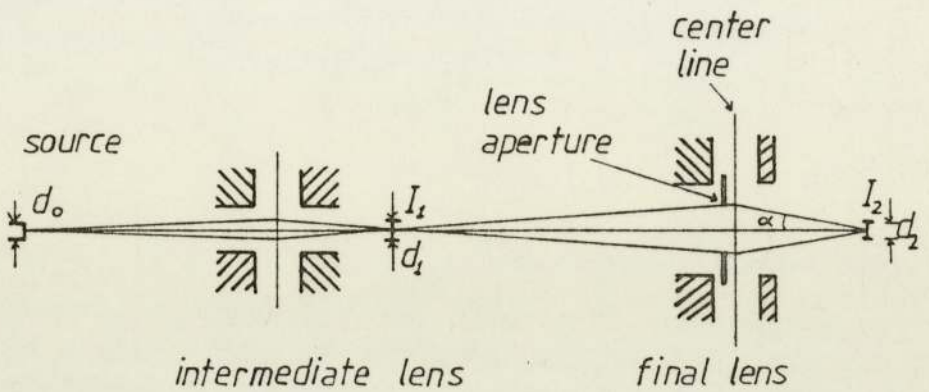

Figure 1.7 Schematic representation of a two-stage demagnifying electron probe forming system.

The ultimate performance of any probe forming system depends on the brightness of the electron source (Haine and Linder 1967). The most common electron source is the triode gun with hairpin filament, which is generally employed if the total probe size is greater than 0.1 μm, corresponding to probe currents of more than a few micro-amperes (Venables, 1976). A thermionic source produces a spot with an approximately Gaussian distribution of halfwidth in the region of 40 to 50 μm. In the present investigation the required electron spot sizes are in the region of 0.1 to 2 μm in diameter and therefore the demagnifying system must provide a demagnification of some 20 to 500 times.

In a two-stage system, such as that shown in figure 1.7, the intermediate lens produces a demagnified image I_1 of the electron source. This is further demagnified by the objective lens which

forms the final image I_2 of diameter d_2 on the x-ray target. The x-ray target plane is usually fixed and cannot easily be changed and therefore the required demagnification is obtained by varying the excitation of the intermediate lens while operating the objective lens at its optimum excitation.

It is generally important that the final image should be physically accessible, that is, well clear of the lens body, to allow for target manipulation, the extraction of x-rays from the specimen and for visual inspection, if necessary, with an optical microscope. A large solid angle around the specimen is also desirable for the optimum positioning of the x-ray detector for micro-x-ray fluorescence analysis.

The condition of accessibility is difficult to fulfil without allowing the lens aberrations to increase to a point where they seriously enlarge the diameter of the electron probe. This can be minimised by restricting the maximum lens aperture, but this reduces the maximum available probe current. The successful design is one which reconciles these conflicting requirements with the minimum sacrifice to performance.

The aberrations of the intermediate lens are not normally significant since its aperture angle is considerably less than that of the objective. Hence when designing a probe forming system, the design of the objective lens must be considered first. One may then proceed with the design of the intermediate lens. In the present work attention has therefore been concentrated on the design requirements of the objective lens.

With the recent development in the miniaturization of magnetic lenses and especially the development of the single polepiece lens for micro-x-ray sources (Harris and Mulvey, 1976; Pugh and West, 1977; Christofides and Mulvey, 1980), it is now possible to consider the optimum design of a single polepiece objective lens for a micro-

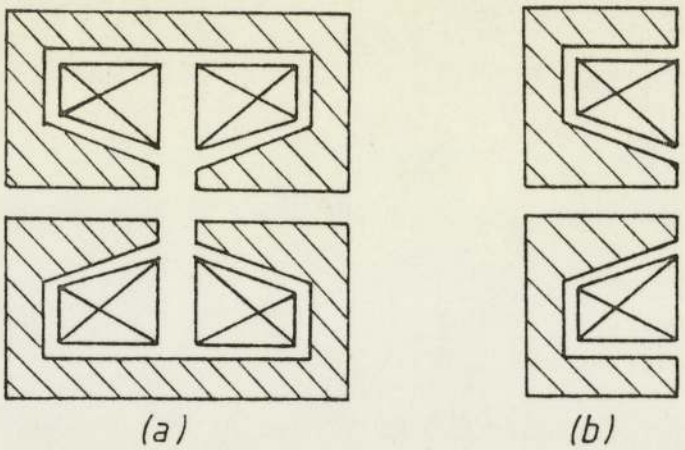

Figure 1.8 Schematic representation of magnetic electron lenses. a) a symmetric conventional lens and b) a single polepiece lens.

x-ray source. This will involve a study of the saturation behaviour of the polepiece.

Figure 1.8 shows the difference between single polepiece and conventional lenses. In a conventional lens, figure 1.8 a), the axial magnetic flux density distribution is contained within the body of the lens; this is electron optically efficient but it restricts the optimum positioning of the detector. In a single polepiece lens, figure 1.8 b), however, most of the axial magnetic flux density distribution lies outside the body of the lens; this could possibly increase the lens aberrations but it allows more room for the optimum positioning of the x-ray detector. Provided that the aberrations are kept at an acceptable level a single polepiece lens appears to be eminently suitable objective lens for the probe forming system of a micro-x-ray source (see appendix B).

Because of the asymmetric nature of the axial magnetic flux density distribution, there are two possible orientations in which such a lens may be used to focus an electron beam in a micro-x-ray source. Figure 1.9 shows two rays, one for each lens orientation. A parallel electron beam entering the axial magnetic flux density distribution of a lens will experiance a different strength of

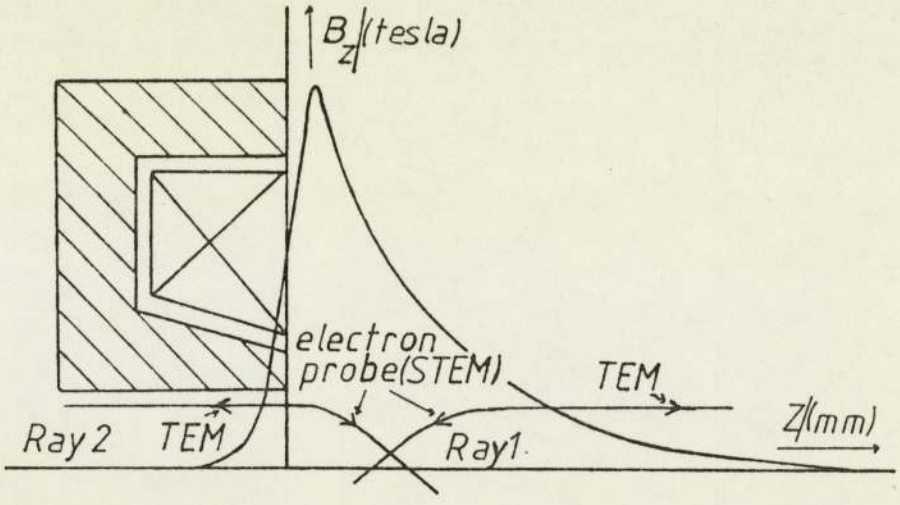

Figure 1.9 Diagram defining the two orientations for which a magnetic lens may be used to focus the beam.

magnetic flux, depending on which lens orientation is used. The parallel electron beam entering the sharp slope of the axial magnetic flux density distribution will be referred to as ray 2 beam orientation and the parallel electron beam entering the shallow slope of the axial magnetic flux density distribution will be referred to as ray 1 beam orientation. The electron optical properties of a single polepiece lens are different for each beam orientation. Once the electron optical properties for each beam orientation have been computed, these can then be applied to a Transmission Electron Microscope (TEM) and to a Scanning Transmission Electron Microscope (STEM).

The electron optical properties of the magnetic electron lens depend mainly on the shape and strength of its axial magnetic flux density distribution. The shape and strength of this distribution, for a given lens, depends strongly on the lens excitation used, the size of the bore in the lens polepieces and the magnetic properties of the magnetic circuit.

Figure 1.10 shows the B/H curve of a typical magnetic material (soft iron) used for lens construction. Initially the B/H curve rises linearly with a sharp slope until it reaches a certain value

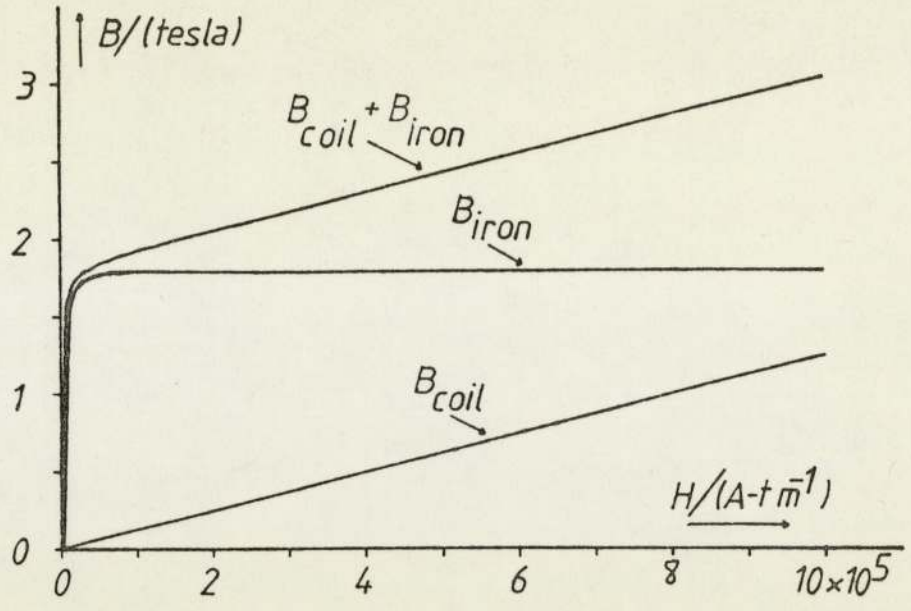

Figure 1.10 The B/H curve of soft iron.

of magnetic flux density. This region is called the linear region of the B/H curve. When a lens is operated in this region, its axial magnetic flux density distribution increases linearly with lens excitation. After this region, the B/H curve increases less sharply and not linearly. At this region, the magnetic material of the lens starts to saturate and the axial magnetic flux density distribution of the lens does not increase linearly with lens excitation. Here the shape of the axial magnetic flux density distribution may be affected more than its strength.

A good lens design should take full advantage of both regions of the B/H curve. In the linear region, the relative size of the bore in the lens polepiece is the main parameter which affects the shape of the axial magnetic flux density distribution, which is of course independent of the lens excitation. In the non-linear region, the shape of the polepiece is an important parameter which affects the shape of the axial magnetic flux density distribution; this shape varies considerably with lens excitation.

The saturation flux density of soft iron is 1.8 Tesla and for

Permendur is 2.4 Tesla. For the purpose of calculation the linear region of the B/H curve has been assumed to extend to 2 Tesla in the following analysis.

Suppose that the axial magnetic flux density distribution and the electron optical properties of a given lens at a given electron accelerating voltage are known. If the lens dimensions and lens excitation are scaled by a factor n, then by Kelvin's rule, the flux density at corresponding points in the original and scaled model is unaltered. If further the original relativistically corrected accelerating voltage ($V_{r_{orig}}$) is scaled by a factor n^2, then $NI/V_r^{\frac{1}{2}}$ is the same in the original and scaled model. Hence the trajectories in the scaled model are similar to those in the original lens. Thus the electron optical properties of the original lens are scaled by a factor n.

In the linear region of the B/H curve the magnetic flux density is proportional to the lens excitation. Thus for purposes of comparison the excitation NI of a lens with a given shape can be scaled linearly by a factor $2/B_{pf}$ so that its poleface flux density B_{pf} becomes 2 Tesla, the limit of the linear region. The lens excitation NI is given by :

$$NI = (2/B_{pf})\ NI_A \quad \text{- - - - - - - - - - - - - - -1.4}$$

where

NI_A is the original lens excitation giving a poleface flux density B_{pf}.

Further more it should be remembered that if the dimensions of any lens are scaled by a geometrical factor n and the lens excitation is also scaled by the same factor n, the flux density at corresponding points in the original and scaled lens are identical irrespective of excitation. In the linear region of the B/H curve the geometrical factor n can be combined with equation 1.4 into one factor G given by :

$$G = (B_{pf}/2)(NI_G/NI_A) \text{ - - - - - - - - - - - - - - - - - } 1.5$$

where

NI_G is the lens excitation for a particular geometrical scaling factor G.

The scaling factor G ensures that the scaled dimensions and electron optical properties of a lens are expressed for a lens excitation which provides a poleface flux density B_{pf} of 2 Tesla.

In the non-linear region of the B/H curve, both the strength and shape of the axial magnetic flux density distribution of a lens change with lens excitation. Thus the linear relationship in equation 1.5 giving the geometrical factor G cannot be used in this region of the B/H curve. A lens intented to operate in the non-linear region of the B/H curve, must first be optimised in the linear region of the B/H curve by the use of the geometrical factor G given by equation 1.5.

Once a lens is optimised in the linear region of the B/H curve, then to obtain its electron optical properties in the non-linear region of the B/H curve as a function of lens excitation and at a given electron accelerating voltage, for example 50 KV, the axial magnetic flux density distribution of the lens must be computed at several lens excitations. Each axial magnetic flux density distribution will give one value of each of the electron optical properties at the given electron accelerating voltage of 50KV. The lens excitation giving the optimum electron optical properties is thus the optimum lens excitation of the lens at 50 KV under the non-linear region of the B/H curve. The optimum lens excitation also gives the optimum shape and strength of the axial magnetic flux density distribution of the lens under the non-linear region of the B/H curve for the given electron accelerating voltage of 50 KV.

Once the optimum lens excitation and electron optical properties of a lens have been obtained under the non-linear region of the B/H curve and at a given electron accelerating voltage, these together with the lens dimensions can be scaled to any electron accelerating voltage by using the geometrical scaling factor n.

There are a number of computer programs available which compute the axial magnetic flux density distribution and electron optical properties of magnetic electron lenses (Munro,1975; Nasr, 1981; these are detailed in appendix C). These programs were used in the design of an objective lens suitable for the probe forming system of a multi-purpose micro-x-ray source.

The preliminary work of Juma and Mulvey (1980) on the axial magnetic flux density distribution of single polepiece lenses, was used as a starting point for optimising the bore of the objective lens as described in chapter 2.

In chapter 3 the best lens design for the probe forming system of a multi-purpose micro-x-ray source is compared with previous objective lenses of micro-x-ray sources (Harris and Mulvey,1976; Pugh and West, 1977; Rockett and Brundin, 1980). The superiority of the lens design of the present work as an objective lens for a micro-x-ray source is shown clearly from these comparisons.

In the light of the computed results an objective lens suitable for the probe forming system of a micro-x-ray source was constructed and tested experimentally. The experimental work and the experimental results are discussed in chapter 4.

An electron focusing technique previously proposed and used by Pugh and West (1977) was investigated experimentally in order to clarify the mechanism of detecting the point of focus. An account of this investigation is also given in chapter 4. The mode of operation of this focusing method is now clearer and it subsequently formed an integral part of the experimental micro-x-ray source.

It is shown that objective lenses designed primarily for micro-x-ray sources, after appropriate scaling, are also suitable as objectives in high resolution electron microscopes. The optimised lens designs are compared with existing objective lenses incorporated in commercially available high resolution electron microscopes. These comparisons are discussed in chapter 3. In the same chapter a critical assessment of the high resolution lens designs proposed by Cleaver (1980) is made. This assessment was only possible from the conclusive evidence of the present investigation.

2 The objective lens

2.1 Optimising the lens bore

The performance of any magnetic lens may be improved, in general, by increasing the peak value of the axial magnetic flux density distribution and reducing its halfwidth. In a single polepiece lens high flux densities can only be achieved by careful design of the magnetic circuit and careful positioning of the exciting coil. The later consideration is usually unimportant in a conventional twin-polepiece lens. The BASIC lens shown in figure 2.1, the starting point of the present investigation, illustrates these points.

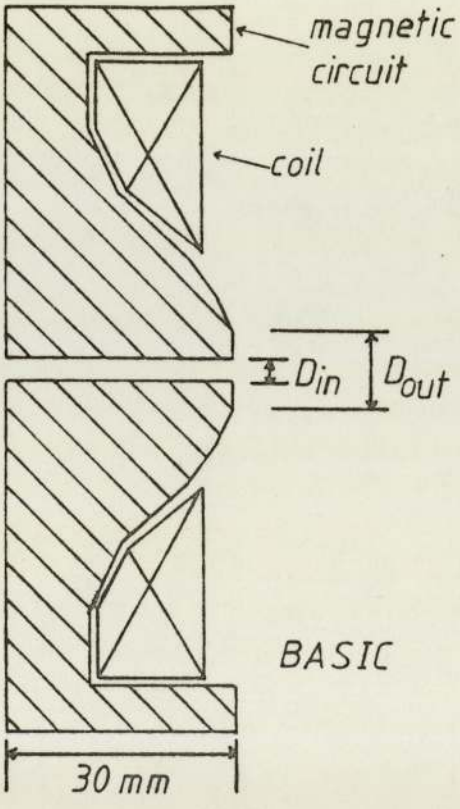

Figure 2.1 Schematic representation of the BASIC lens.

The shape of the magnetic circuit and especially of the polepiece of this lens was chosen so that the maximum flux density inside the magnetic circuit will be in the neighbourhood of the polepiece tip. The coil windings are also of a complicated shape, in order to occupy all the available area.

By keeping all the other dimensions of the BASIC lens unchanged, but varying the bore diameter D_{in}, a number of different axial magnetic flux density distributions were obtained using the Munro program M12 (see appendix C). This program assumes that the magnetic permeability of the lens magnetic circuit is high ($\mu = 10^4$).

These field distributions, shown in figure 2.2, may be identified by the corresponding bore ratio D_{in}/D_{out}.

From this figure, it can be seen that when the bore ratio is very small, the maximum flux density inside the magnetic circuit does not occur at the tip of the polepiece but further in from the tip. This is a consequence of the shape and position of the lens coil (see appendix D) which is not a limiting factor in the linear magnetic region but becomes important in lenses in which the polepiece tip is strongly saturated. As the bore ratio increases the maximum flux density inside the magnetic circuit moves towards the polepiece tip and also increases in value sharply. This is due to the presence of the bore which causes the axial lines of magnetic force to come closer to each other at the inner polepiece tip.

The peak of the axial magnetic flux density distribution decreases with increasing bore ratio and also shifts away from the tip of the polepiece. The spread of the axial magnetic flux density distribution inside the lens bore increases as the bore ratio increases. This has the effect of increasing the halfwidth of the axial magnetic flux density distribution. The peak and halfwidth of the axial magnetic flux density distribution of a lens are related to the electron optical properties of the lens. As the peak decreases and the halfwidth increases with increasing bore ratio, it is expected that the electron optical properties of the lens will become worse.

The electron optical properties of the axial magnetic flux density distributions of figure 2.2, were computed by the Munro

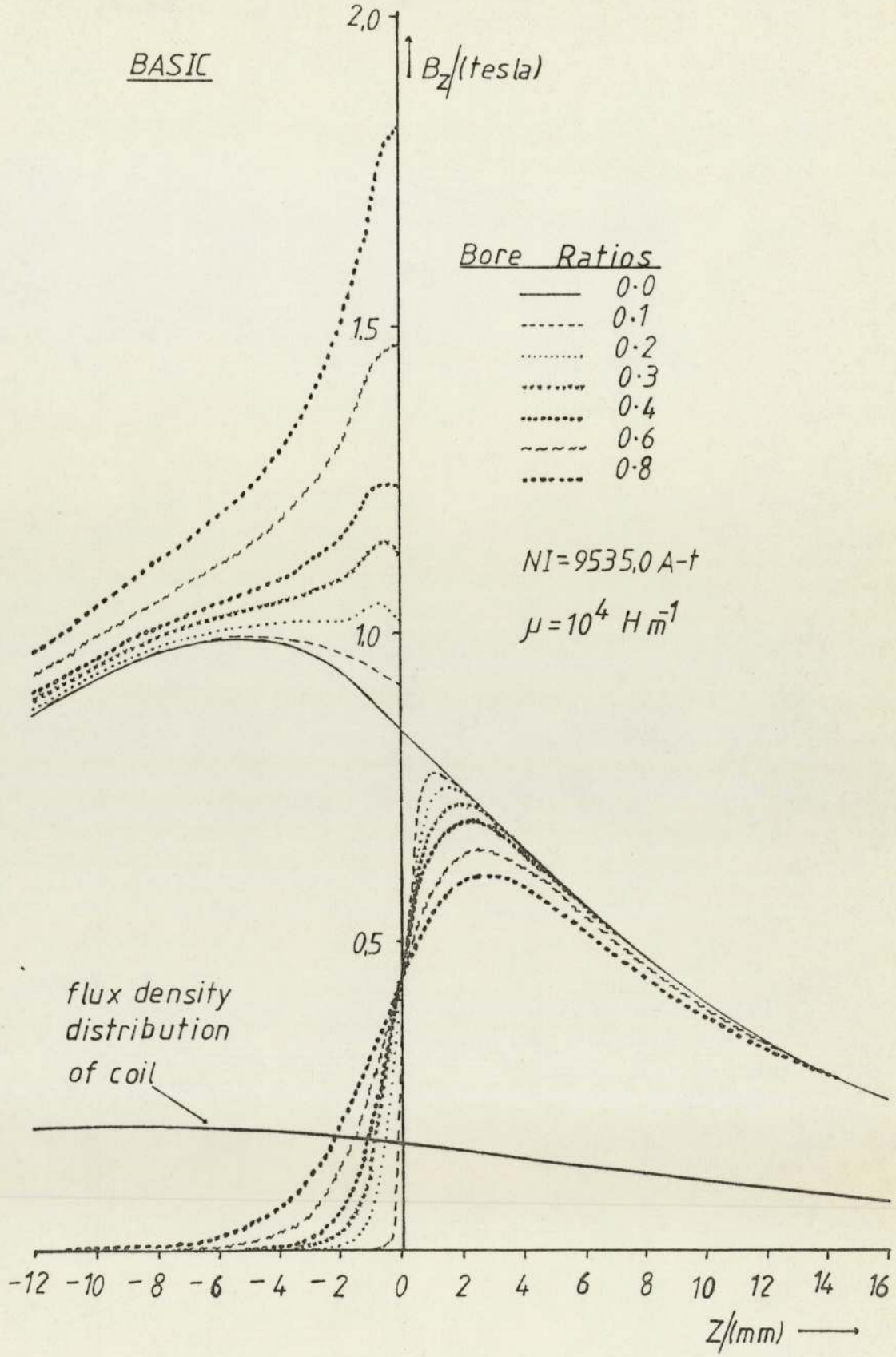

Figure 2.2 Variation of the axial magnetic flux density distribution for the BASIC lens with bore rario D_{in}/D_{out}.

program M21, for ray 1 and ray 2 beam orientations, as defined by figure 1.9.

By using the scaling factor G, given by equation 1.5, it would be possible to compare these field distributions of the BASIC lens, at a standard poleface flux density of 2 Tesla. This would be a useful comparison if the original poleface flux density of each field distribution were a maximum at the polepiece tip. However as can be seen from figure 2.2, this is not true for all the field distributions. If the flux density reaches a maximum elsewhere than at the polepiece tip, such a lens, when operated under non-linear magnetic conditions, will exhibit saturation effects before the polepiece tip reaches saturation. In view of this it is perhaps more realistic to use the maximum flux density inside the polepiece as a criterion of comparison rather than the magnetic flux density at the polepiece tip itself. Therefore in subsequent comparisons, the value of B_{pf} in equation 1.5 , has been replaced by the maximum magnetic flux density B_{pp} within the polepiece. As stated previously, in an ideal design the flux densities B_{pp} and B_{pf} would be identical.

2.1.1 Comparison of the electron optical properties for ray 2 beam orientation

The calculated electron optical properties of the BASIC lens, subject to the above conditions are shown in the following figures.

The original calculations were carried out at an electron accelerating voltage V_r = 100 KV. In order to give the curves a universal character, the electron optical properties in these curves are expressed in the form $C_s(10^5/V_r)^{\frac{1}{2}}$ with a corresponding excitation $NI(10^5/V_r)^{\frac{1}{2}}$. This is possible since a linear relation is assumed to exist between the flux density distribution and the excitation.

Figure 2.3 shows the variation of the spherical aberration

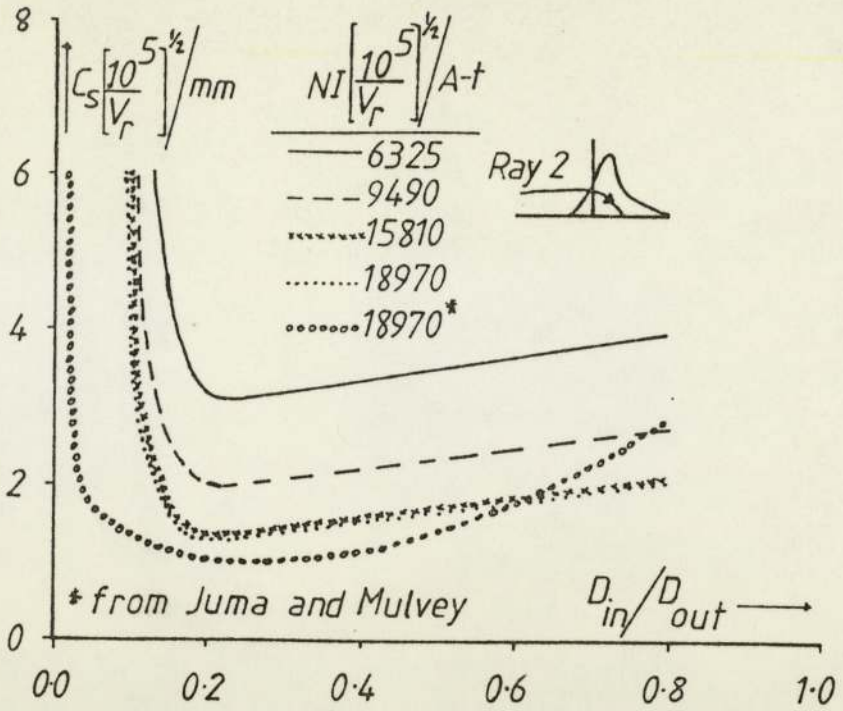

Figure 2.3 The variation of the spherical aberration coefficient of the BASIC lens, as a function of lens bore ratio, at different lens excitations, for ray 2 beam orientation. The experimental results of Juma and Mulvey are added for comparison.

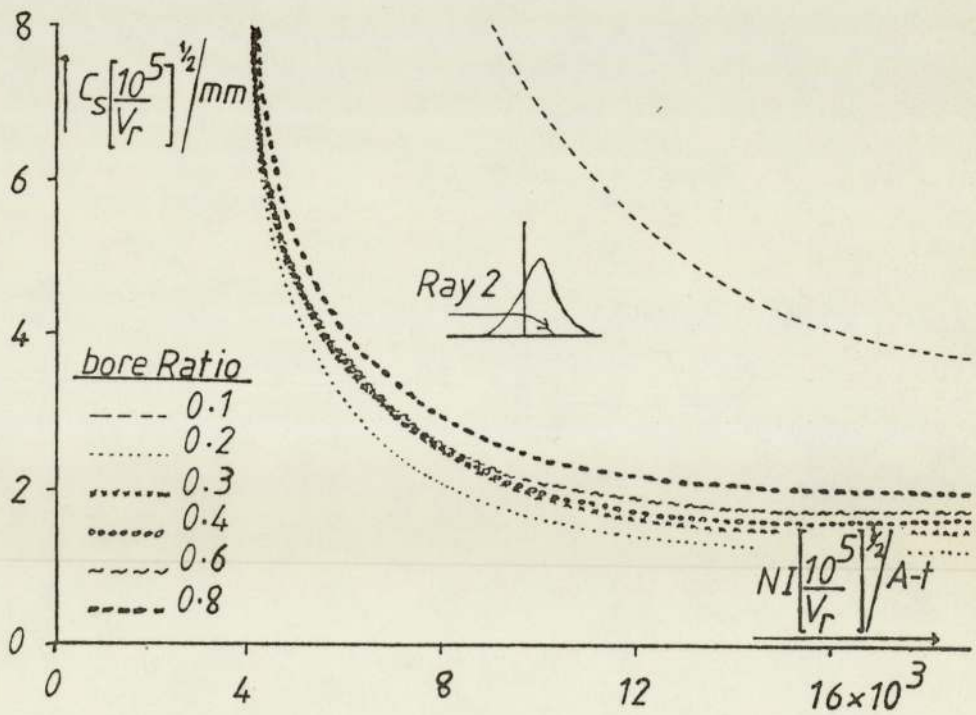

Figure 2.4 The variation of the spherical aberration coefficient of the BASIC lens, as a function of lens excitation, at different lens bore ratios, for ray 2 beam orientation.

coefficient $C_s(10^5/V_r)^{\frac{1}{2}}$ of the BASIC lens, as a function of lens bore ratio D_{in}/D_{out}, for different lens excitations $NI(10^5/V_r)^{\frac{1}{2}}$(ray 2). Figure 2.4 shows the variation of the spherical aberration coefficient $C_s(10^5/V_r)^{\frac{1}{2}}$ of the BASIC lens, as a function of lens excitation $NI(10^5/V_r)^{\frac{1}{2}}$, for different bore ratios D_{in}/D_{out} (ray 2).

In both these figures the spherical aberration coefficient decreases with increasing lens excitation, sharply at low lens excitations but levelling off at high lens excitations. The spherical aberration coefficient decreases initially with increasing bore ratio, passing through a minimum at a bore ratio of 0.2. For bore ratios higher than 0.2, the spherical aberration coefficient increases but only slowly.

Juma and Mulvey's results (1980) from their experimental rectangular polepiece lens show similar variations of the spherical aberration coefficient and lens bore ratio. Their minimum spherical aberration occurs at the same lens excitation as in the present work and is shown for comparison purposes in figure 2.3. From this curve can be seen that in the Juma and Mulvey rectangular lens the minimum spherical aberration coefficient occurs at a bore ratio of 0.25, while that of the BASIC lens occurs at a lens bore ratio of 0.2. The minimum value of the spherical aberration coefficient of the rectangular lens is slightly lower than that of the BASIC lens.

Although the lenses are different in shape and although one lens was studied theoretically and the other experimentally, the spherical aberration coefficient of both lenses show similar variation with lens excitation and lens bore ratio.

Figure 2.5 shows the variation of the chromatic aberration coefficient $C_c(10^5/V_r)^{\frac{1}{2}}$ of the BASIC lens, as a function of the lens excitation $NI(10^5/V_r)^{\frac{1}{2}}$, at different lens bore ratios D_{in}/D_{out} (ray 2). Figure 2.6 shows the variation of the objective focal

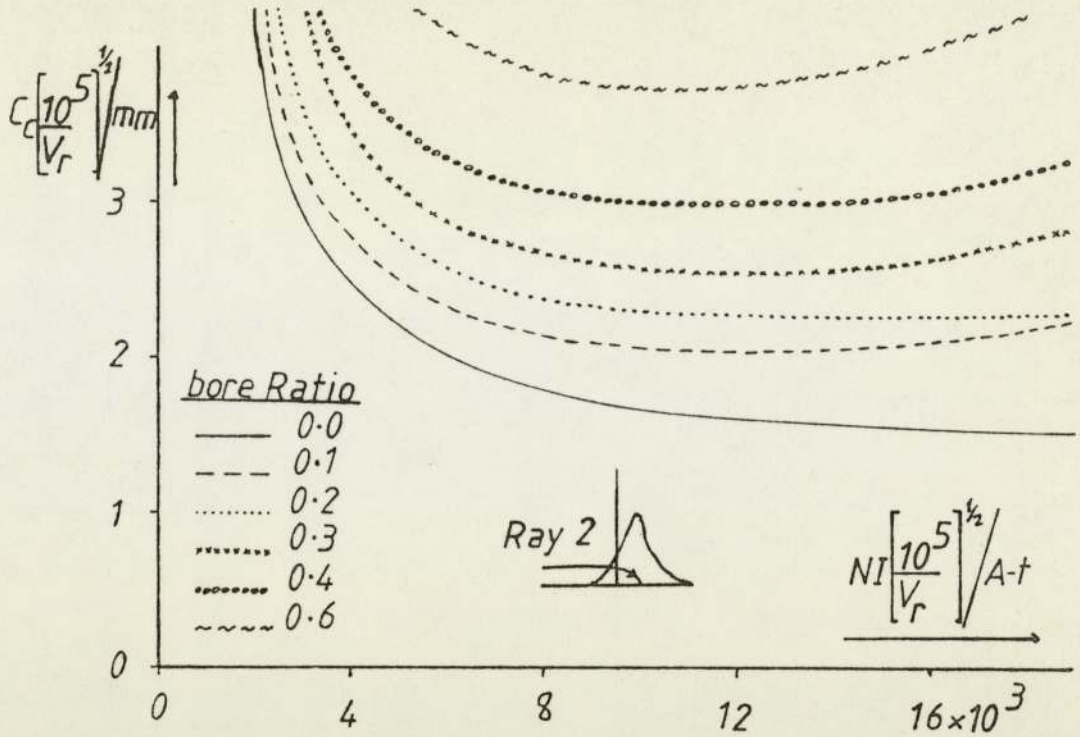

Figure 2.5 The variation of the chromatic aberration coefficient of the BASIC lens, as a function of lens excitation, at different lens bore ratios, for ray 2 beam orientation.

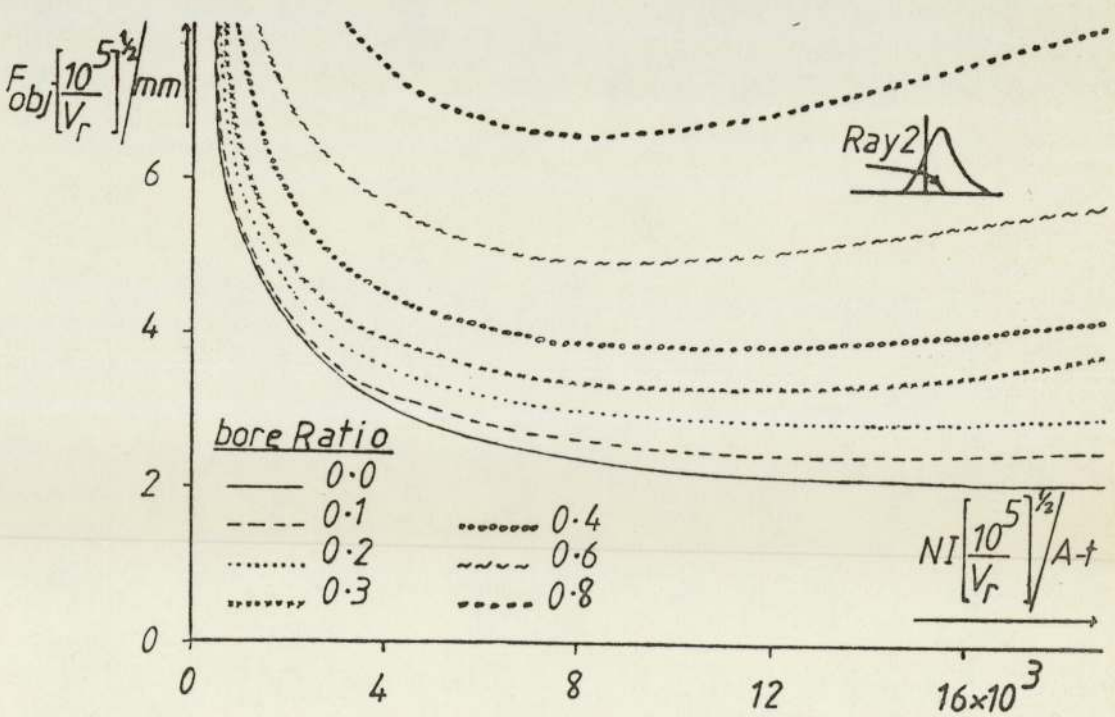

Figure 2.6 The variation of the objective focal length of the BASIC lens, as a function of lens excitation, at different lens bore ratios, for ray 2 beam orientation.

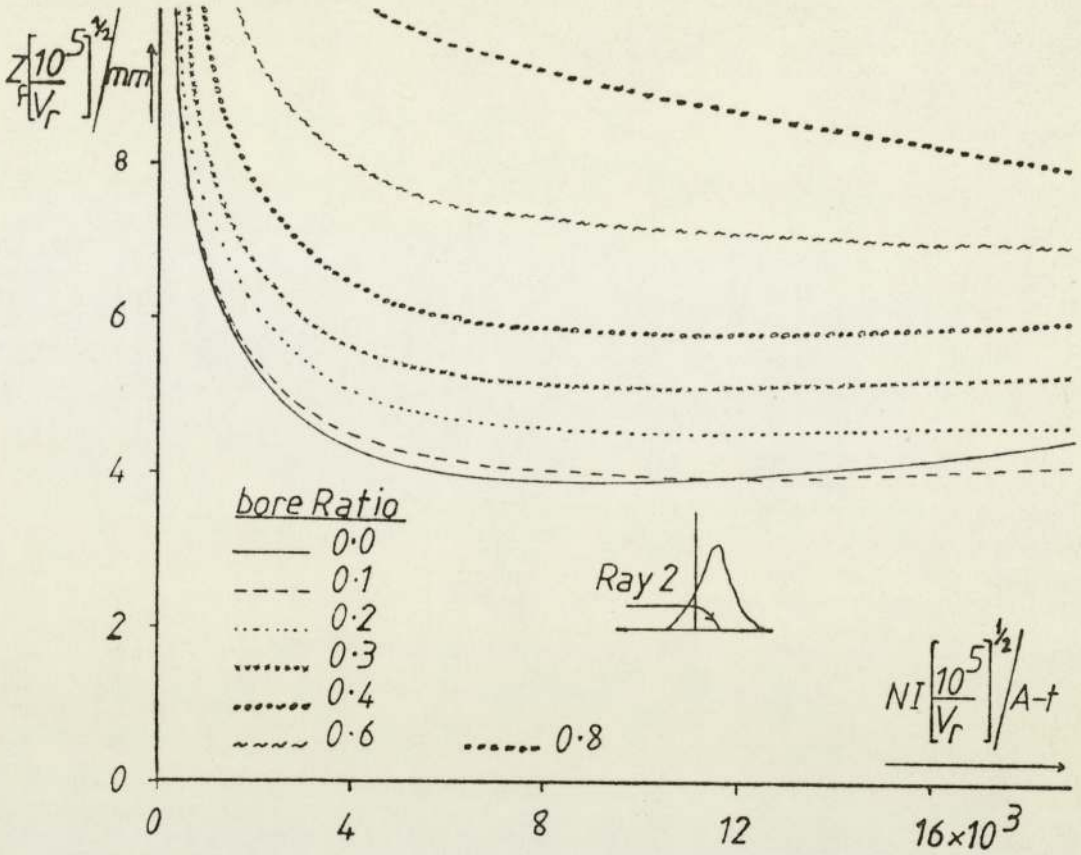

Figure 2.7 The variation of the working distance of the BASIC lens, as a function of lens excitation, at different lens bore ratios, for ray 2 beam orientation.

length $F_{obj}(10^5/V_r)^{\frac{1}{2}}$ of the BASIC lens, as a function of lens excitation $NI(10^5/V_r)^{\frac{1}{2}}$, for different lens bore ratios D_{in}/D_{out} (ray 2). Figure 2.7 shows the variation of the working distance $Z_f(10^5/V_r)^{\frac{1}{2}}$ of the BASIC lens, as a function of lens excitation $NI(10^5/V_r)^{\frac{1}{2}}$, for different lens bore ratios D_{in}/D_{out} (ray 2).

The main feature of figures 2.5, 2.6 and 2.7, is that the relevant focal property in each figure increases as the lens bore ratio increases. This is due to the dependence of these properties on the slope of the axial magnetic flux density distribution dB/dz, which the incoming electron beam faces on entering the axial magnetic flux density distribution of a lens. An axial magnetic flux density distribution with an infinite slope facing the incoming electron beam, will give the lowest values of chromatic aberration coefficient, objective focal length and working distance.

A lens with zero bore ratio, which can be approximated in practice by inserting a bore small in diameter compared to that of the polepiece, has an axial magnetic flux density distribution with an infinite slope facing the incoming electron beam in ray 2 beam orientation. Such a lens gives particularly low values of the chromatic aberration coefficient, objective focal length and working distance, as shown by figures 2.5, 2.6 and 2.7 respectively.

As the bore ratio increases the slope of the axial magnetic flux density distribution decreases and hence the chromatic aberration coefficient, objective focal length and working distance will also increase but only slowly. It should be notted that the spherical aberration coefficient increases rapidly as the bore ratio tends to zero. In practice therefore there will be a conflict between the requirement to reduce chromatic and spherical aberration to the lowest possible value. This is illustrated in table 2.1 which shows the conditions for (a) minimum chromatic aberration with its associated spherical aberration and other parameters and (b) minimum spherical aberration together with the associated chromatic aberration and other parameters.

Table 2.1 The optimum electron optical properties and lens excitations of the scaled BASIC lens with zero and 0.2 lens bore ratios for ray 2 and an electron accelerating voltage V_r.

$\frac{D_{in}}{D_{out}}$	NI $\left[\frac{10^5}{V_r}\right]^{\frac{1}{2}}$ (A-t)	X $\left[\frac{10^5}{V_r}\right]^{\frac{1}{2}}$ (mm)	$C_s \left[\frac{10^5}{V_r}\right]^{\frac{1}{2}}$ (mm)	$C_c \left[\frac{10^5}{V_r}\right]^{\frac{1}{2}}$ (mm)	$F_{obj} \left[\frac{10^5}{V_r}\right]^{\frac{1}{2}}$ (mm)	$Z_f \left[\frac{10^5}{V_r}\right]^{\frac{1}{2}}$ (mm)
0.0	16000	67.4	∞	1.55	2.10	4.15
0.2	16000	81.7	1.30	2.25	2.85	4.60

For example, at an electron accelerating voltage V_o = 200 KV (V_r = 240 KV), the BASIC lens with a bore ratio of 0.2 will have an external diameter X of 126.55 mm and must be operated at a lens excitation of 24780 A-t in order to provide its minimum electron optical properties, which are C_s = 2.0 mm, C_c = 3.5 mm, F_{obj} = 4.4 mm and Z_f = 7.1 mm. For a 1 μm diameter electron spot, provided that $d_g = d_s$, the E.H.T. supply must be stable to one part in a thousand, a requirement which can easily be met.

The scaled BASIC lens with 0.2 bore ratio, has a relatively low chromatic aberration coefficient and can be regarded as a favourable compromise, if a lens with low spherical and low chromatic aberration coefficients is required. This lens will be suitable for a micro-x-ray source.

For x-ray work an electron accelerating voltage V_r of 50 KV is sufficient. Table 2.2 gives the electron optical properties and excitation of the scaled lens with 0.2 bore ratio, at an electron accelerating voltage V_r of 50 KV.

Table 2.2 The optimum electron optical properties and excitation of the scaled BASIC lens with 0.2 bore ratio, for ray 2 and an electron accelerating voltage V_r of 50 KV.

V_r/KV	NI/A-t	X/mm	C_s/mm	C_c/mm	F_{obj}/mm	Z_f/mm
50	11314	57.8	0.92	1.59	2.02	3.25

The probe current that a probe forming system with such a lens can supply to an x-ray target is 11.06 μA, in a 1 μm diameter spot, assuming an electron gun brightness of $2.5 \times V_o$ A $cm^{-2} sr^{-1}$. This current corresponds to a power density input to the x-ray target of

7.04×10^7 watts cm^{-2} at an electron accelerating voltage V_r of 50 KV. This value of power density input agrees well with the value given in figure 1.5 in the introduction. For a 1 μm diameter electron spot, provided that $d_g = d_s$, the E.H.T. supply must be stable to one part in a thousand, a requirement which can easily be met. The difference between the objective focal length and the working distance given in table 2.2 is large enough to accommodate an electron beam aperture. From the above discussion it is clear that such a lens is suitable as the objective lens of the probe forming system of a micro-x-ray source.

2.1.2 Comparison of the electron optical properties in ray 1 beam orientation

Figure 2.8 shows the variation of the spherical aberration coefficient $C_s(10^5/V_r)^{\frac{1}{2}}$ of the BASIC lens, as a function of lens bore ratio D_{in}/D_{out}, for different lens excitation $NI(10^5/V_r)^{\frac{1}{2}}$ (ray 1). Figure 2.9 shows the variation of the spherical aberration coefficient $C_s(10^5/V_r)^{\frac{1}{2}}$ of the BASIC lens, as a function of lens excitation $NI(10^5/V_r)^{\frac{1}{2}}$, for different lens bore ratios D_{in}/D_{out} (ray 1).

These two figures show that the spherical aberration coefficient has a minimum at a lens excitation of $4300(V_r/10^5)^{\frac{1}{2}}$ and decreases with decreasing bore ratio. In practice a lens with a bore diameter small compared with the diameter of the poleface will have characteristics indistinguishable from those of a lens with no bore. In such a lens the electron beam may be brought to a focus inside the bore and its aberrations will increase rapidly as shown in both figures.

Juma and Mulvey's results for ray 1 beam orientation arrive at essentially the same conclusions. For comparison purposes figure

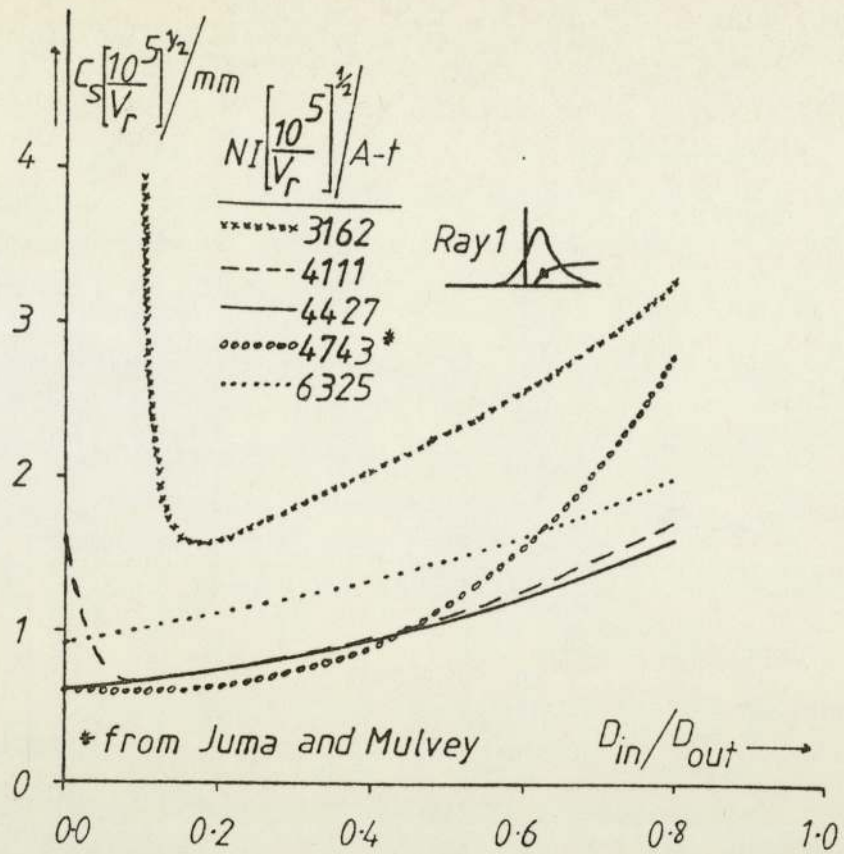

Figure 2.8 The variation of the spherical aberration coefficient of the BASIC lens, as a function of lens bore ratio, at different lens excitations, for ray 1 beam orientation. The experimental results of Juma and Mulvey are added for comparison.

2.8 shows their curve of the minimum spherical aberration coefficient for a given bore ratio. The corresponding lens excitation $NI(10^5/V_r)^{\frac{1}{2}}$ is some 7% higher than the value calculated here, which is possibly due to experimental error. However the discrepancy in the spherical aberration coefficient values at large values of the bore ratio D_{in}/D_{out} is probably due to an incorrect assessment of the peak value of magnetic flux B_{pp} in the experimental lens of Juma and Mulvey since they were not able to measure this quantity directly. Fortunately this discrepancy occurs at bore ratios far removed from the optimum condition. In the important region of small bore ratio in figure 2.8 there is remarkly good agreement between the experimental values and those calculated here.

Figures 2.10 and 2.11 show the variation of the chromatic

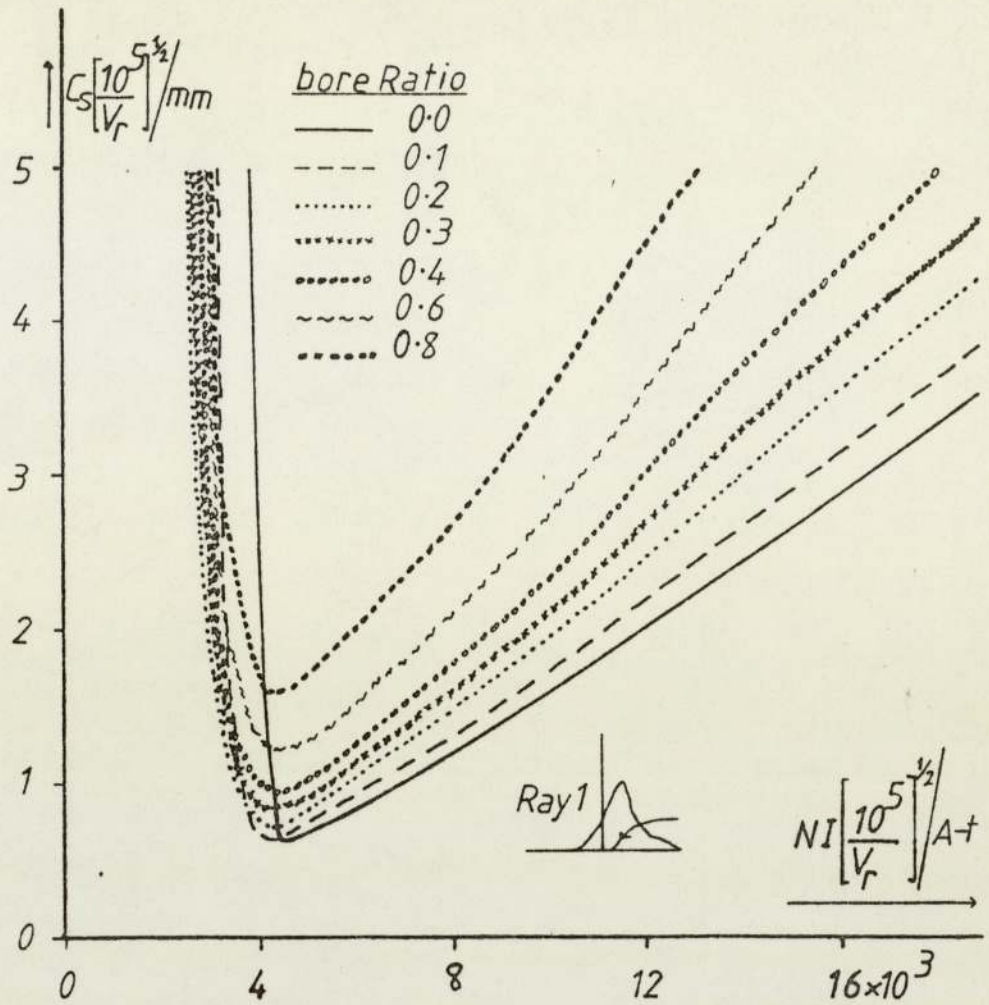

Figure 2.9 The variation of the spherical aberration coefficient of the BASIC lens, as a function of lens excitation, at different lens bore ratios, for ray 1 beam orientation.

aberration coefficient $C_c(10^5/V_r)^{\frac{1}{2}}$ and the closely related objective focal length $F_{obj}(10^5/V_r)^{\frac{1}{2}}$ of the BASIC lens, respectively as a function of lens excitation $NI(10^5/V_r)^{\frac{1}{2}}$, for different lens bore ratios D_{in}/D_{out}, for ray 1 beam orientation.

These curves show that the chromatic aberration coefficient and the objective focal length decrease initially with lens excitation, reaching a minimum value at a lens excitation in the region of $3400(V_r/10^5)^{\frac{1}{2}}$ A-t. It should be noted that in ray 1 beam orientation, the minimum spherical and minimum chromatic aberration

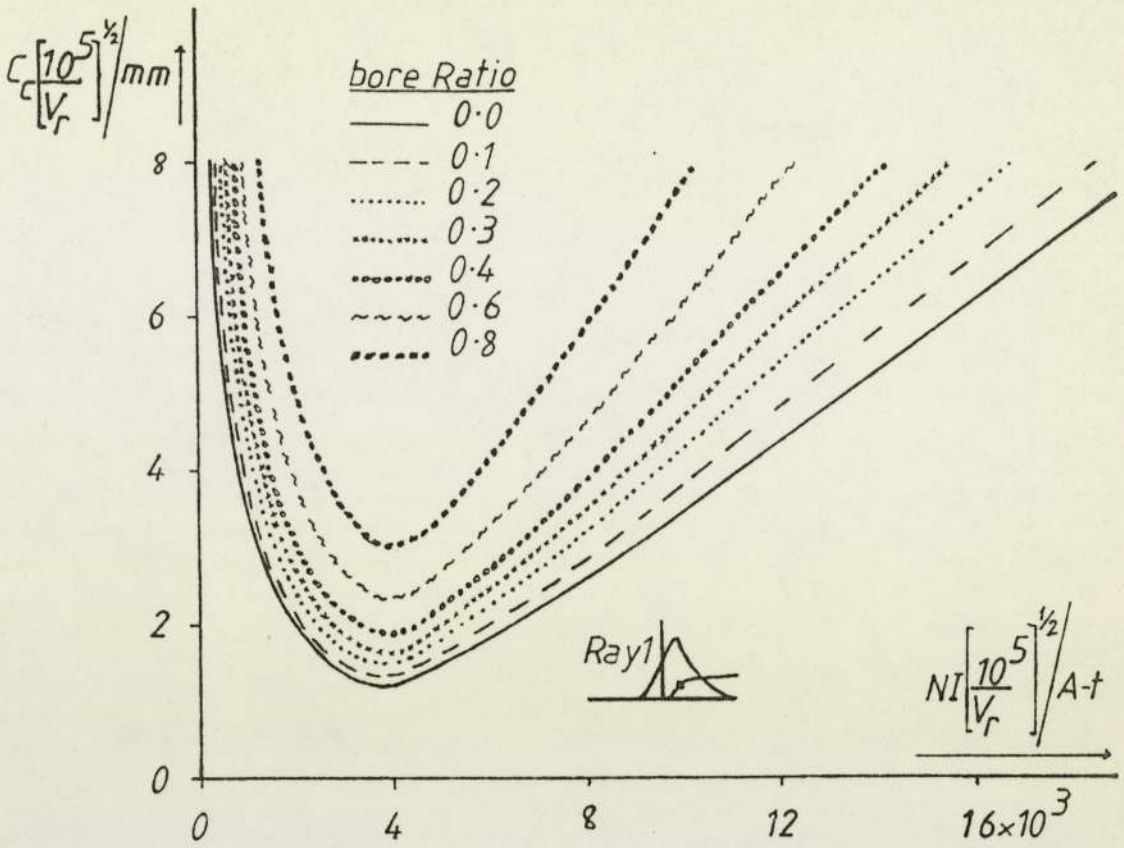

Figure 2.10 The variation of the chromatic aberration coefficient of the BASIC lens, as a function of lens excitation, for different lens bore ratios, for ray 1 beam orientation.

coefficients occur at about the same lens excitation.

Figure 2.12 shows the variation of the working distance $Z_f(10^5/V_r)^{\frac{1}{2}}$ of the BASIC lens, as a function of lens excitation $NI(10^5/V_r)^{\frac{1}{2}}$, for different lens bore ratios D_{in}/D_{out}, for ray 1 beam orientation.

The working distance increases very sharply with increasing lens excitation, having a negative value (i.e. focus inside the polepiece bore) upto a lens excitation of $4300(V_r/10^5)^{\frac{1}{2}}$ A-t and then it has a positive value. As the bore of the BASIC lens is reduced in size the working distance becomes shorter. It is therefore clear from the above figures that the optimum place for a specimen or x-ray target is at zero working distance, i.e. in contact with

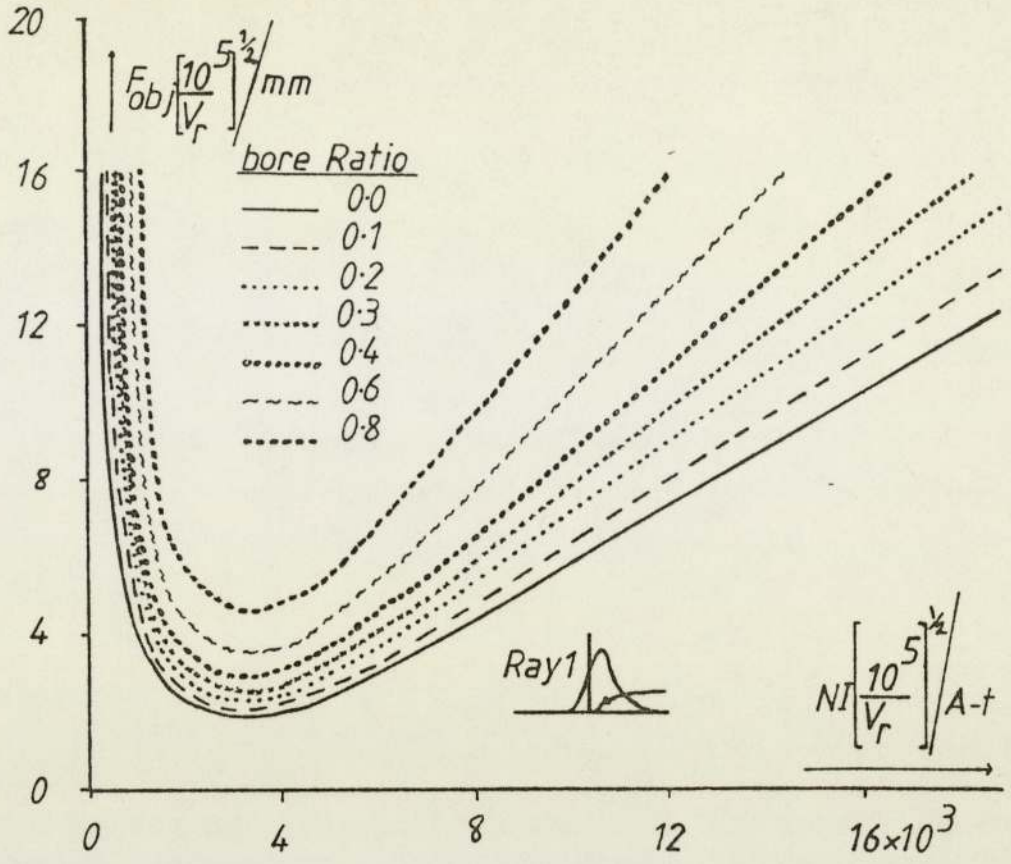

Figure 2.11 The variation of the objective focal length of the BASIC lens, as a function of lens excitation, at different lens bore ratios, for ray 1 beam orientation.

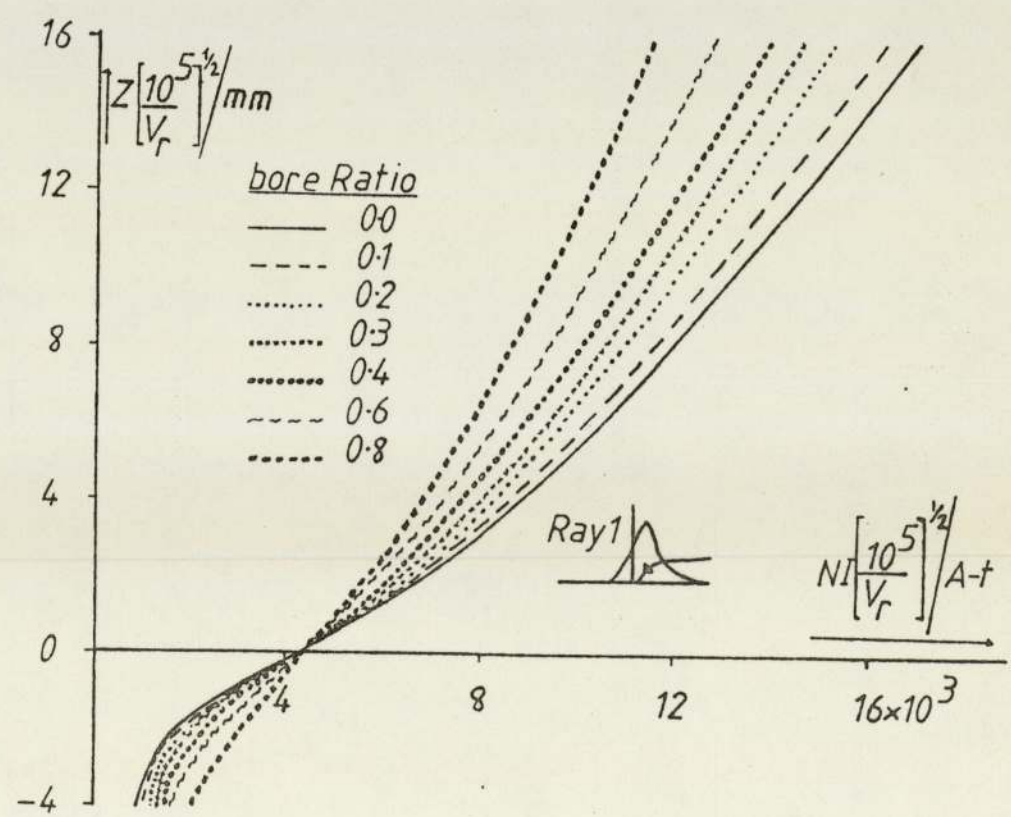

Figure 2.12 The variation of the working distance of the BASIC lens, as a function of lens excitation, at different lens bore ratios, for ray 1 beam orientation.

the poleface of the polepiece, since at this point the aberrations are at a minimum.

Table 2.3 summarises the corresponding electron optical properties and excitations of the scaled BASIC lens with negligibly small bore ratio and zero working distance, for ray 1 beam orientation, at electron accelerating voltages V_r of 50 and 100 KV.

Table 2.3 The electron optical properties and excitations of the scaled BASIC lens with zero bore ratio and zero working distance at electron accelerating voltages V_r of 50 and 100 KV(B_{pp} =2T).

V_r/KV	NI/A-t	X/mm	C_s/mm	C_c/mm	F_{obj}/mm
50	3040	12.7	0.43	0.88	1.48
100	4300	18.0	0.60	1.25	2.10

For example if the scaled BASIC lens in ray 1 beam orientation is operated at an electron accelerating voltage V_r of 50KV, it will provide a probe current of 18.6 μA in an electron spot diameter of 1 μm on the x-ray target, assuming an electron gun brightness of $2.5xV_o$ A $cm^{-2}sr^{-1}$. This probe current corresponds to a power density of $1.18x10^9$ watts cm^{-2}, which can melt a semi-infinite copper target, as can be seen from figure 1.5. For a 1 μm spot diameter, provided that $d_g = d_s$, the E.H.T. supply must be stable to three parts in a thousand.

2.1.3 Performance of the BASIC lens for ray 1 and ray 2

In the previous sub-sections, the optimum bore ratio was determined for ray 1 and ray 2. For each beam orientation the dimensions of the BASIC lens must be scaled by a different scaling factor G in order to achieve their optimum electron optical properties.

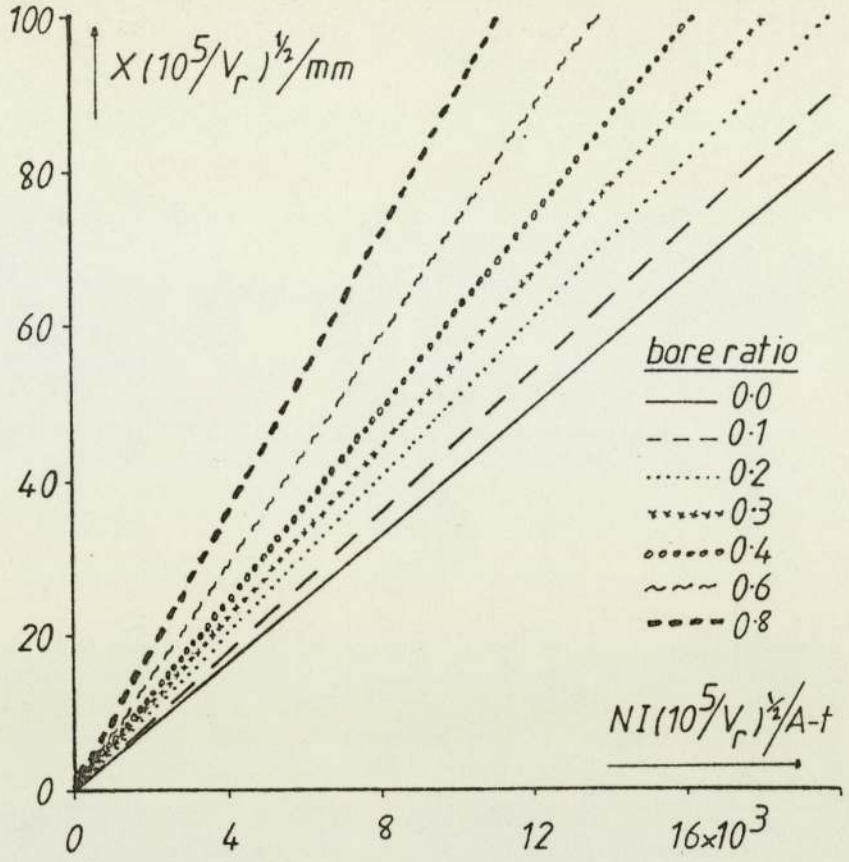

Figure 2.13 The variation of the external diameter of the BASIC lens, as a function of lens excitation, for different lens bore ratios.

Figure 2.13 shows the variation of the external diameter $X(10^5/V_r)^{\frac{1}{2}}$ of the BASIC lens, as a function of lens excitation $NI(10^5/V_r)^{\frac{1}{2}}$, for different lens bore ratios D_{in}/D_{out}. Figure 2.14 shows the variation of the current density $\sigma(V_r/10^5)^{\frac{1}{2}}$ in the coil windings of the BASIC lens, as a function of lens excitation $NI(10^5/V_r)^{\frac{1}{2}}$, for different lens bore ratios D_{in}/D_{out}.

The curves in figures 2.13 and 2.14 are the same for ray 1 and ray 2 since the original magnetic flux density B_{pp} is the same for both beam orientations at a given lens excitation and a given geometrical scaling factor G. For a given electron accelerating voltage V_r, the optimum lens excitation and the optimum bore ratio are different for each beam orientation and therefore the optimum dimensions and the optimum current density (σ) of the BASIC lens

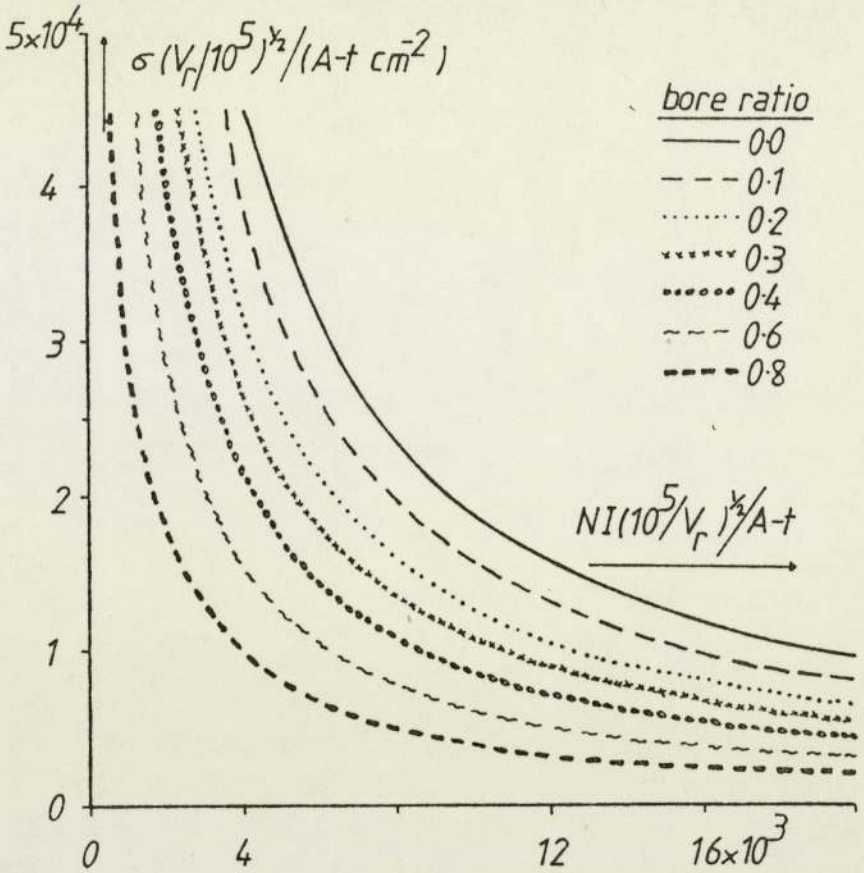

Figure 2.14 The variation of the current density in the coil windings of the BASIC lens, as a function of lens excitation, for different lens bore ratios.

will be different for each beam orientation.

As an example of the use of the curves for the design of a probe forming objective lens for an electron accelerating voltage V_r =50 KV, table 2.4 gives the optimum electron optical properties of a BASIC lens for both beam orientations, assuming a maximum flux density B_{pp} of 2 Tesla in the polepiece.

From table 2.4 the BASIC lens for ray 1 has smaller focal properties and aberrations than the BASIC lens for ray 2. However, ray 1 lens is much smaller (X = 12.7 mm) than the corresponding ray 2 lens (X = 57.8 mm, the relative sizes of these lenses are shown in figure 2.15). In the other hand its excitation of 3040 A-t is much lower than the corresponding ray 2 lens (11314 A-t). The

Table 2.4 Optimisation of spherical and chromatic aberration coefficients with their associated electron optical properties and other parameters of the BASIC lens, at an electron accelerating voltage V_r of 50 KV, for both beam orientations (B_{pp} = 2T).

Coefficient minimised	Ray	D_{in}/D_{out}	NI/A-t	X/mm	C_s/mm	C_c/mm	F_{obj}/mm	Z_f/mm
$C_s + C_c$	1	0.0	3040	12.7	0.43	0.88	1.48	0.0
C_s	2	0.2	11314	57.8	0.92	1.59	2.02	3.25
C_c	2	0.0	11314	47.7	∞	1.10	1.48	2.93

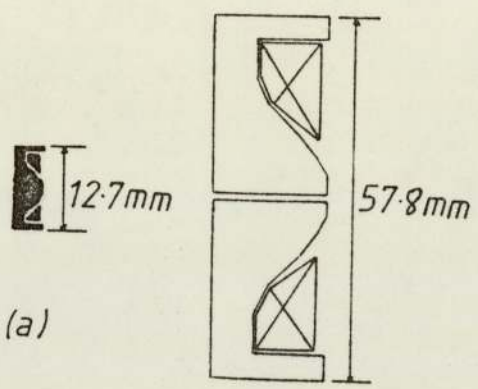

Figure 2.15 The relative dimensions of the scaled BASIC lens, for operation at an electron accelerating voltage V_r of 50 KV. a) ray 1, b) ray 2.

current density in the coil windings of the ray 1 lens is 62335 A-t/cm^2. To achieve such a current density, a superconducting coil would be needed; its small dimensions would also present technological difficulties.

Although the BASIC ray 2 lens has slightly inferior electron optical properties, the current density in its coil windings is 14065 A-t/cm^2, which can be achieved with water-cooled windings.

Also its outside dimensions of 57.8 mm present no constructional difficulties.

It should be pointed out that at higher voltages the lens dimensions increase and the current density in the windings decrease. At an electron accelerating voltage V_r of 50 KV, the BASIC ray 2 lens provides the only viable practical solution.

2.3 Reduction in coil current density and saturation effects

The current density in the coil windings of the ray 2 lens of figure 2.15 can usefully be reduced without any deterioration in electron optical properties by modifying the magnetic circuit as shown in figure 2.16. There, the lens dimensions were extended to enlarge the coil cross-sectional area, in such a way that the critical features of the BASIC lens polepiece are not changed.

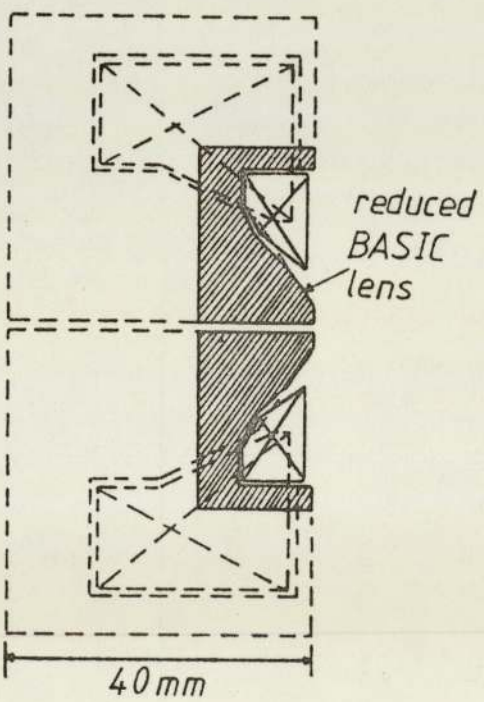

Figure 2.16 Schematic representation of the scaled BASIC ray 2 lens and the proposed expansion of it in order to reduce the current density in its coil windings.

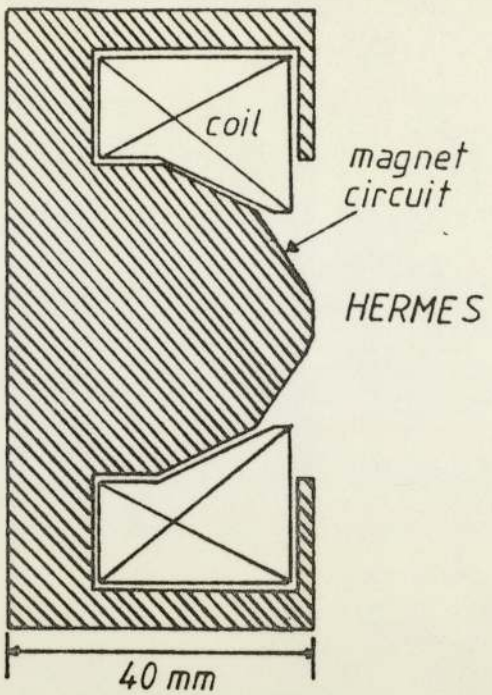

Figure 2.17 Schematic representation of lens HERMES.

In order to check that the electron optical properties of the modified BASIC lens are unaltered, the axial magnetic flux density distributions of both lenses were computed by the Munro program M13, which takes into account the actual B/H curve of the iron circuit. This has the additional advantage that the saturation effects in the polepiece can be taken into consideration.

To compare the saturation behaviour at the polepiece tip of both lenses, it is best to eliminate the influence of the polepiece bore. The BASIC lens with no bore was therefore compared with the new lens with no bore. The new lens is shown in figure 2.17 and will be referred to as lens HERMES from here forthwith.

Typical axial magnetic flux density distributions of the BASIC lens of zero bore and for lens HERMES are shown in figures 2.18 and 2.19 respectively.

From figure 2.18 can be seen that in the BASIC lens, the

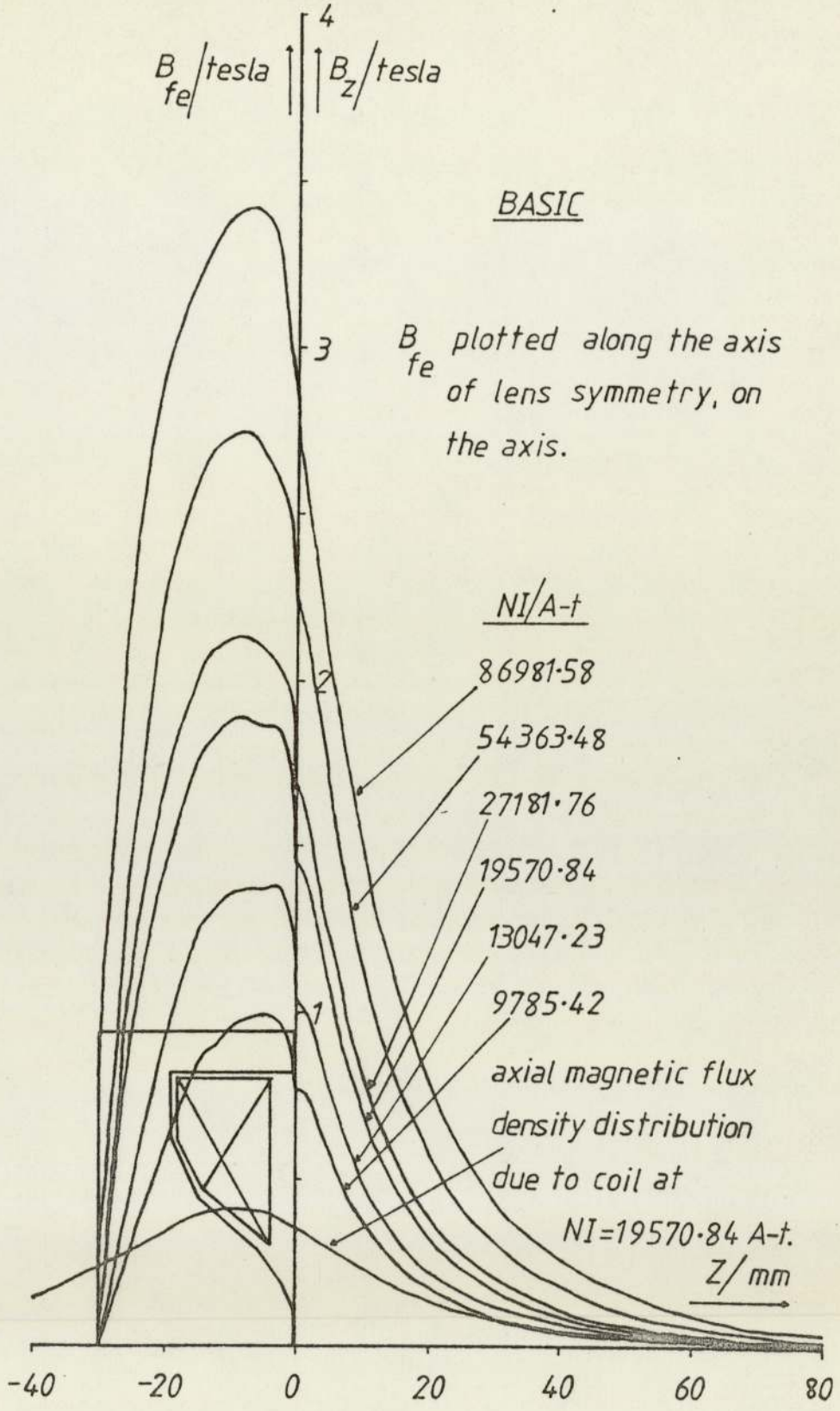

Figure 2.18 Axial magnetic flux density distributions of the BASIC lens with no bore, at different lens excitations.

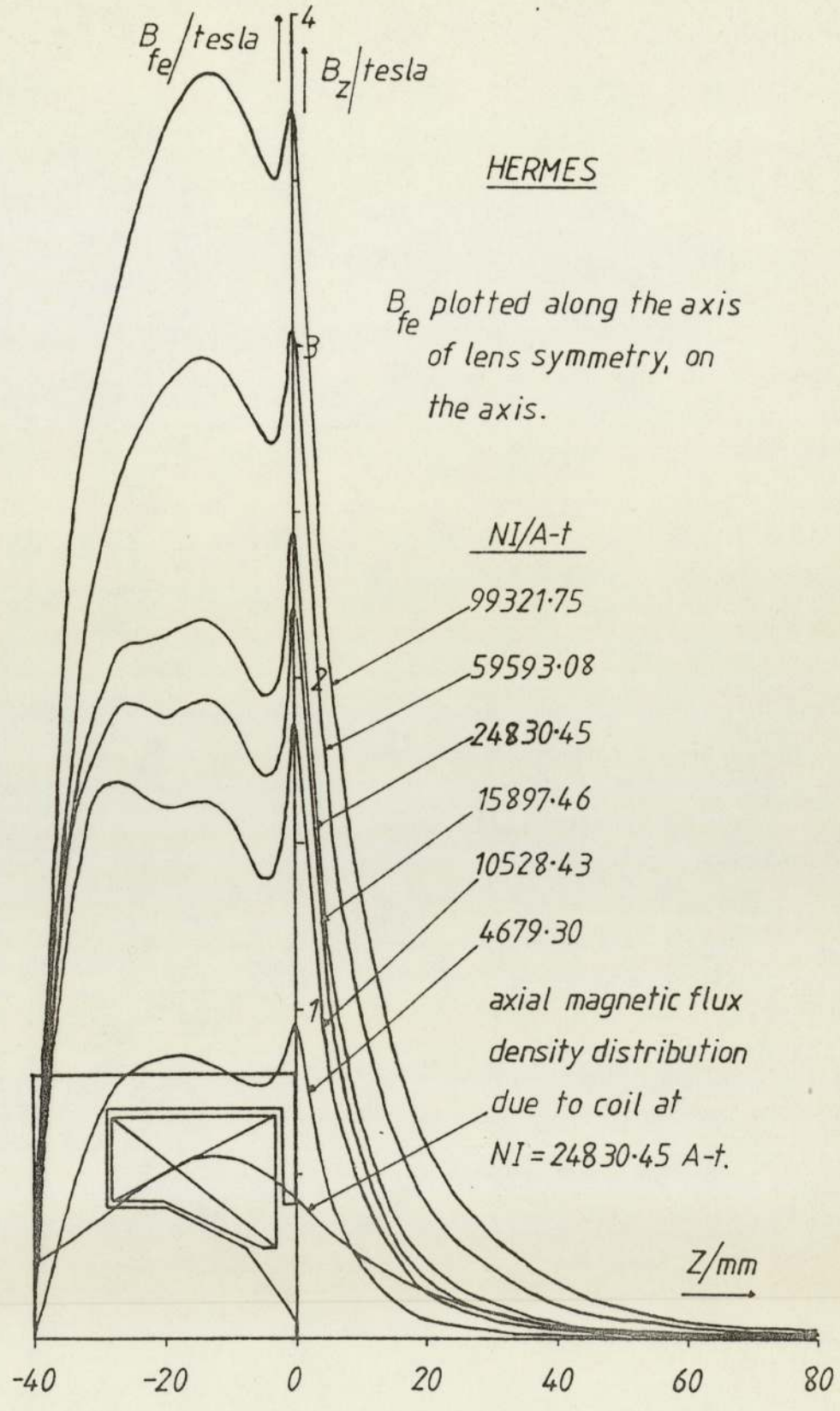

Figure 2.19 Axial magnetic flux density distributions of lens HERMES, at different lens excitations.

maximum flux density occurs not at the poleface but at some distance further back from the polepiece tip. At the polepiece tip itself, the magnetic flux density is considerably lower than it's maximum. Figure 2.18 shows that the position of this peak coincides with the position of the peak of the computed axial magnetic flux density distribution due to the lens coil, also shown in figure 2.18 (see also appendix D). This strongly suggests that at high polepiece saturation flux densities, the position and shape of the coil will exert a dominating influence on the performance of the lens. This is in marked contrast to the effect of the coil in double-polepiece lenses, where the coil plays a minor role.

The most important feature of lens HERMES therefore is that the peak of the magnetic flux density in the magnetic circuit, is at its polepiece tip, as shown in figure 2.19. This indicates that the polepiece tip will saturate first before any other part of the lens polepiece. This feature is due to the extended face-piece of magnetic circuit, placed directly above the polepiece tip; since in this region the shape of the polepiece is exactly the same as that of the BASIC lens with no bore.

At high lens excitations where most of the polepiece saturates, again the axial magnetic flux density distribution of the coil is a dominant factor, as can be seen by the variation of the second broader peak of the magnetic flux density in the magnetic circuit, which appears in the same position as the peak of the axial magnetic flux density distribution of the coil. At high lens excitations this peak becomes bigger than the peak which is present at the tip of the polepiece. At this excitation, the axial magnetic flux density distribution of the coil begins to assume an unfavourable shape and further increase in excitation

leads to a worsening of the lens aberrations.

From figures 2.18 and 2.19, can further be observed that some irregularities occur in the magnetic flux density inside the magnetic material of the lens polepiece. These irregularities take place when the polepiece is approaching saturation and are present at the positions where changes occur in the shape of the polepiece. These irregularities could be due to inherent defects in Munro's finite element programs in dealing with sharp changes in the shape of the magnetic circuit and at regions where the finite element meshes change size.

The contribution B_{iron} of the magnetisation of the polepiece, to the axial magnetic flux density distribution, over a given range of lens excitation, is a useful guide in assessing a lens design over this range of lens excitation. In a good design, at lens excitations where saturation of the polepiece occurs, the contribution B_{iron} to the total axial magnetic flux density distribution is equal to the saturation flux density of the magnetic material, as shown in figure 1.10 (1.8 Tesla for soft iron, 2.4 Tesla for Permendur).

To calculate B_{iron}, the contribution of the coil, B_{coil}, computed by program BIOT, is subtracted from the corresponding total axial magnetic flux density ($B_{total} = B_{iron} + B_{coil}$), which is the quantity computed by Munro's program.

The contribution B_{iron} due to the magnetisation of the polepiece tip, for the BASIC lens with no bore and for lens HERMES, were determined at the polepiece tip ($z = 0$) and shown in figures 2.20 and 2.21 respectively.

Figure 2.20 shows that the design of the BASIC lens with no bore, is not optimum under saturation conditions. The flux density

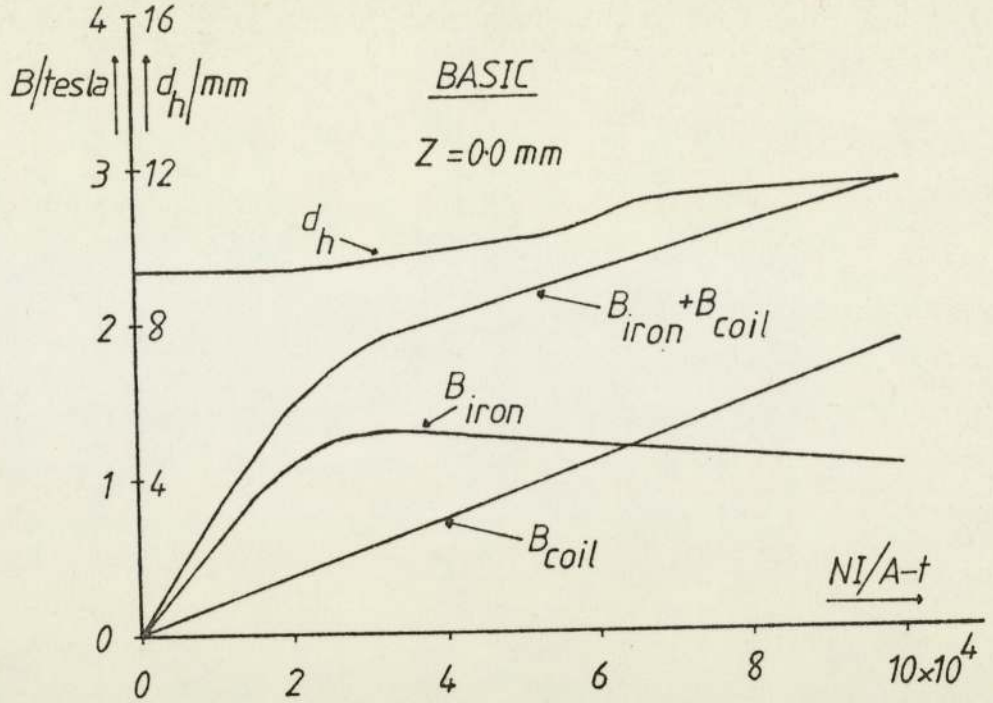

Figure 2.20 The variation of the magnetisation of the iron at the polepiece tip and the variation of the effective halfwidth of the axial magnetic flux density distribution (for ray 1) of the BASIC lens with no bore, as a function of lens excitation.

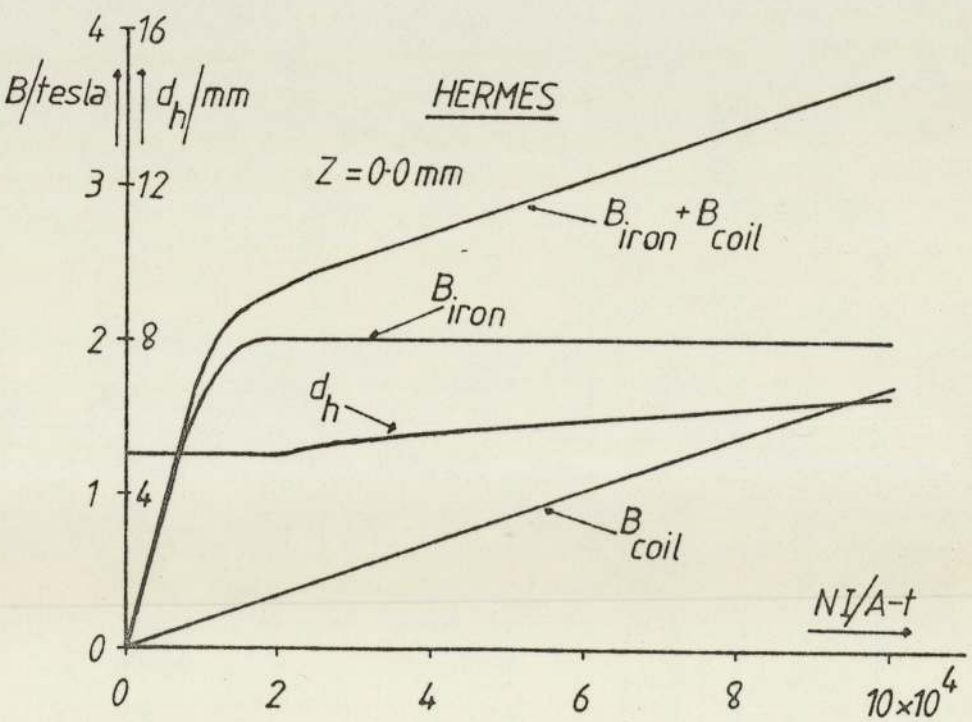

Figure 2.21 The variation of the magnetisation of the iron at the polepiece tip and the variation of the effective halfwidth (for ray 1) of the axial magnetic flux density distribution of lens HERMES, as a function of lens excitation.

B_{iron} reaches a maximum value of 1.3 Tesla at a lens excitation of 35000 A-t after which it drops steadily with increasing lens excitation. This drop indicates that the iron is not saturated at the polepiece tip. Ideally B_{iron} should increase with lens excitation untill it reaches a value in the region of 1.8 Tesla and then should remain constant. If however the polepiece saturates elsewhere than at the polepiece tip, the polepiece tip will fail to saturate even at high lens excitations.

From figure 2.21 can be seen that the design of lens HERMES exploits fully the magnetisation of the iron at the polepiece tip. Here B_{iron} reaches a value of about 2 Tesla at a lens excitation of 20000 A-t and remains at 2 Tesla for higher values of lens excitation. The value of 2 Tesla is slightly higher than the value of 1.8 Tesla, given by the B/H curve used in the computations. This apparent increase could be due to computation errors in the finite element program caused by the finite mesh size. This discrepancy is not so important as the fact that the value of B_{iron} at $z = 0$ is of the correct order and is constant over a large range of lens excitations.

In figures 2.20 and 2.21, the variation of the effective halfwidth d_h of the axial magnetic flux density distribution of the BASIC lens with no bore and of lens HERMES, are also shown as a function of lens excitation respectively.

The effective halfwidth d_h is a parameter which is related to the electron optical properties of a probe forming lens and it is different for ray 1 and ray 2 beam orientations. Appendix E explains the definition of the effective halfwidth d_h.

In figures 2.20 and 2.21 the effective halfwidth d_h for ray 1 is shown, since the effective halfwidth for ray 2 beam orientation of a lens with no bore is meaningless.

At low lens excitations the effective halfwidth is constant since it is mainly due to the magnetisation of the magnetic material. As the magnetic material starts to saturate and the axial magnetic flux density of the coil starts to contribute significantly to the halfwidth of the total axial magnetic flux density distribution of the lens, the halfwidth of the coil distribution B_{coil}, begins to predominate. At large lens excitations, the halfwidth of the total axial magnetic flux density distribution of the lens will be mainly that of the axial magnetic flux density distribution of the coil, which will increase the effective halfwidth of the lens for both beam orientations. An increase in the effective halfwidth indicates a deterioration of the electron optical properties of the lens. Ideally the halfwdth of the coil should be matched to that of the magnetised polepiece (see appendix D), ensuring a constant effective halfwidth. In a lens with a constant effective halfwidth the electron optical properties will improve continuously with increasing excitation.

From figures 2.20 and 2.21 can be seen that the effective halfwidth of lens HERMES is considerably smaller than that of the BASIC lens and it should be expected that lens HERMES has superior electron optical properties than the BASIC lens with no bore.

At a close inspection of the polepiece tip of lens HERMES, reveals that this can be considered as a spherical polepiece tip with a radius of 10 mm, as shown in figure 2.22.

At high lens excitations the flux density B_{iron} reaches a constant value. Figure 2.23 shows the axial distribution of B_{iron} of the polepiece tip of lens HERMES at three different lens excitations (NI = 24830.45, 59593.08, 99321.75). The three curves lie almost on top of one other, as would be expected from the previous discussion.

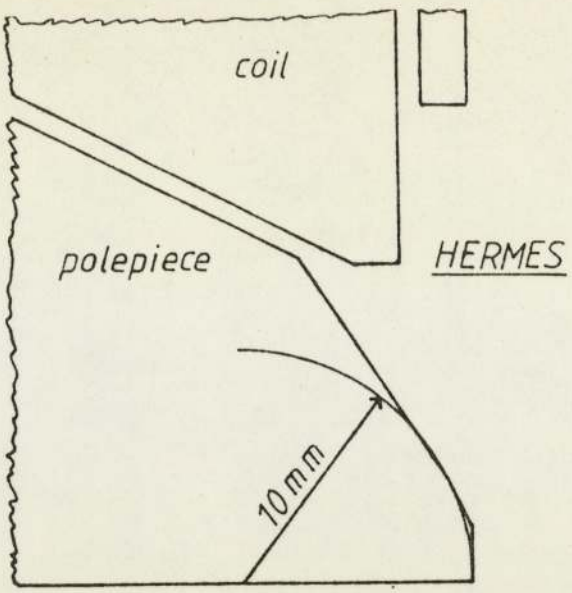

Figure 2.22 The polepiece tip of lens HERMES, matched to a sphere of 10 mm radius.

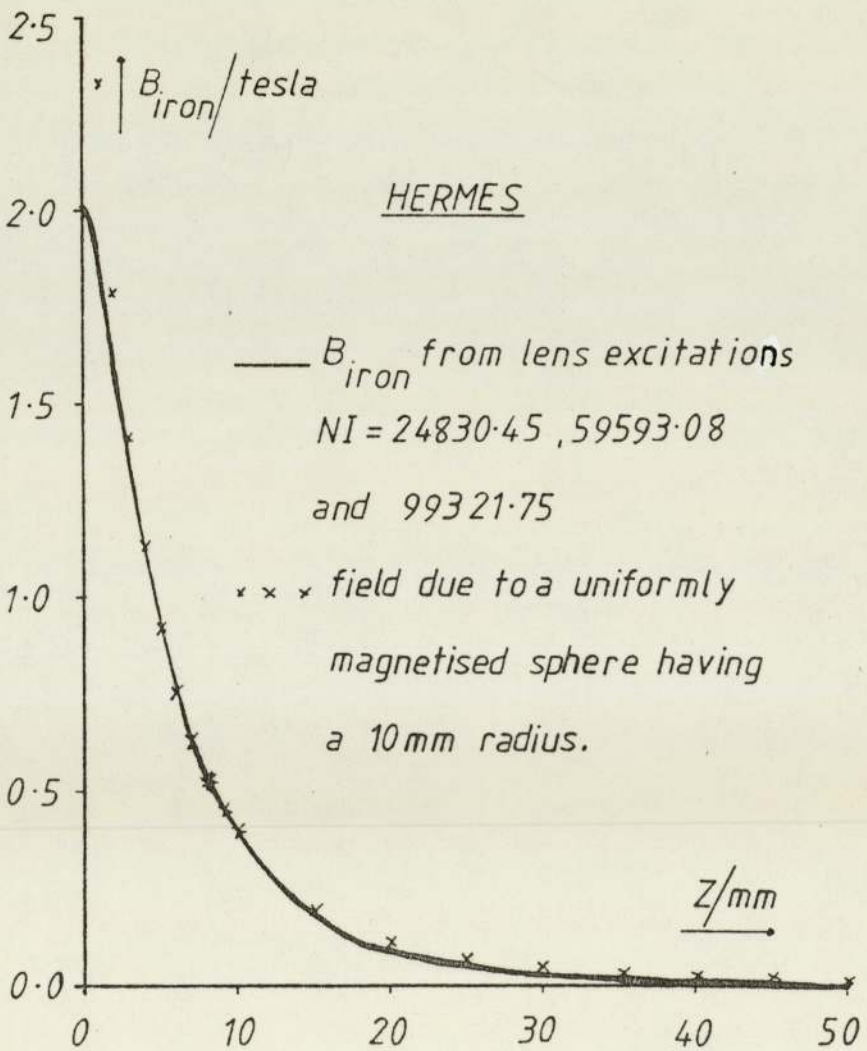

Figure 2.23 The magnetisation of lens HERMES polepiece tip matched to the magnetisation of a sphere having a 10 mm radius.

On the same figure the axial magnetic flux density distribution of a uniformly magnetised sphere of 10 mm radius is also shown. Although the polepiece tip of lens HERMES is not magnetised uniformly, but by a rather more complicated field from its coil, the B_{iron} distribution from its polepiece tip tends to have the shape of that from a spherical polepiece. In fact the only discrepancies between the spherical field and the shape of the B_{iron} distribution of lens HERMES polepiece tip occurs very close to the peak of the distributions. The above observations agree with the predictions of appendix D on the shape of the polepiece of a single polepiece lens.

2.3 Practical considerations and further lenses arising from lens HERMES

2.3.1 Lens HERMES II, lens HERMES III and lens ZEUS

From figure 2.21 it was seen that lens HERMES takes full advantage of saturation up to a lens excitation of 20000 A-t, with no increase in its effective halfwidth of 5.0 mm. At 40000 A-t, its effective halfwidth increases by 12%.

For the practical applications considered in the present work, an objective lens operated at an electron accelerating voltage V_r of 50 KV, will almost never require a lens excitation higher than 20000 A-t. Hence for the practical applications considered in the present work, lens HERMES may be regarded as a near optimum design.

From the calculations made on the BASIC lens under non-saturation conditions (high permeability), a bore ratio of 0.2 in ray 2 beam orientation, was found to be the best choice for an objective single polepiece lens. A bore ratio of 0.2 in lens HERMES, will give the lens shown in figure 2.24. This lens will be referred to as lens HERMES II from here forthwith.

As discussed in the introduction, the axial magnetic flux density distribution of a conventional double-polepiece lens, is contained within the body of the lens. This is electron optically efficient and it could probably provide more favourable electron optical properties than a single polepiece lens. If the electron optical properties of such a lens are considerably more favourable than those of a single polepiece lens, then these, may outweight the restrictions that such a lens imposes on the optimum positioning of the x-ray detector. For this reason a conventional asymmetric lens with the main features of lens HERMES II, as shown in figure 2.25, was also investigated. This lens will be referred to as lens ZEUS from here forthwith.

To further illustrate the importance of the coil position and shape in single polepiece lenses when operated under saturation conditions, a further lens with the same magnetic circuit as lens HERMES II, but having a very much smaller coil was investigated. This lens is shown in figure 2.26 and it will be referred to as lens HERMES III from here forthwith.

Munro's program M13 was used to compute the axial magnetic flux density distributions of lenses HERMES II, HERMES III and ZEUS, at different lens excitations.

Figures 2.27, 2.28 and 2.29 show examples of the axial magnetic flux density distributions of lenses HERMES II, HERMES III and ZEUS respectively.

Because these lenses have bores, the magnetic flux density distributions B_{fe} in the magnetic circuit, was plotted on the last mesh inside the magnetic cicuit along the length of the bores of these lenses. This mesh is at 0.63 mm from the axis and 0.13 mm inside the magnetic circuit.

From figure 2.27 it can be seen that the variation of the

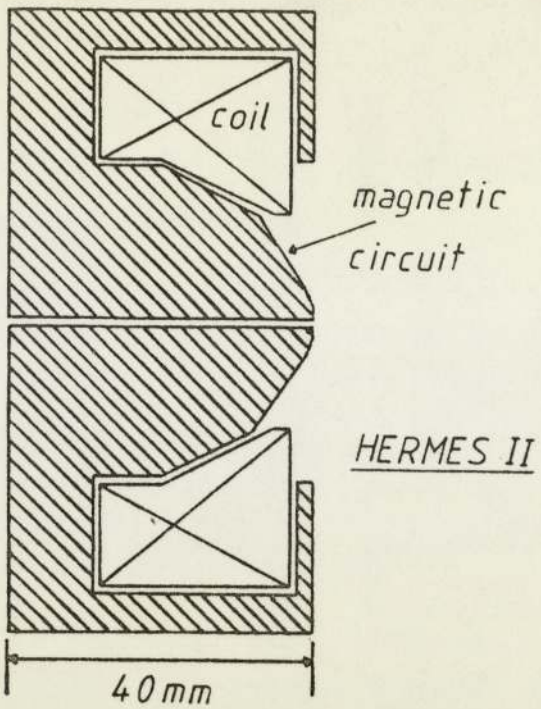

Figure 2.24 Cross-sectional diagram of lens HERMES II.

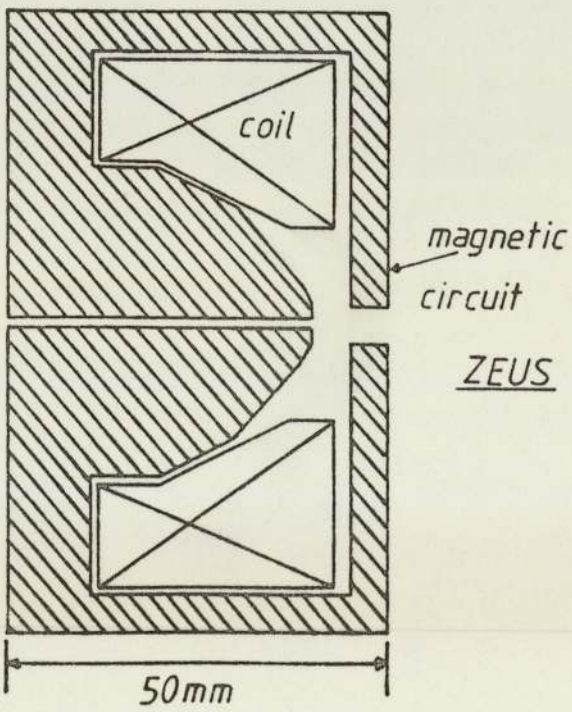

Figure 2.25 Cross-sectional diagram of lens ZEUS.

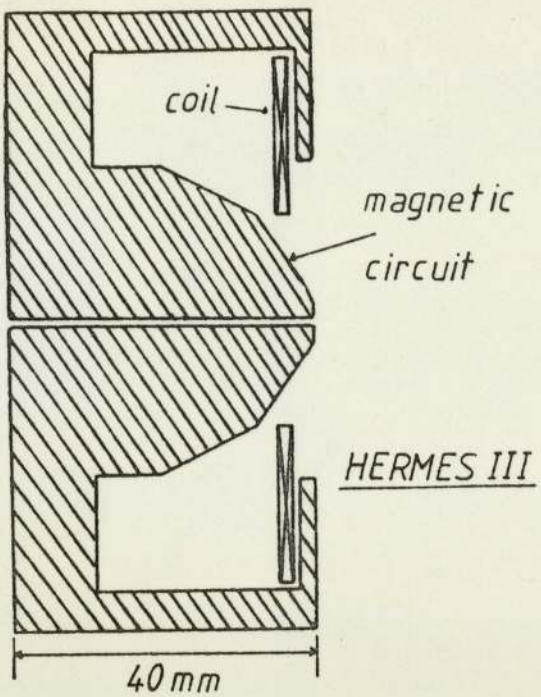

Figure 2.26 Cross-sectional diagram of lens HERMES III.

magnetic flux density inside the magnetic circuit of lens HERMES II, is similar to that of lens HERMES. At very high lens excitations where the coil of lens HERMES II dominates, the axial magnetic flux density distribution of lens HERMES II, has secondary peaks present inside its bore. These are due to the effect of the sharp changes in the polepiece shape and due to the effect of the coil, when the polepiece is approaching saturation. This effect is undesirable since it will effect the electron optical properties of lens HERMES II in ray 2 beam orientation. These secondary peaks will eventually impose a limit on how far lens HERMES II can be operated under saturation conditions.

From figure 2.28, the effect of the coil position and shape in single polepiece lenses can be seen clearly. Although the coil of lens HERMES III does not meet Marai's criteria (see appendix D) and it is still not in the optimum position, it is a much better

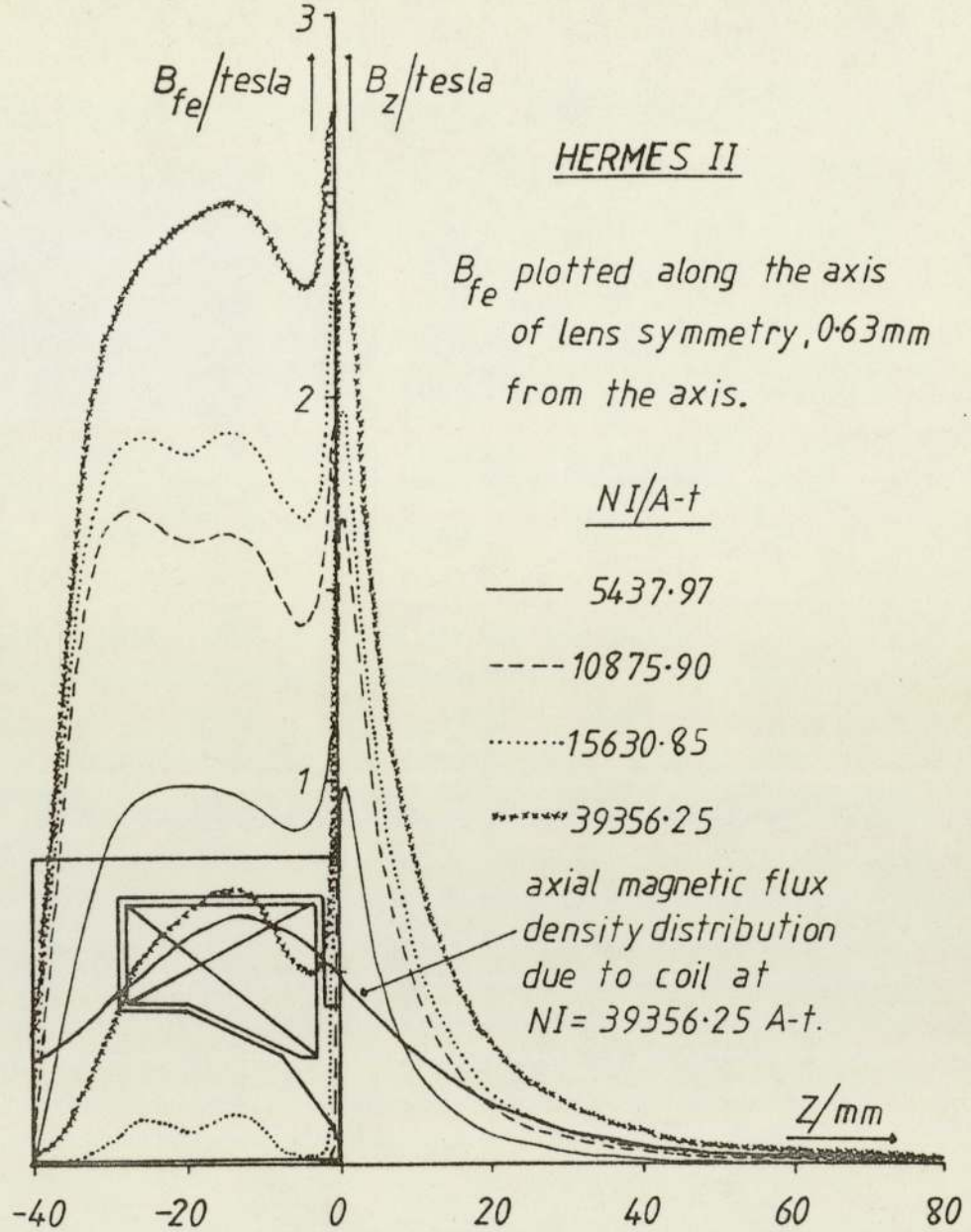

Figure 2.27 Axial magnetic flux density distributions of lens HERMES II, at different lens excitations.

coil design, as can be seen by its influence on the magnetisation of the polepiece of lens HERMES III. The magnetic flux density in the magnetic circuit of lens HERMES III, has a maximum at the polepiece tip and falls off along the polepiece length.

Since the coil of lens HERMES III is very small, the cross-sectional area of its polepiece, behind the coil, can be increased substantially so that most of the irregularities in the magnetic

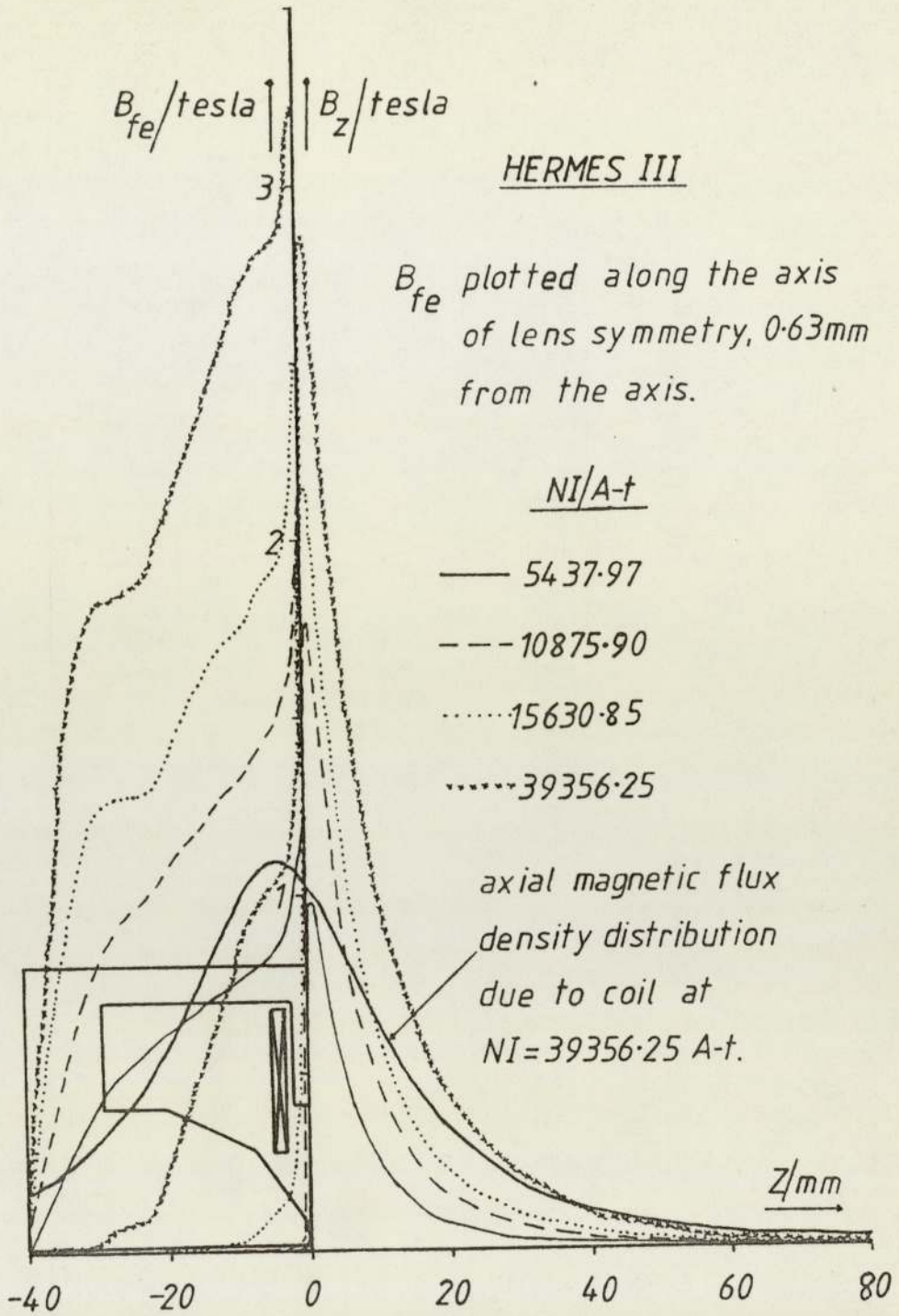

Figure 2.28 Axial magnetic flux density distributions of lens HERMES III, at different lens excitations.

flux density can be removed.

Overall, lens HERMES III, can be regarded to behave better than lens HERMES II under saturation conditions. The only difficulty that may arise with lens HERMES III, is that the current density in its coil windings may impose a limit in a practical lens

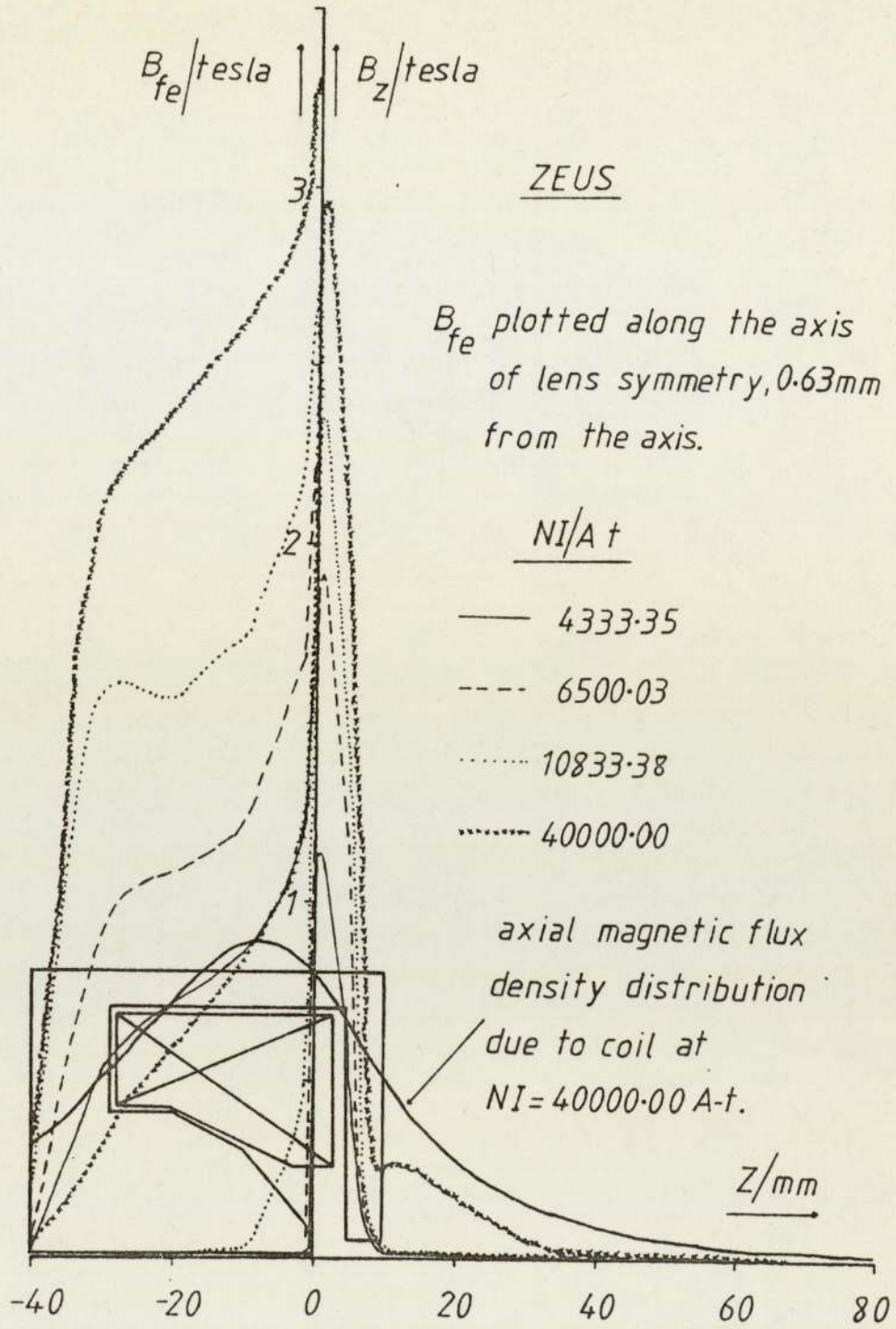

Figure 2.29 Axial magnetic flux density distributions of lens ZEUS, at different lens excitations.

operated at high lens excitations. In practice this limit will be set by the maximum current density a superconducting coil can withstand. This is in the region of 100000 A-t/cm^2. This current density in the coil of lens HERMES III is encountered when the lens is operated at a lens excitation of around 40000 A-t. This lens

excitation implies that although the position and shape of the coil of lens HERMES III is not quite optimum, in practice, this will influence but never dominate its electron optical properties, as can be seen by the variation of the magnetic flux density along the length of polepiece and by the shape of the axial magnetic flux density distribution at a lens excitation of 39356 A-t, shown in figure 2.28.

From figure 2.29 it can be seen that the second polepiece of lens ZEUS has the effect of suppressing the influence of the coil at large z values. The secondary peaks due to the changes in lens ZEUS polepiece shape and due to its coil, never exceed the peak of the magnetic flux density which occurs at the tip of its main polepiece. This implies that saturation starts at the polepiece tip and progresses towards the back of the main polepiece, with increasing lens excitation. This also implies that the shape and position of the coil is less critical in conventional lenses than in single polepiece lenses.

As the main polepiece of lens ZEUS is progressively saturating from its tip, with lens excitation, the axial magnetic flux density distribution, spreads towards the back of the lens in a gradual way, without any sharp irregularities or secondary peaks. This spread could be ideal in improving the electron optical properties of lens ZEUS in ray 2 beam orientation.

At high lens excitations the second polepiece of lens ZEUS, will also start to saturate. This will allow the coil to influence the axial magnetic flux density distribution in the region of the second polepiece. This is seen as a second peak in the axial magnetic flux density distribution, which is present just outside the second polepiece. This second peak will affect the electron optical properties of lens ZEUS in ray 1 beam orientation.

Figures 2.30, 2.31 and 2.32, show the variation of the

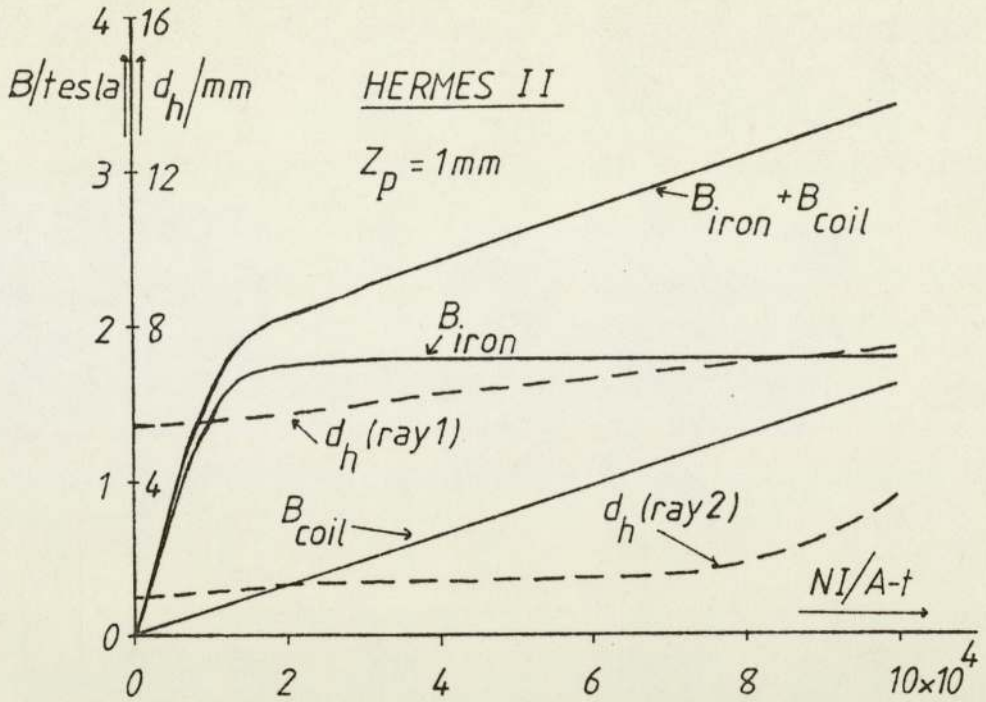

Figure 2.30 The variation of the magnetisation of the polepiece tip and the variation of the effective halfwidth (ray 1 and ray 2) of HERMES II, as a function of lens excitation.

magnetisation B_{iron} of the polepiece tip of HERMES II, HERMES III and ZEUS, as a function of lens excitation NI, respectively. This magnetisation is considered at the position Z_p, where the peak of the axial magnetic flux density distribution occurs in these lenses (Z_p = 1 mm).

Figures 2.30, 2.31 and 2.32, also show the variation of the effective halfwidth d_h for HERMES II, HERMES III and ZEUS, for ray 1 and ray 2, as a function of lens excitation, respectively.

Before discussing these figures, the reader must remember that the dimensions of these lenses were optimised for operation in ray 2 beam orientation at an electron accelerating voltage V_r of 50 KV. The same dimensions of these lenses will be optimum for ray 1 beam orientation but at a very much higher electron accelerating voltage V_r. From sub-section 2.1.3, can be seen that the ratio of the optimum BASIC lens dimensions for ray 2 to the

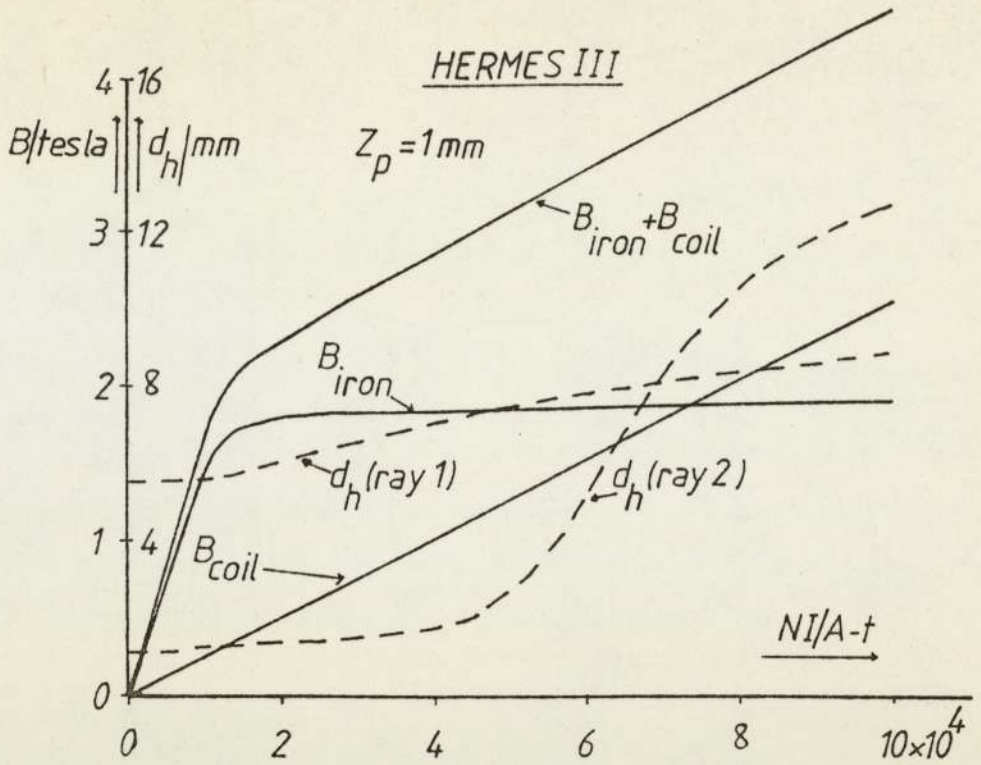

Figure 2.31 The variation of the magnetisation of the polepiece tip and the variation of the effective halfwidth (ray 1 and ray 2) of HERMES III, as a function of lens excitation.

optimum BASIC lens dimensions for ray 1 is 3.74 (i.e. $X_{ray\ 1}/X_{ray\ 2}$ = 3.74). Therefore the factor $(V_r(ray\ 1)/V_r(ray\ 2))^{\frac{1}{2}}$ = 3.74, where in the present work V_r(ray 2) is 50 KV, giving V_r(ray 1) to be 700 KV. Also the effective halfwidth d_h for ray 1 of the above lenses, as shown in figures 2.30, 2.31 and 2.32, should be expected to be of the order of 3.74 times bigger than the effective halfwidth of these lenses in ray 2 beam orientation.

From figure 2.30, can be seen that HERMES II takes full advantage of the magnetisation B_{iron} of its polepiece tip, which reaches a constant value of 1.8 Tesla at a lens excitation of 20000 A-t. This remains constant at 1.8 Tesla for higher lens excitations.

The effective halfwidth for ray 2 of HERMES II, has a constant value of 1.1 mm upto a lens excitation of 6500 A-t. For higher

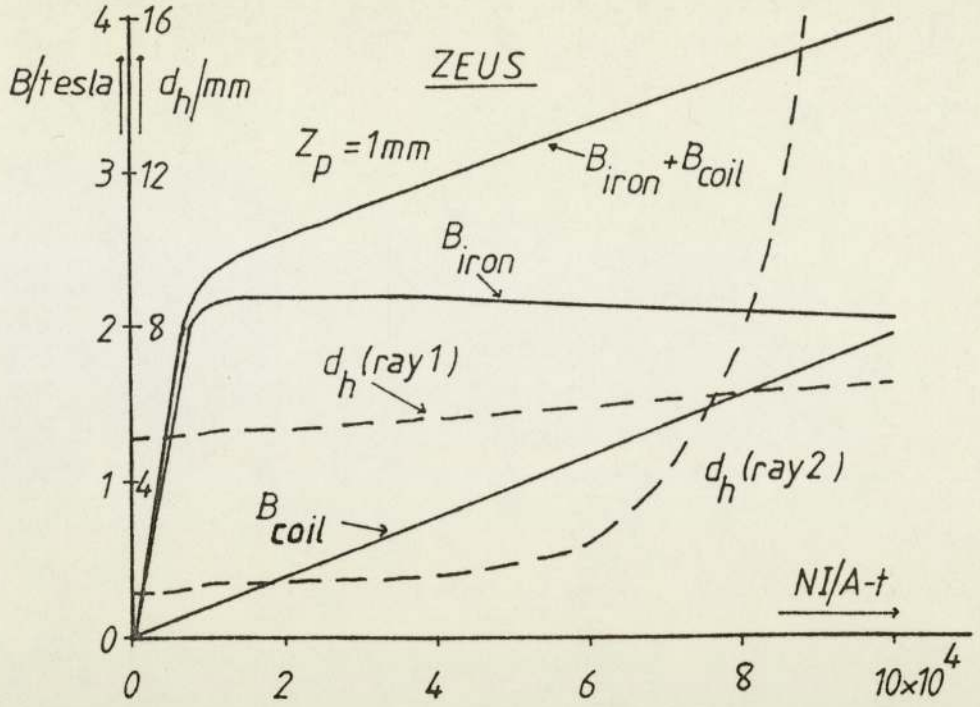

Figure 2.32 The variation of the magnetisation of the polepiece tip and the variation of the effective halfwidth (ray 1 and ray 2) of ZEUS, as a function of lens excitation.

lens excitations the effective halfwidth for ray 2, increases slowly upto a lens excitation of 80000 A-t. At lens excitations higher than 80000 A-t, this effective halfwidth increases more sharply. At these lens excitations the coil of HERMES II becomes the dominant factor as can be seen from figure 2.27. Although the coil of HERMES II becomes the dominant factor in ray 2 beam orientation, ray 1 is not affected as can be seen by the variation of the effective halfwidth for ray 1 beam orientation shown in figure 2.30. This effective halfwidth (ray 1) has a constant value of 5.5 mm upto a lens excitation of 6500 A-t. For higher lens excitations it increases slowly, with a value of 7.2 mm at a lens excitation of 100000 A-t.

For ray 2 beam orientation the change in the effective halfwidth of HERMES II at relatively low lens excitations, may well improve its electron optical properties, since this increase in

the effective halfwidth is mainly due to the saturation of its polepiece tip. The saturation of the polepiece tip at these lens excitations will effectively reduce slightly the sharp slope of the axial magnetic flux density distribution, which may be more favourable for ray 2 beam orientation.

From figure 2.31, can be seen that HERMES III, also takes full advantage of the magnetisation of its polepiece tip. The magnetisation of its polepiece tip reaches a value of 1.8 Tesla at a lens excitation of 20000 A-t. For higher lens excitations the magnetisation increases very slowly having a value of 1.9 Tesla at a lens excitation of 100000 A-t. This increase is probably due to computational errors.

For the same lens excitation as for HERMES II, the peak value of the axial magnetic flux density distribution ($B_{iron} + B_{coil}$) of HERMES III, is considerably higher. This is due to the increased contribution of the small coil of HERMES III, close to the peak of its total axial magnetic flux density distribution.

The main effect of the small coil of HERMES III is concentrated at its polepiece tip and this has the effect of increasing the effective halfwidth for both beam orientations, more than the effective halfwidth of HERMES II for the same lens excitation. The effective halfwidth of HERMES III for ray 2 is the same as that of lens HERMES II upto a lens excitation of 35000 A-t and then it increases sharply with increasing lens excitation.

The effective halfwidth of lens HERMES III for ray 1 is the same as that of lens HERMES II upto a lens excitation of 15000 A-t and then it increases more than that of lens HERMES II with increasing lens excitation.

Figure 2.32, also indicates that ZEUS takes full advantage of the magnetisation of its main polepiece. The magnetisation of its main polepiece reaches a value of 2.2 Tesla at a lens excitation

of 15000 A-t and retains this value upto a lens excitation of 40000 A-t. For higher lens excitations the magnetisation decreases slowly with a value of 2.05 Tesla at a lens excitation of 100000 A-t. The value of the magnetisation of the main polepiece of lens ZEUS is higher than the value of 1.8 Tesla that it should been according to the B/H curve used in the computations for lens excitations higher than 7000 A-t. This discrepancy is probably due to computational errors. The important fact is that the magnetisation of lens ZEUS main polepiece tip reaches the saturation magnetic flux density of 1.8 Tesla.

The effective halfwidth of lens ZEUS for ray 2 has a constant value of 1.15 mm upto a lens excitation of 6000 A-t and then it increases steadily upto a lens excitation of around 50000 A-t. For higher lens excitations this effective halfwidth increases very sharply. At these lens excitations the coil of lens ZEUS is the dominant factor affecting its characteristics. Again the domination of lens ZEUS coil does not effect the effective halfwidth for ray 1, which has a constant value of 5.15 mm upto a lens excitation of 6000 A-t and then it increases slowly having a value of 6.5 mm at a lens excitation of 100000 A-t.

The increase in the effective halfwidth of lens ZEUS for ray 2, is mainly due to the saturation of its main polepiece. This has the effect of changing the slope of its axial magnetic flux density distribution on the side closest to the main polepiece. This change of slope in this side of the axial magnetic flux density distribution may favour the electron optical properties of lens ZEUS for ray 2 beam orientation.

The shape of the other side of the axial magnetic flux density distribution, closest to the second polepiece of lens ZEUS, does not change very much. Also at high lens excitations, a second peak in the axial magnetic flux density distribution occurs just outside

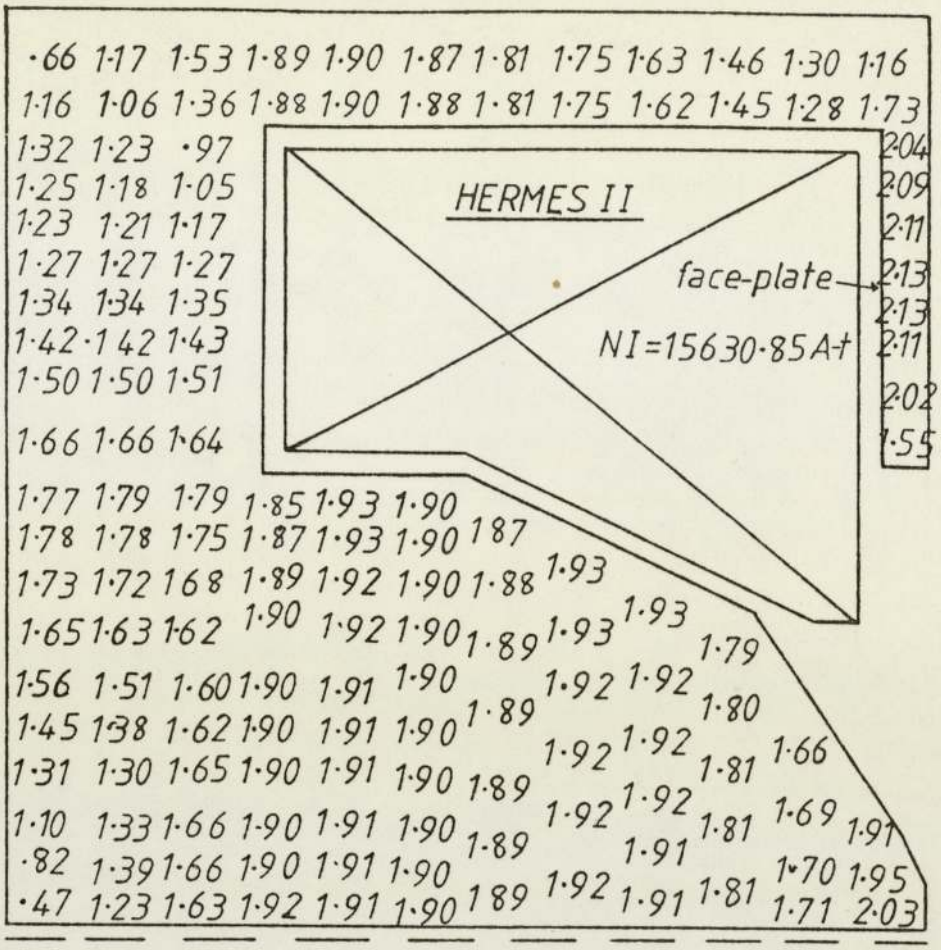

Figure 2.33 Cross-sectional diagram of lens HERMES II with values of magnetic flux density throughout the magnetic circuit.

the second polepiece of lens ZEUS, which suggests that saturation of lens ZEUS polepieces may not improve its electron optical properties for ray 1 beam orientation.

So far the emphasis has been on the saturation of the polepieces of these lenses. A good lens design should not saturate elsewhere before its polepieces are completely saturated.

Figures 2.33 and 2.34 show the cross-sectional diagrams of lens HERMES II and lens ZEUS with values of magnetic flux density throughout the magnetic circuit, respectively.

In both figures the values of the magnetic flux density close to the external diameter of these lenses are almost as high as they

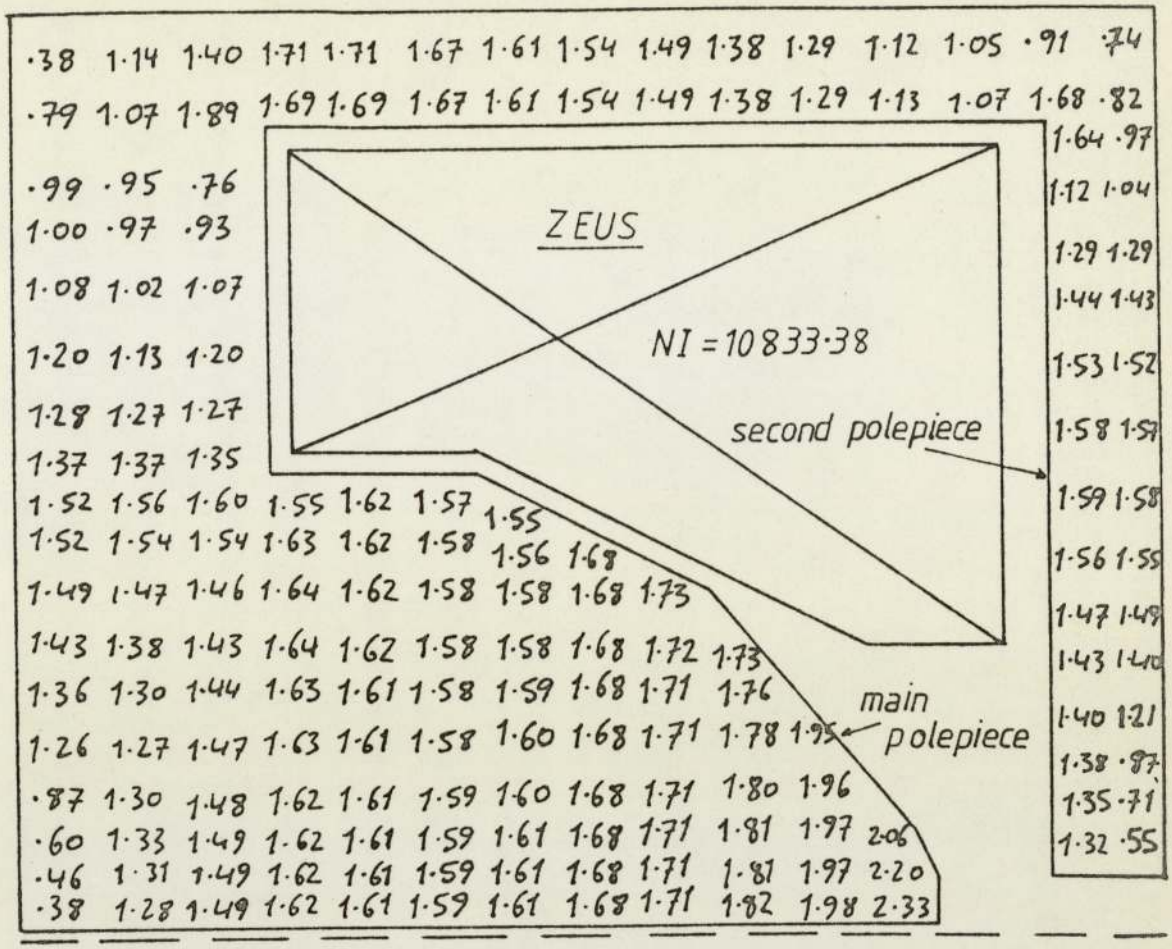

Figure 2.34 Cross-sectional diagram of lens ZEUS with values of magnetic flux density throughout the magnetic circuit.

are in the polepieces of both lenses. This clearly shows that this part of the magnetic circuit of these lenses saturates at the same time as their polepieces. This should be avoided in a good lens design. This part of the magnetic circuit of these lenses must be increases in cross-section, so as to relax the magnetic flux density present in this region of the magnetic circuit.

The magnetic flux density in the second polepiece of lens ZEUS, as shown in figure 2.34, is slightly lower than the magnetic flux density in the main polepiece. This second polepiece will start to saturate as the main polepiece is halfway saturated. By increasing the thickness of this second polepiece, saturation can be avoided

in this polepiece untill the main polepiece is completely saturated.

The magnetic flux density in the face-plate of lens HERMES II which is situated above its polepiece tip, as shown in figure 2.33, is very much higher than what it is in its polepiece. This face-plate will saturate before the polepiece starts to saturate. The main function of this face-plate is to concentrate the magnetic flux in the region of the polepiece tip, so that the magnetic flux density in the polepiece will be highest at its tip. Although this face-plate saturates before the polepiece tip, it still maintains the magnetic flux density at the polepiece tip higher than the rest of the polepiece for a large range of lens excitation. In fact the magnetic flux density at the polepiece tip of lens HERMES II, stops being the highest in the polepiece at around a lens excitation of 100000 A-t.

In order to illustrate the role of this face-plate more clearly, the axial magnetisation distribution B_{iron}, the axial coil distibution B_{coil} and the total axial magnetic flux density distibution $B_{iron} + B_{coil}$ of the scaled BASIC lens of figure 2.15(b), lens HERMES II, lens HERMES III and lens ZEUS, at a given lens excitation NI, are shown respectively in figures 2.35, 2.36, 2.37 and 2.38.

From these figures can be seen that the magnetisation of the polepiece tip of lenses which have a face-plate (lens HERMES II and lens HERMES III), contribute more flux density to their total axial magnetic flux density distribution than the scaled BASIC lens which does not have a face-plate. Also lens HERMES II and HERMES III use less lens excitation to magnetise their polepieces than the scaled BASIC lens.

Although the face-plate of lens HERMES II and lens HERMES III help to concentrate the magnetisation at their polepiece tips, the

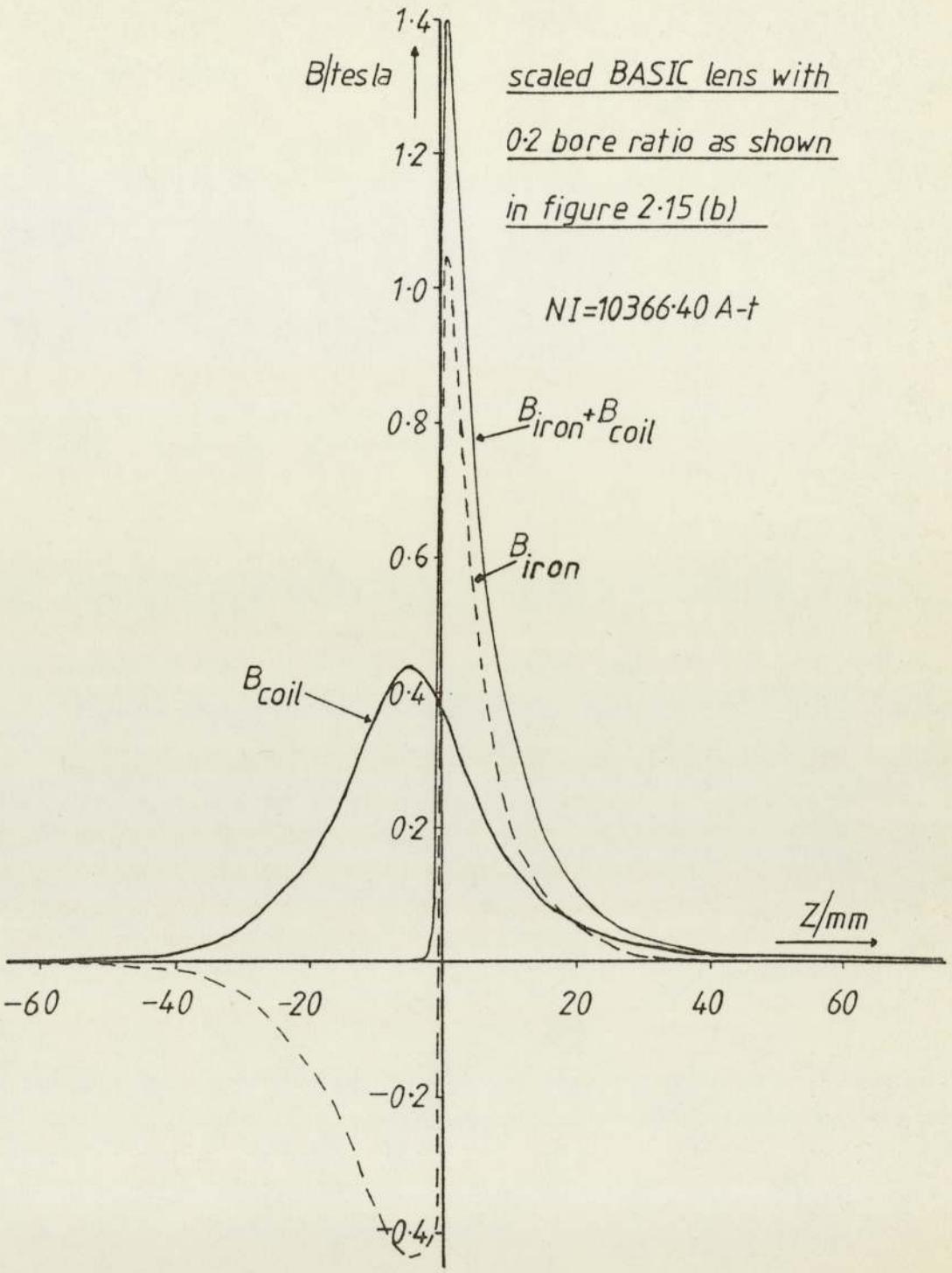

Figure 2.35 The axial magnetic flux density distributions of the scaled BASIC lens of figure 2.15(b), at a lens excitation NI = 10366.40 A–t.

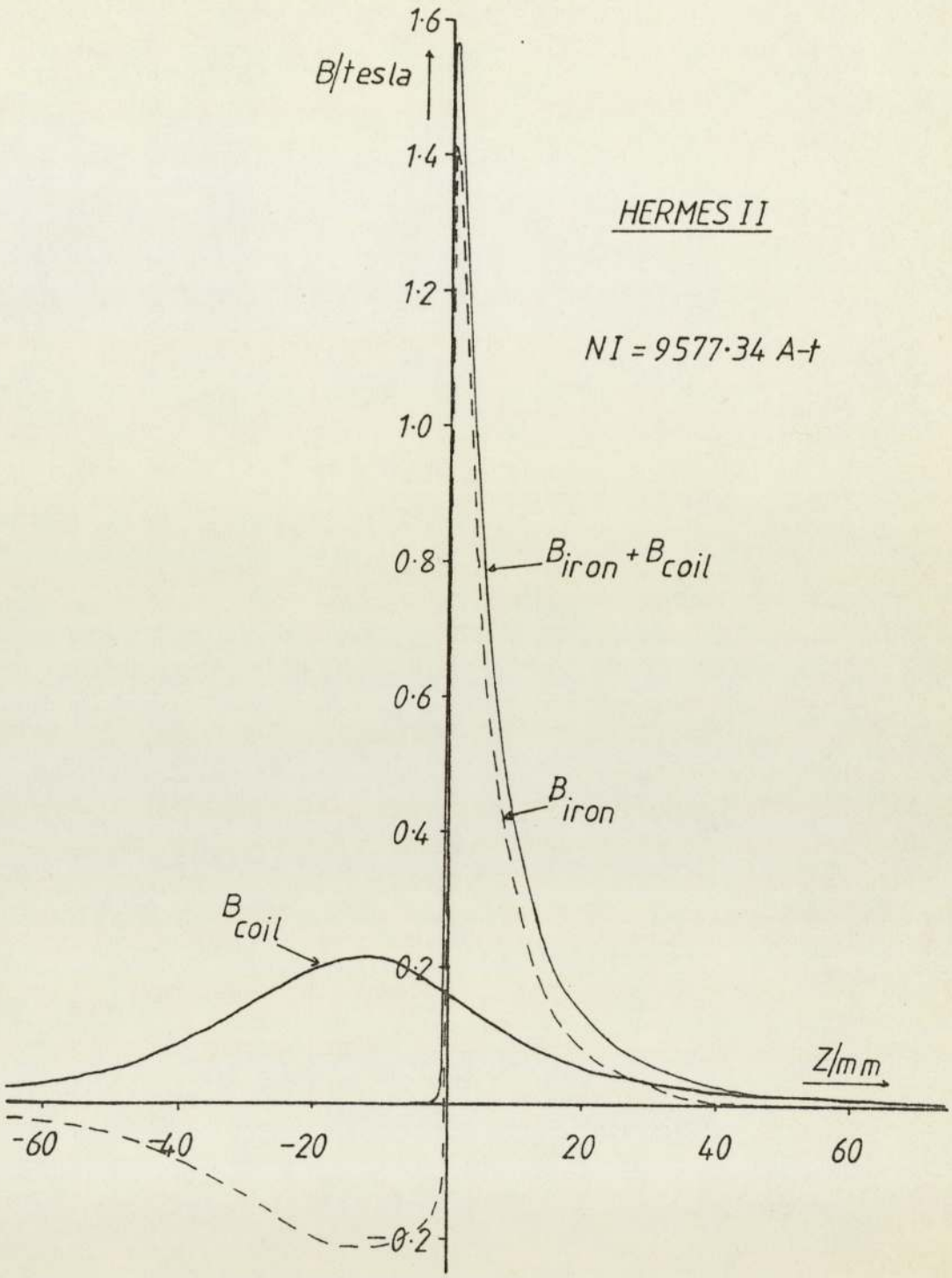

Figure 2.36 The axial magnetic flux density distributions of lens HERMES II, at a lens excitation NI = 9577.34 A-t.

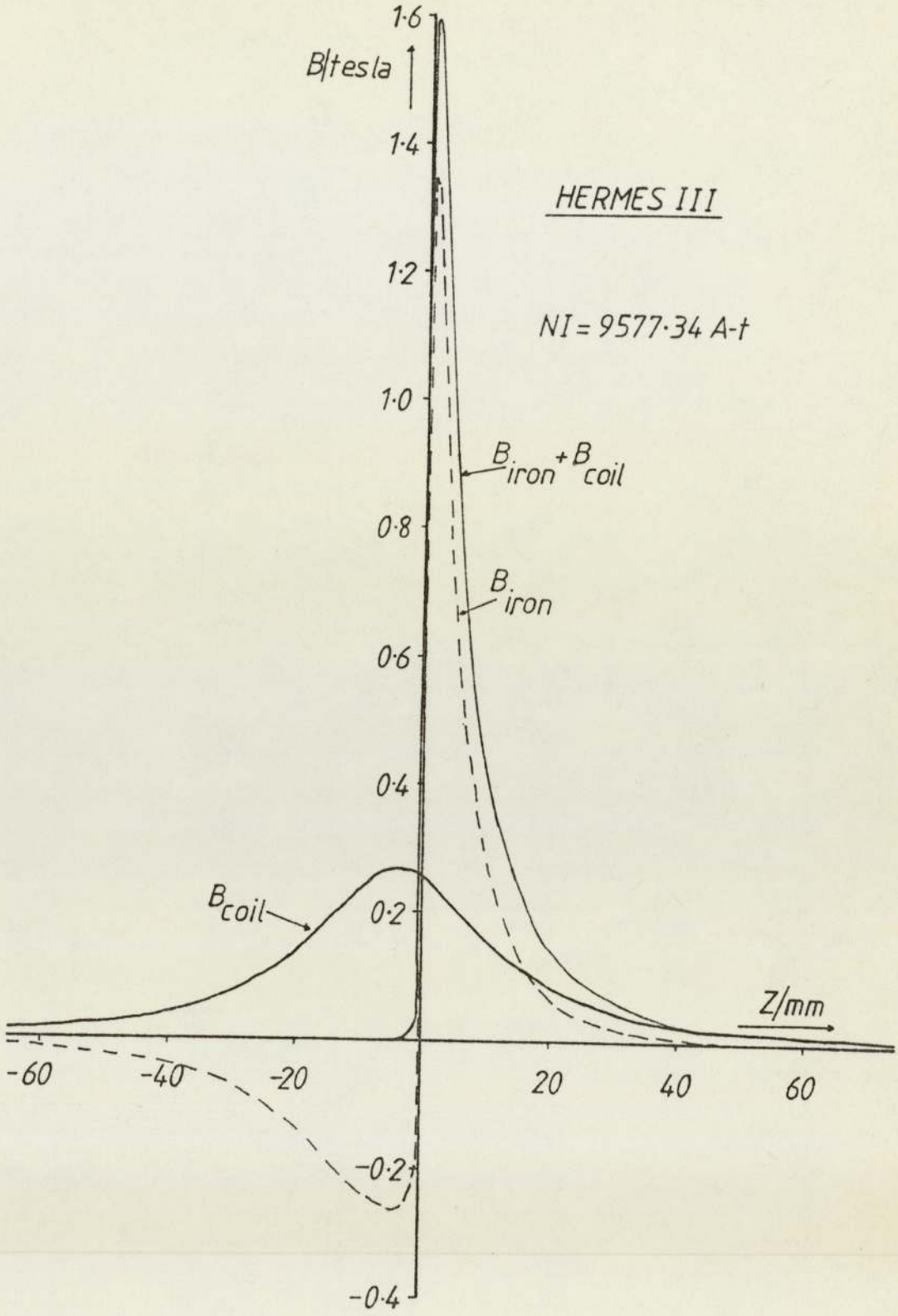

Figure 2.37 The axial magnetic flux density distributions of lens HERMES III, at a lens excitation NI = 9577.34 A-t.

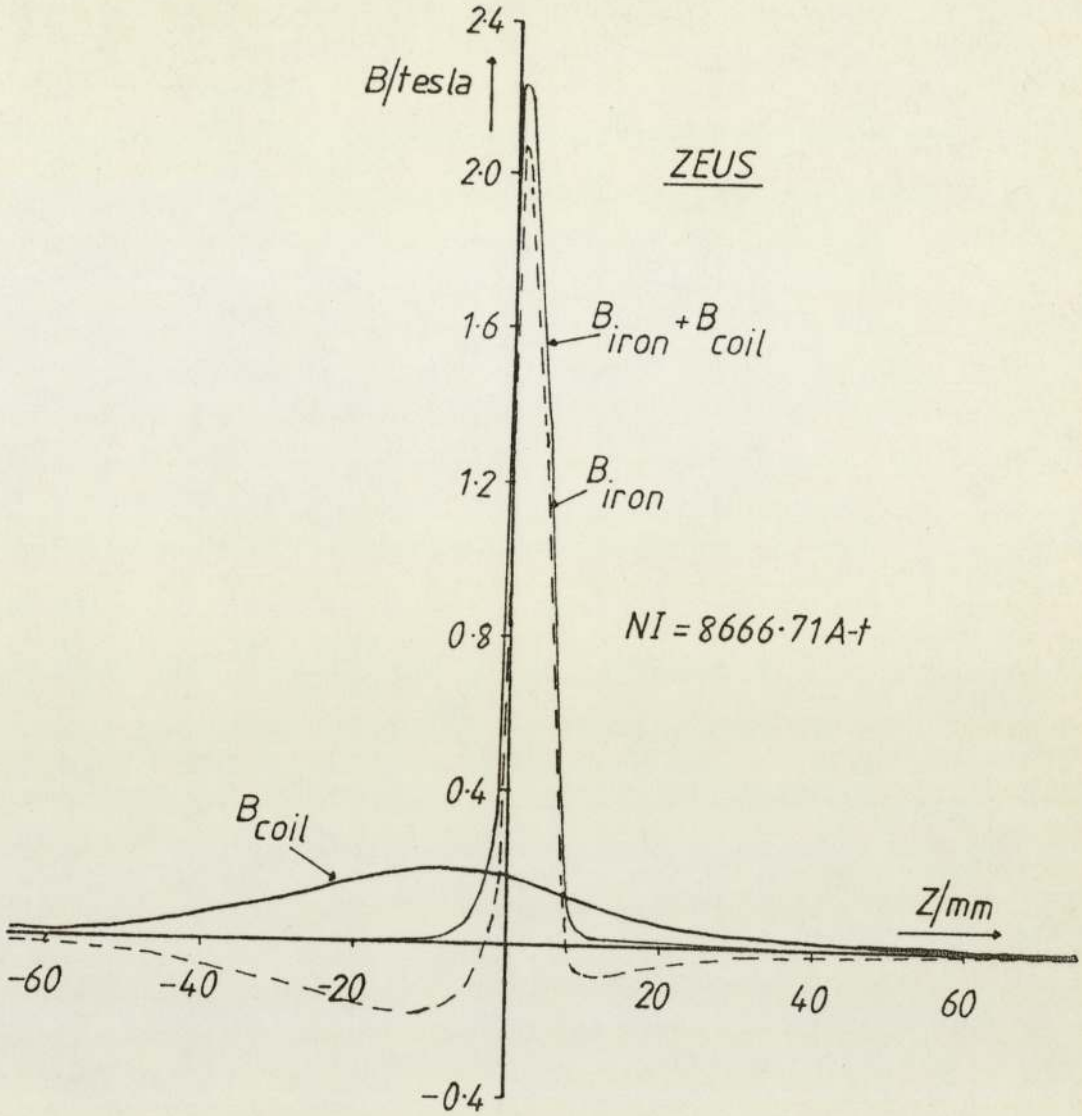

Figure 2.38 The axial magnetic flux density distributions of lens ZEUS, at a lens excitation NI =8666.71 A-t.

effect of this face-plate is not as strong as a second polepiece such as that of lens ZEUS. The second polepiece of lens ZEUS provides a much higher concentration of magnetic flux density at its polepiece tip and at a lower lens excitation than the lenses with a face plate, as can be seen from figure 2.38.

From figures 2.36 and 2.37, the effect of the small coil of lens HERMES III can be seen. This uses the same excitation as the coil of lens HERMES II, but it contributes more magnetic flux density to its total axial magnetic flux density distribution than

lens HERMES II contributes to its axial magnetic flux density distribution.

The total area under the axial magnetisation distribution B_{iron} of any lens should be equal to zero. A close inspection of figures 2.35, 2.36, 2.37 and 2.38, will reveal that the area under the positive region of the axial magnetisation distribution B_{iron}, is bigger than the area under the negative region. This was noticed throughout the present investigation which uses Munro's finite element programs to compute the axial magnetic flux density distributions of magnetic lenses. The precentage by which the magnetisation in the positive region exceeds that of the negative region varies from one lens design to another. It also varies for the same lens design at different lens excitations. This variation was always found to be between 5% and 10%.

The most probable source of these discrepancies could be due to the finite mesh sizes of the finite element programs. These probable computational errors explain why in some cases the value of the magnetisation B_{iron} of a fully saturated polepiece tip of some lenses exceeds the value of 1.8 Tesla dictated by the B/H curve used in the computations.

2.3.2 Lens APHRODITE and lens ATHENA

Two further lenses were investigated. These lenses have large conical bores and they are intended for use in ray 1 beam orientation. These are shown in figures 2.39 and 2.40. The lens of figure 2.39 will be referred to as lens APHRODITE and the lens of figure 2.40 will be referred to as lens ATHENA from here fortwith.

In ray 1 beam orientation these lenses can only be operated at high electron accelerating voltages since their optimum dimensions at low electron accelerating voltages will impose two technological

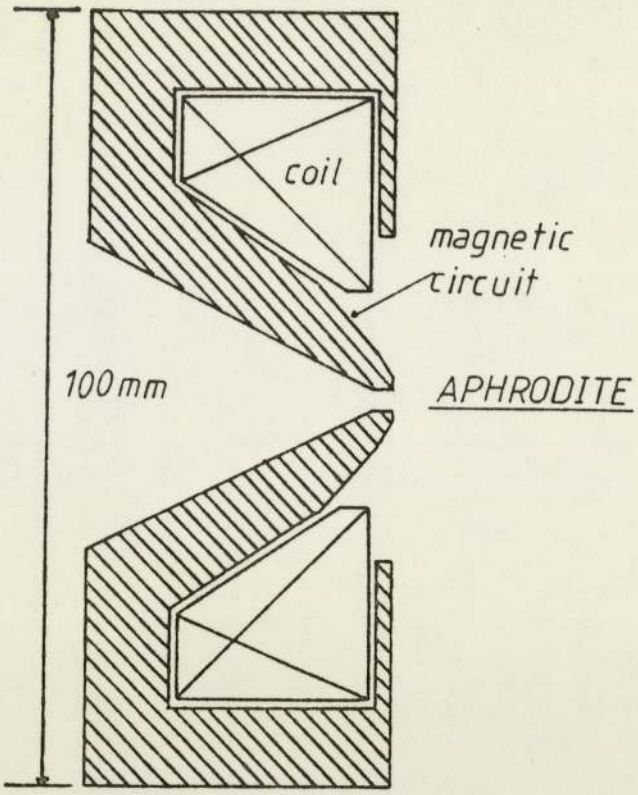

Figure 2.39 Cross-sectional diagram of lens APHRODITE.

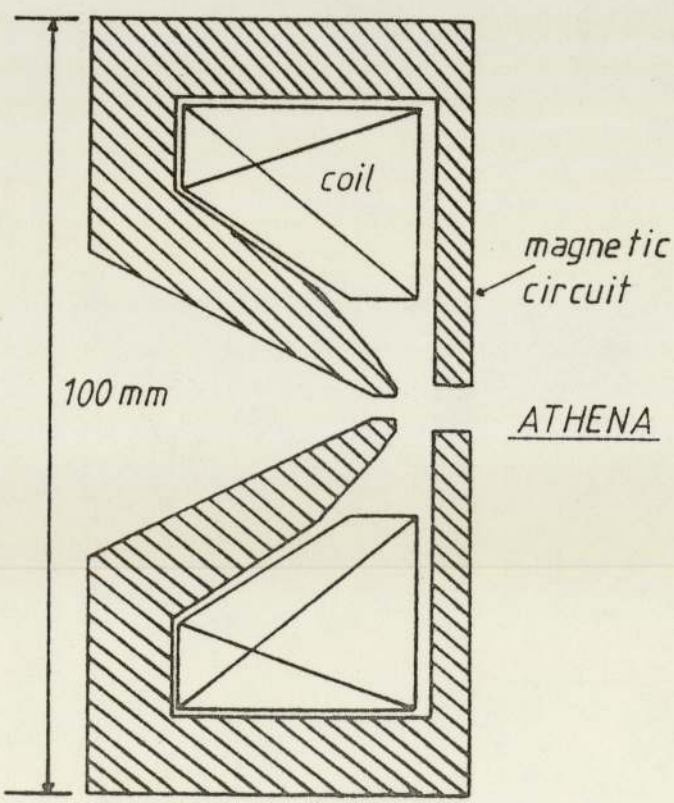

Figure 2.40 Cross-sectional diagram of lens ATHENA.

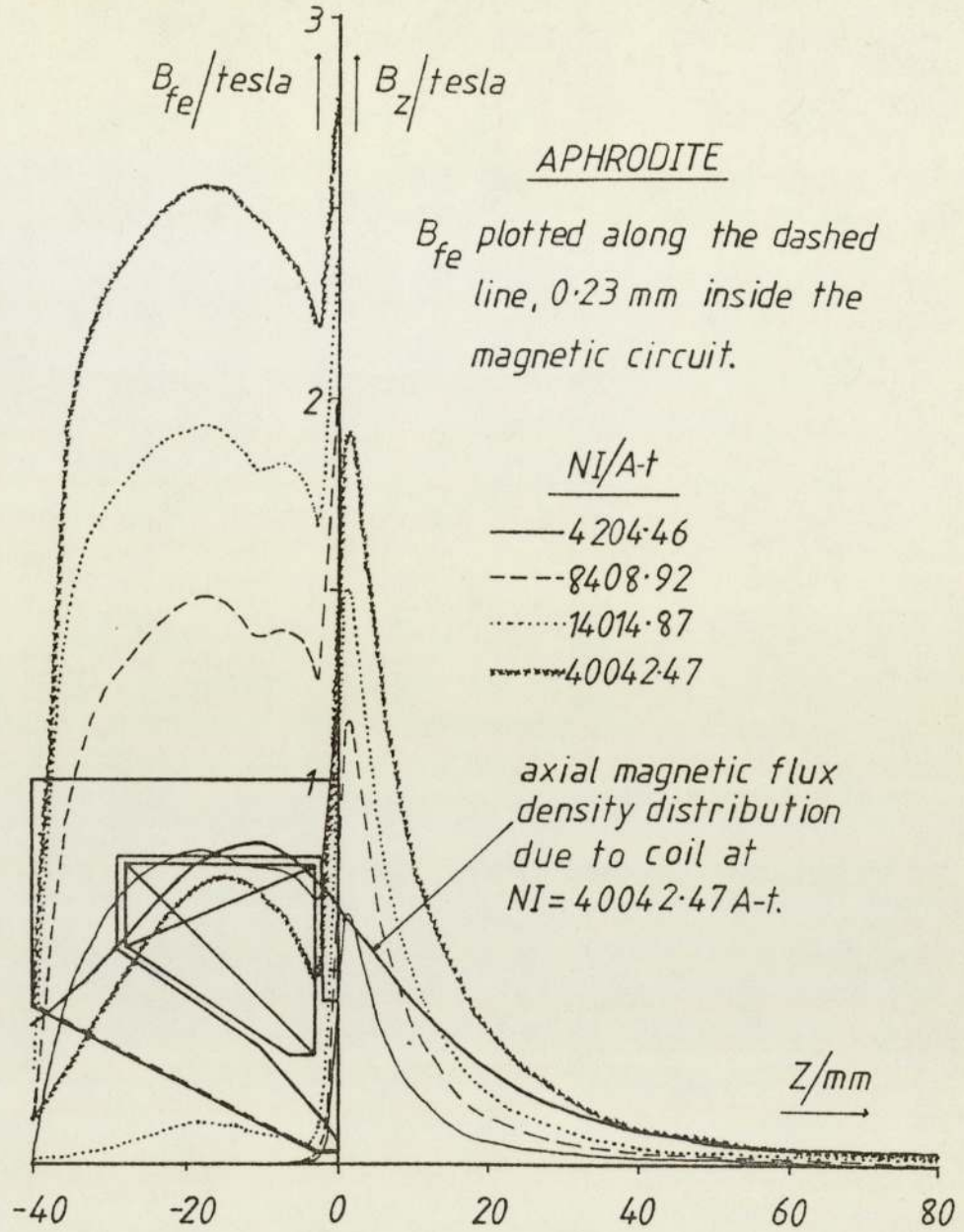

Figure 2.41 Axial magnetic flux density distributions of lens APHRODITE, at different lens excitations.

limits. The first limit will be one of constructional difficulties which is imposed by the very small optimum dimensions these lenses will have at low electron accelerating voltages. The second limit will be imposed by the maximum current density their coil can carry. This limit will be set by the maximum current density a superconducting coil can provide.

These lenses are intended to show the possibility of

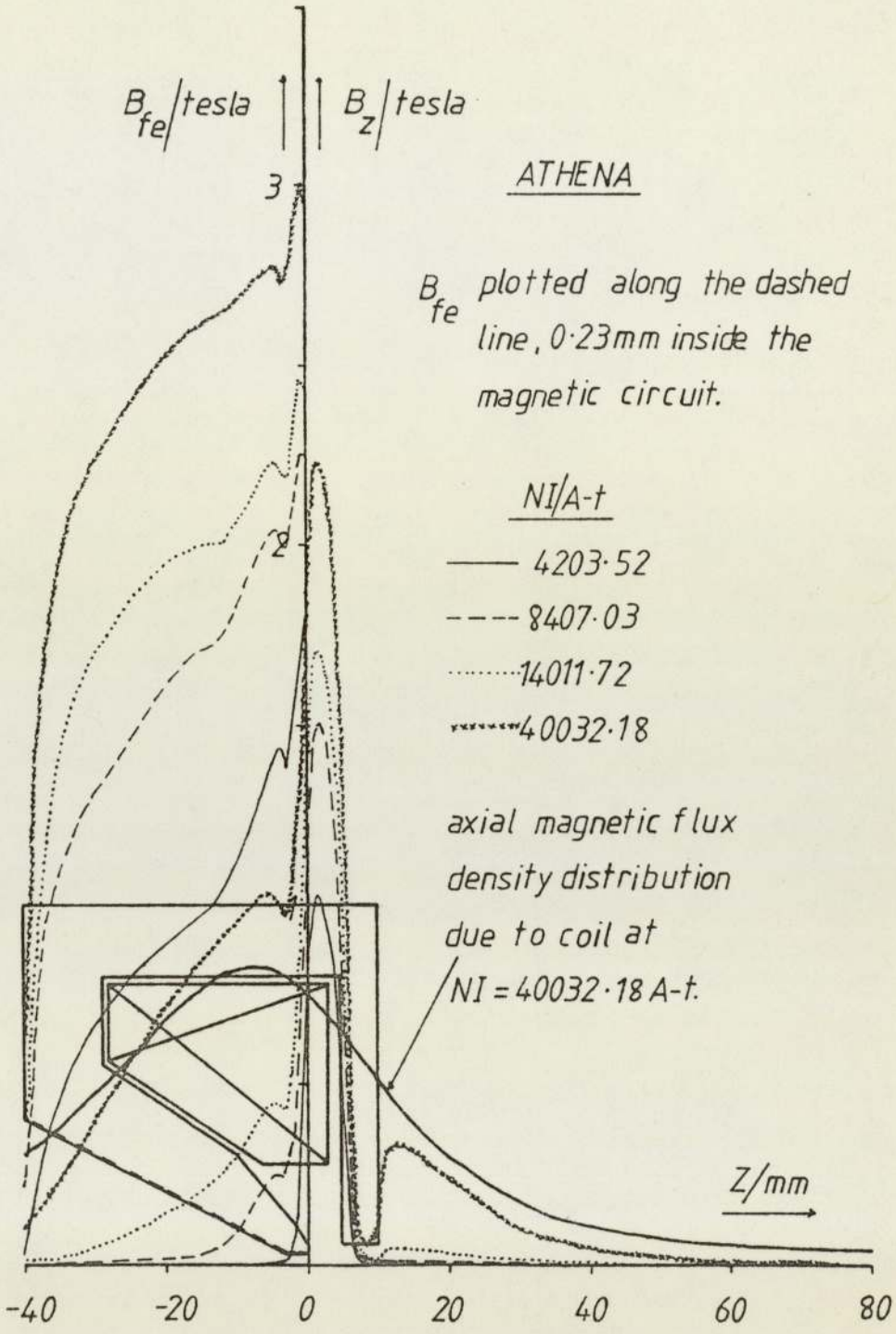

Figure 2.42 Axial magnetic flux density distributions of lens ATHENA, at different lens excitations.

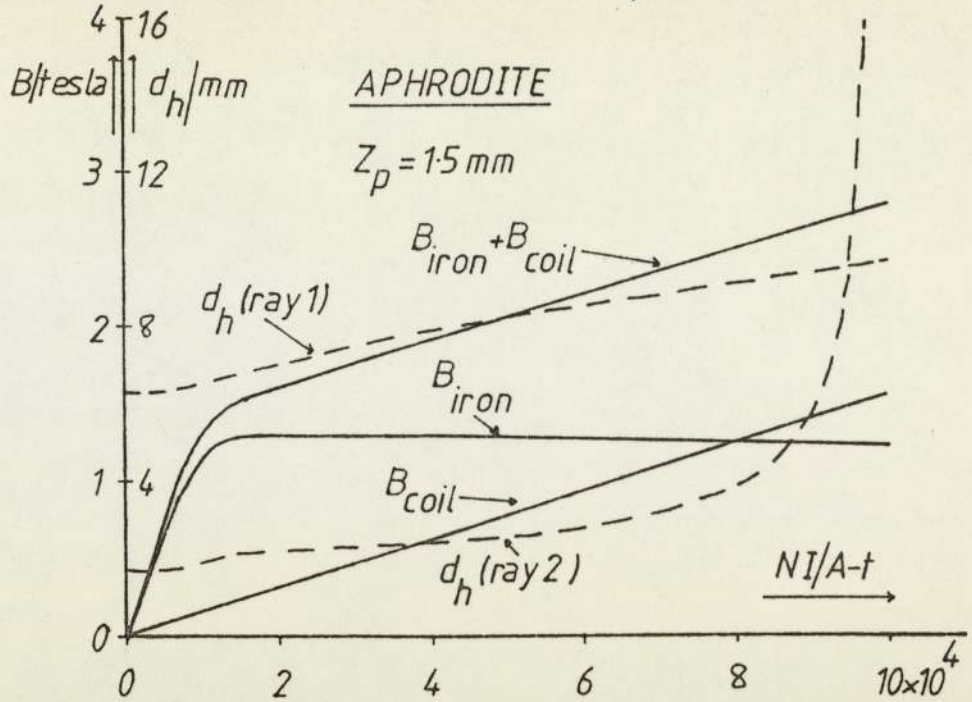

Figure 2.43 The variation of the magnetisation of the polepiece tip and the variation of the effective halfwidth (ray 1 and ray 2) of lens APHRODITE, as a function of lens excitation.

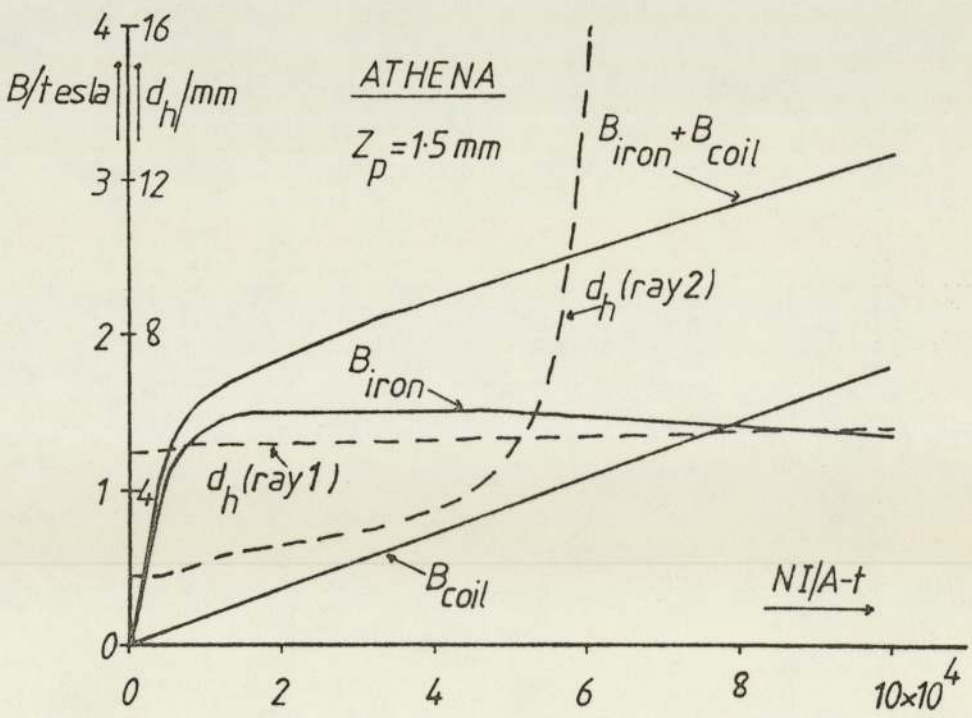

Figure 2.44 The variation of the magnetisation of the polepiece tip and the variation of the effective halfwidth (ray 1 and ray 2) of lens ATHENA, as a function of lens excitation.

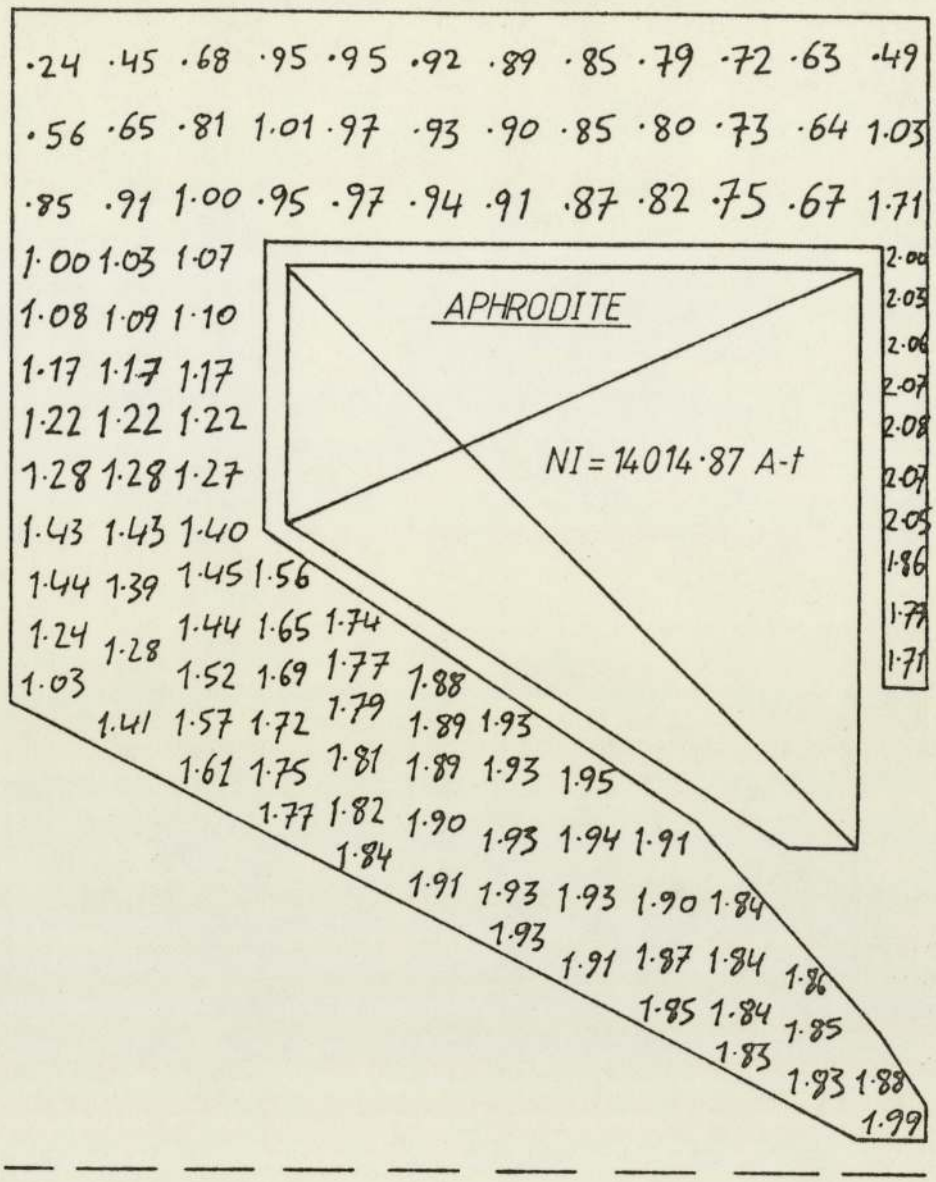

Figure 2.45 Cross-sectional diagram of lens APHRODITE with values of magnetic flux density throughout the magnetic circuit.

constructing compact high electron accelerating voltage micro-x-ray sources, if such micro-x-ray sources are required in the future.

The characteristicts of these lenses under saturation conditions are illustrated in figures 2.41, 2.42, 2.43, 2.44, 2.45 and 2.46.

From these figures the effect of the large conical bores of lens APHRODITE and lens ATHENA can clearly be seen.

The important feature of these lenses that should be noted by

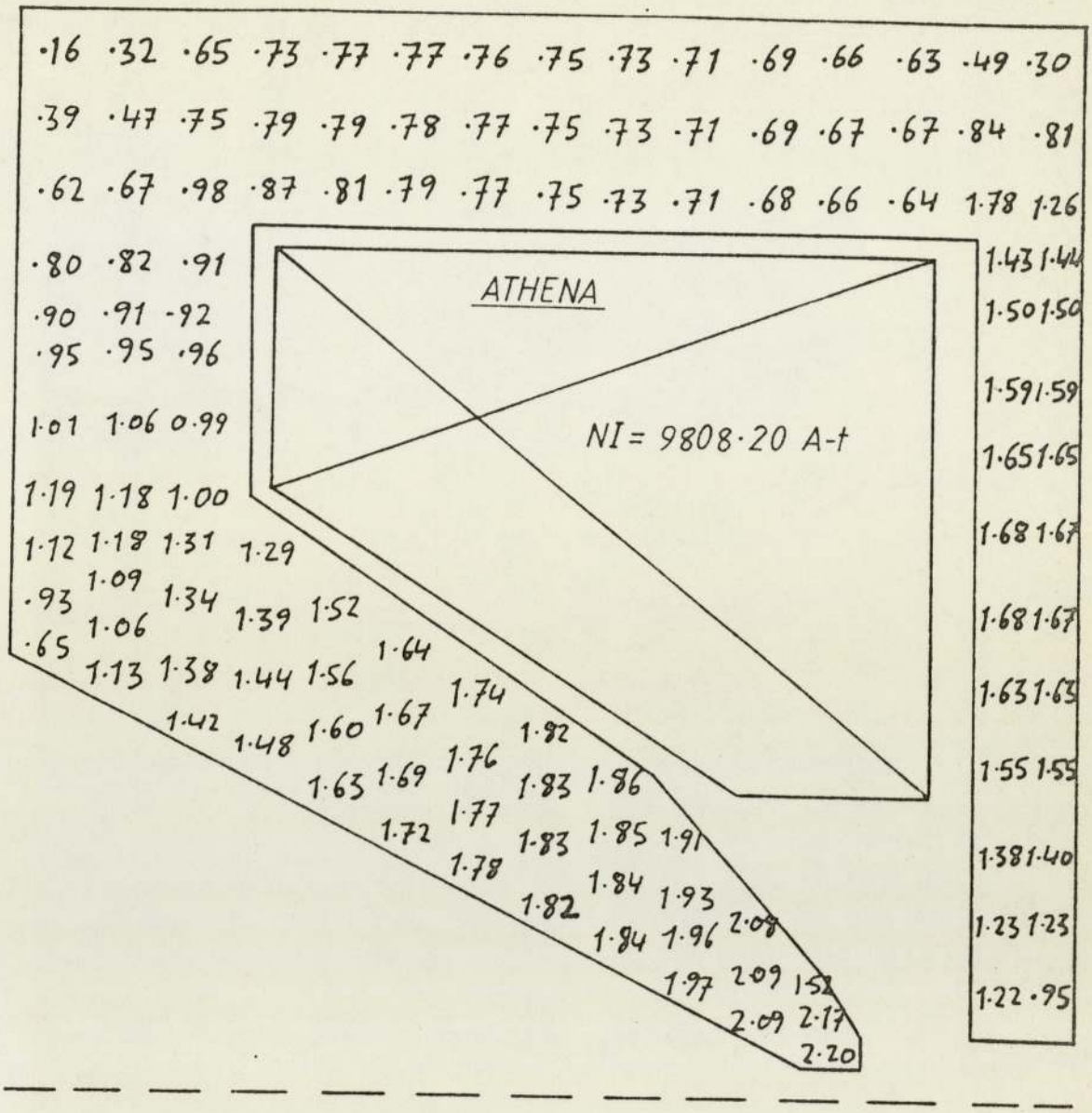

Figure 2.46 Cross-sectional diagram of lens ATHENA with values of magnetic flux density throughout the magnetic circuit.

the reader, is the relaxation of the magnetic flux density close to the external diameters of these lenses, those cross-section in this region of their magnetic circuits is larger than that of the previous lenses of this investigation. The magnetic flux density in this region is considerably less than the magnetic flux density in the polepieces of these lenses as shown in figures 2.45 and 2.46.

2.3.3 Discussion

In this section has been illustrated so far that a single pole-piece objective lens can be designed to take advantage of the saturation of its polepiece. The limits imposed on such a lens design are mainly technological, imposed by the maximum possible current density in the optimum coil of such a lens.

It is possible to achieve an optimum objective lens design to operate at extreme saturation conditions by optimising the shape and position of the lens coil. The shape of the polepiece of such a lens design is only important in the region in which the polepiece starts to saturate. In the linear region of the B/H curve, the important feature of an objective lens is its bore ratio (i.e. its relative bore diameter). In the non-linear region of the B/H curve, the shape and position of the lens coil is the important feature of an objective lens.

From the lenses investigated in this section, it appears that the best single polepiece lens for operation in ray 2 beam orientation, is lens HERMES III, for which the magnetisation of its polepiece has a maximum value at its tip and falls off gradually towards the back of its polepiece. As seen from the behaviour of lens APHRODITE, it is possible to have a small conical bore in lens HERMES II and lens HERMES III, without a significant alteration on the magnetisation of their polepieces. Lens HERMES III with a conical bore will be affected less than lens HERMES II with a conical bore, mainly due to the shape and position of their respective coils.

From the conventional asymmetric lenses, lens ZEUS appears the best lens, for which a small conical bore is also possible as seen from the behaviour of lens ATHENA.

For both symmetric and asymmetric conventional lenses, the

effect of the coil shape and position does not appear to be very important at lens excitations close to the region at which the polepieces of such lenses start to saturate, since the magnetic strength of such lenses is mainly concentrated in the gap between their polepieces. At high lens excitations, at which the polepieces are extremely saturated, then the coil position and shape will become as important as in single polepiece lenses.

Before a commitment is made as to which one of the lenses investigated so far is the most suitable objective lens for the probe forming system of a micro-x-ray source, their electron optical properties must be investigated. The electron optical properties are the ultimate criterion for the suitability of a lens for a particular application.

2.4 The electron optical properties of the lenses under saturation conditions

The lenses of the present work were designed to operate in ray 2 beam orientation at an electron accelerating voltage V_r of 50 KV. As discussed in sub-section 2.3.1(pages 65 and 66), the same lens dimensions of these lenses are optimum for ray 1 beam orientation as well, provided that they are operated at an electron accelerating voltage V_r of 700 KV.

When these lenses in ray 1 beam orientation are scaled down so that they give their optimum electron optical properties at an electron accelerating voltage V_r of 50 KV, which is sufficient for a micro-x-ray source, the dimensions of these lenses will become so small that they will present technological problems in constructing them. Therefore these lenses operated in ray 1 beam orientation will not be suitable for a micro-x-ray source, but they may be suitable as objective lenses for high resolution electron microscopy.

The electron optical properties of these lenses, for both beam orientations, are expressed in the following sub-sections in graphical form as a function of the scaling factor n, so as to make the curves of each lens as universal as possible.

Since in ray 2 beam orientation, used in a micro-x-ray source, the x-ray target is placed infront of the polepiece tip and never inside the bore, the electron optical properties of these lenses were plotted upto a lens excitation NI/n, required to focus the electron beam at the same plane as the polepiece tip (i.e. upto Z_f/n = 0.0 mm).

The electron optical properties of lens HERMES were not computed for ray 2 beam orientation, since a lens with no bore cannot be used in this beam orientation.

One important point the reader must remember when studying the figures giving the electron optical properties of these lenses, is that for each lens excitation, the axial magnetic flux density distribution of each lens is different; the peak value of which is given as a function of lens excitation by figures 2.21, 2.30, 2.31, 2.32, 2.43 and 2.44, for the lenses HERMES, HERMES II, HERMES III, ZEUS, APHRODITE and ATHENA, respectively.

2.4.1 The electron optical properties of the lenses in ray 2 beam orientation

Figures 2.47, 2.48, 2.49, 2.50 and 2.51, show the variation of the electron optical properties of the lenses HERMES II, HERMES III, ZEUS, APHRODITE and ATHENA, respectively, as a function of lens excitation NI/n, for ray 2 beam orientation. The dashed vertical line in these figures indicates the lens excitation at which the effective halfwidth d_h of these lenses starts to increase.

By comparing figures 2.47, 2.48, 2.49, 2.50 and 2.51, with each other, can be seen that the spherical and chromatic aberration

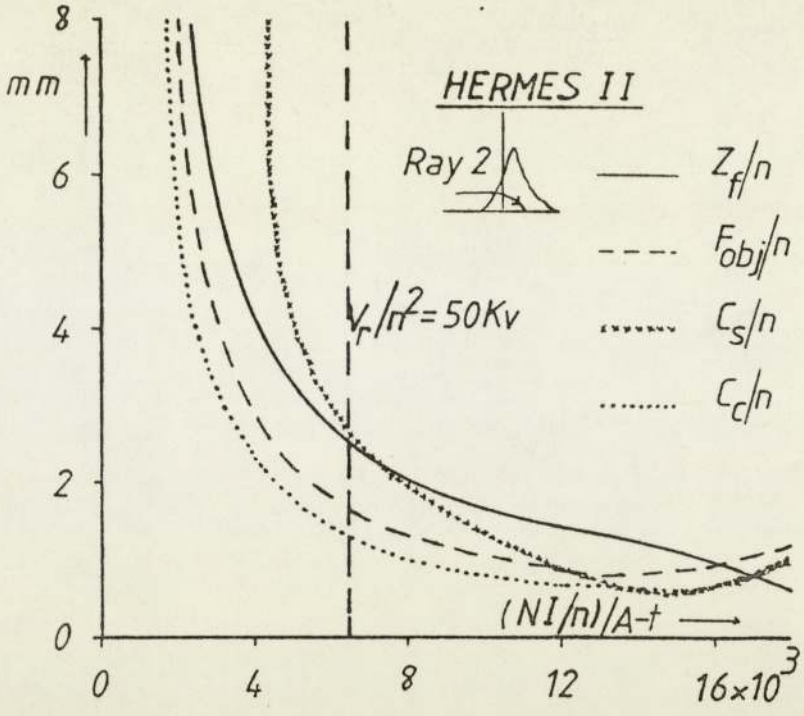

Figure 2.47 The variation of the electron optical properties of lens HERMES II, as a function of lens excitation. The dashed vertical line indicates the lens excitation at which the effective halfwidth starts to increase.

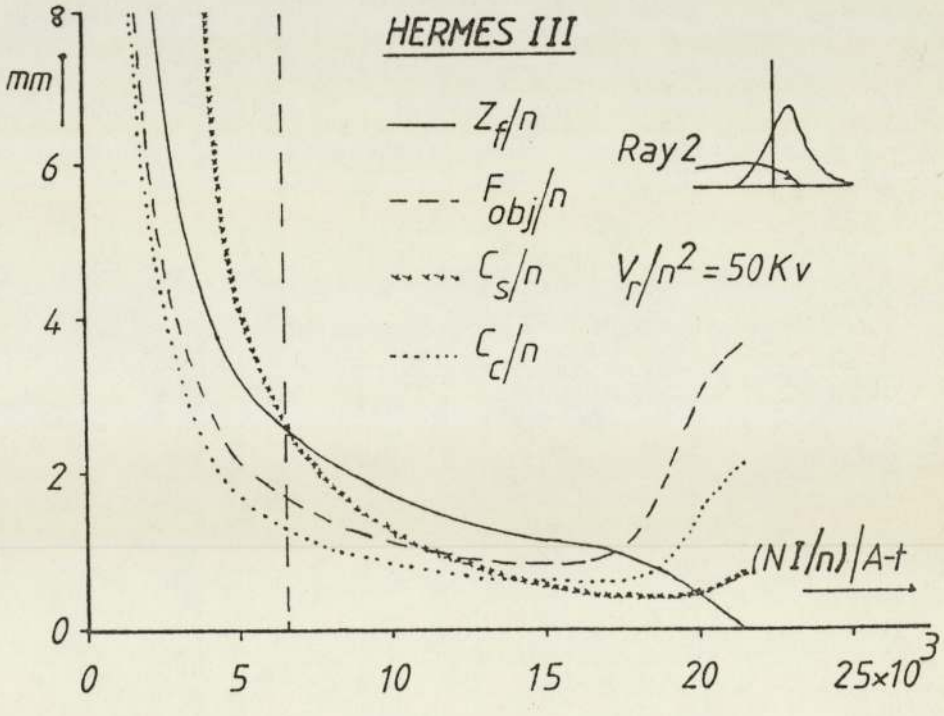

Figure 2.48 The variation of the electron optical properties of lens HERMES III, as a function of lens excitation. The dashed vertical line indicates the lens excitation at which the effective halfwidth starts to increase.

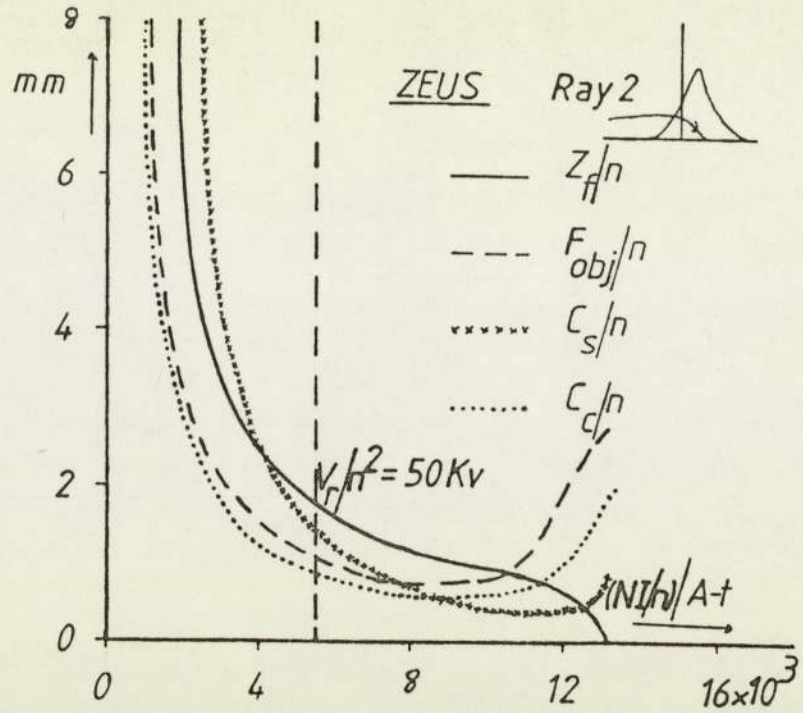

Figure 2.49 The variation of the electron optical properties of lens ZEUS, as a function of lens excitation. The dashed vertical line indicates the lens excitation at which the effective halfwidth starts to increase.

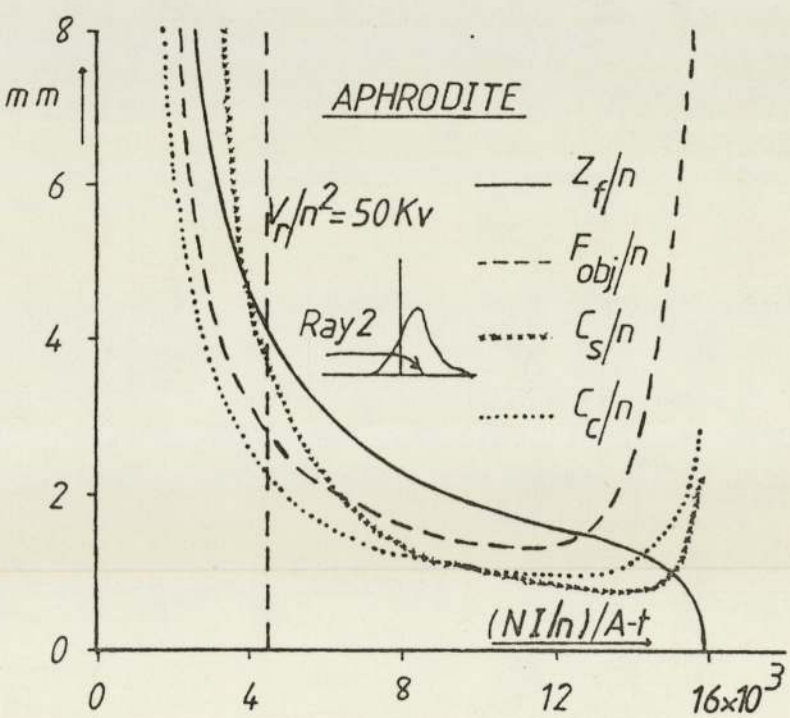

Figure 2.50 The variation of the electron optical properties of lens APHRODITE, as a function of lens excitation. The dashed vertical line indicates the lens excitation at which the effective halfwidth starts to increase.

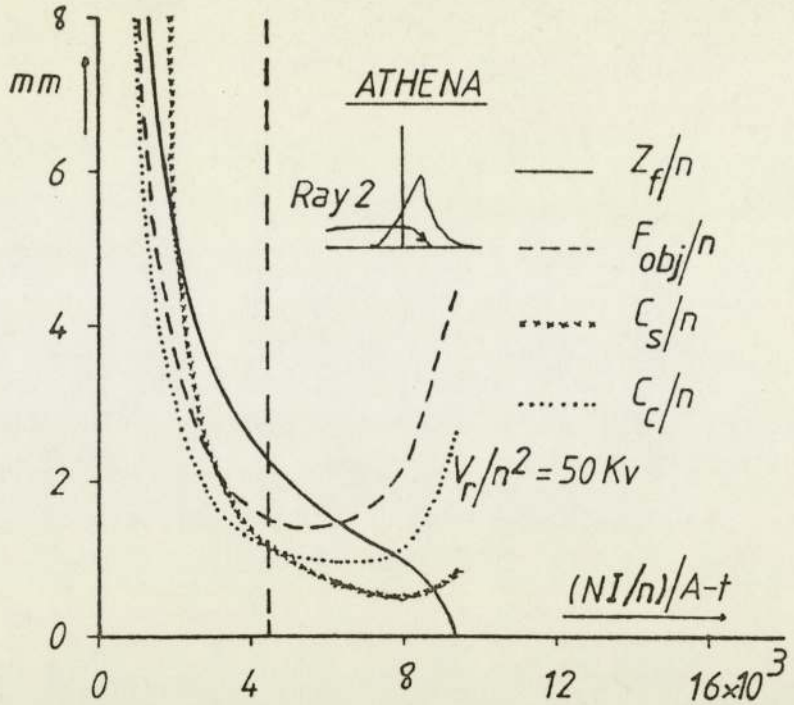

Figure 2.51 The variation of the electron optical properties of lens ATHENA, as a function of lens excitation. The dashed vertical line indicates the lens excitation at which the effective halfwidth starts to increase.

coefficients (C_s/n and C_c/n), of all lenses reach a value below 1 mm at a certain range of lens excitation, different for each lens. This range of lens excitation being lower for the asymmetric conventional lenses (ZEUS and ATHENA), than for the single polepiece lenses (HERMES II, HERMES III and APHRODITE).

Within this range of lens excitation, the working distance Z_f/n, has a value lower than 2 mm at the low end of the range and a value around 1 mm at the high end of the range.

The objective focal length F_{obj}/n, in the same range of lens excitation NI/n, has a value less than 1.0 mm for lenses HERMES II, HERMES III and ZEUS and a value less than 1.5 mm for lenses APHRODITE and ATHENA. The difference between the working distance and the objective focal length, in this range of lens excitation, is sufficient to allow the use of an electron beam aperture in

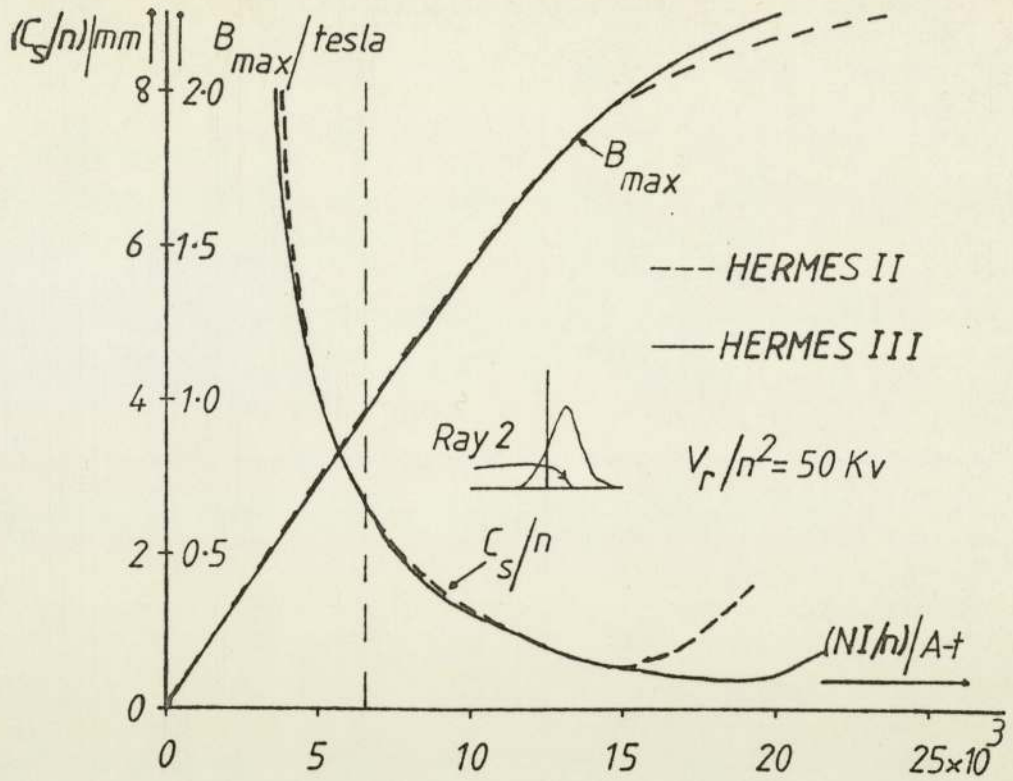

Figure 2.52 The variation of the spherical aberration coefficient and the variation of the peak value of the axial magnetic flux density distribution of the lenses HERMES II and HERMES III, as a function of lens excitation.

each lens, if one is required.

From figures 2.47, 2.48, 2.49, 2.50 and 2.51, can also be seen that the range of lens excitation giving the minimum electron optical properties for each lens, is consistantly higher than the lens excitation at which the effective halfwidth d_h of each lens starts to increase. This suggests that a certain amount of saturation of the lens polepiece tip is essential for minimising the electron optical properties of these lenses, in ray 2 beam orientation.

By comparing the electron optical properties of lens HERMES II with those of lens HERMES III, the importance of the coil shape and position in a single polepiece lens can further be illustrated. Figure 2.52 shows the variation of the spherical aberration

coefficient C_s/n and the peak value B_{max} of the axial magnetic flux density distribution of the lenses HERMES II and HERMES III, as a function of lens excitation NI/n. From this figure it can be seen that the optimum spherical aberration coefficient of lens HERMES III has a lower value and it occurs at a higher lens excitation than that of lens HERMES II. The peak value of the axial magnetic flux density distribution of lens HERMES III, at the lens excitation giving the optimum spherical aberration coefficient, is higher than that of lens HERMES II.

If the coil of lens HERMES III is further optimised to meet Marai's criteria (see appendix D), one expects, that the optimum spherical aberration coefficient of such a lens can further be reduced and be given at a higher lens excitation at which the peak value of its axial magnetic flux density distribution will also be higher than that of lens HERMES III.

In order to choose which one of these lenses was a suitable objective lens for the probe forming system of a multi-purpose micro-x-ray source, two additional criteria were used in comparing these lenses. The semi-angle α_s formed by the plane of the target and the body of the lens, gives the maximum solid angle in which an x-ray detector can be positioned. As this semi-angle increases the ease of optimising the position of the x-ray detector increases. An electron beam aperture is usually used with objective lenses. The use of such an aperture is only possible if the difference between the working distance and the objective focal length, is large enough to accommodate the thickness of the aperture. In the present work, a difference between the working distance and the objective focal length in the region of 0.25 to 0.30 mm at an electron accelerating voltage V_r of 50 KV, was assumed to be sufficient for the accommodation of an electron beam aperture.

Table 2.5 compares the electron optical properties of the lenses HERMES II, HERMES III, ZEUS, APHRODITE and ATHENA, at a lens excitation at which the spherical aberration coefficient has a minimum value at an electron accelerating voltage V_r of 50 KV. In the same table the peak value B_{max} of the axial magnetic flux density distribution and the semi-angle α_s formed by the plane of the target and the body of the lens, are also given for each lens at the lens excitation which gives the minimum spherical aberration coefficient.

In table 2.5 the electron optical properties of the lenses (ZEUS, HERMES III and APHRODITE) which cannot accommodate an electron beam aperture at the lens excitation giving the minimum spherical aberration coefficient, are also given at a lens excitation which allows the accommodation of an electron beam aperture.

Table 2.5 Comparison of the lenses HERMES II, HERMES III, ZEUS, APHRODITE and ATHENA, under conditions suitable for the objective lens of the probe forming system of a multi-purpose micro-x-ray source, at an electron accelerating voltage V_r of 50 KV, in ray 2 beam orientation.

LENS	NI/A-t	Z_f/mm	F_{obj}/mm	C_s/mm	C_s/mm	B_{max}/T	α_s/°
HERMES II	14535	1.20	0.85	0.57	0.60	1.950	90
HERMES III	17590	0.93	1.01	0.41	0.60	2.152	90
ZEUS	11181	0.80	1.15	0.35	0.72	2.315	15.20
APHRODITE	13417	1.40	1.85	0.72	1.03	1.425	90
ATHENA	7826	1.05	2.05	0.50	1.10	1.465	18.53
ZEUS*	8944	1.10	0.78	0.55	0.55	2.075	15.69
HERMES III*	14864	1.15	0.85	0.58	0.62	1.974	90
APHRODITE*	11181	1.70	1.35	0.90	1.00	1.290	90
ATHENA*	5590	1.78	1.40	0.82	1.00	1.245	20.05

* properties at a lens excitation allowing the accommodation of an electron beam aperture.

From table 2.5, can be seen that at the lens excitation giving the respective minimum spherical aberration coefficient of each lens, only lens HERMES II can accommodate an electron beam aperture. At the lens excitation at which the rest of the lenses can accommodate an electron beam aperture, only lens ZEUS has spherical and chromatic aberration coefficients lower than lens HERMES II. Since lens HERMES II provides a larger semi-angle α_s than lens ZEUS, then lens HERMES II can be regarded the better lens for use as the objective lens of the probe forming system of a multi-purpose micro-x-ray source.

Although the rest of the lenses may not be suitable for the objective lens of the probe forming system of a micro-x-ray source, they may be suitable as objective lenses for high resolution electron microscopy, as will be seen in chapter 3.

2.4.2 The electron optical properties of the lenses in ray 1 beam orientation

Figures 2.53, 2.54, 2.55, 2.56, 2.57 and 2.58, show the variation of the electron optical properties of the lenses HERMES, HERMES II, HERMES III, APHRODITE, ZEUS and ATHENA, respectively, as a function of lens excitation NI/n, at an electron accelerating voltage V_r of 700 Kv, for ray 1 beam orientation.

By comparing figures 2.53, 2.54, 2.55 and 2.56, which show the variation of the electron optical properties of the single polepiece lenses, it can be seen that HERMES which has no bore, gives the lower values of objective focal length F_{obj}/n, chromatic and spherical aberration coefficients (C_c/n and C_s/n), for which their minimum values occur in a range of lens excitation NI/n from 10750 to 12500 A-t. The working distance Z_f/n of lens HERMES is zero at a lens excitation NI/n of 12000 A-t, which is within the range of

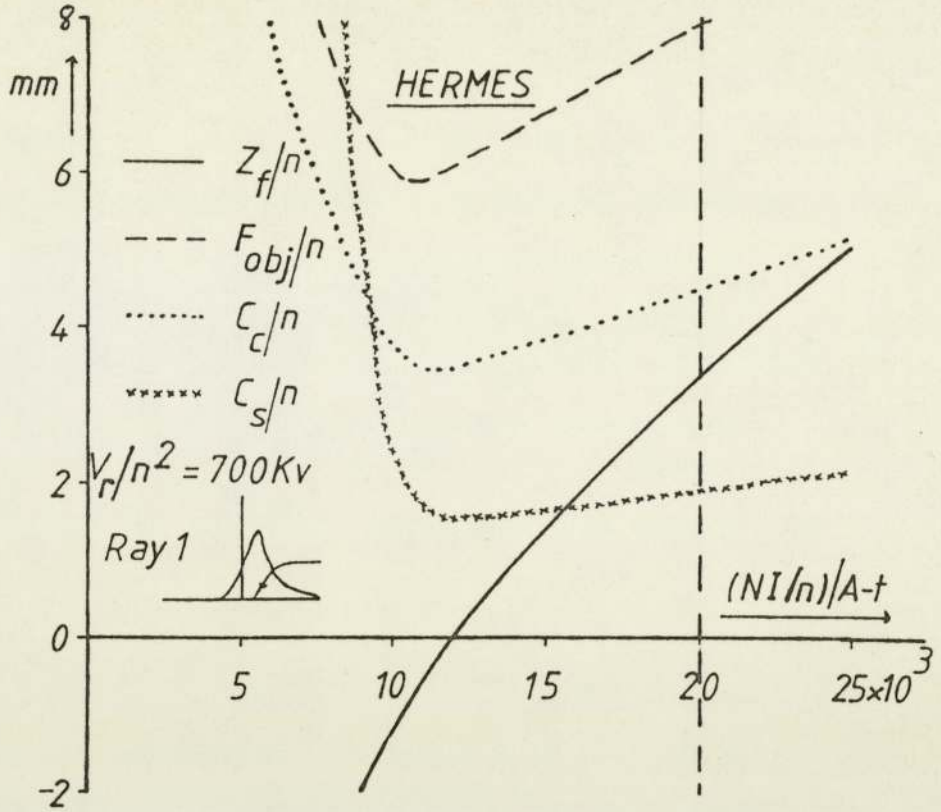

Figure 2.53 The variation of the electron optical properties of lens HERMES, as a function of lens excitation. The dashed vertical line indicates the lens excitation at which the effective halfwidth starts to increase.

lens excitation giving its minimum electron optical properties.

The range of lens excitation NI/n, giving the minimum electron optical properties of lenses HERMES II and HERMES III, is slightly higher than that of lens HERMES, extending from 11000 to 14000 A-t. In this range of lens excitation the values of the electron optical properties of the lenses HERMES II and HERMES III are exactly the same.

The minimum values of the electron optical properties of lens APHRODITE, occur at an even higher range of lens excitation NI/n than the rest of the single polepiece lenses. This range of lens excitation extends from 11500 to 16000 A-t.

The minimum values of the objective focal length F_{obj}/n, the chomatic and spherical aberration coefficients (C_c/n and C_s/n) of

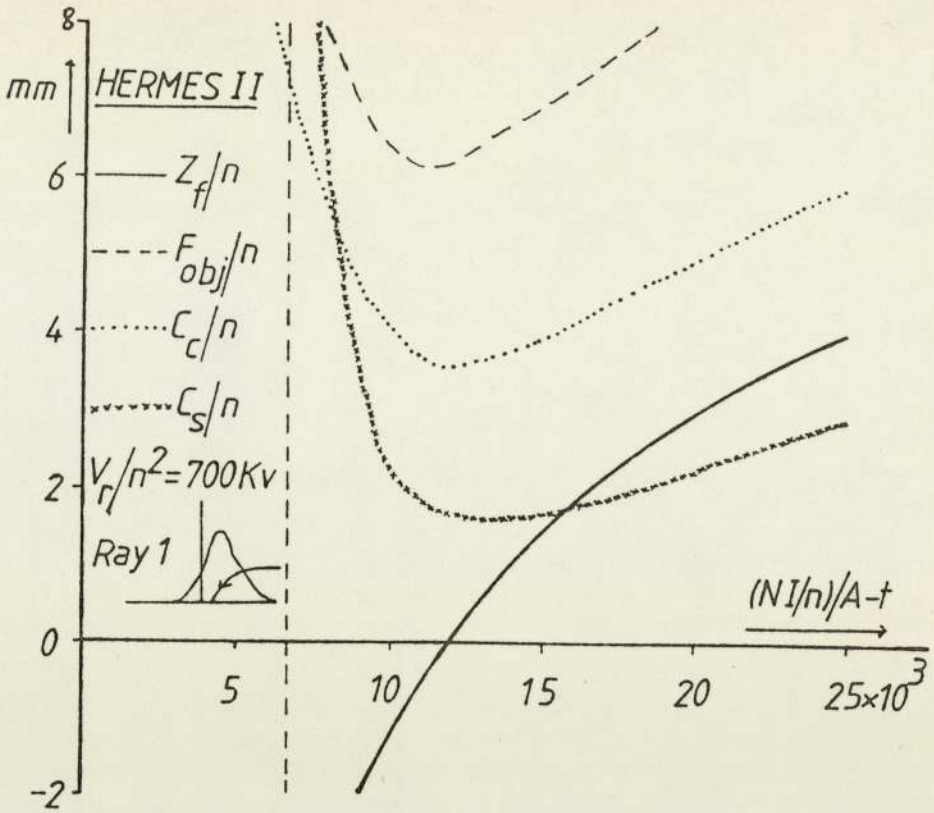

Figure 2.54 The variation of the electron optical properties of lens HERMES II, as a function of lens excitation. The dashed vertical line indicates the lens excitation at which the effective halfwidth starts to increase.

the lenses HERMES II and HERMES III are slightly higher than those of lens HERMES. The corresponding values of lens APHRODITE are higher than those of the lenses HERMES II and HERMES III.

The reason why the electron optical properties of lenses HERMES II, HERMES III and APHRODITE are worse than those of lens HERMES, is due to the way the polepiece of these lenses saturates with increasing lens excitation. The shape of the axial magnetic flux density distribution of these lenses, which the incoming electron beam faces in ray 1 beam orientation does not change substantialy with increasing lens excitation. Thus the electron optical properties of these lenses achieve their minimum values, mainly by the strength of the axial magnetic flux density distribution.

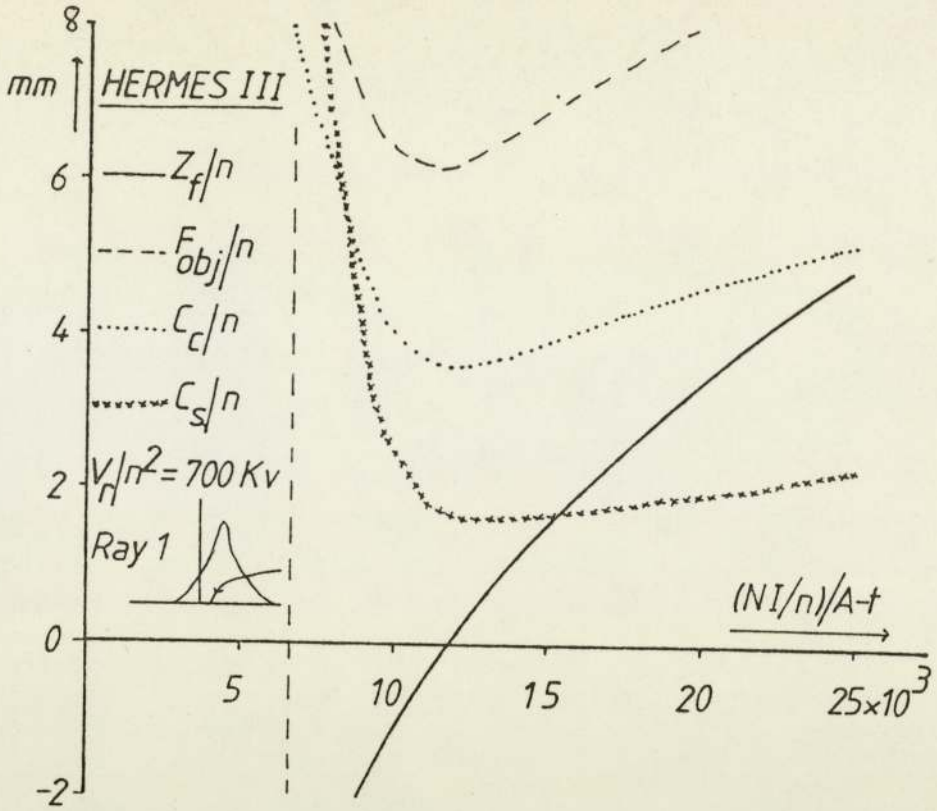

Figure 2.55 The variation of the electron optical properties of lens HERMES III, as a function of lens excitation. The dashed vertical line indicates the lens excitation at which the effective halfwidth starts to increase.

After a small range of lens excitation over which the effective halfwidth of these lenses in ray 1 beam orientation is constant, this effective halfwidth increases slowly with increasing lens excitation. This increase in the effective halfwidth is due to the saturation of the polepiece tip, which increases substantially the effective halfwidth for ray 2 beam orientation. The substantial increase in the effective halfwidth for ray 2 beam orientation, effects the rate by which the strength of the axial magnetic flux density distribution increases with increasing lens excitation. Thus at lens excitations higher than the critical lens excitation which affects the rate by which the strength of the axial magnetic flux density distribution increases, the electron optical properties of the single polepiece lenses tend to increase with increasing

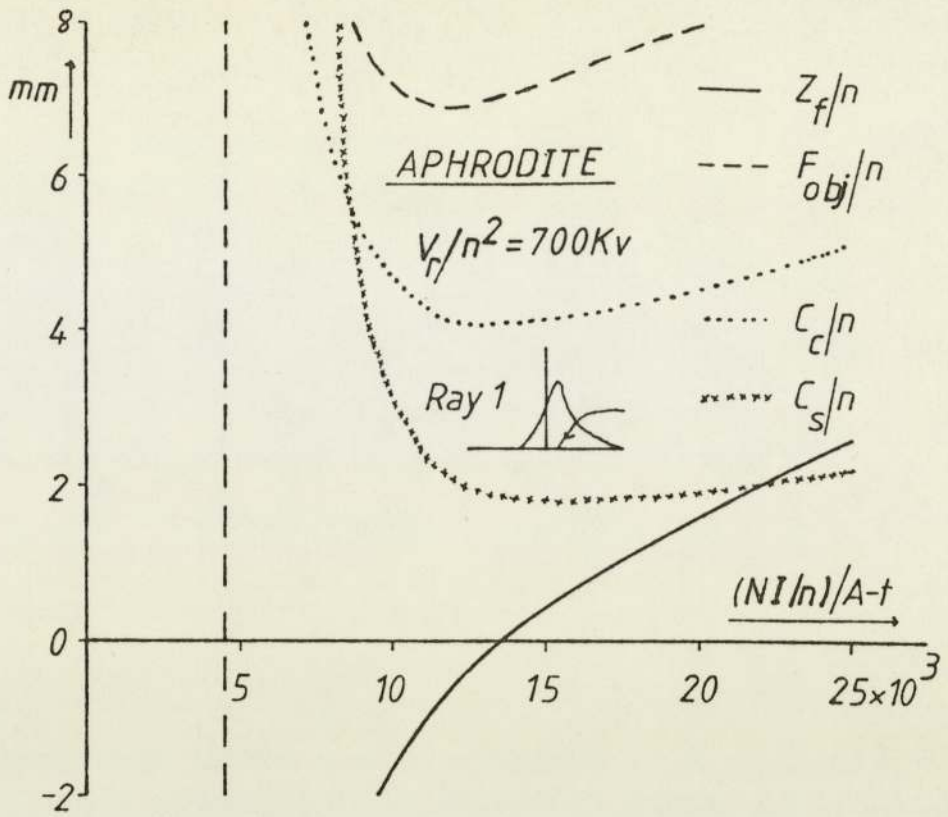

Figure 2.56 The variation of the electron optical properties of lens APHRODITE, as a function of lens excitation. The dashed vertical line indicates the lens excitation at which the effective halfwidth starts to increase.

lens excitation.

Therefore single polepiece lenses operated in ray 1 beam orientation, achieve their minimum electron optical properties at a lens excitation which gives an optimum strength of the axial magnetic flux density distribution. This can further be illustated by comparing the spherical aberration coefficient of lenses HERMES II and HERMES III, as shown in figure 2.59. The minimum value of the spherical aberration coefficient, is the same for both lenses and it occurs at the same lens excitation. At this lens excitation the axial magnetic flux density distribution of each lens has the same strength. This can be seen by the variation of the peak value B_{max} of the axial magnetic flux density distribution of both lenses, which is also shown in figure 2.59, as a function of lens

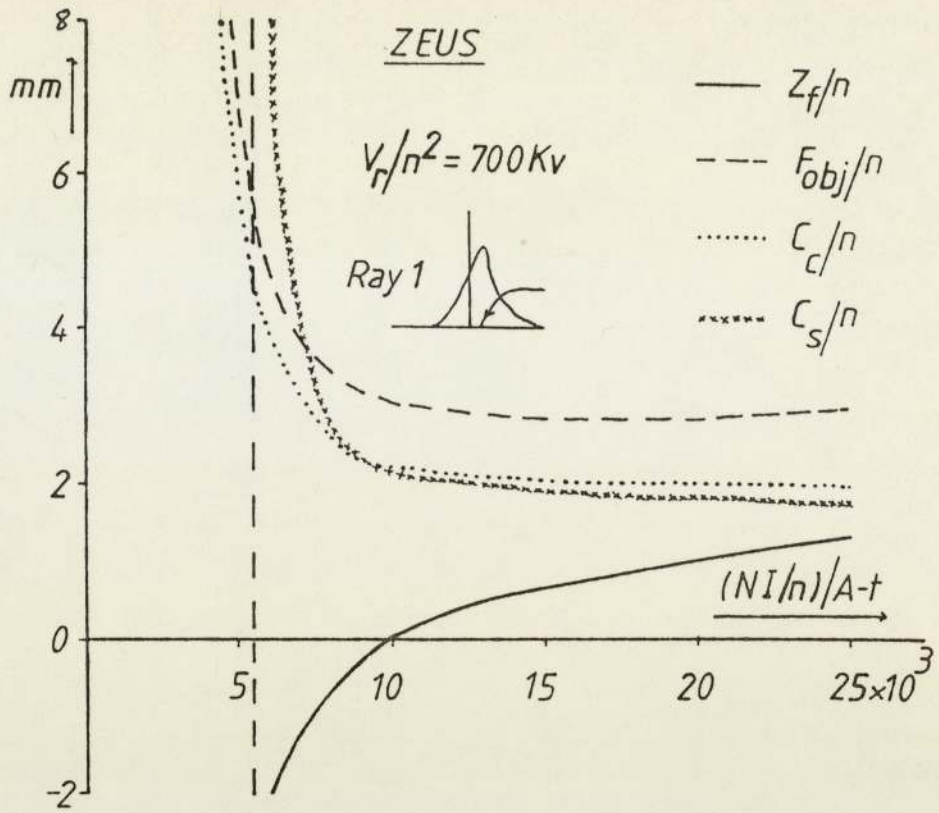

Figure 2.57 The variation of the electron optical properties of lens ZEUS, as a function of lens excitation. The dashed vertical line indicates the lens excitation at which the effective halfwidth starts to increase.

excitation NI/n.

From figures 2.57 and 2.58, can be seen that the asymmetric conventional lenses, ZEUS and ATHENA, behave different from the single polepiece lenses in ray 1 beam orientation.

The aberrations of these lenses decrease with increasing lens excitation, even well above the lens excitation at which the respective objective focal lengths of these lenses start to increase. Again the reason for this phenomenon is the way in which the main polepiece of these lenses saturates with increasing lens excitation. The shape of the axial magnetic flux density distribution which the incoming electron beam sees in ray 1 beam orientation, does not change substantially, since the second polepiece of these lenses does not saturate with the same rate as

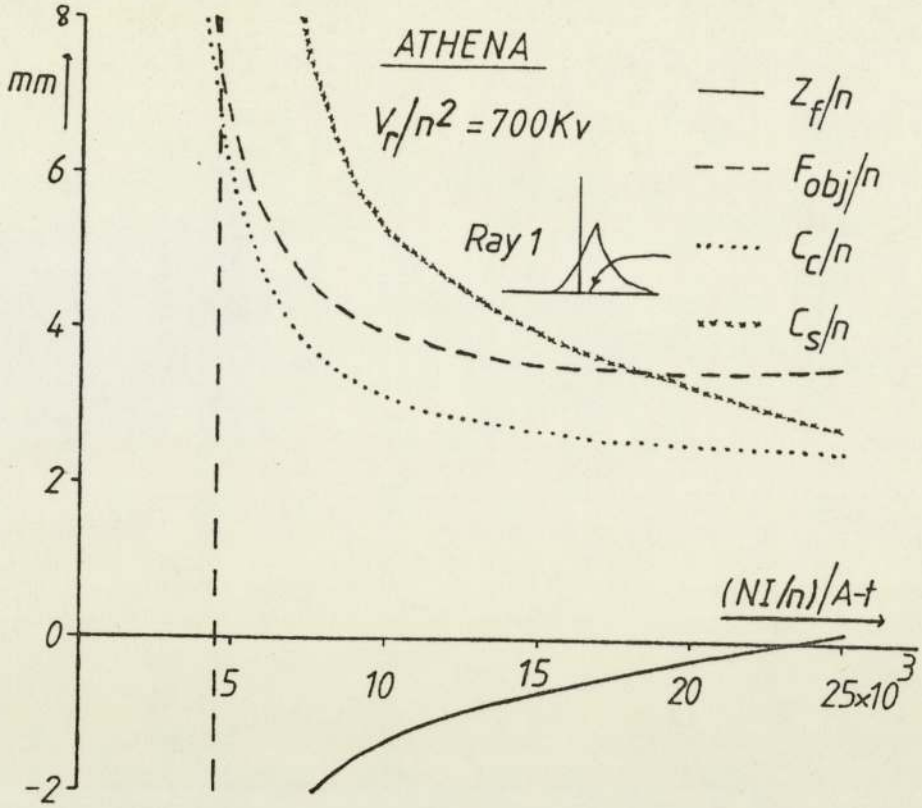

Figure 2.58 The variation of the electron optical properties of lens ATHENA, as a function of lens excitation. The dashed vertical line indicates the lens excitation at which the effective halfwidth starts to increase.

their main polepieces. Thus this shape of the axial magnetic flux density distribution for ray 1 beam orientation is not optimum. The aberrations decrease purely by the effect of the increasing strength of the axial magnetic flux density distribution with increasing lens excitation. The optimum strength of the axial magnetic flux density distribution of these lenses is achieved before the minimum values of their respective aberrations is reached. The aberrations further decrease due to the small change in the shape of the axial magnetic flux density distribution which the incoming electron beam in ray 1 beam orientation faces. This change is due to the slight saturation of the second polepieces of these lenses.

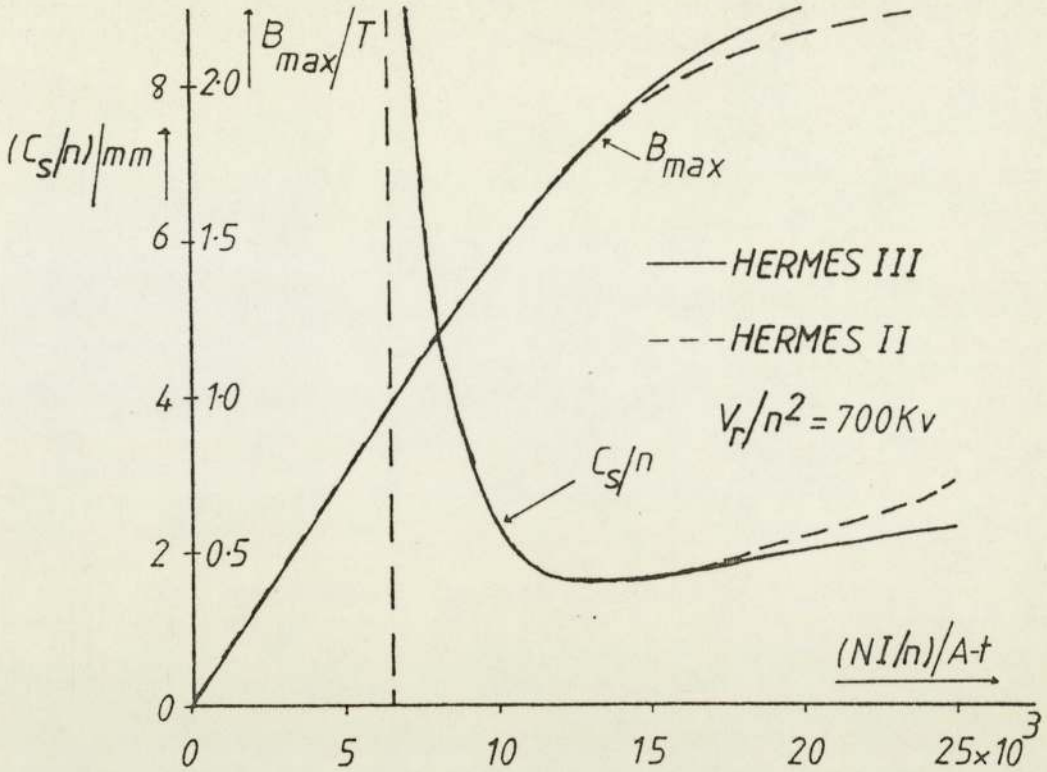

Figure 2.59 The variation of the spherical aberration coefficient and the variation of the peak value of the axial magnetic flux density distribution of the lenses HERMES II and HERMES III, as a function of lens excitation.

The effect of the saturation of the main polepieces of these lenses, has the effect of delaying the lenses from reaching the optimum strength of their axial magnetic flux density distributions. This can be seen by the fact that lens ATHENA, which has a large conical bore in its main polepiece and it saturates at lower lens excitations than the main polepiece of lens ZEUS, requires more than twice the lens excitation of lens ZEUS to focus the electron beam at the same plane as its polepiece tip.

Eventually, at a very high lens excitation at which the second polepiece of these lenses saturates substantially so that the axial magnetic flux density distribution achieves an optimum shape on its side affecting ray 1 beam orientation, the aberrations of these lenses will reach their respective minimum values. This lens

Table 2.6 Comparison of the optimum electron optical properties of lenses HERMES, HERMES II, HERMES III, APHRODITE, ZEUS and ATHENA, at an electron accelerating voltage V_r of 700 KV, in ray 1 beam orientation.

LENS	NI/A-t	C_s/mm	C_c/mm	F_{obj}/mm	Z_f/mm
HERMES	12000	1.56	3.51	6.11	0.00
HERMES II	12500	1.61	3.65	6.30	0.40
HERMES III	12500	1.61	3.65	6.30	0.40
APHRODITE	16250	1.82	4.22	7.40	0.75
ZEUS*	25000	1.70	1.99	2.92	1.32
ATHENA*	25000	2.76	2.48	3.55	0.15

* The values of the electron optical properties of lenses ZEUS and ATHENA are not at the lens excitation giving their respective minimum spherical aberration coefficient.

excitation will be higher for lens ATHENA than for lens ZEUS.

Although the aberrations of lens ZEUS decrease steadily with increasing lens excitation, this decrease is very slow above lens excitations more than 10000 A-t. For example the values of spherical and chromatic aberration coefficients (C_s/n and C_c/n) of lens ZEUS at 10000 A-t, are 2.1 and 2.2 mm respectively. These reduce to 1.7 and 2.0 mm respectively at a lens excitation NI/n of 25000 A-t. The percentage decrease of these aberrations are 19% and 9.1% respectively. To achieve these, an increase in the lens excitation of 150% is required.

Table 2.6 gives the electron optical properties of lenses HERMES, HERMES II, HERMES III, APHRODITE, ZEUS and ATHENA, at a lens excitation which gives the minimum value of the spherical aberration coefficient of each lens and an electron accelerating voltage V_r of 700 KV, for ray 1 beam orientation.

Although the minimum values of the spherical aberration

coefficients of lenses ZEUS and ATHENA are not reached at the lens excitation NI/n of 25000 A-t, lens HERMES may still be considered the best objective lens operated in ray 1 beam orientation, since lens HERMES uses only a lens excitation NI/n of 12000 A-t to reach its minimum spherical aberration coefficient. Lenses ZEUS and ATHENA use a lot of lens excitation in saturating their main polepiece, which does not offer any advantage for ray 1 beam orientation. Although Lenses ZEUS and ATHENA may eventually achieve a spherical aberration coefficient lower than lens HERMES, it will be at the expence of a very high lens excitation which will not be cost effective compared with the modest lens excitation at which lens HERMES achieves its minimum spherical aberration coefficient.

Since lens HERMES has no bore its applications are limited. For high resolution electron microscopy, a single polepiece lens with a small bore will be of advantage and be competitive with asymmetric conventional lenses operated in ray 2 beam orientation, as it will be seen in the next chapter of this work.

3 Comparison of the lenses with existing objective lenses

3.1 Comparison with high resolution objective lenses

It is convenient in comparing the resolving power of electron microscopes to make use of the optical transfer function, in particular, the spatial frequency at which the transfer coefficient becomes zero before it begins to oscillate. The corresponding spacing (σ_o) is given by (Humphreys and Spence, 1980) :

$$\sigma_o = 0.7(C_s\lambda^3)^{\frac{1}{4}} \quad \text{- - - - - - - - - - - - - - - - - - 3.1}$$

where

λ is the electron wavelength

With thick specimens the chromatic aberration coefficient may set a more stringent limit and in a second approximation, this must be included in the transfer function. However, it is still useful to employ the parameter σ_o, in comparing potential high resolution microscopes.

In order to compare microscopes operating at different electron accelerating voltages V_o, it is convenient to refer their corresponding σ_o values to a standard electron accelerating voltage; in this case V_o = 600 KV. Table 3.1 shows sixteen possible designs of objective lenses. Columns 3 and 4 show the published values of C_s and σ_o at the normal operating voltage, while columns 5 and 6 show the expected C_s and σ_o values of the relevant lenses scaled to an electron accelerating voltage V_o = 600 KV.

The row data for the commercial instruments was obtained from manufacturers specifications and published literature. These values do not necessarily represent ultimate performance. Nevertheless table 3.1 indicates that the objective lenses of the present work are competitive with commercial instruments.

Table 3.1 Comparison of high resolution instruments at V_o = 600 Kv.

INSTRUMENT	V_o/KV	Published C_s/mm	δ_o/nm at V_o	C_s/mm at V_o = 600 KV	δ_o/nm at V_o = 600 KV
Cambridge HREM	600	3.30	0.20	3.30	0.20
SIEMENS 102	120	—	0.36	—	0.22
JEOL 120CX	120	0.70	0.28	1.87	0.17
JEOL 200CX	200	1.20	0.26	2.40	0.19
Philips EM400	120	1.10	0.32	2.94	0.20
HERMES II (ray 2)	48	0.57	0.39	2.50	0.19
HERMES III (ray 2)	48	0.41	0.36	1.80	0.17
ZEUS (ray 2)	48	0.35	0.35	1.53	0.17
APHRODITE (ray 2)	48	0.72	0.42	3.26	0.20
ATHENA (ray 2)	48	0.50	0.38	2.19	0.18
HERMES (ray 1)	475	1.56	0.19	1.83	0.14
HERMES II (ray 1)	475	1.61	0.19	1.89	0.14
HERMES III (ray 1)	475	1.61	0.19	1.89	0.14
APHRODITE (ray 1)	475	1.82	0.19	2.13	0.18
ZEUS (ray 1)	475	1.70	0.19	1.99	0.18
ATHENA (ray 1)	475	2.76	0.22	3.23	0.20

By using high flux density objective lenses designed to take advantage of the saturation of their polepiece tips, it is possible to stretch the limit of spatial resolution beyond the present limit of 0.20 nm given by the operational Cambridge High Resolution Microscope.

3.2 Critical assessment of Cleaver's work (1980)

Cleaver (1980) has studied a number of asymmetric and symmetric conventional lenses in order to obtain the best objective lens polepiece shape under saturation conditions. The object of his study was to achieve an optimum lens design for high resolution electron microscopy. He based his study on the polepiece shapes shown in figure 3.1; these were assumed to be made of Permendur.

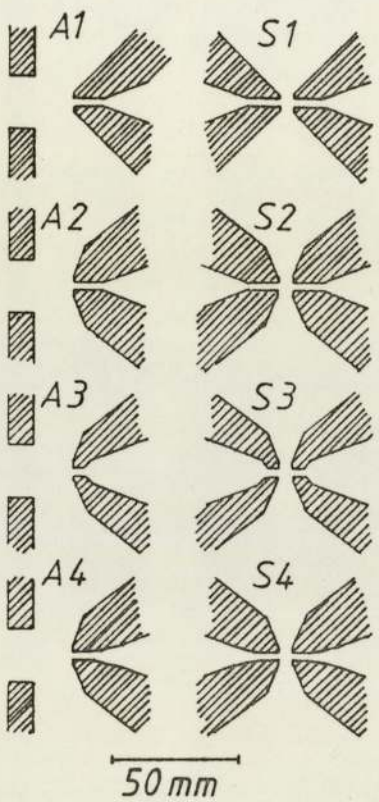

Figure 3.1 Lens polepiece shapes. Asymmetric lenses : gap 15 mm and 20 mm diameter; coordinate origin at face of small-bore polepiece. Symmetric lenses : gap 5 mm, bores 3 mm diameter; coordinate origin at centre of gap. Initial external cone semi-angles either 45° or 67°. (Cleaver, 1980).

In describing the performance of these lenses under saturation conditions, Cleaver stated that " Increasing polepiece saturation can initially have the effect of rounding off regions of high axial field, and so reducing the spherical aberration coefficient;

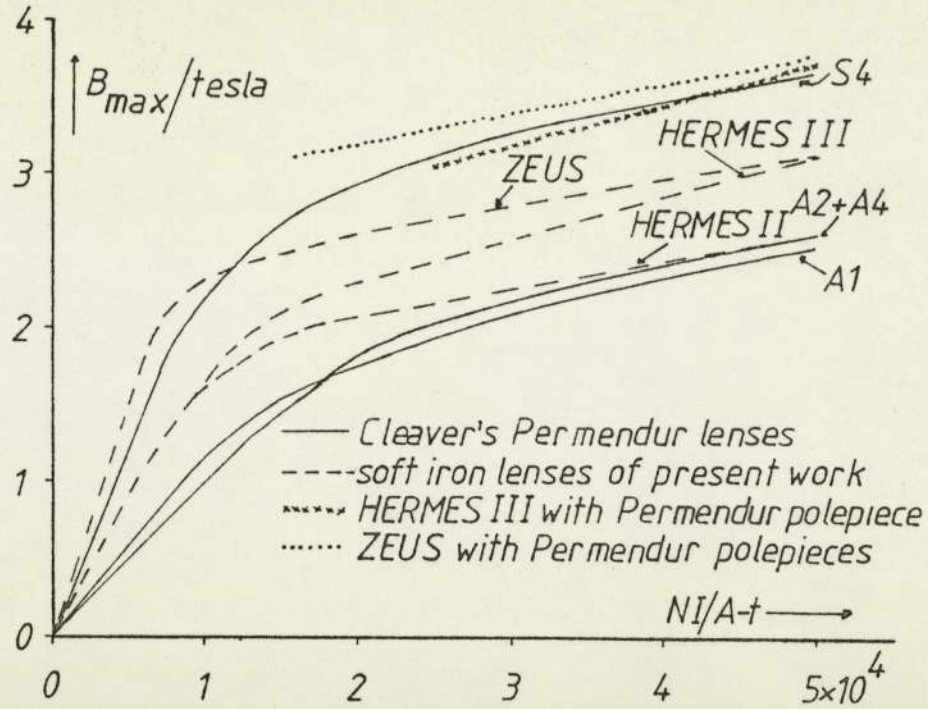

Figure 3.2 The variation of the peak value of the axial magnetic flux density distribution of Cleaver's lenses S4, A1, A2, A4 and that of lenses ZEUS, HERMES II and HERMES III, as a function of lens excitation.

eventually, however, the broadening of the field distribution always becomes dominant and the aberration increases with saturation".

This statement holds for Cleaver's lenses and in fact it holds for the lenses of the present work, but Cleaver failed to see the importance of the lens coil, whose shape and position is the most important feature of a highly saturated lens; influencing the broadening of the field distribution.

The optimisation of the coil shape and position in saturated lenses, is as important, if not more, as the optimisation of the polepiece shape of such lenses. This is illustrated by figure 3.2, which compares the peak value B_{max} of the axial magnetic flux density distribution of Cleaver's best lenses with those of the best lenses of the present work.

In compering the curves of figure 3.2, the reader must remember

that Cleaver assumed that his lenses were made of Permendur, while the lenses of the present work were assumed to be made of soft iron.

The polepiece shapes of lenses ZEUS and HERMES II are optimised and although their coils are not optimised, their peak values B_{max}, are higher than those of Cleaver's asymmetric lenses A1, A2, A3 and A4. By optimising the coil shape and position, the peak value B_{max}, can further be increased, as shown by the curve of lens HERMES III, which has the same polepiece shape as lens HERMES II.

At high polepiece saturation it is possible to extrapolate linearly, to a first approximation, the peak values of the soft iron polepieces of lenses ZEUS and HERMES III, to represent Permendur polepieces. These extrapolations are also shown in figure 3.2. Although the coil shape and position of the single polepiece lens HERMES III are not quite optimum, the extrapolated (Permendur) peak values of this lens are similar to those of Cleaver's best symmetric conventional lens S4. Although the coil of lens ZEUS is not optimised at all, and although lens ZEUS is an asymmetric conventional lens, its extrapolated (Permendur) peak values are higher than those of Cleaver's best symmetric conventional lens S4.

If the polepieces of lens ZEUS are made of Permendur and its coil is optimised, then its peak values B_{max}, will become very much higher than those of the symmetrical conventional lens S4. The optimisation of the coil shape and position of such a lens will limit the broadening of its axial magnetic flux density distribution with increasing polepiece saturation; effectively reducing further its aberrations.

3.3 Comparison with existing micro-x-ray sources

3.3.1 Basic theory and assumptions

In order to compare the performance of a number of lenses used in micro-x-ray sources, a set of parameters has to be calculated for each lens. The most important parameters for this comparison are the Gaussian electron spot size (d_g) produced by the lens on the x-ray target, the electron beam current (I) striking the x-ray target and the power (W_c) dissipated by the lens coil.

The Gaussian electron spot size is closely related to the ultimate x-ray source size of a micro-x-ray source, while the electron current striking the target is directly related to the x-ray flux produced in the x-ray target. The power dissipated in the lens coil is related to the economics of building and running of a lens.

To ensure that these parameters are calculated under the same conditions for each lens, the following assumptions were made with reference to figure 3.3 and applied to all lenses compared in this sub-section.

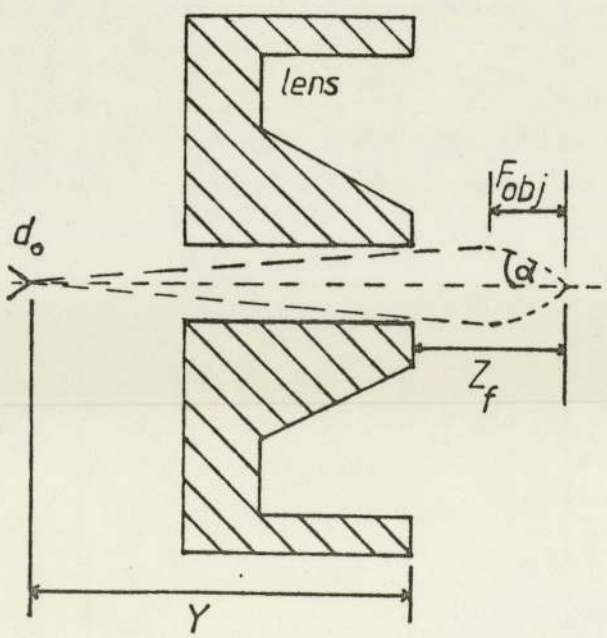

Figure 3.3 Diagram defining the parameters used in the comparison of micro-x-ray sources.

Assuming that the effective electron source size d_o of the electron gun is 50 μm in diameter and is located at a distance Y from the tip of the lens polepiece, then the Gaussian electron spot size formed on the x-ray target is given by :

$$d_g = d_o F_{obj} / (Y + (Z_f - F_{obj})) \text{ - - - - - - - - - - - - } 3.2$$

This equation holds true for a single lens probe forming system micro-x-ray source, where the required demagnification is achieved by moving the x-ray target along the axis of lens symmetry.

The electron current (I) striking the target is given by the electron gun brightness (β), the solid angle ($\omega = \pi\alpha^2$) and the area $\pi d^2/4$ of the electron spot, i.e. :

$$I = \beta \pi^2 \alpha^2 d^2/4 \text{ - - - - - - - - - - - - - - - - } -3.3$$

Spherical aberration has the effect of spreading the electron current (I) into an area larger than that given by the Gaussian spot size d_g. This is clearly undesirable so a beam aperture is used to restrict the semi-angle α.

The minimum disc of confusion due to spherical aberration is given by :

$$d_s = C_s \alpha^3/2 \text{ - - - - - - - - - - - - - - - - - } 3.4$$

Clearly the disc of minimum confusion d_s should be smaller than the Gaussian diameter d_g. For example $d_s \leqslant d_g/2$, the corresponding

angle α is given by $C_s\alpha^3/2 \leqslant d_g/2$, i.e. $\alpha \leqslant (d_g/C_s)^{1/3}$. Hence equation 3.3 becames :

$$I = \frac{\pi^2}{4}\beta d_g^{8/3} C_s^{-2/3} \quad \text{- - - - - - - - - - - - - - - - 3.5}$$

If the electron optical performance of two lenses is identical, preference should be given to that which is the more economic. A parameter which can discriminate between such lenses is the power (W_c) dissipated in the lens coil. This is given by :

$$W_c = I_c^2 R_c \quad \text{- 3.6}$$

where

I_c is the current supplied to the lens coil

R_c is the resistance of the coil windings.

Equations 3.2, 3.5 and 3.6, were used to compare lens HERMES II with existing objective lenses as used in the probe forming systems of existing micro-x-ray sources.

3.3.2 Theoretical comparisons

Since lens HERMES II is the most suitable lens, from the lenses studied in the present work, for the objective lens of the probe forming system of a multi-purpose micro-x-ray source, this lens was compared with three existing lenses which have been employed in micro-x-ray sources. The first lens is an experimental lens made in this department (Harris and Mulvey, 1976), originally designed for a micro-x-radiography source. This lens is shown in figure 3.4 and will be referred to as the HARRIS/MULVEY lens from here forthwith. A special feature of this lens is the protrusion of its polepiece from the lens body, enabling it to be used in standard creep testing and fatique equipment.

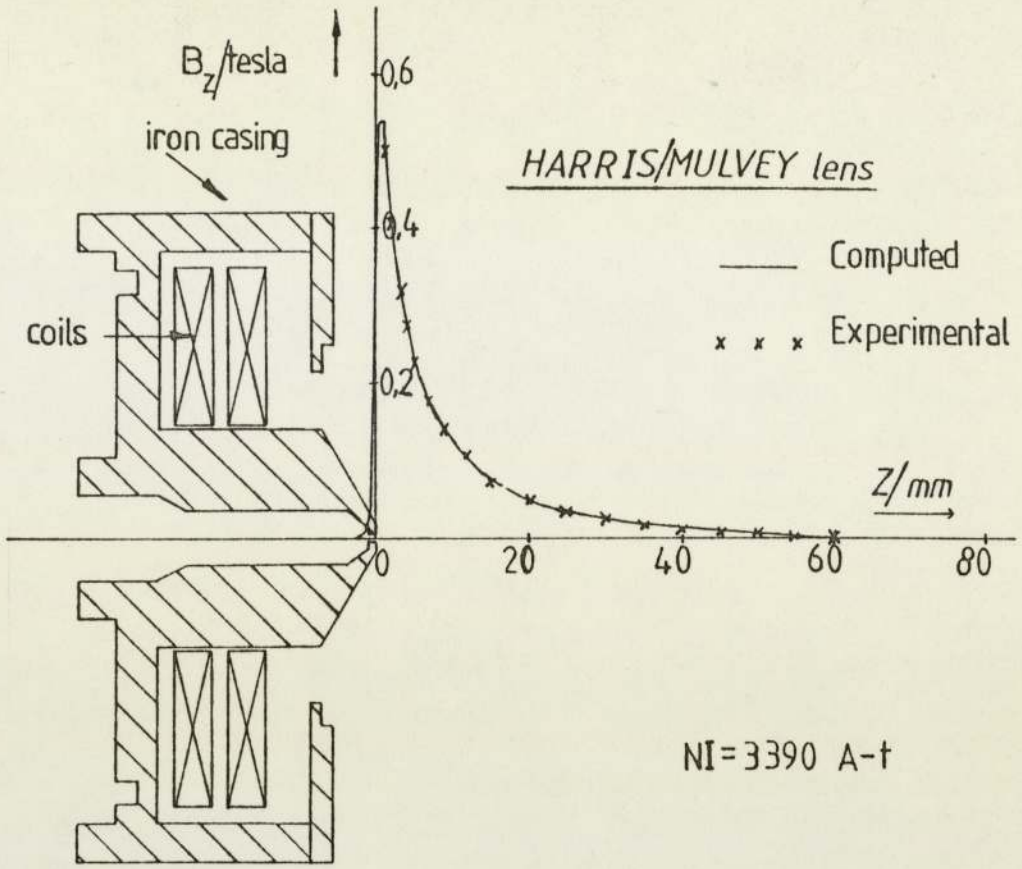

Figure 3.4 Cross-sectional diagram of the HARRIS/MULVEY lens with its axial magnetic flux density distribution at a lens excitation NI = 3390 A-t.

The second lens is that of a microfocus x-ray tube (Pugh and West, 1977), which is presently operational and commercially available as a micro-x-ray source. This lens is shown in figure 3.5 and will be referred to as the PUGH/WEST lens from here forthwith.

The last lens is that of an x-ray calibration source (Rockett and Brundin, 1980), designed for laser fusion work. This lens is shown in figure 3.6 and will be referred to as the ROCKETT/BRUNDIN lens from here forthwith.

The HARRIS/MULVEY and the PUGH/WEST lenses where designed to operate at relatively low electron accelerating voltages (circa 25 KV). The electron gun filament associated with these lenses is

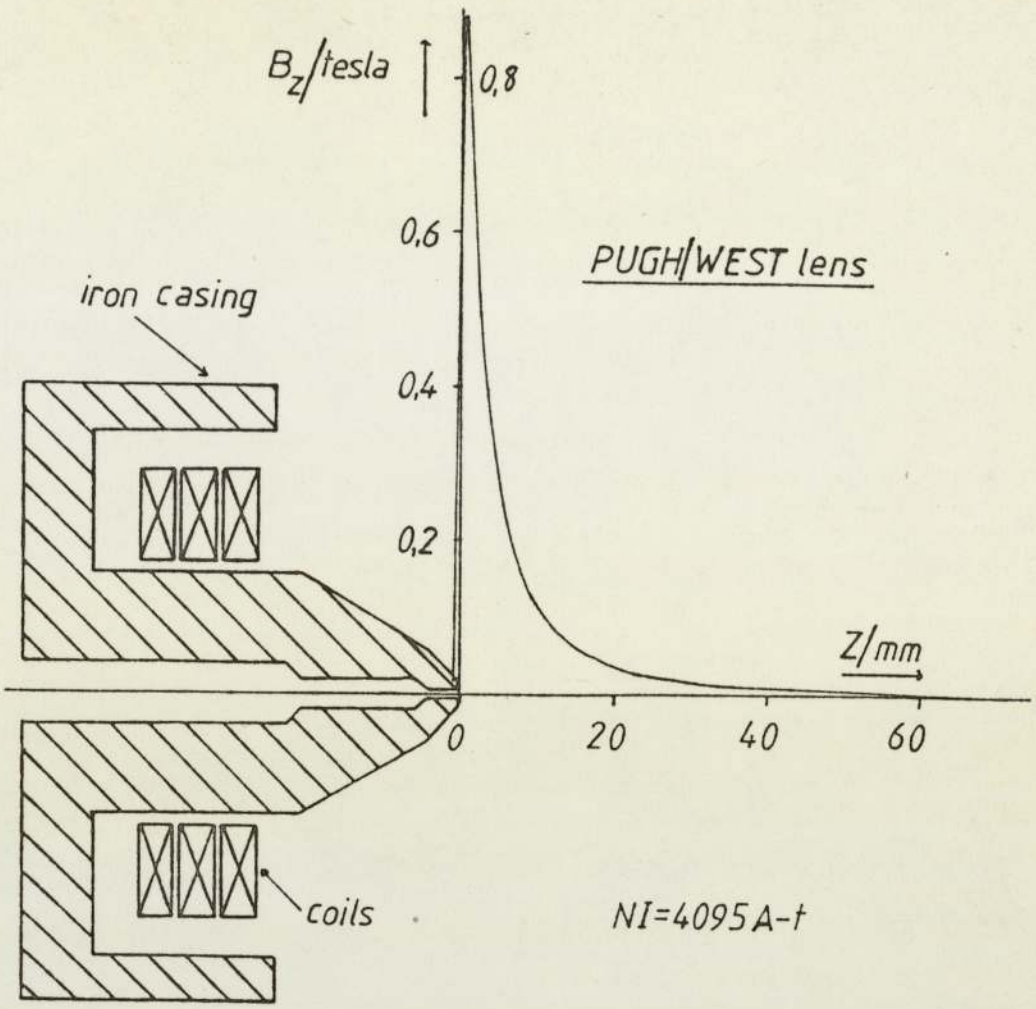

Figure 3.5 Cross-sectional diagram of the PUGH/WEST lens with its axial magnetic flux density distribution at a lens excitation NI = 4095 A-t.

positioned 75 mm (Y = 75 mm) from the tip of their polepieces. The ROCKETT/BRUNDIN lens was designed to operate upto an electron accelerating voltage of 50 KV and its electron gun filament is placed at 140 mm (Y = 140 mm) from its polepiece tip.

From figures 3.4, 3.5 and 3.6 can be seen that if these lenses are operated at high lens excitations, then saturation will take place somewhere in the middle of their polepieces before it takes place at their polepiece tips. Clearly this is an additional factor which must be taken into account when comparing these lenses.

The Gaussian electron spot size (d_g), the electron current (I) striking the x-ray target and the power (W_c) dissipated in the coil

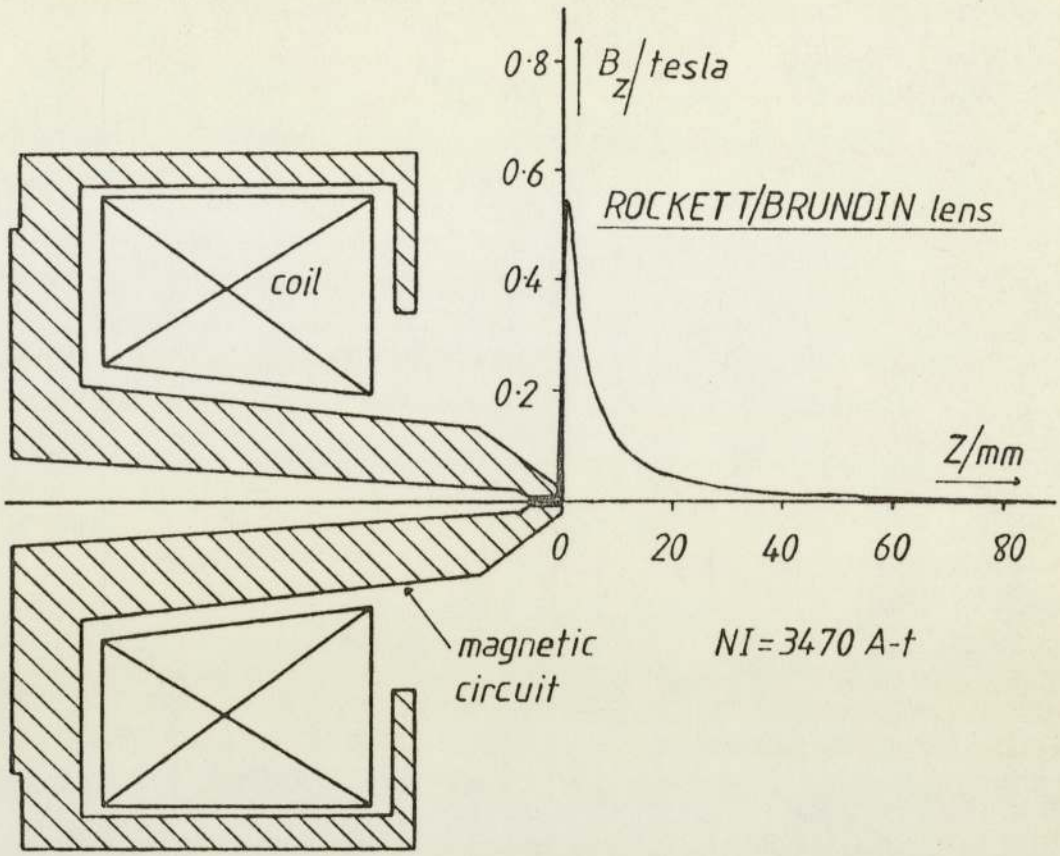

Figure 3.6 Cross-sectional diagram of the ROCKETT/BRUNDIN lens with its axial magnetic flux density distribution at a lens excitation NI = 3470 A-t.

of the lens, for the HARRIS/MULVEY, the PUGH/WEST lens and lens HERMES II, were calculated at 25 KV and at 50 KV electron accelerating voltage, assuming that their electron gun filament is placed at Y = 75 mm.

Figures 3.7 and 3.8 compare lens HERMES II with the HARRIS/MULVEY lens at 25 KV and at 50 KV, respectively. From these figures can be seen that lens HERMES II is superior to the HARRIS/MULVEY lens in all respects. Lens HERMES II provides smaller Gaussian spot sizes and more electron current at a given working distance Z_f. Also lens HERMES II dissipates less power in its coil in achieving this performance. The HARRIS/MULVEY lens is also

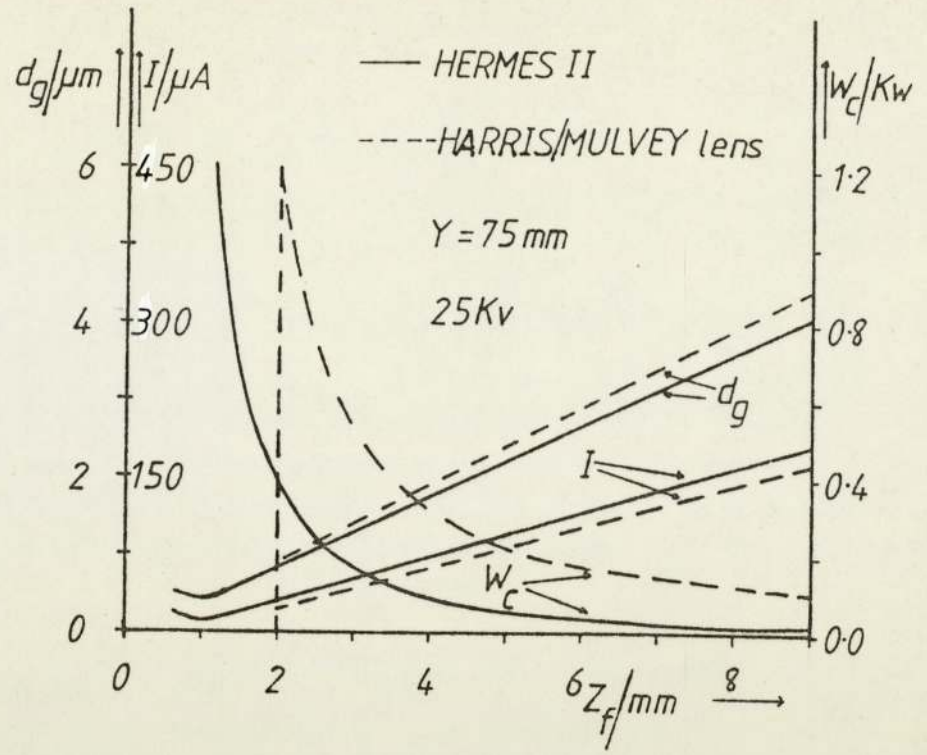

Figure 3.7 The variation of the Gaussian spot size, the electron current and the power dissipated in the lens coil, as a function of the working distance, at 25 KV, for lens HERMES II and the HARRIS/MULVEY lens.

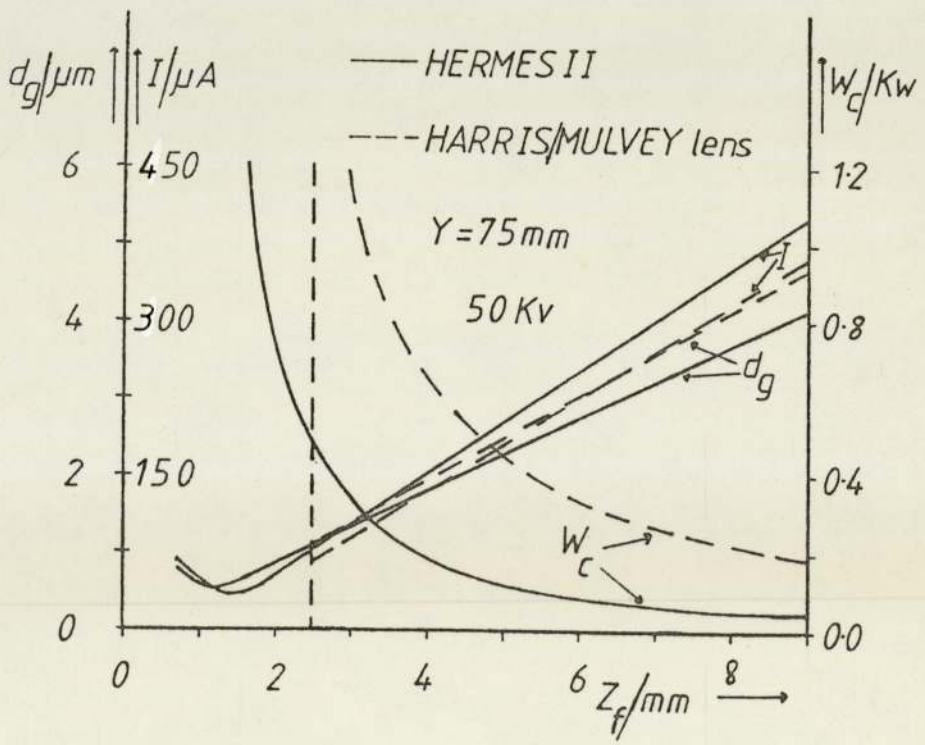

Figure 3.8 The variation of the Gaussian spot size, the electron current and the power dissipated in the lens coil, as a function of the working distance, at 50 KV, for lens HERMES II and the HARRIS/MULVEY lens.

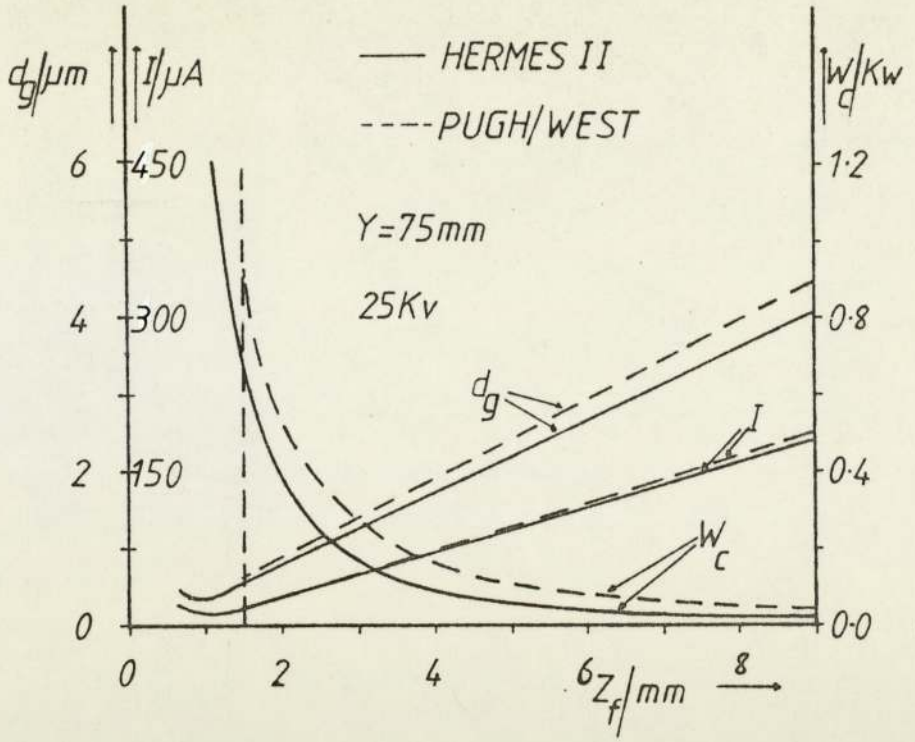

Figure 3.9 The variation of the Gaussian spot size, the electron current and the power dissipated in the lens coil, as a function of the working distance, at 25 KV, for lens HERMES II and the PUGH/WEST lens.

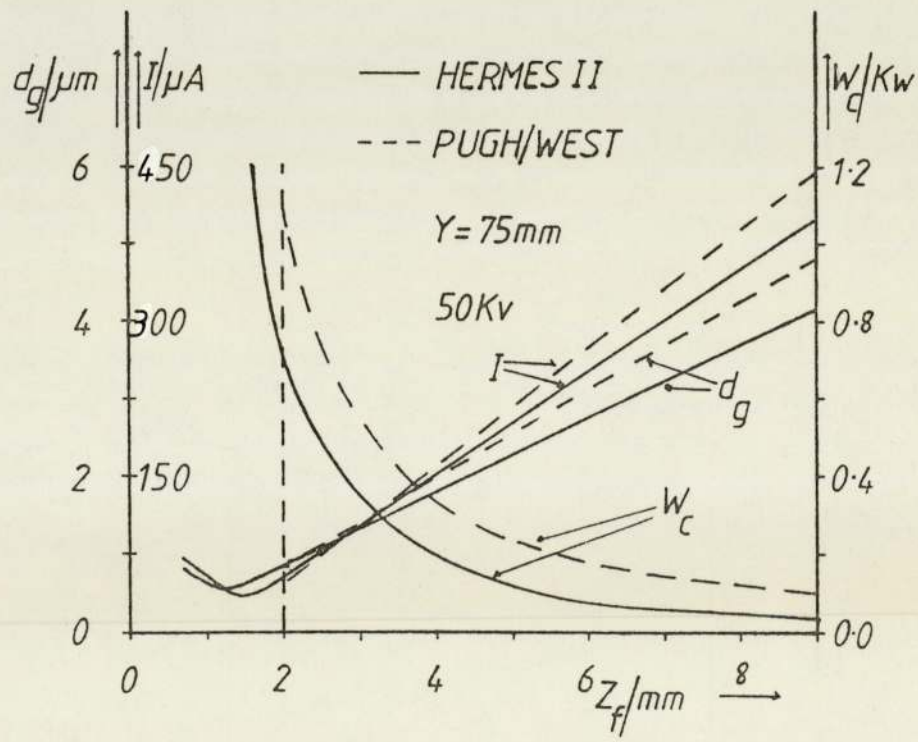

Figure 3.10 The variation of the Gaussian spot size, the electron current and the power dissipated in the lens coil, as a function of the working distance, at 50 KV, for lens HERMES II and the PUGH/WEST lens.

limited by undesirable saturation effects at a position in its polepiece far removed from the tip. The minimum working distance achieved by the HARRIS/MULVEY lens, before saturation affects its performance, is indicated in both figures by a vertical dashed line.

Figures 3.9 and 3.10 compare lens HERMES II with the PUGH/WEST lens at 25 KV and at 50 KV, respectively. From these figures can be seen that again lens HERMES II is superior to the PUGH/WEST lens, since for a given Gaussian spot size, lens HERMES II provides more electron current and dissipates less power in its coil than the PUGH/WEST lens. The PUGH/WEST lens is also limited by undesirable saturation effects at a position in its polepiece far removed from the tip. The minimum working distance achieved by the PUGH/WEST lens, before saturation affects its performance, is indicated in both figures by a dashed vertical line.

Table 3.2 summarises the electron current, the working distance and the power dissipated in the lens coil for a number of Gaussian spot sizes, for lens HERMES II, the HARRIS/MULVEY lens and the PUGH/WEST lens.

Table 3.2 Summary of the properties of lens HERMES II, the HARRIS/MULVEY lens and the PUGH/WEST lens as used for micro-x-ray sources.

LENS		HERMES II			HARRIS/MULVEY			PUGH/WEST		
V_r/Kv	d_g/μm	I/μA	W_c/w	Z_f/mm	I/μA	W_c/w	Z_f/mm	I/μA	W_c/w	Z_f/mm
25	1	12.5	240	2.40	9.0	985	2.20	11.0	465	2.15
	2	27.7	70	4.50	22.0	300	4.15	26.0	160	4.10
	3	44.5	49	6.70	36.0	175	6.10	41.5	80	6.05
	4	59.0	26	8.80	48.0	120	8.05	56.0	58	8.05
50	1	22.5	540	2.30	-	-	-	18.5	920	2.20
	2	57.5	150	4.40	46.0	620	4.10	57.0	335	4.00
	3	92.0	70	6.50	75.0	340	6.00	87.0	195	5.75
	4	127.5	40	8.65	102.5	235	7.75	121.0	140	7.55

From table 3.2, can be seen, for example, that at an electron accelerating voltage of 25 KV and a Gaussian electron spot diameter d_g, of 1 μm, lens HERMES II provides an electron current (I) of 12.5 μA at a working distance Z_f of 2.40 mm. For the same electron accelerating voltage and the same Gaussian spot size, the HARRIS/MULVEY lens provides an electron current (I) of 9.0 μA at a working distance Z_f of 2.20 mm and the PUGH/WEST lens provides an electron current (I) of 11.0 μA at a working distance of 2.15 mm. To achieve the above performance lens HERMES II, the HARRIS/MULVEY lens and the PUGH/WEST lens dissipate a power of 240, 985 and 465 watts in their coils respectively.

The Gaussian spot size (d_g), the electron current (I) and the power (W_c) dissipated in the lens coil, for lens HERMES II and the ROCKETT/BRUNDIN lens were calculated at 25 KV and at 50 KV, assuming that the electron gun filament is placed at Y = 140 mm.

Figures 3.11 and 3.12 compare lens HERMES II with the ROCKETT/BRUNDIN lens at 25 KV and at 50 KV, respectively. From figure 3.11, can be seen that the ROCKETT/BRUNDIN lens is superior to lens HERMES II in all respects, provided that the minimum Gaussian spot size is more than 0.75 μm in diameter. The ROCKETT/BRUNDIN lens is limited by saturation at unfavourable places in its polepiece and is thus not able to provide Gaussian spot sizes less than 0.75 μm in diameter.

From figure 3.12 can be seen that lens HERMES II provides more electron current in a given Gaussian spot size than the ROCKETT/BRUNDIN lens, although lens HERMES II, dissipates more power in its coil than the ROCKETT/BRUNDIN lens. Lens HERMES II can provide Gaussian spot sizes down to 0.3 μm in diameter, while the ROCKETT/BRUNDIN lens is limited to spot sizes bigger than 0.9 μm, due to undesirable saturation effects in its polepiece.

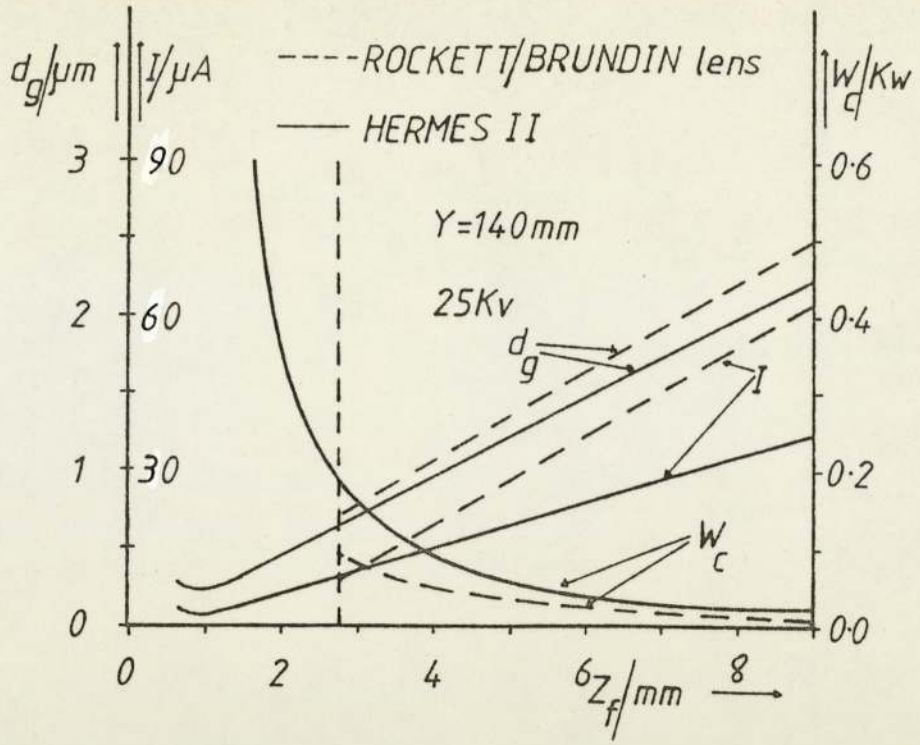

Figure 3.11 The variation of the Gaussian spot size, the electron current and the power dissipated in the lens coil, as a function of the working distance, at 25 KV, for lens HERMES II and the ROCKETT/BRUNDIN lens.

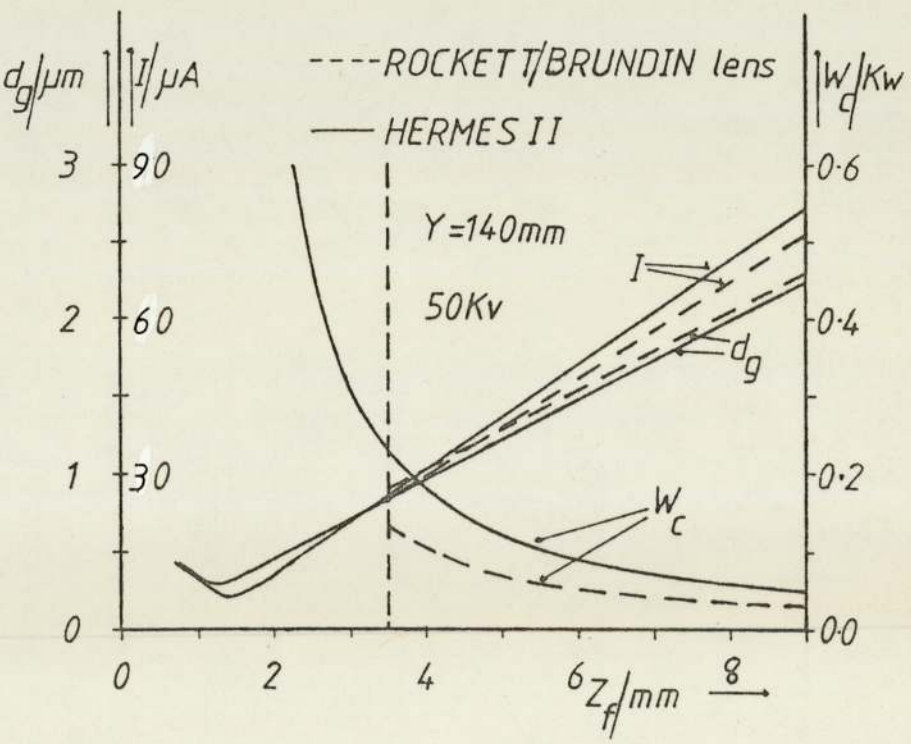

Figure 3.12 The variation of the Gaussian spot size, the electron current and the power dissipated in the lens coil, as a function of the working distance, at 50 KV, for lens HERMES II and the ROCKETT/BRUNDIN lens.

Table 3.3 Summary of the properties of lens HERMES II and the ROCKETT/BRUNDIN lens as used for micro-x-ray sources.

LENS		HERMES II			ROCKETT/BRUNDIN		
V_r/Kv	d_g/μm	I/μA	W_c/w	Z_f/mm	I/μA	W_c/w	Z_f/mm
25	0.5	2.3	285	2.20	-	-	-
	1.0	5.2	82	4.15	6.0	55	3.80
	1.5	7.8	35	6.15	11.0	30	5.55
	2.0	11.0	25	8.10	16.0	19	7.30
50	0.5	4.0	615	2.20	-	-	-
	1.0	10.7	165	4.15	9.5	110	3.85
	1.5	17.5	90	6.10	15.7	55	5.85
	2.0	24.0	60	8.05	21.8	39	7.80

The minimum Gaussian spot sizes the ROCKETT/BRUNDIN lens can achieve before saturation affects its performance is indicated in both figures by a dashed vertical line.

Table 3.3 summarises the electron current, the working distance and the power dissipated in the lens coil for a number of Gaussian spot sizes, for lens HERMES II and the ROCKETT/BRUNDIN lens. For example, at an electron accelerating voltage of 50 KV and a Gaussian spot size (d_g) of 2.0 μm in diameter, lens HERMES II provides an electron current (I) of 24.0 μA at a working distance (Z_f) of 8.05 mm. At the same electron accelerating voltage and Gaussian spot size, the ROCKETT/BRUNDIN lens provides an electron current (I) of 21.8 μA at a working distance (Z_f) of 7.80 mm. To achieve the above performance, lens HERMES II dissipates a power (W_c) of 60 watts in its coil and the ROCKETT/BRUNDIN lens dissipates a power (W_c) of 39 watts in its coil.

If a micro-x-ray source is required to provide Gaussian spot sizes larger than 1 μm in diameter, then any of the above lenses can be used, simple by placing the x-ray target at the correct working distance. If the x-ray source size is of importance then the lens must be capable of providing Gaussian spot sizes less than

1 μm in diameter. In this case lens HERMES II is the most favourable lens.

The lenses described above can provide any required electron current at the x-ray target, at the expence of Gaussian spot sizes, simply by placing the x-ray target at a large working distance.

3.4 Final refinements of lens HERMES II and lens ZEUS

From the lenses discussed in the previous chapter and the previous sub-section of this chapter, it is clear that lens ZEUS is the best choice for an objective lens as far as the electron optical properties are concerned. This lens when suitably scaled, has strong possibilities as a high resolution objective lens in the field of electron microscopy. Lens HERMES II is the best choice as the objective lens of the probe forming system of a micro-x-ray source.

Before these lenses were constructed and tested experimentally, a number of important refinements were made. From figures 2.33 and 2.34, was evident that the cross-sectional area of the magnetic circuit of both lenses close to their external diameter, needs to be increased in order to reduce the magnetic flux density in this part of the magnetic circuit of both lenses. Also the cross-sectional area of the second polepiece of lens ZEUS, needs to be increased for the same reason.

From figures 2.47 and 2.49 it was evident that the lower spherical and chromatic aberration coefficients of lens HERMES II and lens ZEUS, are achieved at lens excitations lower than 16000 and 12000 A-t respectively. The effective halfwidth of lens HERMES II in ray 2 beam orientation, at this lens excitation increases from 1.10 to 1.35 mm (i.e. by 22.7%) and the effective halfwidth of lens ZEUS in ray 2 beam orientation, increases from 1.15 to 1.45

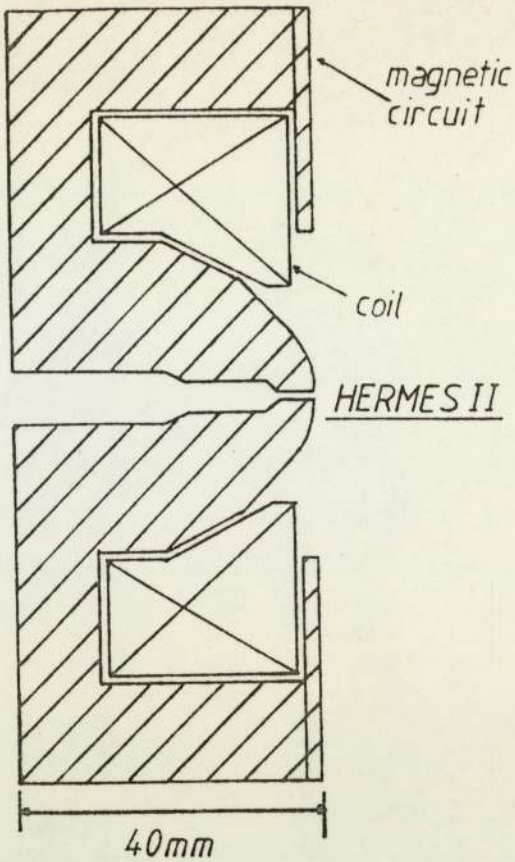

Figure 3.13 Refined cross-sectional diagram of lens HERMES II.

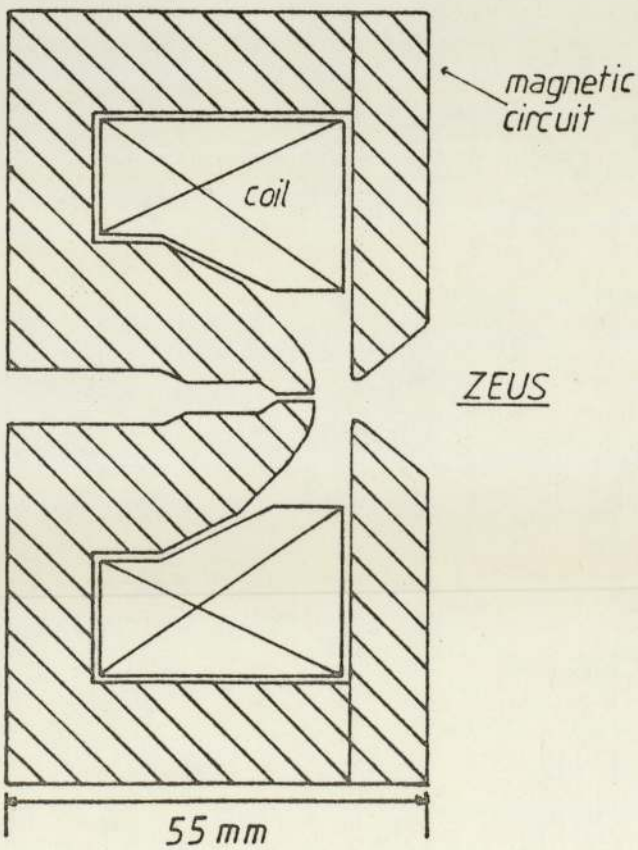

Figure 3.14 Refined cross-sectional diagram of lens ZEUS.

mm(i.e. by 26.1%), as can be seen from figures 2.30 and 2.32 respectively. At these lens excitations the polepiece tips of both lenses saturate over only a small distance of approximatly 2 - 3 mm. It is possible therefore to open up the back bores of both lenses to form conical or step down bores, without affecting the electron optical properties of either lens. Also the polepiece tips of both lenses, in the region where saturation takes place, must be smooth so as to avoid saturation irregularities.

Figures 3.13 and 3.14 show the refined cross-sectional diagrams of lens HERMES II and lens ZEUS respectively. The polepiece tips of both lenses are made spherical with a 10 mm radius. The step down bores stop at 5 mm from the polepiece tip of the lenses. The cross-sectional area of the magnetic circuit near the external diameter of the lenses is doubled in thickness and also the second polepiece of lens ZEUS is doubled in thickness and its bore made conical.

Both lenses were constructed and their electron optical properties tested experimentally. The constructional details of both lenses are given in appendix F. The apparatus used in all the experimental work and the experimental results are discussed in chapter 4.

4 Experimental work, Results and Discussion of Results

4.1 Introduction

In this chapter a number of simple experiments are discussed in the light of the preceding calculations. Each experiment deals with a particular aspect of the micro-x-ray source design.

The apparatus in each case will vary in relation to the necessary relevant requirements. In order to maintain a degree of continuity within the framework of this discussion, each experiment will be dealt with as a separate but related unit.

4.2 Electron optical properties of lenses HERMES II and ZEUS

4.2.1 Measurement of the axial magnetic flux density distribution

The axial magnetic flux density distribution of lenses HERMES II and ZEUS was measured experimentally using a Hall probe (Model 120 Gaussmeter, Bell inc.), as shown in figure 4.1. The size of the Hall probe (5 mm in diameter) being larger than the bore of the two lenses, the axial magnetic flux density distribution could only be measured outside the polepiece of the lenses.

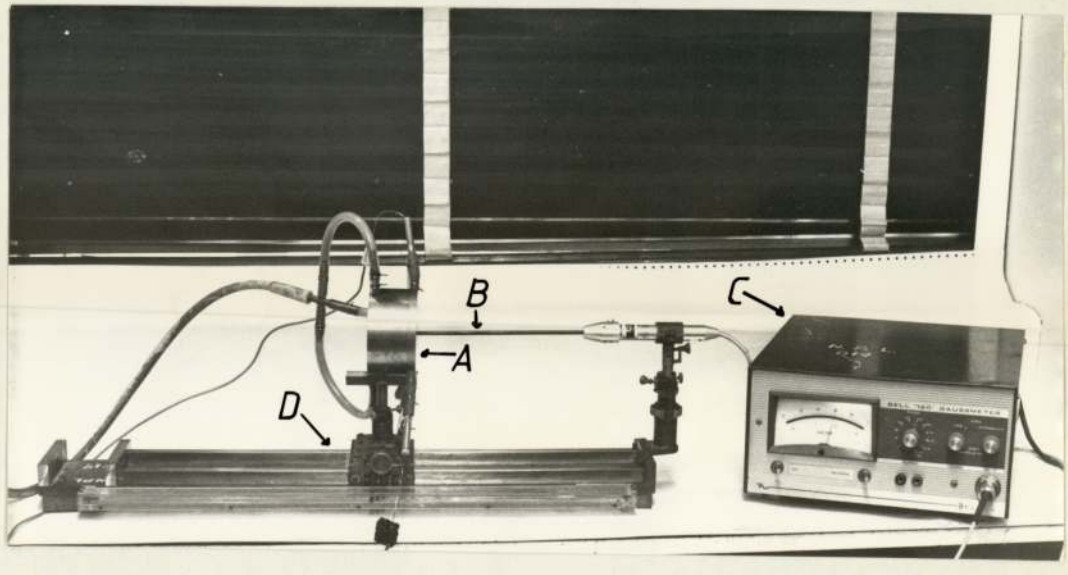

Figure 4.1 Photograph showing the experimental arrangement for measuring the axial magnetic flux density distribution of lenses. A is the lens (ZEUS), B is the Hall probe, C is the Gaussmeter and D is a vernier scale.

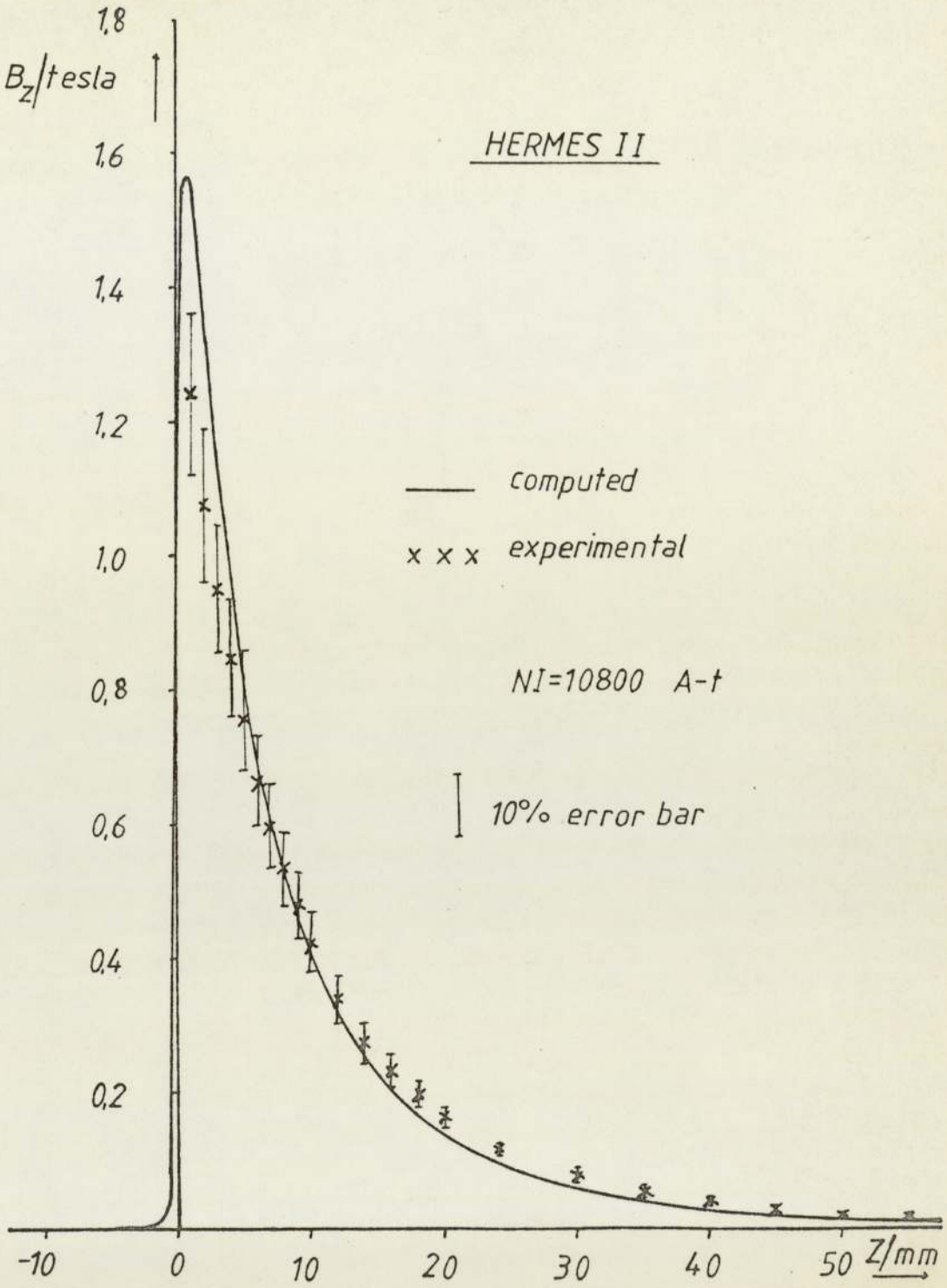

Figure 4.2 Computed and experimentally measured axial magnetic flux density distribution of lens HERMES II at a lens excitation NI = 10800 A–t.

Figures 4.2 and 4.3 show the computed and experimentally measured axial magnetic flux density distributions of lenses HERMES II and ZEUS, respectively, at a given lens excitation. The computed and measured distributions are fairly close to each other.

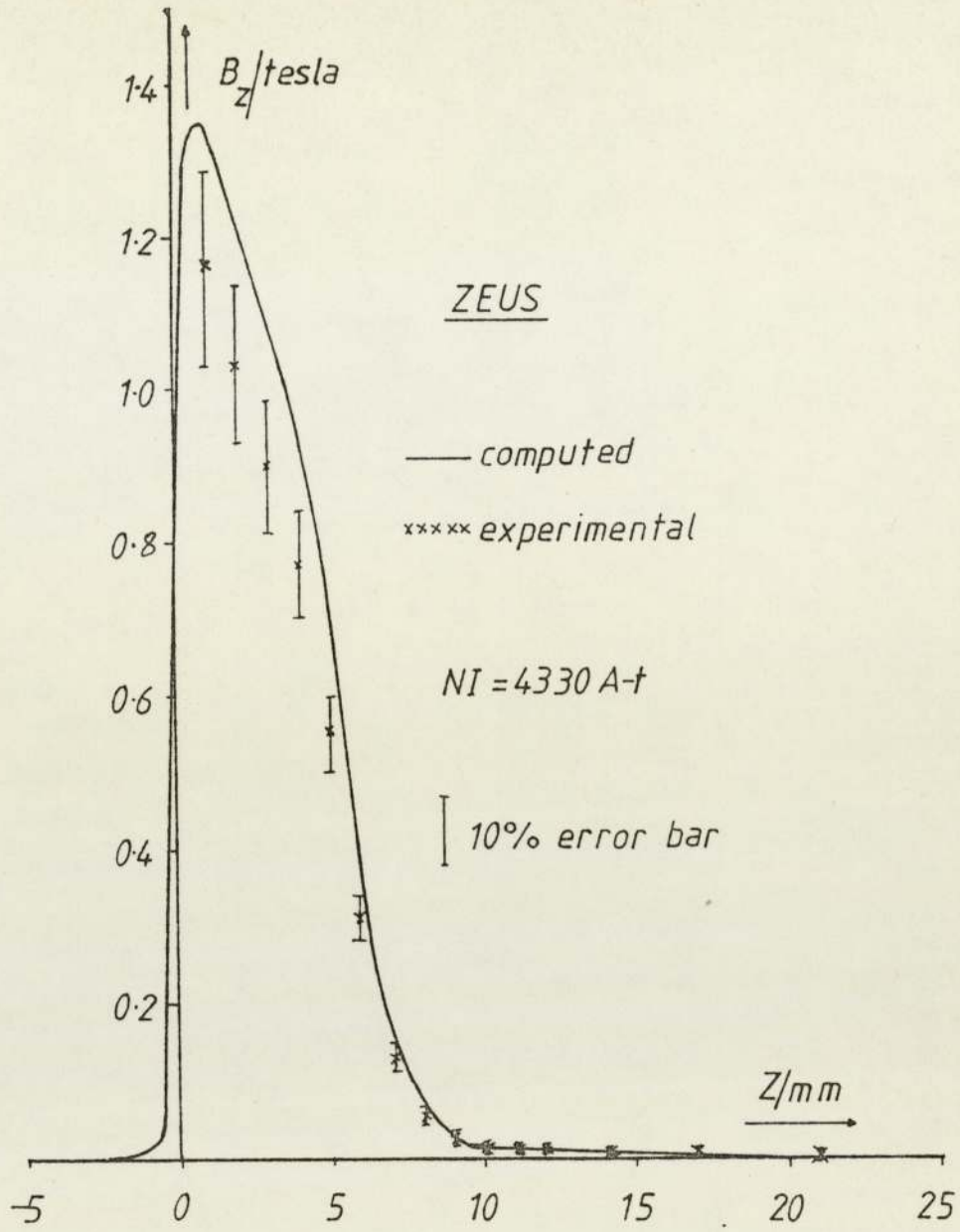

Figure 4.3 Computed and experimentally measured axial magnetic flux density distribution of lens ZEUS at a lens excitation NI = 4330 A-t.

The discrepancy between the computed and measured distributions, is atributed partly to inherent errors in the computer program M13 when used to compute the axial magnetic flux density distribution of magnetic lenses (Nasr and Mulvey, 1981) and partly to experimental errors due to the finite size of the Hall probe. These discrepancies could also be due to the magnetisation properties of the magnetic material (Swedish iron) from which the lenses are

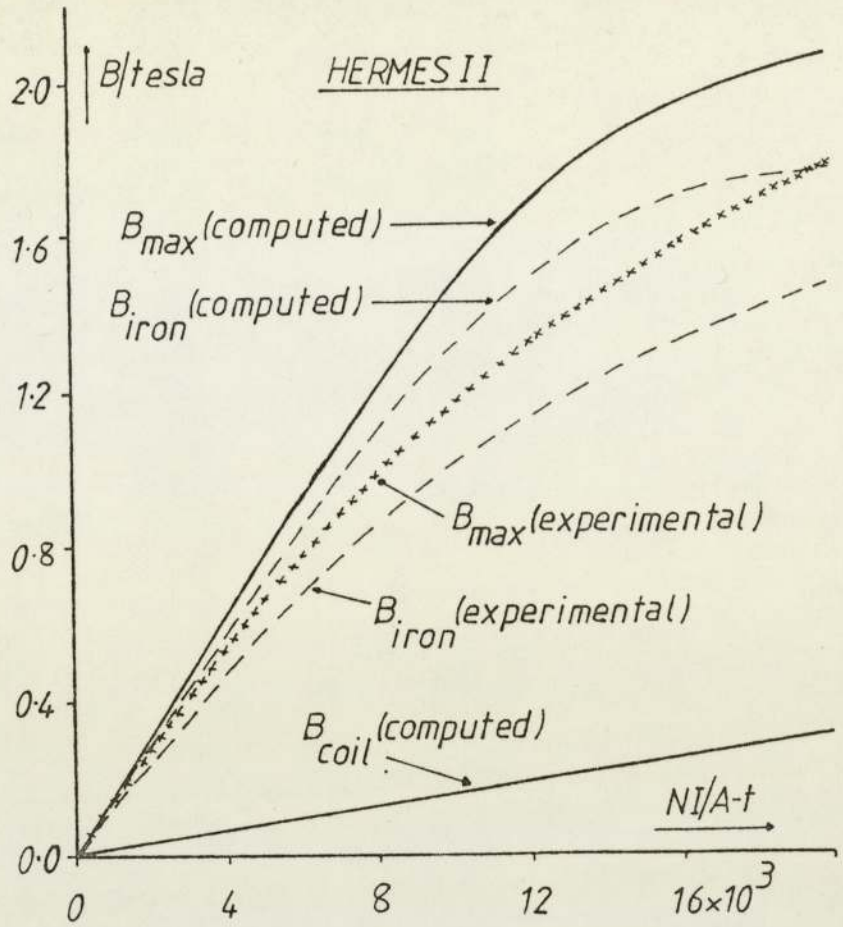

Figure 4.4 The variation of the computed and measured magnetisation of the polepiece tip of lens HERMES II, as a function of lens excitation.

constructed. The B/H curve used in the computations is a standard B/H curve of soft iron and may not be the same as that of the polepiece material.

The above discrepancies can be seen more clearly from figures 4.4 and 4.5, which show the variation of the computed and measured peak values B_{max} of the axial magnetic flux density distributions of lenses HERMES II and ZEUS, respectively, as a function of lens excitation NI. Figures 4.4 and 4.5 also show the variation of the coil B_{coil} and the iron B_{iron} contributions to the peak value B_{max}, as a function of lens excitation NI, for lenses HERMES II and ZEUS, respectively.

From figure 4.5 the computational errors are clearly seen. The

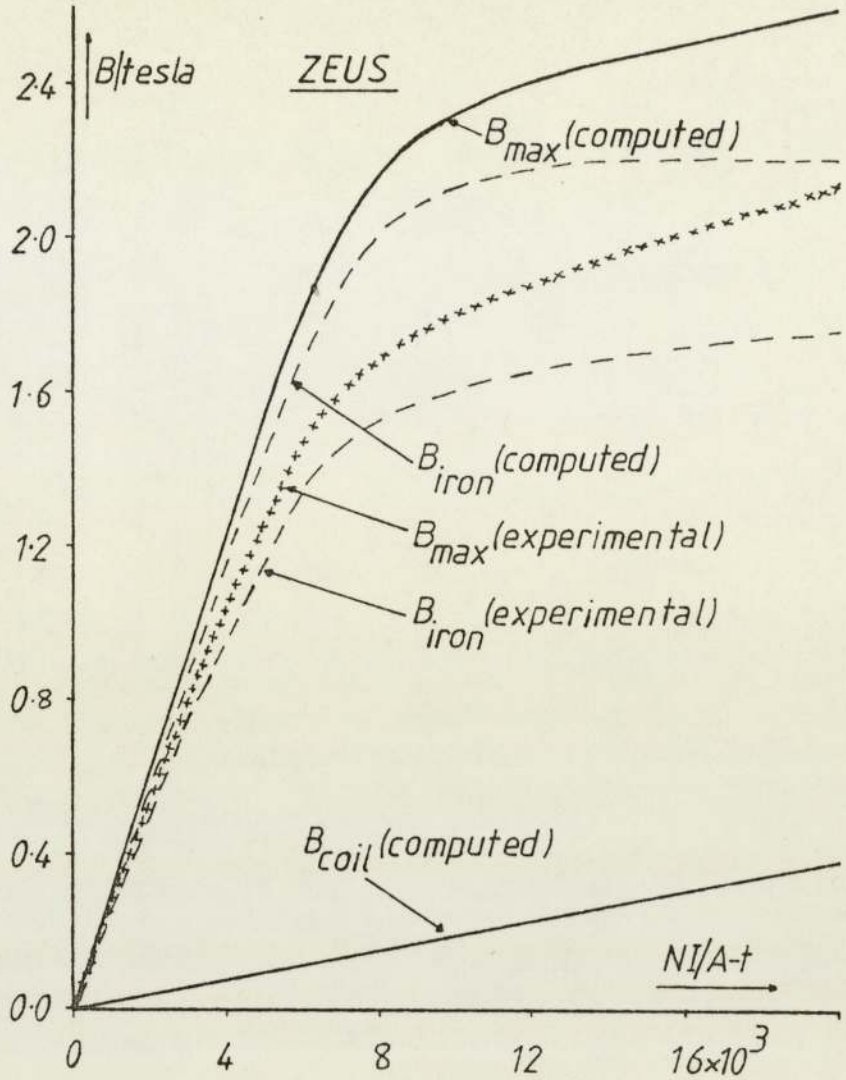

Figure 4.5 The variation of the computed and measured magnetisation of the polepiece tip of lens ZEUS, as a function of lens excitation.

values of B_{iron} calculated from the computed values of B_{max} are higher than the expected values dictated by the B/H curve used in the computations (figure 1.10) of B_{max}, while the B_{iron} values calculated from the experimentally measured B_{max} values, tend to level off at high lens excitations, close to the saturation flux density of 1.8 Tesla; typical saturation flux density of a soft iron polepiece.

From figure 4.4 the values of B_{iron} calculated from the computed B_{max} values tend to agree with the values given by the B/H curve

used in the computations of B_{max}; perhaps a better choice of mesh size was used in the computations. Large discrepancies still exist between the computed and measured B_{max} values in this figure. These could be atributed to the B/H curve of Swedish iron, which may be different from the one used in the computations. This can be identified as a source of error by the fact that the computed and measured B_{max} values of figure 4.4, tend to come closer together at high lens excitation, while those of figure 4.5 come parallel to each other at high lens excitations.

4.2.2 Measurement of the working distance and the spherical aberration coefficient of the lenses.

Any method which requires the observation of a projected image on a fluorescent screen in order to measure experimentally the spherical aberration coefficient (Castaing,1951; O'Dell, 1979), must be ruled out in the case of a probe forming system, since the specimen is almost always immersed in the axial magnetic flux density distribution. The axial magnetic flux density distribution which is present after the specimen, will distord the electron trajectories reaching the screen to form the image as shown in figure 4.6. This distorted image will not give the correct information required to measure the spherical aberration coefficient.

Because of the above reasons, the spherical aberration coefficient of the objective lens of a probe forming system can best be estimated experimentally by occulting the beam with a wire of small diameter.

The minimum disc of confusion ($d_{min} = d_s$) formed by the marginal and the paraxial rays close to the focal plane is given by :

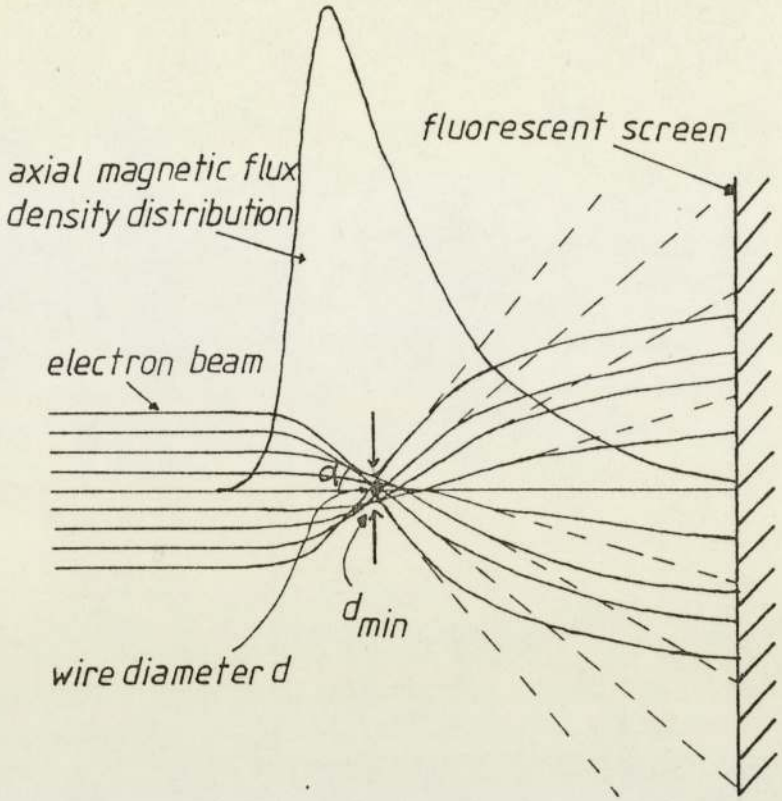

Figure 4.6 Diagram illustrating the occulting test.

$$d_{min} = C_s \alpha^3/2 \text{ - - - - - - - - - - - - - - - - - } 4.1$$

By using a thin wire of known diameter as a specimen and focusing the electron beam on this wire in such a way that the wire image just disappears from the fluorescent screen, then at this point, the diameter of the specimen wire will be equal to the diameter of the minimum disc of confusion. In order to use equation 4.1, the semi-angle α must be known. This is given by :

$$\alpha = \tan^{-1}(r_o/F_{obj}) \text{ - - - - - - - - - - - - - - - - } 4.2$$

where

r_o is the radius of the lens aperture (or the radius of the bore if no aperture is used).

The radius r_o is obtained by direct measurement. The objective focal length of the lens is not known and is difficult to measure experimentally, especially for a single polepiece lens. However the distance from the specimen wire to the polepiece of the lens can be measured directly from the z-control of the specimen stage of the apparatus. This distance is the working distance Z_f of the lens. This experimentally measured working distance can be compared with the computed working distance at the same lens excitation. If the two working distances agree with each other, then it is likely that the computed objective focal length will not be much different from the actual focal length. If this is the case, then the computed objective length can be used in equation 4.2 to give an estimate of the semi-angle α.

In the present work this procedure was found to be the most satisfactory one for a probe forming system objective lens and it was used in equation 4.2 to give an estimate of the spherical aberration coefficient. The accuracy of the estimated values of the spherical aberration coefficients obtained from the above method, will depend on the accuracy of agreement between the computed and the actual objective focal length of the objective lens, but this is a less important source of error than that of deciding when the beam is cut off by the wire.

The experiments to estimate the spherical aberration coefficient, were carried out on an electron optical bench (Intercol MKII Y70, Hilger and Watts ltd., London, England, 1966). Figure 4.7 shows the electron optical column, comprising of the electron gun (A), the lens (B), the specimen stage (C), the X-ray camera (D), an electron fluorescent screen (E) and a Geiger counter (F).

The complete vacuum system is contained in a separate cabinet.

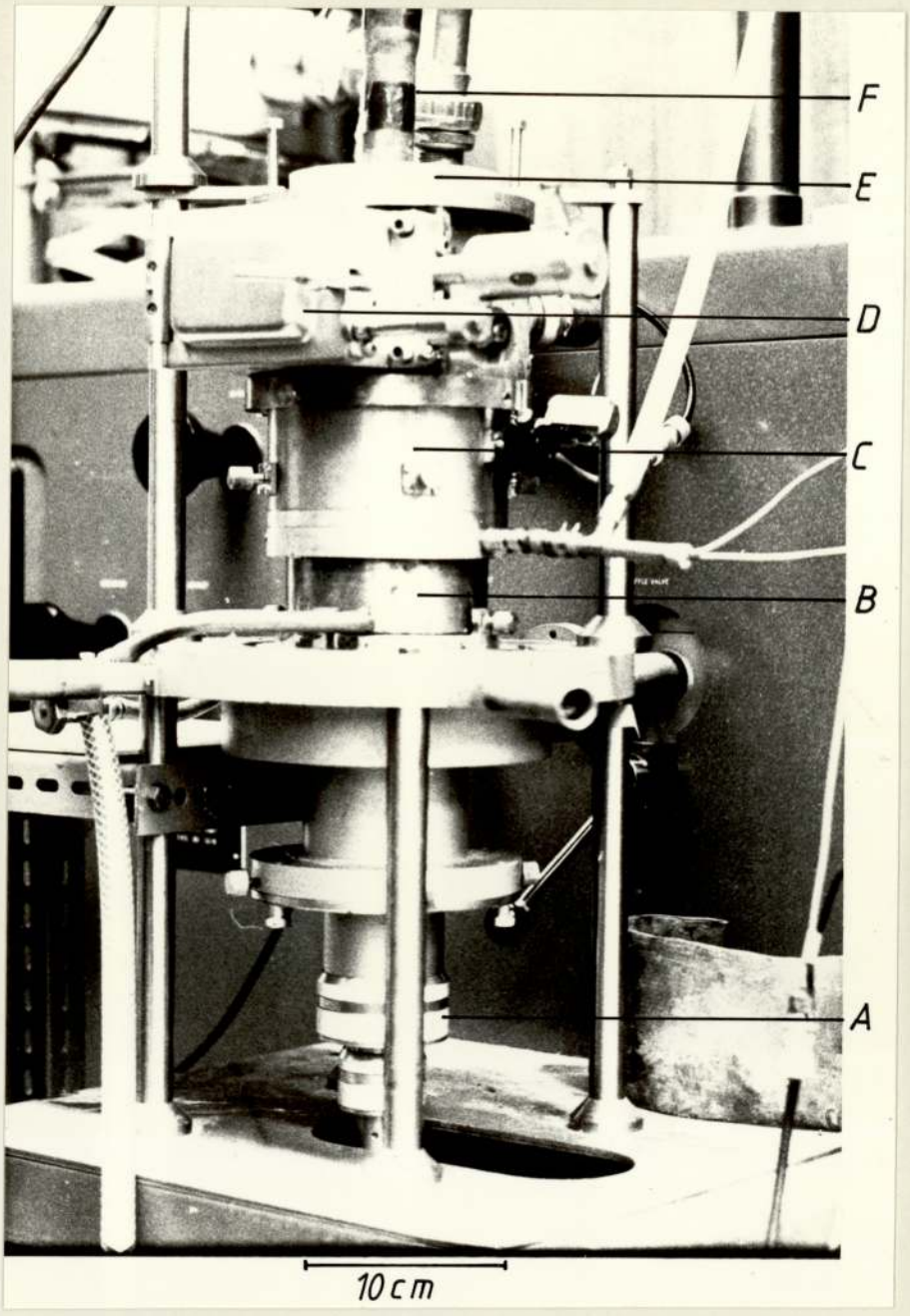

Figure 4.7 Photograph showing the electron optical column used for most of the experimental work. A is the electron gun, B is the objective lens (HERMES II), C is the x-y-z-control specimen stage, D is the x-ray camera, E is the electron fluorescent screen and F is a Geiger counter.

The system embodies a diffusion pump which is backed by a two stage rotary vacuum pump.

The original electron gun of the electron optical bench was designed to operate up to an electron accelerating voltage of 30 KV. This was modified to operate upto 50 KV. Effectively the electrical

console of the original electron gun was replaced by a model 853 type MR50HS BB Brandenburg high voltage generator.

The lens current was provided by a Franell (H60/25 constant current/constant voltage) stabilised power supply. This can supply a maximum constant current of 25 Amperes at a voltage of up to 60 volts.

The specimen stage incorporates x-y-z- movement controls. The specimen holder of this stage is electrically isolated from the rest of the instrument so that the specimen (target) current can be monitored by a type D63, Telequipment oscilloscope.

The x-ray camera (the camera of a JEOL superscope JEM-SS was modified for this purpose), which uses 35 mm role film, is mounted in the camera chamber. This chamber was specialy constructed to accommodate the camera and is also connected to the vacuum system by external vacuum connections.

The electron fluorescent screen which is situated on top of the camera chamber was made by evaporating a solution of "Willemite" and 5% Collodion on a plane glass disc, which was previously coated with a thin layer of aluminium. The screen is electrically connected to earth so as to avoid charging up of the screen. A protective lead glass disc was placed on top of the screen. This can be removed when required to measure the x-ray flux passing through the screen with the aid of a Geiger counter.

In the present experiment the camera was removed so that it was not interfering with the formation of the electron image on the fluorescent screen.

The specimen wires were mounted on the specimen holder. The lens was excited at a fixed lens excitation (NI) and by varying the electron accelerating voltage and/or the position of the specimen wire, the condition required for estimating the spherical aberration

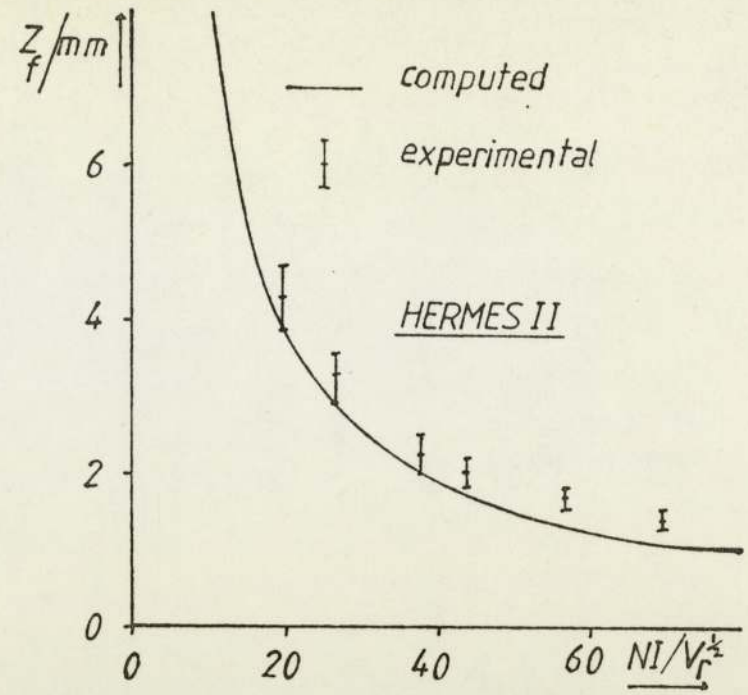

Figure 4.8 The variation of the computed and measured working distance of lens HERMES II, as a function of the lens excitation parameter. The error bars indicate an experimental error of 10%.

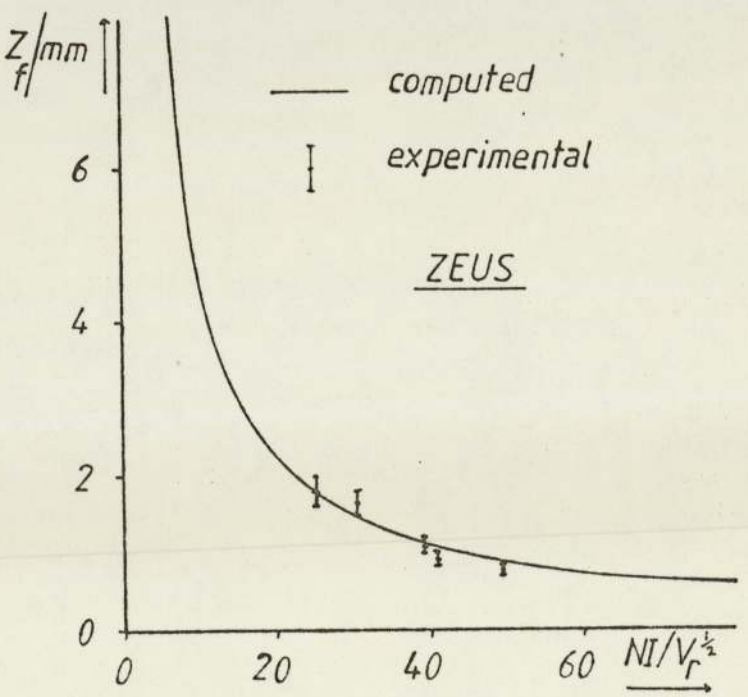

Figure 4.9 The variation of the computed and measured working distance of lens ZEUS, as a function of the lens excitation parameter. The error bars indicate an experimental error of 10%.

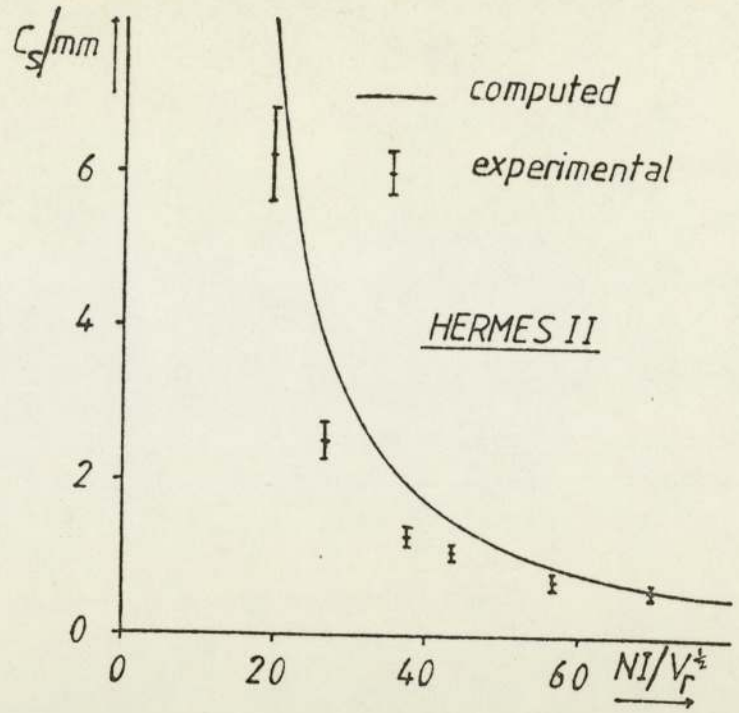

Figure 4.10 The variation of the computed and estimated spherical aberration coefficient of lens HERMES II, as a function of lens excitation parameter. The error bars indicate an experimental error of 10%

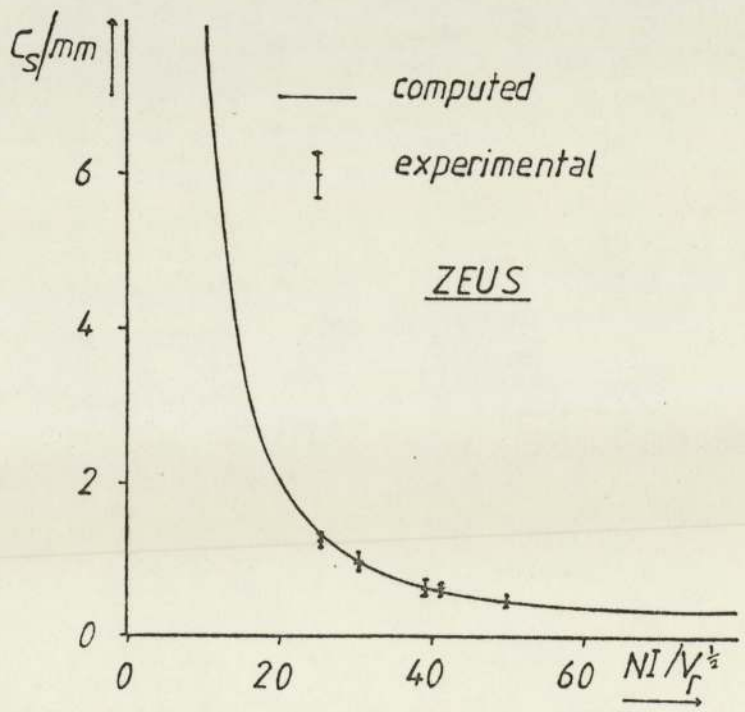

Figure 4.11 The variation of the computed and measured spherical aberration coefficient of lens ZEUS, as a function of the lens excitation parameter. The error bars indicate an experimental error of 10%.

coefficient is met.

Figures 4.8 and 4.9 show the variation of the computed and measured working distance Z_f of lenses HERMES II and ZEUS respectively, as a function of the lens excitation parameter $NI/V_r^{\frac{1}{2}}$. The computed and measured curves of lens ZEUS agree well with each other, while the measured working distance of lens HERMES II is slightly larger than the computed one. This could be an advantage since the focal plane will be further away from the polepiece tip. This will allow a greater flexibility in handling the lens apertures and the x-ray target.

Figures 4.10 and 4.11 show the variation of the computed and estimated spherical aberration coefficients C_s of lenses HERMES II and ZEUS respectively, as a function of the lens excitation parameter $NI/V_r^{\frac{1}{2}}$. The computed and estimated curves of lens ZEUS agree well with each other while the estimated spherical aberration coefficients of lens HERMES II are lower than the computed ones.

The discrepancy between the computed and experimentally obtained working distance and spherical aberration coefficients of lens HERMES II are largely associated with errors in the computer program in computing the axial magnetic flux density distribution of single polepiece lenses.

Although the computed and experimentally obtained properties of lens HERMES II are not in perfect agreement with each other, the experimentally obtained properties are more favourable for the probe forming system of a micro-x-ray source, than the computed properties.

4.3 Electron beam focusing technique

4.3.1 Introduction

The electron optical column discussed in sub-section 4.2.2, is essentially the micro-x-ray source used in the present work, with lens HERMES II as its objective lens. An x-ray transmission target is used and is placed in the correct position by the specimen holder of the specimen stage. Specimens for microradiography are placed at a small distance (around 1 mm) above the x-ray target.

A problem which arises when using a transmission x-ray target, is the difficulty of correctly focusing the electron beam onto the target. An electron image can no longer be formed on the electron fluorescent screen, since all the electrons are stopped by the x-ray target. The replacement of the electron fluorescent screen by an x-ray fluorescent screen is not totally satisfactory, since the x-ray image formed on the screen, especially at low x-ray intensities, is faint and not easily recognisable when in focus, even in complete darkness. An electron focusing technique previously used by Pugh and West (1977) was therefore planned to be used in the present equipment.

According to Pugh and West, for the focusing technique to work, it is necessary to modulate the electron beam at a frequency f and monitor the frequency of the nett current entering the x-ray target (target current) while varying the lens excitation at a frequency f. When the frequency of the target current contains a maximum second harmonic (2f) then the beam is focused on the x-ray target. Pugh and West do not give any explanation of the causes of this effect. Only two observations were reported. Firstly, before the electron beam focusing technique will work, the electron beam must be incident on the target for a short time, while altering the lens excitation so that the beam is brought in

and out of focus a few times. Secondly the magnitude of the target current reduces as the electron spot size on the x-ray target is reduced.

An attempt has been made in the present work to give an explanation to the causes of this effect. The principles of using this technique, the instrument modifications required to accommodate it in the micro-x-ray source and the results obtained by using this technique are discussed below.

4.3.2 Causes and basic principles of the focusing technique

The causes that give rise to the focusing signal may be due to a simple process or a number of processes taking place under the electron beam on the x-ray target. One may consider the following hypothesis.

It is possible for an electrically insulating layer to be formed on the x-ray target under the electron beam, possibly by impurities or by fragments of diffusion pump oil cracking under the electron beam. If this is so then a negative charge density may be built up in this insulating layer, changing its potential, which will have the effect of allowing more electrons to be reflected or emitted as secondary electrons from the target. This charge density will increase and hence be more effective when the electron spot decreases in size. This is because the total charge is the same for all spots under the same beam, but the charge density increases as the electron spot decreases.

The observations of Pugh and West discussed in the introduction of this section tend to support such a hypothesis. If this hypothesis is correct then it should be possible to focus the electron beam by observing the drop in the direct target current, as the electron beam is focused without any modulation of the electron beam.

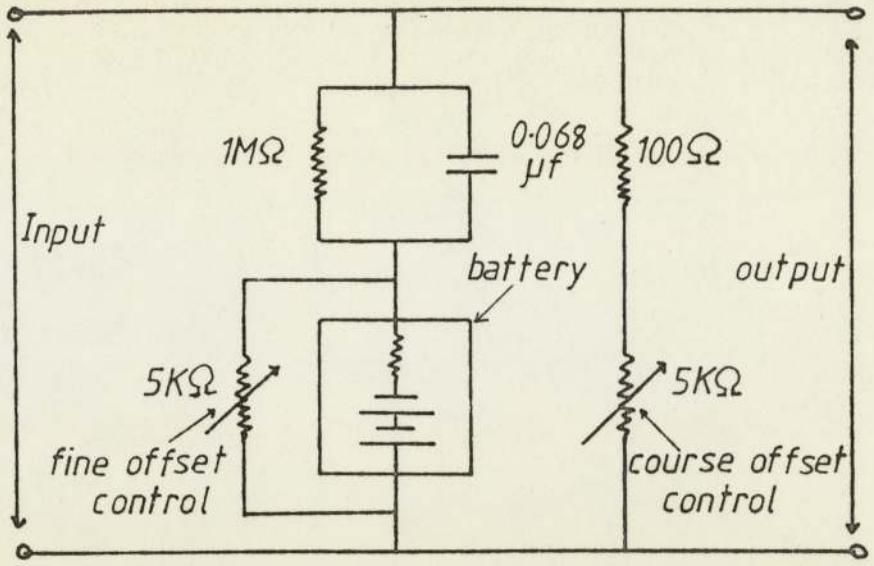

Figure 4.12 Schematic representation of the circuit used to offset the target current.

Simple experiments were caried out to try to observe this drop in the direct target current. Since this drop is very small compared with the magnitude of the target current, the later was offset by the use of the circuit shown in figure 4.12, before it was monitored by the oscilloscope. A drop in the direct current was in fact observed as the electron beam was brought to focus. Further it was observed that the drop in the target current is sharper at small working distances than it was at large ones. Unfortunately due to the large offset of the target current necessary, there was a large interference pick up from the surroundings, mainly from the E.H.T. of the electron gun power supply, thus it was not possible to record accurately this drop of target current on a chart recorder.

Figure 4.13 shows a set of freehand curves excluding these random effects, that illustrate what happens when the electron beam is slowly brought in and out of focus.

Curve A of figure 4.13, represents focusing at very small working distances (close to the polepiece tip). At these working

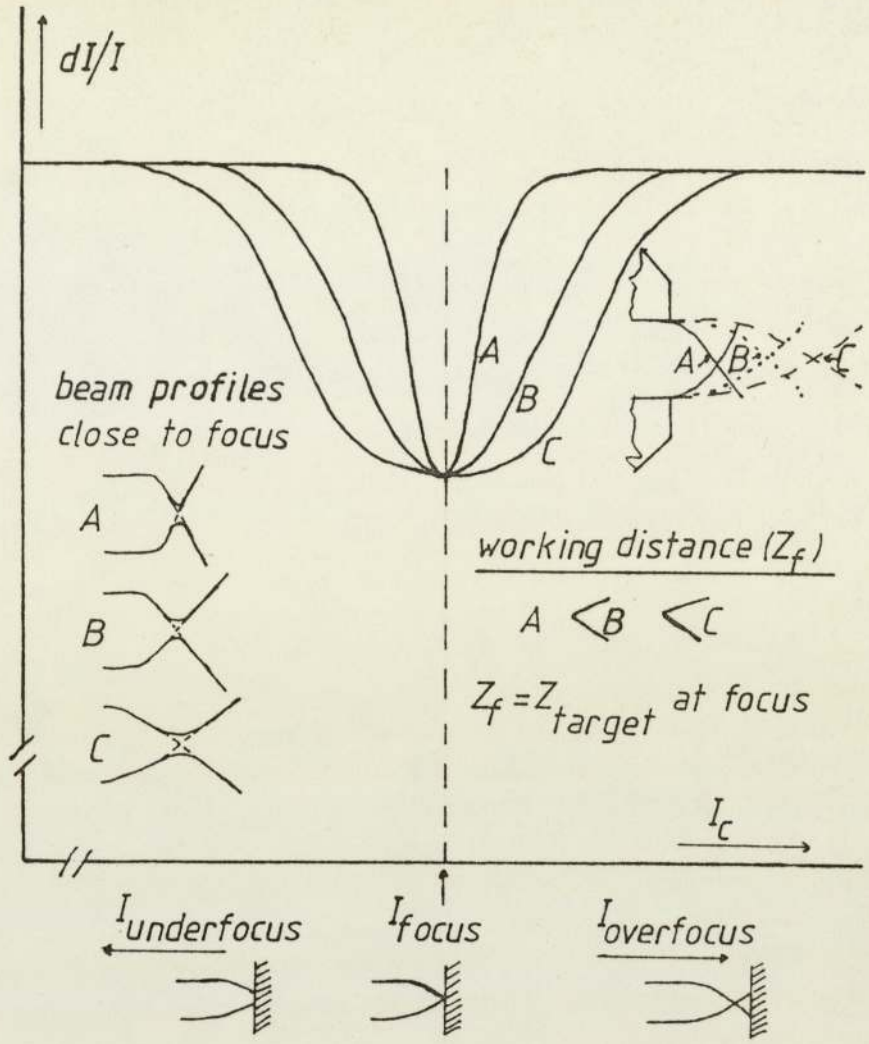

Figure 4.13 A set of freehand curves showing the principles of focusing an electron beam by observing the drop in the direct target current as the beam is brought to focus.

distances, the beam semi-angle α is large. As the target is moved towards the focal plane, a sharp drop in the target current is observed. Here the focusing of the electron beam on the x-ray target is very critical and a very small defocusing can be tolerated.

At larger working distances, such as those represented by B in figure 4.13, the beam semi-angle α is smaller. As the target moves towards the focal plane the drop in the target current is more gradual. Here the focusing of the electron beam on the x-ray target is less critical than it was at A and a larger defocusing

can be tolerated.

At very large working distances such as those represented by C in figure 4.13, the beam semi-angle α is very small and effectively the drop in the target current, as the target moves towards the focal plane, is even more gradual than it was at B. Here an even larger defocusing can be tolerated.

Using the above method to focus the beam on the x-ray target is very tedious and difficult especially when the target is placed at a large working distance. This is due to the difficulty in judging when the maximum drop in the target current occurs. It is much easier to see a change in the waveform of the target current when the modulated focusing technique is used.

The principles of operation of the modulated focusing technique may be explained better by considering the three cases shown in figure 4.14.

a) shows the case where the electron beam is overfocused. In the first half of the modulation cycle, the electron beam will be overfocused but the spot area will increase as the modulation current increases. Therefore the charge density in the insulating layer under the electron beam will be decreasing with increasing modulation current. The secondary electron emission will be decreasing with increasing modulation current and this will be seen as an increasing target current with increasing modulation current.

In the second half of the modulation cycle the beam will still be overfocused but the spot area will decrease as the modulation current decreases. Therefore the charge density in the insulating layer under the beam will be increasing with decreasing modulation current. The secondary electron emission will be increasing with decreasing modulation current and this will be seen as a decreasing target current with decreasing modulation current.

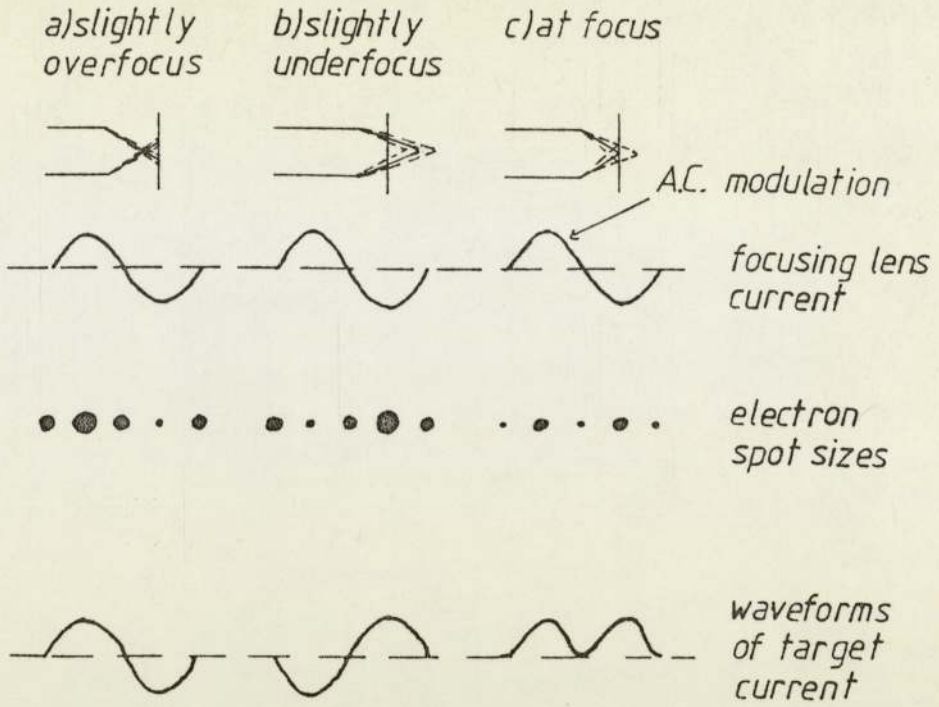

Figure 4.14 Schematic representation of the principles of the modulated focusing technique.

The modulation cycle and the target current cycle will be of the same frequency and almost in phase with each other; the target current cycle leading by a small amount the modulation cycle.

b) shows the case where the electron beam is underfocused. In the first half of the modulation cycle the beam will be underfocused but the spot area will decrease as the modulation current increases. Therefore the charge density in the insulating layer under the beam will increase with increasing modulation current and this will be seen as a decreasing target current with increasing modulation current.

In the second half of the modulation cycle the beam will still be underfocused but the spot area will increase as the modulation current decreases. Therefore the charge density in the insulating layer under the beam will decrease with decreasing modulation current and this will be seen as an increasing target current with decreasing modulation current.

The modulation cycle and the target current cycle will be of the same frequency and almost $\pi/2$ out of phase with each other; the target current cycle leading by a small amount the modulation cycle.

c) shows the case where the electron beam is on focus. In the first half of the modulation cycle the beam will be overfocused and the spot area will increase with increasing modulation current. Therefore the charge density in the insulating layer under the beam will be decreasing with increasing modulation current. The secondary electron emission will be decreasing with increasing modulation current and this will be seen as an increasing target current with increasing modulation current.

In the second half of the modulation cycle the beam will be underfocused and the spot area will increase with decreasing modulation current. Therefore the charge density in the insulating layer under the beam will be decreasing with decreasing modulation current. The secondary electron emission will be decreasing with decreasing modulation current and this will be seen as an increasing target current with decreasing modulation current.

The target current cycle will have a frequency twice that of the modulation current cycle. The target current cycle will again lead the modulation cycle by a small amount.

The slight phase lead of the target current over the modulation current cycle is due to a capacitative effect in the insulating layer. This will be discussed later in this section.

The amplitude of the modulation cycle can be increased to a level where any outside interference pick up by the oscilloscope will no longer be significantly large to interfere with the focusing technique. It is easier to focus the electron beam by observing the changes in the waveform of the target current than by observing a small drop in the magnitude of the direct target current.

4.3.3 Instrument modifications

In order to incorporate the focusing technique in the micro-x-ray source, a small modification to the instrument was necessary. This involved the provision of a small coil in the electron optical column to provide the electron beam modulation. The best place for this coil in the present instrument was thought to be inside the body of lens HERMES II, together with its focusing coil. In order to accommodate the modulation coil and the focusing coil in the body of lens HERMES II, the focusing coil was replaced by one made of slightly thinner wire (0.8 mm diameter copper wire) and again providing the same number of Ampere-turns as before (see appendix F). The modulation coil was constructed from the same wire as that of the focusing coil and consists of 70 turns of wire. This was placed behind the focusing coil as shown in figure 4.15.

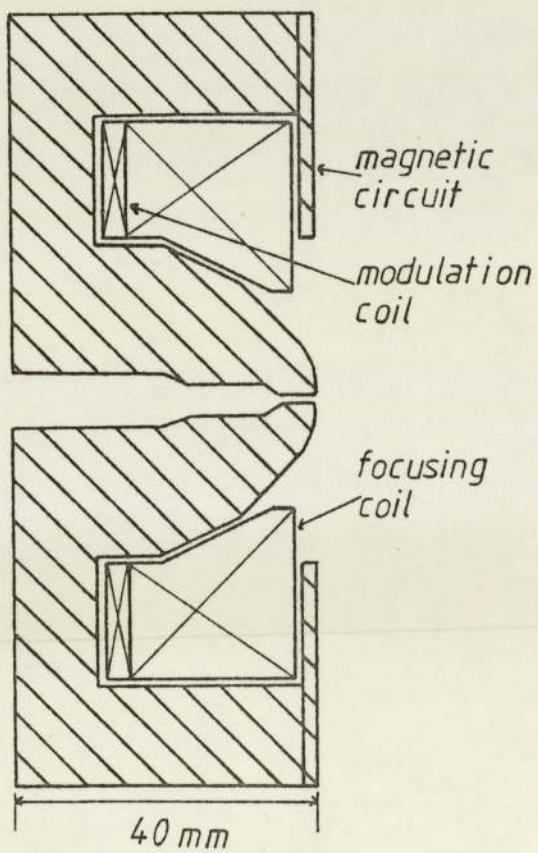

Figure 4.15 Cross-sectional diagram of lens HERMES II showing the modulation coil (70 turns) situated behind the focusing coil (450 turns).

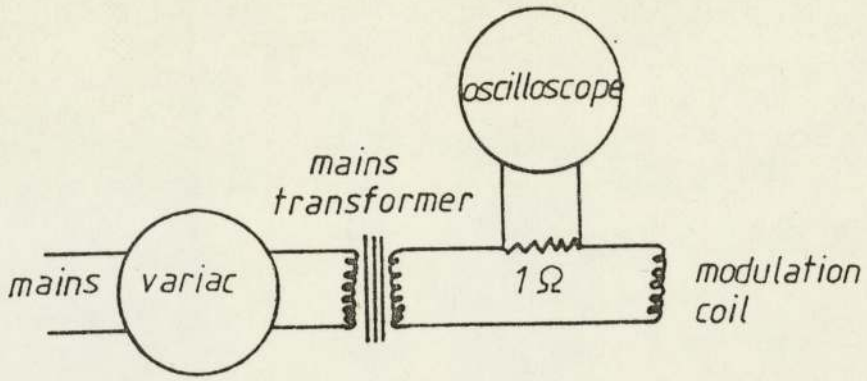

Figure 4.16 Schematic representation of the modulation coil power supply.

The power supply of the modulation coil is shown in figure 4.16. The frequency of modulation is 50 Hz mains frequency. A variac (Duratrak type V6HMTF, input 240 V, output 0 to 270 V 3 A) was used to control the amplitude of the modulation. A mains transformer (input 240 V, output 5.25 V 32 A) was used to reduce the voltage and increase the current to the modulation coil. A small resistance (1Ω) was placed in series with the coil. This was used to monitor the current supplied to the modulation coil, by observing the voltage across the resistance on the oscilloscope.

4.3.4 Results

Figure 4.17 shows a set of results obtained to demonstrate the operation and sensitivity of the modulated focusing technique, using a transmission copper target 25 μm thick, placed at a working distance of 3 mm. The results were obtained using an electron accelerating voltage V_r of 30 KV. The specimen grid (1500 mesh per inch, bar width 3 μm) was positioned 1 mm above the target. The plane of the photographic film was at 103 mm above the specimen grid. The microradiographs were further enlarged photographically by approximately four times. The total microradiograph

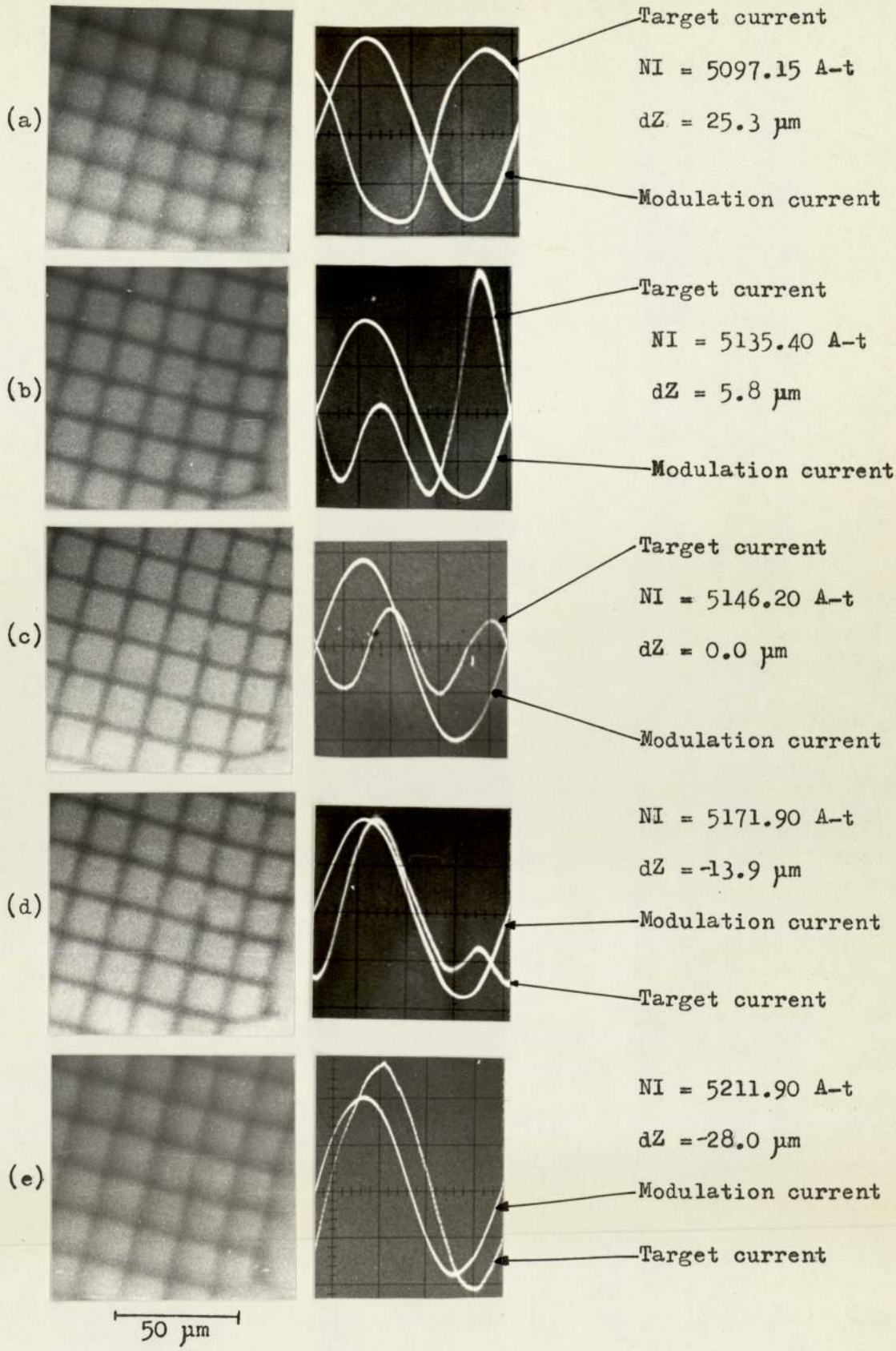

Figure 4.17 A set of microradiographs of a 1500 mesh per inch silver grid (bar width 3 μm), showing the principles and sensitivity of the modulated focusing technique. The photograph next to each microradiograph shows the waveform observed on the oscilloscope. The modulation coil excitation NI_m = 63 A-t, providing a modulation $NI_m/NI \approx 1.2\%$.

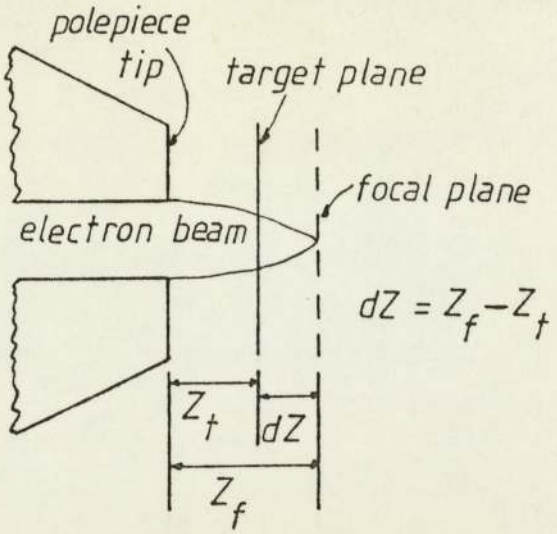

Figure 4.18 Diagram defining the distance (dZ) between the target and focal planes.

magnification is in the region of 412 times. The target current was 10.2 μA and the microradiograph exposure time was 45 seconds.

In figure 4.17, microradiograph (a) shows the resulting x-ray image of the silver grid, when the electron beam is underfocused by an amount dZ = 25.3 μm, where dZ is the difference between the working distance Z_f and the target distance Z_t (i.e. $dZ = Z_f - Z_t$, as defined by figure 4.18). The waveform observed on the oscilloscope, shown by the photograph next to this microradiograph, agrees with the explanation given previously for figure 4.14 b).

Microradiograph (b) shows the resulting x-ray image of the silver grid, when the electron beam is underfocused by an amount dZ = 5.8 μm. Here the modulation is large enough to bring the electron beam to focus during its first half of the cycle only, as shown by the photograph next to this microradiograph.

Microradiograph (c) is obtained when the electron beam is focused on the x-ray target (i.e. dZ = 0.0 μm). The observed waveform on the oscilloscope, shown by the photograph next to this microradiograph, agrees with the explanation given for figure 4.14

c).

Microradiograph (d) shows the resulting x-ray image of the silver grid when the electron beam is overfocused. Here the modulation is large enough to bring the electron beam into focus during a part of its second half of its cycle, as shown by the photograph next to this microradiograph. Here dZ = -13.9 μm.

Microradiograph (e) shows the resulting x-ray image of the silver grid when the beam is overfocused by an amount dZ =-28.0 μm. The waveform observed on the oscilloscope, shown by the photograph next to this microradiograph, agrees with the explanation given for figure 4.14 a).

Figure 4.19 is an optical micrograph of the copper target in the region of the electron spots, after it was used to obtain the results of figure 4.17. The magnification of this optical micrograph is approximately 400 times. This optical micrograph clearly indicates the formation of some kind of a layer on the target under the influence of the electron beam. This layer and the fact that the target current leads the modulation current slightly, indicate that this layer is an electrically insulating layer acting as a leaky capacitance, which can be represented by the circuit diagram shown in figure 4.20.

The phase shift of such a circuit is given by :

$$\tau = CR_i \text{ - - - - - - - - - - - - - - - - - - } 4.3$$

This phase shift is the same in all the photographs of figure 4.17 and has a value of approximately 2.5 milliseconds, which suggests that the product CR_i is constant throughout the focusing of the electron beam.

If the insulating layer on the x-ray target can be regarded as

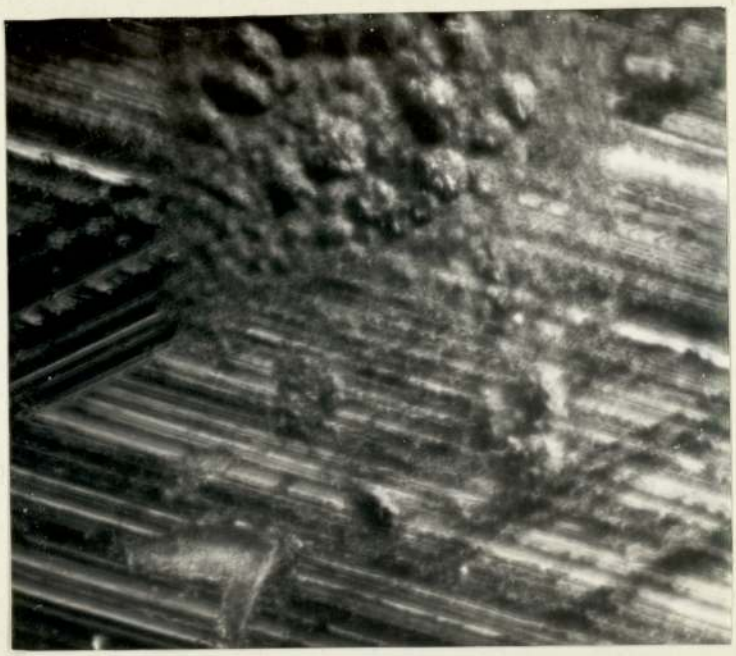

Figure 4.19 Optical micrograph of the x-ray target showing a layer being built up after the target was exposed to the electron beam. 50 μm

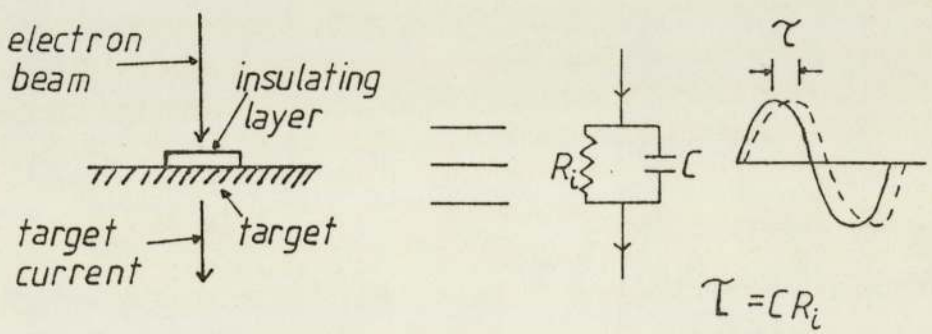

Figure 4.20 Diagram showing an equivalent circuit for the insulating layer formed on the x-ray target.

a cylindrical leaky capacitance those cross-sectional area A is the same as the electron spot area formed on the x-ray target, then its capacitance (C) is given by :

$$C = \varepsilon \xi_0 A / 4\pi \ell_i \quad \text{- 4.4}$$

where

ℓ_i is the height of the cylinder

ε is the permitivity of the insulating layer

ε_o is the permitivity of free space

A is the cross-sectional area of the cylinder

The corresponding resistance (R) of such a cylindrical insulating layer is given by :

$$R_i = \rho_i \ell / A \quad \text{-- -- -- -- -- -- -- -- -- -- -- -- -- -- -- -- -- -- -- --} \quad 4.5$$

where

ρ_i is the resistivity of the insulating layer

By combining equations 4.3, 4.4 and 4.5, the phase shift τ is given by :

$$\tau = CR_i = \varepsilon \varepsilon_o \rho_i / 4\pi \quad \text{-- -- -- -- -- -- -- -- -- -- -- -- -- -- --} \quad 4.6$$

which is a quantity depending only on the electric properties of the insulating layer.

For a phase shift (τ) of approximately 2.5 milliseconds, a permitivity in the range of 2 - 6, and a resistivity of approximately 10^9 ohm metres is required. These values are similar to those of hydrocarbons. This suggests that the insulating layer formed on the x-ray target is probably made up of diffusion oil being cracked under the electron beam.

The results obtained from the above investigation of the modulated focusing technique, support strongly the hypothesis put forward at the begining of sub-section 4.3.2. This focusing technique was used throughout the preliminary experiments discussed below.

4.4 Maximum power sustained by a copper target

As discussed in chapter 1, there is a range of electron spot sizes for which water cooling may not be required on a transmission x-ray target, since most of the heat generated by the electron beam striking the target may be conducted away by the x-ray target holder.

To determine this range of electron spot sizes, simple experiments were carried out using the apparatus shown in figure 4.7. In these experiments the x-ray target was made of a thin copper foil, which was bombarded by the electron beam. By increasing steadily the beam current and keeping the electron accelerating voltage constant, it is possible to burn holes of given dimensions in the x-ray target. By monitoring the current conducted away by the target, the power density required to burn a hole of a given diameter in the x-ray target, can be obtained.

If the power density required to burn a hole in the transmission x-ray target is higher than that required to damage a semi-infinite x-ray target (see figure 1.5), then water cooling of the target will not help. If on the other hand the power density required to burn a hole in the transmission target is less than that required to damage a semi-infinite target, then water cooling is helpful in increasing the power density in a transmission x-ray target.

Table 4.1 shows the results obtained experimentally by burning holes in a transmission copper foil x-ray target, 25 μm thick and of radius 1.5 mm, at an electron accelerating voltage V_r of 30 KV, using the power retention factor p for copper equal to 0.63, as used by Vine and Einstein (1963).

Figure 4.21 shows the experimental results (crosses) together with the theoretical results previously shown (figure 1.5) for a semi-infinite copper target (solid line), at an electron

Table 4.1 Experimental results obtained by burning holes in a copper transmission target, 25 μm thick of radius 1.5 mm, at an electron accelerating voltage V_r of 30 KV.

d_g/μm	I_t/μA	w/watts	(w/p)/watts	spot area/cm^{-2}	W/watts cm^{-2}
6.5	86	2.58	4.095	33.18×10^{-8}	1.23×10^{7}
5.0	114	3.42	5.429	19.63×10^{-8}	2.77×10^{7}
3.5	126	3.78	6.000	9.62×10^{-8}	6.24×10^{7}
2.5	140	4.20	6.667	4.91×10^{-8}	1.36×10^{8}
1.5	104	3.12	4.952	1.77×10^{-8}	2.80×10^{8}

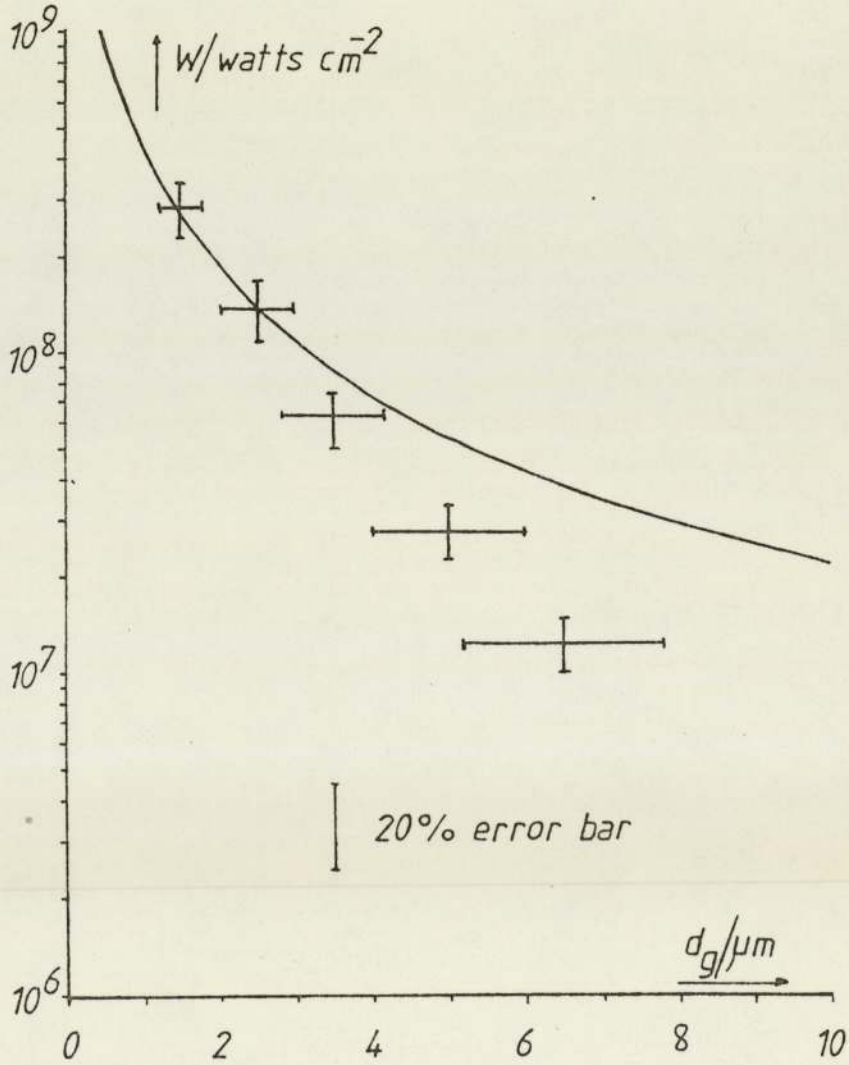

Figure 4.21 Comparison of theoretical and experimental maximum power density required to burn a copper target at an electron accelerating voltage V_r of 30 KV.

accelerating voltage V_r of 30 KV. At small electron spot sizes the experimental and theoretical results agree well with each other. As the spot size on the x-ray target becomes bigger than about one eighth of the target thickness ($d_g > \ell/8$), the maximum power density required to burn the 25 μm copper foil is appreciably less than that predicted theoretically for a semi-infinite copper target.

Hence if the electron spot size diameter on a thin copper target is less than one eighth of the foil thickness, the target may be regarded as a semi-infinite copper target, for which water cooling is not required.

For spot size diameters bigger than this, the target cannot be regarded as a semi-infinite target. The target will melt before the limit of power density set by the melting point of a semi-infinite copper target is reached. For such cases the target may be made to appear semi-infinite to the electron beam, by cooling or rotating the x-ray target.

Figure 4.22 shows the performance of the micro-x-ray source of the present work in comparison with the performance of existing x-ray sources (Ely, 1980). Line B shows the theoretical loading of rotating anode tubes, assuming that the anode makes 15000 revolutions per minute. Line A shows the theoretical limit of a stationary target, set by the melting point of copper. For small spot sizes (less than around 20 μm in diameter) this line splits into a number of lines which depend on the range of electron penetration in the x-ray target. The spliting of this line is not shown in figure 4.22, but it is shown in detail by figure 1.5.

From figure 4.22 can be seen that for electron spot sizes less than around 3 μm in diameter, the power loading that can be achieved with a stationary target is much higher than the limiting line B of rotating anode tubes; indicading the fact that the target

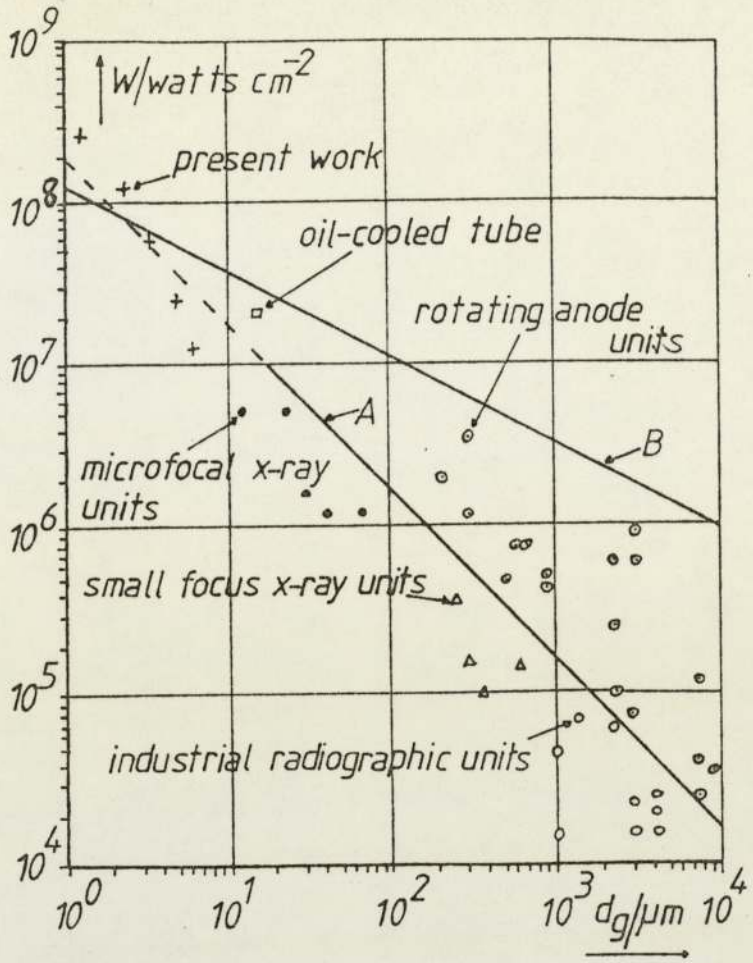

Figure 4.22 Power loading on x-ray focal spots. A : Theoretical loading of a stationary copper target (melting point). B : Theoretical loading of rotating anode tubes (15000 r.p.m.).

speeds required to improve the target loading of small spot sizes, by rotating the x-ray target, are very much higher than 15000 revolutions per minute and thus are not viable.

Figure 4.23 shows two scanning electron micrographs of a typical hole burned in a copper target, 25 μm thick, by a 30 KV electron beam of 2.8×10^7 watts cm^{-2}.

The two electron micrographs show the region around the hole at different magnifigations. The first one shows the hole and the surrounding area of the target. The second one shows in more detail the hole itself, which has the appearance of the crater of a volcano.

Figure 4.23 Scanning electron micrographs showing, at different magnifications, a hole burned in a copper foil x-ray target, 25 μm thick, by a 30 KV electron beam of 2.8×10^{7} watts cm^{-2}.

4.5 X-ray resolution and Microradiography

4.5.1 X-ray resolution

In order to estimate qualitatively the x-ray resolution that could be achieved with the experimental micro-x-ray source, the apparatus shown in figure 4.7 was used to obtain sets of microradiographs of a specimen grid with known bar width ("1500 mesh per inch" silver grid, bar width 3 μm), at different electron accelerating voltages.

A typical set of microradiographs is shown in figure 4.24. The experimental conditions for each microradiograph are shown in table 4.2. For this set of microradiographs, a transmission copper x-ray target 25 μm thick was used, positioned by the specimen stage 4 mm above the lens polepiece (Z_f = 4 mm). The silver "1500 mesh" grid was held by an "Oyster" type T.E.M. copper grid in place, 1 mm above the X-ray target. The electron source was located 75 mm from the lens polepiece, thus providing Gaussian electron spot sizes on the x-ray target of about 1 μm in diameter.

Table 4.2 Experimental conditions for the set of microradiographs shown in figure 4.24.

Microradiograph	V_r/KV	I_t/μA	Exposure/sec	I_c/Amps
A	15	4.2	120	6.500
B	20	5.2	60	7.100
C	25	7.0	45	7.950
D	30	8.4	30	8.690
E	35	9.3	20	9.420
F	40	10.8	15	10.110
G	45	12.5	15	10.805

As can be seen from figure 4.24, the x-ray resolution improves, as expected, with decreasing electron accelerating voltage. At 15 KV the x-ray resolution can be estimated from the appearance of the broken mesh bar on the right hand side of the microradiograph to be

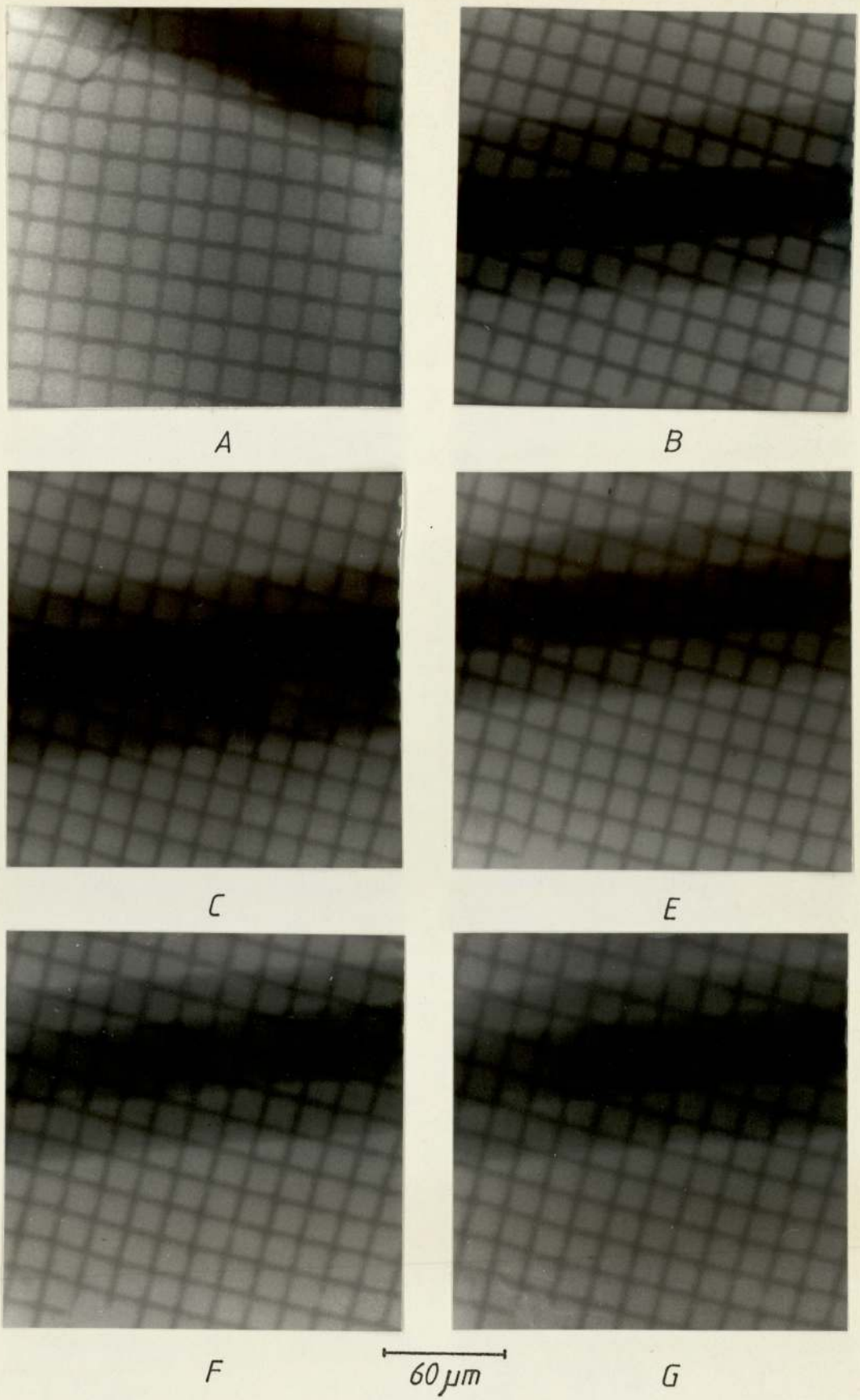

Figure 4.24 Microradiographs of a "1500 mesh" silver grid on an "oyster" type T.E.M. copper grid showing the improvement of x-ray resolution with decreasing electron accelerating voltage V_r.
A 15 KV, B 20 KV, C 25 KV, E 35 KV, F 40 KV and G 45 KV.

in the region of 0.5 - 1.0 μm. At 45 KV the x-ray resolution was likewise estimated to be in the region of 3.0 - 4.0 μm.

The variation of the estimated x-ray resolution from the above microradiographs seems to be better than the effective x-ray source sizes suggested in chapter 1 and shown graphically in figure 1.4. This is mainly due to the fact that the calculations of chapter 1 are based on a solid x-ray target from which the useful x-rays are collected from the same side of the target as the striking electron beam. For the transmission x-ray target used in the present work, the effective x-ray source sizes "seen" by the photographic film are smaller than those from a solid target, because of the better relative positioning of the photographic film in relation to the x-ray target.

The x-ray resolution of the above microradiographs can be improved by using a thinner x-ray target with a higher atomic number than the copper target used for the above microradiographs. The microradiograph for 30 KV (not shown in figure 4.24) is shown in figure 4.25 together with a microradiograph of the same grid, obtained by using a gold target 10 μm thick at the same electron accelerating voltage (30 KV). The target current I_t, for this microradiograph, was 8.6 μA and the exposure time was 25 seconds. The lens focusing current I_c was 8.505 Amperes.

From figure 4.25 the improvement in x-ray resolution can clearly be seen by the broken mesh bars present in both microradiographs.

The x-ray resolution can further be improved by increasing the distance between the electron source and the lens polepiece tip, in order to produce smaller Gaussian spots on the x-ray target and effectivelly smaller x-ray source sizes.

An intermediate lens placed between the electron source and the

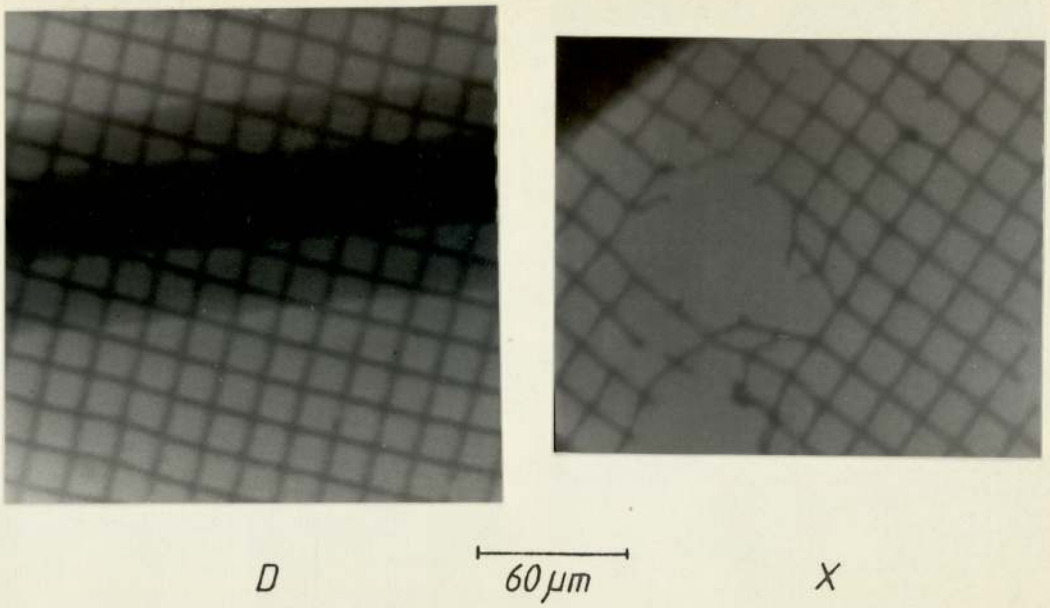

Figure 4.25 Microradiographs of a "1500 mesh" silver grid (bar width 3 μm), showing the improvement of x-ray resolution from a gold target over that from a copper target. D was obtained from a copper target, 25 μm thick, and X was obtained from a gold target, 10 μm thick. The electron accelerating voltage V_r, for both microradiographs, was 30 KV.

objective lens of the micro-x-ray source, can also help to improve the x-ray resolution. This intermediate lens can be used to vary the demagnification and hence the electron spot size on the x-ray target, while the objective lens is operated at its optimum lens excitation.

4.5.2 Microradiography

For some fields of application such as Medicine or Biology, it is sometimes required to take microradiographs of specimens at atmospheric pressure. For this purpose the apparatus of figure 4.7, was slightly modified to permit microradiography at atmospheric pressure.

The specimen stage of the apparatus was replaced by a lead extension tube of the same height as the specimen stage. The x-ray target, which is also required to seal the vacuum, was placed in

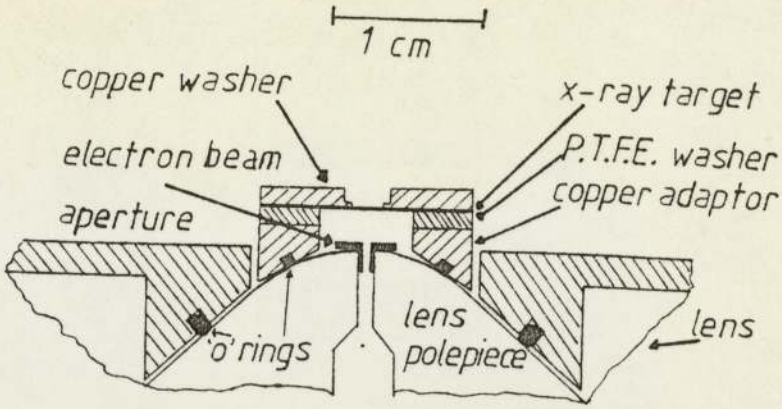

Figure 4.26 Schematic representation of the adaptor which allows the x-ray target to seal the vacuum, in order to obtain microradiographs at atmospheric pressure.

the correct position by the use of a small adaptor shown in figure 4.26. The thin foil target was soldered onto a copper washer, which itself was electrically isolated from the rest of the adaptor by a P.T.F.E. washer, to allow the target current to be monitored.

By placing a specimen above this target, microradiographs could be obtained at atmospheric pressure. Figure 4.27 shows two microradiographs of a greenfly (Aphid), obtained at atmospheric pressure. For these microradiographs, the x-ray target was placed 2.5 mm from the lens polepiece tip (Z_f = 2.5 mm). The lens required a current of 11.890 Amperes to focus the electron beam on the x-ray target. The electron accelerating voltage (V_r) was 20 KV and the target current (I_t) was 6.5 μA. The specimen greenfly, which was anaesthetised by chloroform, was placed 5mm above the x-ray target, thus providing a direct magnification of 25 times at the plane of the photographic film which was placed 125 mm above the x-ray target. The exposure time for these microradiographs was 90 seconds. The microradiographs were further enlarged photographically by approximately 2 times. The overall magnification was therefore in the region of 50 times.

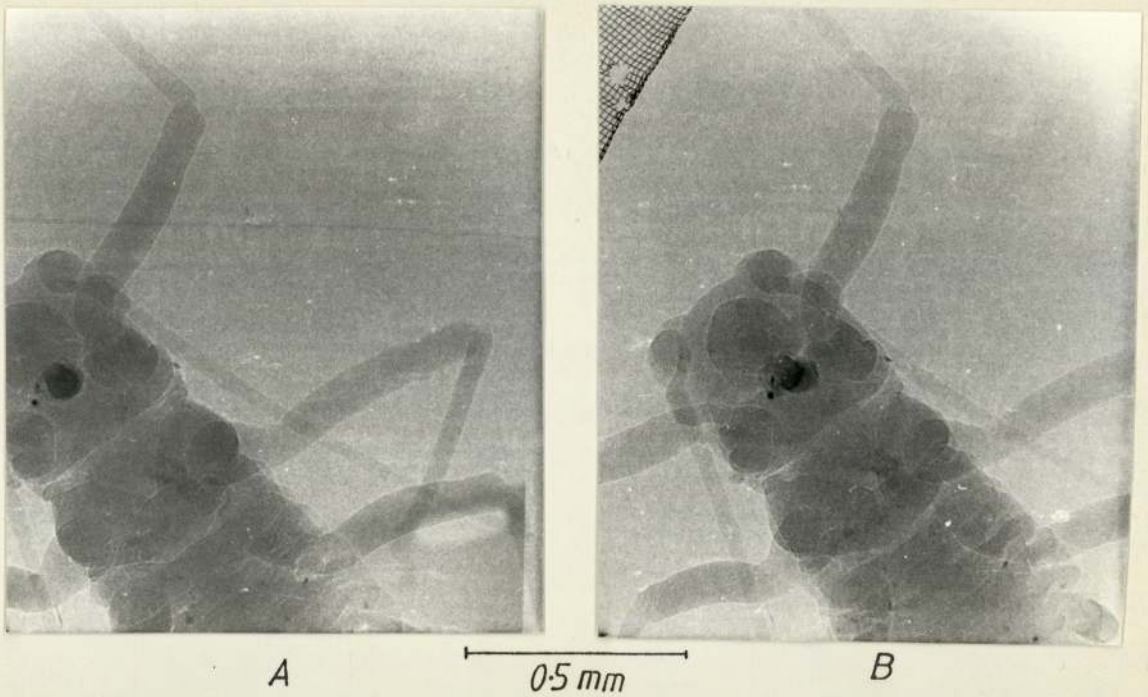

Figure 4.27 Microradiographs of a greenfly (Aphid) at atmospheric pressure. Copper target at an electron accelerating voltage of 20 KV; target current 6.5 μA. Overall magnification 50x.

The white contour around the periphery of the greenfly is due to Fresnel diffraction (see chapter 1, page 4). The fringe width d_f is given by $d_f = (b\lambda)^{\frac{1}{2}}$, where b is the distance between the specimen and the x-ray target and λ is the x-ray wavelength. At 20 KV and b = 5 mm, d_f is in the region of 2 μm, which is in agreement with the observed diffraction fringe width. Fresnel diffraction sets an ultimate limit on the x-ray resolution of the microradiographs. There is thus an optimum spacing of specimen and x-ray target in high resolution work.

The contrast of the microradiographs of a living specimen is poor. The aphid contains a large amount of water which makes it of more or less a uniform density. By freeze-drying the specimen so as to avoid structural changes, a substantial improvement in contrast can be achieved. This clearly cannot be applied to the examination of living specimens, but nevertheless useful information can be obtained.

The black dot present in the head of the aphid is believed to be a lump of magnetite which the aphid uses to orientate itself in the same way as Homing pigeons. In microradiograph A, which was taken early during the experiment, the magnetite seems to be stable in one position. Microradiograph B was taken almost at the end of the experiment and the magnetite seems to be moving from one position to another. It seems that the aphid was overcoming the influence of the anaesthetic and was trying to orientate itself, but since it was in the magnetic field of a single polepiece lens, it seems that the aphid might have been confused. This is perhaps why there doesn't seem to be any external movement of the limbs or the body of the aphid. When the magnetic field was switched off, the aphid walked away!

Figure 4.28 shows a microradiograph of a rock (Schist) sample, containing Quartz and Mica. This microradiograph was taken under the same experimental conditions as the microradiographs of the aphid. The thickness of the rock sample was 255 μm and required an exposure time of 3 minutes. The lightly shaded areas of the rock sample indicate the presence of Quartz since these are more transparent to x-rays than is Mica, which constitutes the dark areas of the sample. Some flakes of Mica of 2 - 3 μm thickness are present in the Quartz, as can be seen at the top of the microradiograph.

Another important feature of the micro-x-ray source is the possibility of obtaining structural information about a crystalline specimen by observing the Kossel diffraction patterns. Diffraction of the divergent x-ray beam takes place at crystal planes which happen to be suitable orientated, thus producing depletion or enhancement conics in the image. These diffraction patterns are more easily observed by generating the divergent x-ray beam in the

Figure 4.28 Microradiograph of a rock (Schist) sample, obtained by copper radiation at an electron accelerating voltage of 20 KV and a target current of 6.5 μA. Overall magnification 50x.

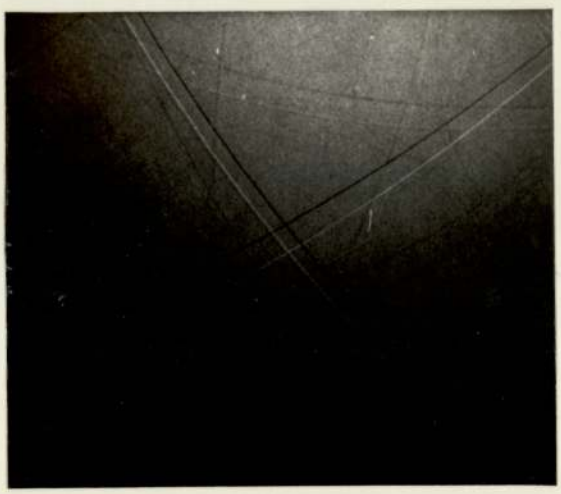

Figure 4.29 An example of Kossel diffraction patterns obtained from a copper foil 25 μm thick, at an electron accelerating voltage of 20 KV and a specimen current of 6.7 μA. White lines represent enhanced conics and the black lines represent depletion conics.

specimen itself (i.e. the x-ray target is replaced by the specimen). The perfection of the conics is strongly dependent on the perfection of the crystal lattice.

Figure 4.29 shows an example of Kossel diffraction patterns, obtained at atmospheric pressure from a copper target 25 μm thick, which at the same time formed the vacuum. The electron accelerating voltage was 20 KV and the specimen current was 6.7 μA. A Kodak electron image plate, type 4463, was placed at 18.5 mm above the specimen and exposed for 5 seconds. The diffraction patterns were enlarged photographically by approximately 4 times. The white lines present in figure 4.28, represent enhanced conics and the black lines represent depletion conics.

4.6 Micro-x-ray fluorescence analysis

Perhaps the most important application of a micro-x-ray source is in the field of x-ray fluorescence analysis. In the present investigation trace analysis of minute samples, such as fragments of glass, was of interest.

To analyse small fragments efficiently, the x-ray beam should be collimated to dimensions comparable with those of the specimen to be analysed. To obtain a general understanding of x-ray fluorescence analysis and to find out the best position for the x-ray detector and specimen in relation to the primary x-ray beam, some x-ray fluorescence analysis was carried out at atmospheric pressure.

The apparatus for microradiography described in the previous sub-section was used with minor modifications. The primary x-ray beam was collimated by the use of tantalum apertures (as used for the objective lens aperture of a scanning electron microscope). This is shown schematically in figure 4.30.

Because of the shape and thickness of the tantalum apertures, only one aperture is required to collimate the x-ray beam down to the required size and at the same time have a well-deffined x-ray beam size at the specimen, as shown by the microradiograph of the

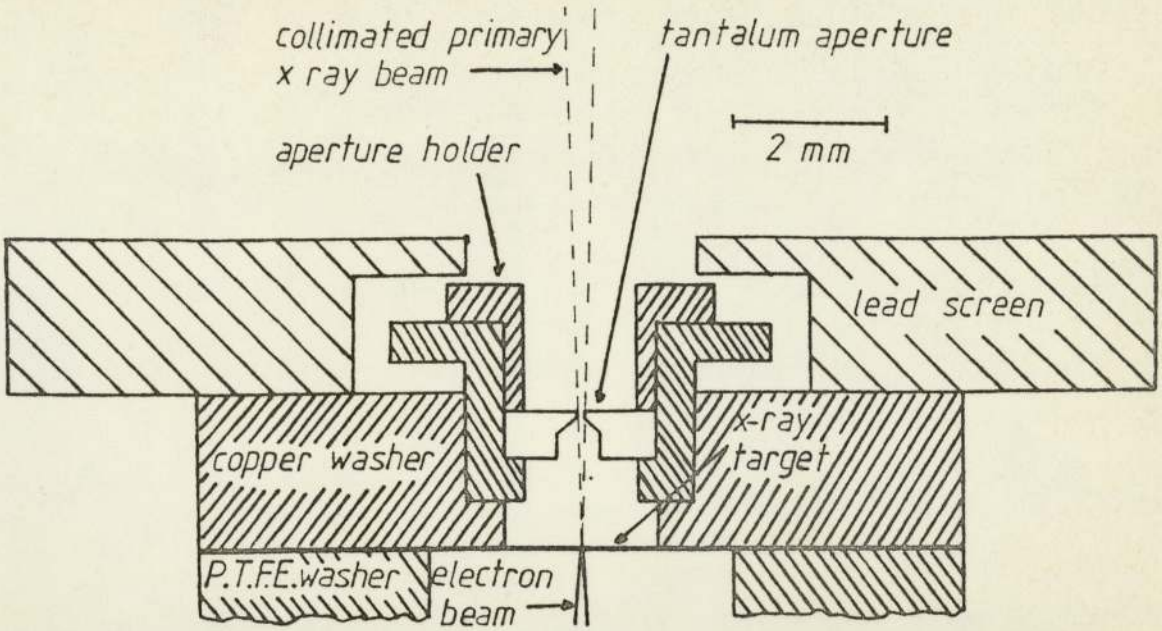

Figure 4.30 Schematic representation of the aperture arrangement used to collimate the primary x-ray beam to the required dimensions.

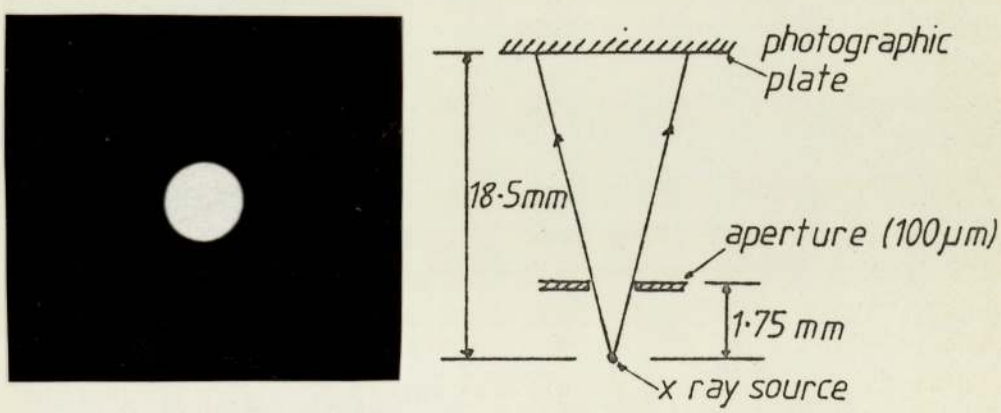

Figure 4.31 Microradiograph of a 100 μm diameter tantalum aperture, collimating the primary x-ray beam. Overall magnification 100x.

x-ray beam collimating aperture in figure 4.31. This is a microradiograph of a 100 μm tantalum aperture placed 1.75 mm above the x-ray target. The photographic plate was placed at 18.5 mm above the x-ray target and thus providing a direct magnification of 10.5 times. At an electron accelerating voltage (V_r) of 20 KV and a target current of 6.0 μA, an exposure time of 5 seconds was required. The microradiograph of figure 4.31 was further enlarged photographically by 9.5 times. At 18.5 mm above the x-ray target

the diameter of the x-ray beam was 1.05 mm. Figure 4.31 shows that the x-ray beam is very well defined with very little, if any, x-ray scattering at the aperture.

The 100 μm tantalum aperture was the smaller one available at the time and it was used to collimate the x-ray beam for tests on x-ray fluorescence analysis. In actual practice a smaller aperture, in the region of 10 μm, would be employed, since as shown in chapter 1 (page 5) the diameter of this aperture controls the specimen resolution.

Before carrying out fluorescence analysis it is desirable to know whether the intensity of the primary x-ray beam is sufficient to fluoresce a specimen. The x-ray counter available was a Philips Geiger counter (Ratemeter PW 4041) which is capable of measuring x-ray count rates up to 500 counts per second. By using this meter together with an x-ray attenuating filter it is possible to estimate the magnitude of the primary beam intensity from the intensity attenuation relation :

$$\bar{I} = \bar{I}_o \exp(-\mu/\rho\, t_o) \quad \text{- - - - - - - - - - - - - 4.7}$$

where

$\bar{I}_o$ is the primary x-ray beam intensity

$\bar{I}$ is the attenuated x-ray intensity

μ/ρ is the mass absorption coefficient of the attenuation filter

t_o is the attenuation filter thickness.

At an electron accelerating voltage (V_r) of 20 KV and a target current of 6.6 μA and using a 50 μm thick gold filter between the Geiger counter and the x-ray target, a count rate of 258 counts per second was registered by the Geiger counter. This corresponds to a primary x-ray beam intensity of 7.75×10^{10} counts per second. This primary intensity is sufficient to produce enough fluorescent

x-rays from a specimen to utilise efficiently a solid state x-ray detector, placed close to the specimen.

The equipment required to carry out multielemental energy dispersive x-ray fluorescence analysis consists of a solid state silicon lithium drifted (Si(Li)) x-ray detector, a multichannel analyser and some form of recorder to store the spectra from the multichannel analyser, in a permanent form. Unfortunately this equipment was not permenently available to the Electron Optics Group of the Department. However, it was possible to borrow the necessary equipment from the Nuclear Research Group of the Department for a short time to carry out a preliminary experiment. This equipment consisted of a silicon lithium drifted (Si(Li)) solid state detector (Kevex-ray, model 2002, serial No. 3140), a 512 channel analyser (Canberra, series 30) and a teleprinter (Teleprinter equipment Ltd, type TRING 4011).

The solid state detector was mounted on the micro-x-ray source as shown in figure 4.32. This was the only way to mount the solid state detector on the micro-x-ray source because of the geometry of this particular detector. This arrangement was far from ideal, but was adequate for preliminary experiments, the results of which could be extrapolated to those of a more favourable arrangement. With the present arrangement, the specimen had to be placed 30.5 mm above the x-ray target. At this point the primary beam diameter was 1.8 mm, which meant that only part of the primary x-ray beam could be used to fluoresce the required specimens, whose dimensions were usually less than 0.5 mm in diameter.

The specimen to detector distance was 5 mm. The detector had an effective area of 30 mm^2, thus providing a detection angle of 1.2 steradians.

A number of specimens were analysed using the apparatus as shown in figure 4.32. All specimens were analysed by x-rays

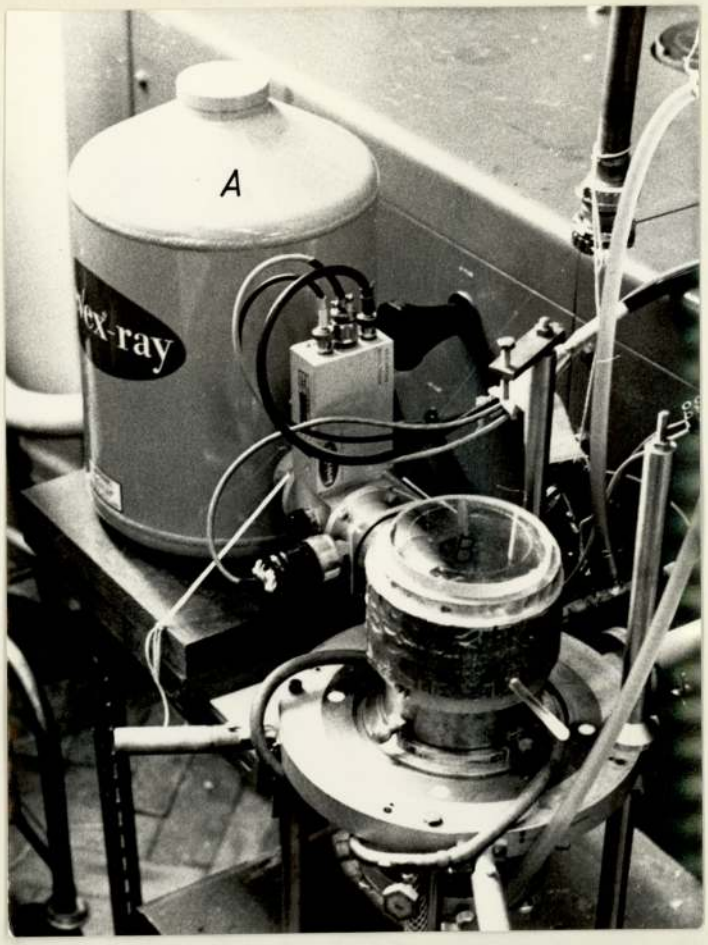

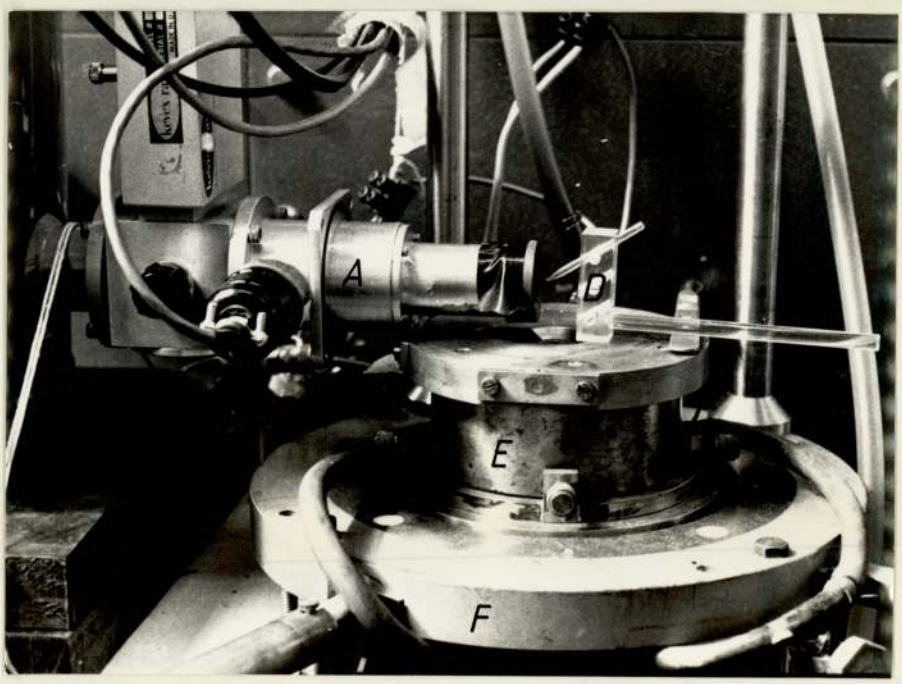

Figure 4.32 Photographs showing the experimental arrangement for micro-x-ray fluorescence analysis. A is the solid state detector, B is a lead glass window, C is a lead shield, D is the specimen holder, E is the objective lens and F is the electron optical bench.

generated by a 20 KV electron beam striking a copper target. For comparison purposes, all specimens were analysed for 300 seconds.

At an electron accelerating voltage (V_r) of 20 KV, x-rays produced from a copper target will consist of the characteristic k_α and k_β x-ray lines of copper in the energy range 8 - 9 Kev, superimposed on a Bremsstrahlung background radiation ranging from 0 - 20 Kev in energy.

Elements with their absorption edges below 9 Kev will be mainly excited by the characteristic copper lines, while elements with their emission lines between 9 - 20 Kev will be excited by the Bremsstrahlung radiation in this range of energy in the primary x-ray beam spectrum.

In order to find out if any spurious lines are present in the primary x-ray beam spectrum, three specimens consisting of pure elements were first analysed. These were titanium, silver and gold. The fluorescent x-ray spectra of these elements are shown in figures 4.33, 4.34 and 4.35 respectively.

The emission of the titanium k_α and k_β characteristic lines are in the energy range 4.5 - 5.0 Kev. These lines are mainly excited by the characteristic copper k-radiation of the primary beam and are shown very clearly in the spectra of figure 4.33. The emission of the characteristic L lines of titanium are in the the energy range 0.45 - 0.53 Kev. These are not shown in the spectra of figure 4.33, since are of very low energy and are absorped by the beryllium window of the solid state detector.

For the silver specimens only the characteristic L lines are shown in the spectra of figure 4.34, since the emission of these lines are in the energy range 2.9 - 3.5 Kev and are mainly excited by the characteristic k-radiation of the primary x-ray beam. The emission of the characteristic k lines of silver are in the energy range 22 - 25 Kev and they are not excited in the present

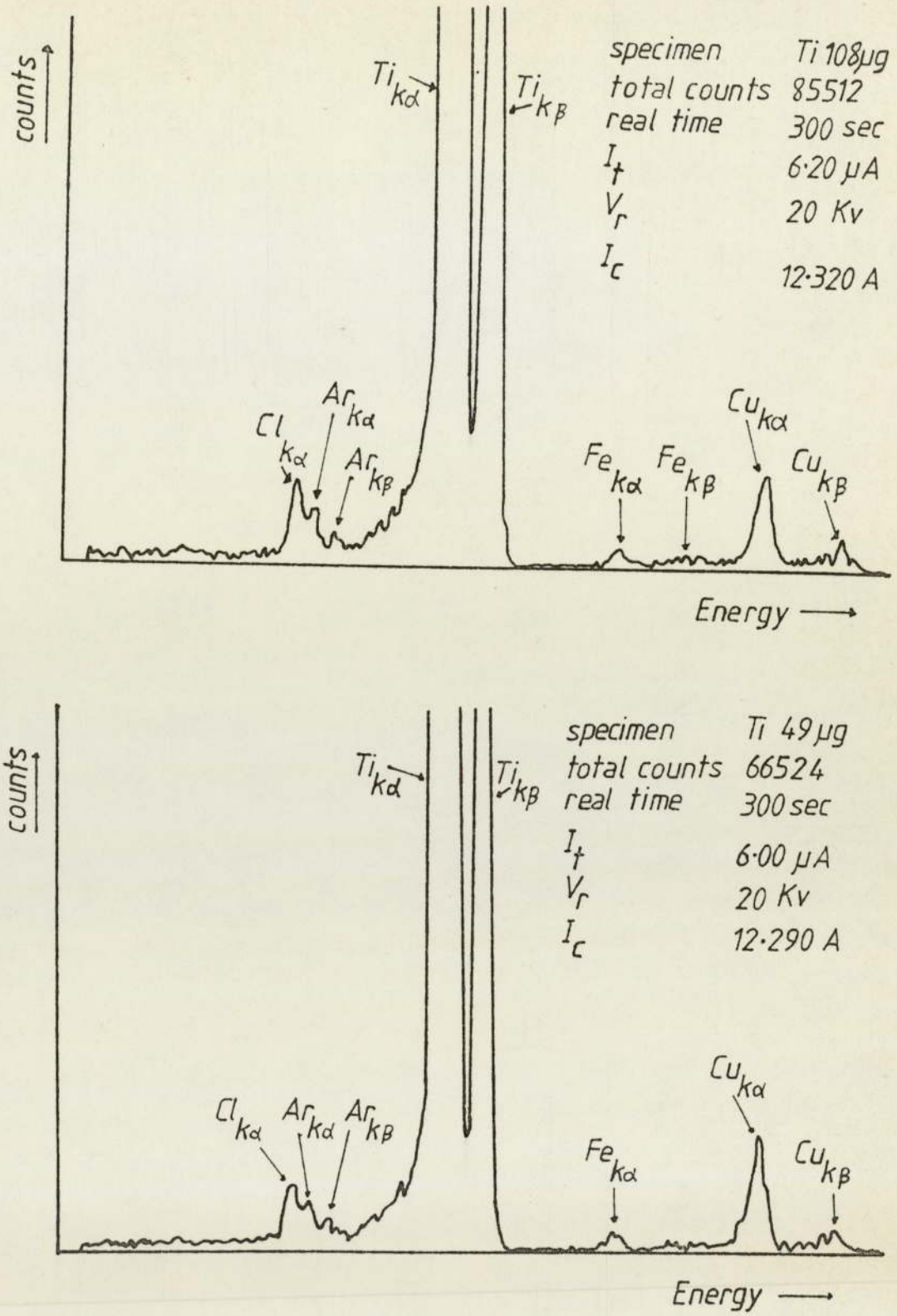

Figure 4.33 X-ray fluorescence spectra obtained from titanium (99.6+%) specimens, showing a number of spurious lines. The copper lines are from scattering of the primary x-ray beam in the specimen. The argon lines are due to the excitation of argon present in air. The chlorine lines are due to the excitation of "Cow Gum" used to hold the specimen in place. The iron lines are probably due to direct electron excitation of the lens polepiece.

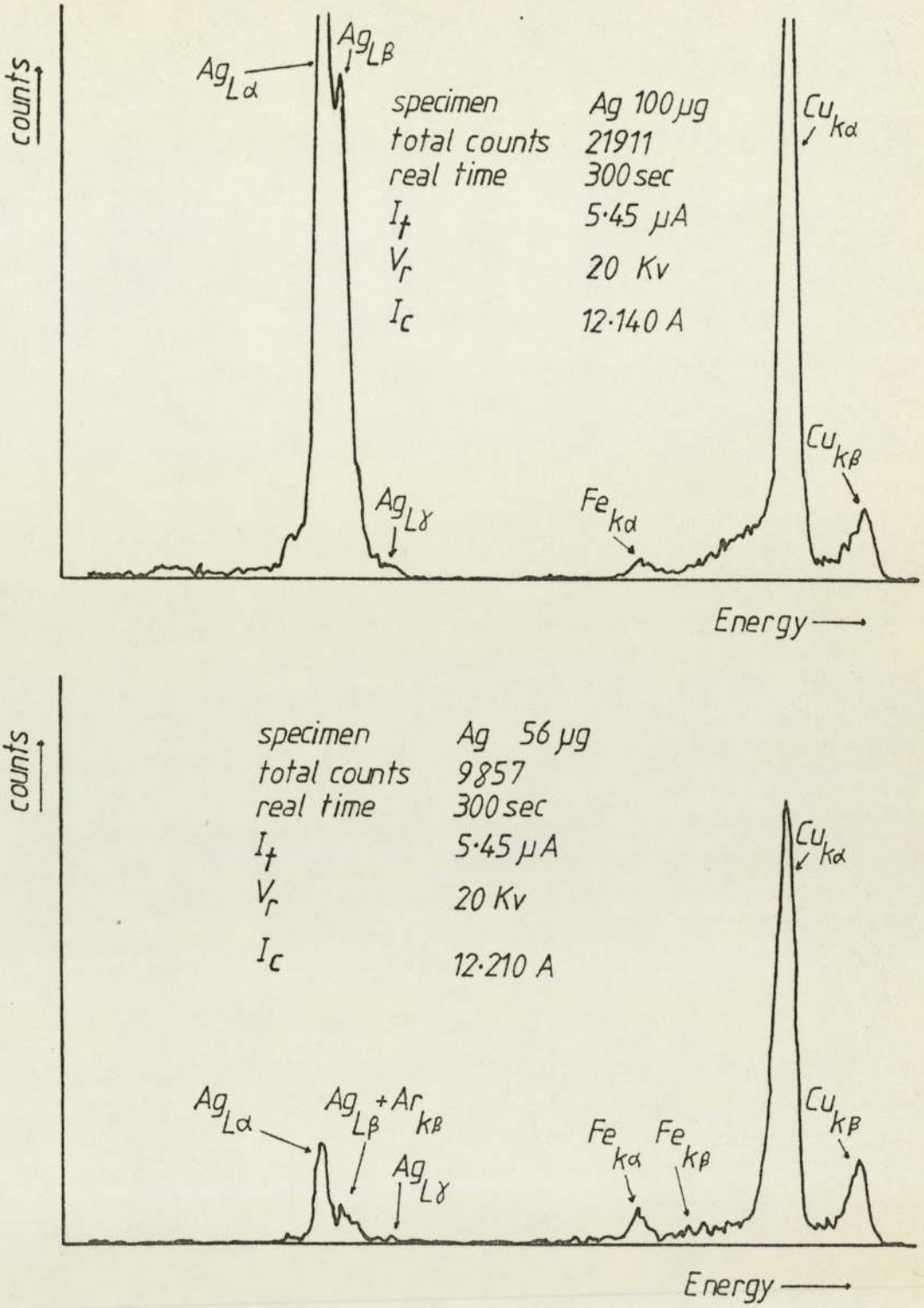

Figure 4.34 X-ray fluorescence spectra obtained from silver (99.99+%) specimens, showing a number of spurious lines. The copper lines are from the scattering of the primary x-ray beam in the specimen. The argon lines are due to the excitation of argon present in air. The iron lines are probably due to direct electron excitation of the lens polepiece.

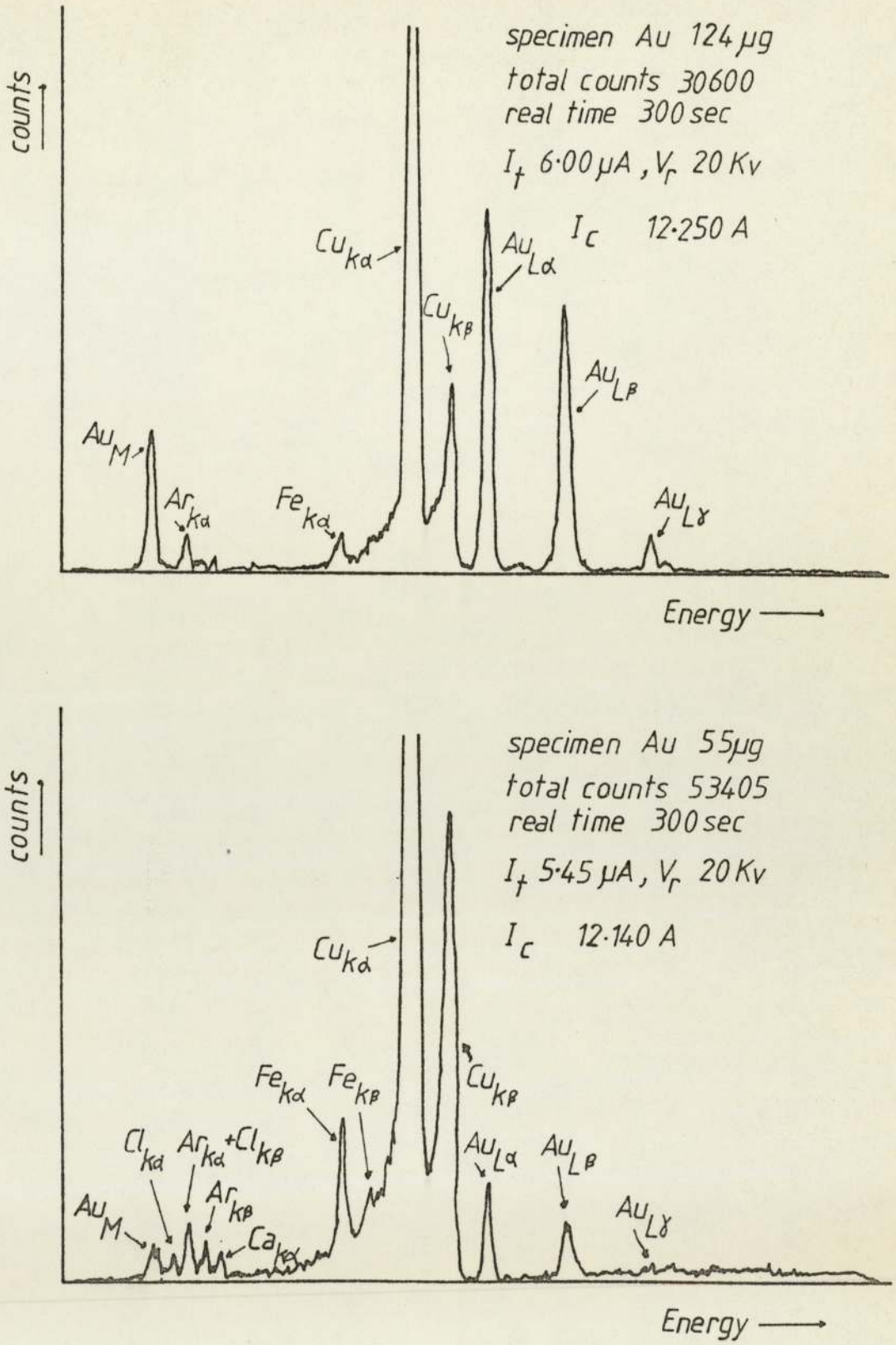

Figure 4.35 X-ray fluorescence spectra obtained from gold (99.99+%) specimens, showing a number of spurious lines. The copper lines are from the scattering of the primary x-ray beam in the specimen. The argon lines are due to the excitation of argon present in air. The chlorine lines are from the excitation of "Cow Gum" used to hold the specimen in place. The iron lines are probably from direct electron excitation of the lens polepiece.

experiments, since the maximum energy of x-rays in the primary beam is only 20 Kev.

The emission of the characteristic k lines of gold are in the energy range 68 - 80 Kev and are not excited in the present experiments. The emission of the characteristic L lines of gold are in the energy range 9.6 - 14.4 Kev and are excited by the Bremsstrahlung radiation present in the energy range 9 - 20 Kev of the primary x-ray beam spectrum. The characteristic M lines of gold are in the energy range 2.1 - 2.2 Kev and are excited by the characteristic k-radiation of the primary x-ray beam spectrum. The characteristic L and M lines of gold are shown in the fluorescence x-ray spectra of figure 4.35.

Ideally one would like to see, in the above spectra, only the characteristic lines of the elements actually present in the specimen. In the above spectra there are characteristic lines of four other elements apart from the characteristic lines of the elements present in the specimens. The argon lines are due to the excitation of argon present in air. These lines can be eliminated by carrying out the experiments in vacuum or in an atmosphere of a gas with lower atomic number, such as nitrogen or hydrogen.

The characteristic chlorine lines are from the "Cow Gum" used to hold the specimen on the perspex rod of the specimen holder. These can be eliminated by using a glue consisting of lower atomic number elements, such as an organic glue made from hydrocarbons.

The characteristic iron lines are from probably the polepiece bore of the lens and are excited by electrons striking the interior of the polepiece bore. To eliminate such lines the bore in the polepiece of the objective lens must be lined with an element with a higher atomic number not easily excited by electrons under the energy range of interest, such as tantalum or a liner made of the same element as the x-ray target.

The characteristic copper lines are due to scattering of the characteristic lines of the primary beam by the specimen. These lines can be eliminated by using an x-ray target of higher atomic number which will produce mainly Bremsstrahlung radiation for exciting a specimen. But even then, a large amount of Bremsstrahlung will be scattered by the specimen which may have the effect of obscuring some of the characteristic lines of elements of low concentration in the specimen. For trace analysis it is best to use monoenergetic x-rays by selective filtering of the background radiation from the primary x-ray beam. The monoenergetic beam can then be used to excite elements in a specimen of lower emission energy than that of the monoenergetic x-ray beam. Scattering of the monoenergetic primary beam will also take place in the specimen, but with the correct choice of the energy of the monoenergetic x-ray beam, the scattered characteristic lines of the monoenergetic beam present in the spectrum, will be far from the lines of the elements present in the specimen and therefore will not interfere with the lines present in the energy range of interest.

Figures 4.36 and 4.37 show the fluorescence x-ray spectra of an aluminium alloy (HE15-W) and a phosphor bronze (BS 369) specimens respectively. The constituent elements of the aluminium alloy are shown in table 4.3 and the constituent elements of the phosphor bronze are shown in table 4.4.

From the spectra of figures 4.36 and 4.37 it can be seen that the minimum mass of an element present in the specimen, detectable with the present inefficient arrangement of the x-ray detector, is in the region of 10^{-8} grammes (3.37×10^{-8} grammes of manganese in the aluminium alloy and 1.36×10^{-7} grammes of tin in the phosphor bronze). This minimum detectable mass is far too large compared with the desired mass of 10^{-12} grammes expected from such a

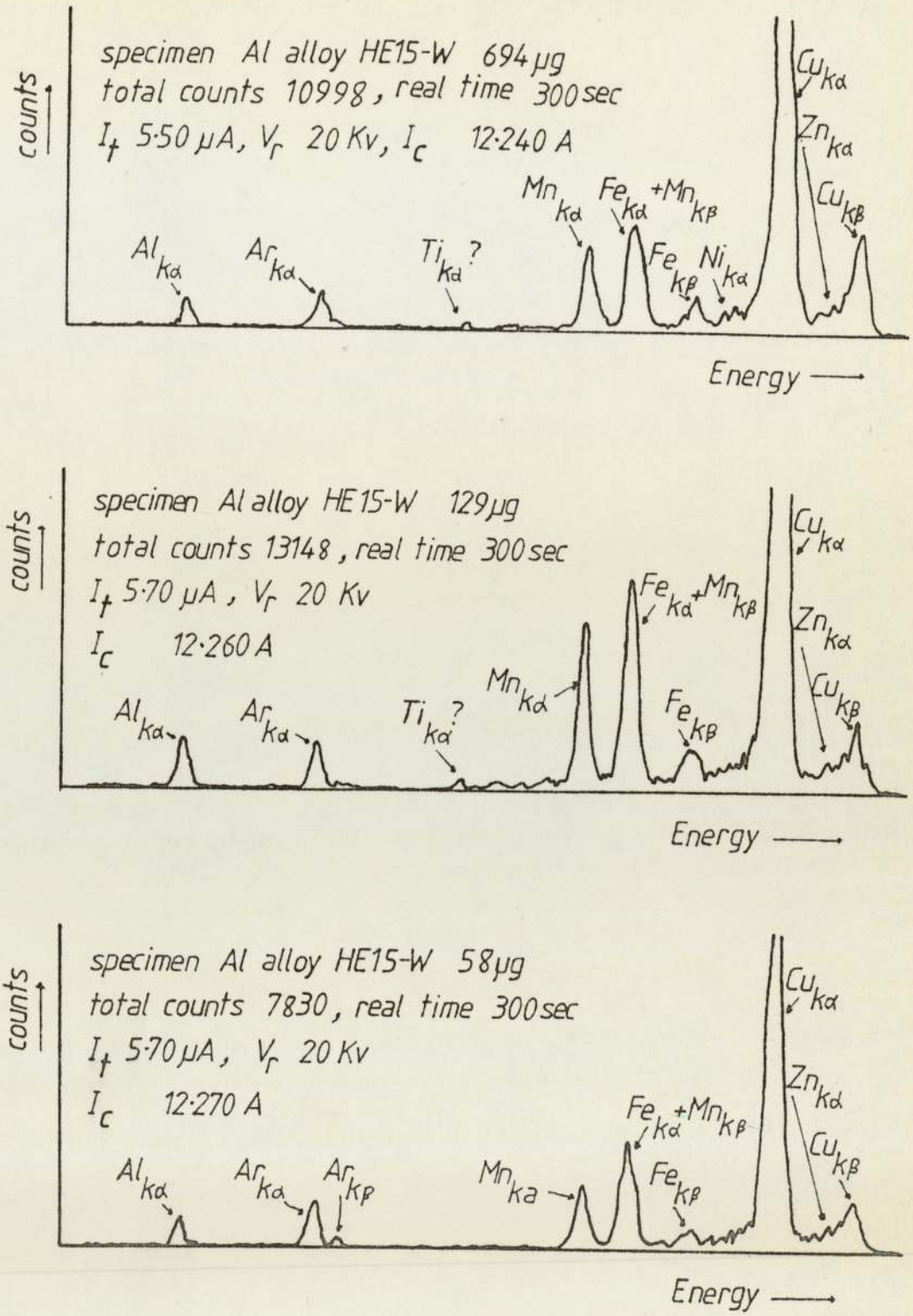

Figure 4.36 X-ray fluorescence spectra obtained from an aluminium alloy (HE15-W) specimens, showing most of the characteristic lines of its constituent elements. The spurious lines of argon are due to the excitation of argon present in air.

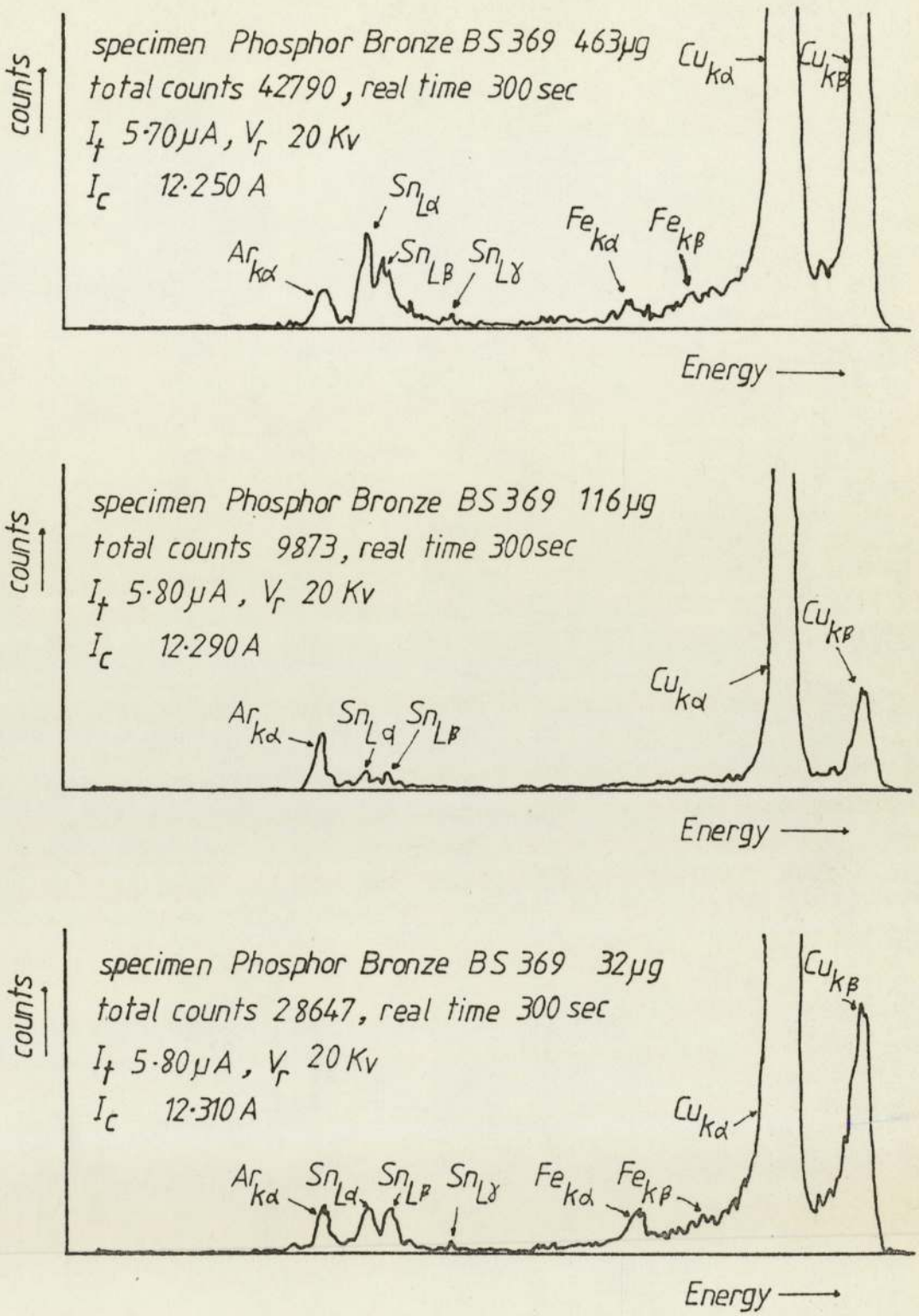

Figure 4.37 X-ray fluorescence spectra obtained from phosphor bronze (BS 369) specimens, showing most of the characteristic lines of its constituent elements. The spurious lines of argon are due to the excitation of argon present in air.

Table 4.3 The constituent elements of HE15-W aluminium alloy.

Constituent elements		Concentration (%)
Copper	Cu	3.5 - 4.8
Magnesium	Mg	0.85
Silicon	Si	0.90
Iron	Fe	1.00
Manganese	Mn	1.20
Nickel	Ni	0.20
Zinc	Zn	0.20
Chromium	Cr	0.30
Titanium	Ti	0.30
Tin	Sn	0.05
Lead	Pb	0.05
Antimony	Sb	0.05
Aluminium	Al	Remainder

Table 4.4 The constituent elements of phosphor bronze (BS 369).

Constituent elements		Concentration (%)
Tin	Sn	4.5 - 6.5
Phosphorous	P	0.02 - 0.4
Total impurities incluting Zinc	Zn	0.20 max.
Copper	Cu	Remainder

technique of x-ray fluorescence analysis.

This large minimum detectable mass is to be expected with the present experimental arrangement of the detector, moreover the experimental results discussed above give pessimistic figures of performance. The very small specimens could not be placed accurately under the primary x-ray beam and so in some cases only part of the specimen was excited by the primary x-ray beam. This can be seen by comparing the spectra obtained from the samples of phosphor bronze of different mass as shown in figure 4.37. For example the total number of counts under the entire spectrum obtained from a mass of 32 μg of phosphor bronze is larger than

that from a 116 μg mass of phosphor bronze. The presence of the calcium k_α line in one of the x-ray fluorescence spectra of gold in figure 4.35, suggest that the perspex rod holding the specimen was more strongly excited than the specimen itself by the primary x-ray beam.

Nevertheless it is possible to extrapolate linearly to a first approximation, the above results to represent those expected to be detected by an ideal arrangement of the x-ray detector and the use of a smaller collimating aperture.

As an example one may consider the aluminium alloy from which the minimum detectable mass of manganese with the present x-ray detector arrangement is 3.37×10^{-8} grammes. This sample is approximately 0.5 mm in diameter. In order for this sample to be excited by all the primary x-ray beam, it must be placed closer to the x-ray target than it was in the above experiments. The correct distance from the x-ray target is 8.5 mm. Thus at this position, to a first approximation, the minimum detectable mass may be expected to reduce by a factor of approximately 4 times. If further the 100 μm tantalum aperture is replaced by a 10 μm aperture and placed at 0.2 mm above the x-ray target, then the minimum detectable mass may be expected to reduce by a factor of 100, if the specimen is placed at a distance of 0.85 mm above the x-ray target. At this distance the specimen will be excited by the same x-ray intensity as if it was at 8.5 mm and using the 100 μm aperture (see chapter 1, page 5).

Therefore for an ideal experimental arrangement the minimum detectable mass of manganese in the aluminium alloy, to a first approximation, would be expected to be in the region of 10^{-11} grammes.

5 Conclusions

The limitations imposed on lens designs operating under saturation conditions, are mainly technological. These are due to the optimum shape and position of the lens coil, those maximum current density, limits the operation of the lens in a given range of lens excitation.

At low electron accelerating voltages, the dimensions of the optimum lens design and especially those of a single polepiece lens in ray 1 beam orientation, present difficulties in accurately constructing the lens.

From the lenses studied in the present work, lens ZEUS is the best choice for an objective lens, giving its optimum electron optical properties by taking advantage of the saturation of its polepiece tip. This is a very good objective lens with strong possibilities as a high resolution objective in the field of electron microscopy. Lens ZEUS in ray 2 beam orientation, gives a spherical aberration coefficient (C_s) of 0.35 mm, at a lens excitation of 11200 A-t and a relativistically corrected electron accelerating voltage (V_r) of 50 KV. At these operating conditions, its chromatic aberration coefficient (C_c) is 0.72 mm, its objective focal length (F_{obj}) is 1.15 mm and its working distance (Z_f) is 0.80 mm.

From the lenses studied in the present work, the best choice of an objective lens for the probe forming system of a multi-purpose micro-x-ray source, is lens HERMES II. This lens provide a large area around its polepiece tip, for the optimum positioning of an x-ray detector. With this lens, the correct positioning and manipulation of the x-ray target and specimen, can be carried out with freedom of any constraints imposed by the lens design. Lens HERMES II in ray 2 beam orientation, gives a spherical aberration

coefficient (C_s) of 0.57 mm at a lens excitation of 14500 A-t and a relativistically corrected electron accelerating voltage (V_r) of 50 KV. At these operating conditions, its chromatic aberration coefficient (C_c) is 0.60 mm, its objective focal length (F_{obj}) is 0.85 mm and its working distance (Z_f) is 1.20 mm.

Lens designs which take advantage of the saturation of their polepiece tips, can be used as high resolution objective lenses, with the possibility of reducing further the limit of spatial resolution; currently being 0.2 nm and given by the operational Cambridge high resolution electron microscope.

The minimum power density that an x-ray target can sustain in the centre of an electron spot formed on a semi-infinite target, is given by a temperature rise close to the melting point of the target material.

For finite x-ray targets, there is a range of electron spot sizes for which the maximum power density is the same as that of a semi-infinite target. A stationary copper target 25 μm thick and 1.5 mm radius can sustain the same maximum power density as a semi-infinite copper target at a relativistically corrected electron accelerating voltage (V_r) of 30 KV, provided that the electron spot diameters formed on this target are smaller than 3 μm. For example when the electron spot diameter is 1.5 μm, the maximum power density, such a target can sustain, is 2.8×10^8 watts cm^{-2}. For electron spot diameters larger than 3 μm, formed on this target, rotating and/or cooling the target will improve the maximum power density to that of the semi-infinite copper target.

The x-ray resolution of a micro-x-ray source is limited by the effective x-ray source size and by Fresnel diffraction. At a relativistically corrected electron accelerating voltage (V_r) of 20 KV, the effective x-ray source size in a copper target 25 μm

thick, was estimated experimentally to be in the region 1 - 1.5 μm, while the x-ray resolution was limited to 2 μm by Fresnel diffraction, if the specimen is placed 5 mm above the x-ray target. There is thus an optimum spacing of specimen and x-ray target in high resolution work.

In micro-x-ray fluorescence analysis, the minimum detectable mass with the present inefficient arrangement of the x-ray detector, is in the region of 10^{-8} grammes (3.37×10^{-8} grammes of manganese in the HE15-W aluminium alloy). For an ideal experimental arrangement, by extrapolation of the above result, this minimum detectable mass would be expected to be in the region of 10^{-11} grammes.

6 Further work required

There are three main areas were more work is required in order to achieve a design of a practical and eventually a commercially viable micro-x-ray source which can help to meet its modern requirements. These are :

a) the heat dissipation in the x-ray target

b) the design of an intermediate lens for the probe forming system of the micro-x-ray source

c) the determination of the optimum position of the x-ray detector.

The existing theories and expressions of the heat dissipation in an x-ray target, make a number of assumptions and approximations which break down for transmission x-ray targets associated with electron spot sizes small compared with the electron penetration in the x-ray target. The theory of heat dissipation in such targets, is quite complex and very tedious to deal with analytically.

It is possible to write a computer program which can deal with the complexity of the heat dissipation problem, taking into account the non-linear thermal properties of the target material and also to deal with non-homogeneous electron beam profiles. The program should deal with finite x-ray targets, with the possibility of target cooling and rotation.

If such a program is written, then the complex problem of heat dissipation in the x-ray target can be solved once and for all, for a large number of target geometries, electron beam profiles and for any range of electron spot size, taking into account the associated electron penetration in the x-ray target. The choice of x-ray target for a particular application can therefore be simplified.

In a two lens probe forming system, the objective lens can be operated at its optimum lens excitation and by varying the lens excitation of the intermediate lens, the required demagnifigation can be achieved to produce the required electron spot size on the x-ray target.

In a micro-x-ray source employing a two stage probe forming system, the x-ray target is fixed at its optimum position, thus making the manipulation of the specimen easier. Also the x-ray detector can be fixed at its optimum position.

The basic design requirements of an intermediate lens are two. The magnetic flux density of the intermediate lens should not interfere with the magnetic circuit of the objective lens, since any interference will effect the performance of the objective lens. The intermediate lens should provide the necessary demagnification to produce the required range of electron spot sizes on the x-ray target, without a substantial influence on the aberrations of the objective lens.

For micro-x-ray fluorescence analysis the major problem is the correct positioning of the x-ray detector, which should be such so as to avoid the direct x-ray beam from the x-ray target and such so that the ratio of the x-ray fluorescence from the specimen to the background (Bremsstrahlung) radiation is as large as possible.

A large amount of experimental work is required to determine the optimum position of the x-ray detector.

By solving the above problems it is then possible to design a complete two lens probe forming multi-purpose micro-x-ray source, capable of meeting most of its modern requirements.

The interface of such a micro-x-ray source with an x-ray sensitive camera, could allow direct viewing of the specimen on a TV monitor. This can help to position the specimen in the correct

place under the primary x-ray beam for micro-x-ray fluorescence analysis. For microradiography, this camera can help to choose the required images before any hard copy is made on a photographic film. This possibility of the use of an x-ray sensitive camera, should also be investigated.

7 References

All references cited in the text, are listed below in alphabetical order.

Alshwaikh A., "Magnetic electron lenses based on the uniformly magnetised ellipsoid", Thesis, The University of Aston in Birmingham, 1979.

Alshwaikh A. and Mulvey T., "The magnetised iron sphere, A realistic theoretical model for single-polepiece lenses", Inst. Phys. Ser. No 36, chapter 1, 1977, pp. 25 - 28.

Archard G.D., "Back scattering of electrons", J. Appl. Phys., vol. 32, 1961, p. 11505.

Beaman D.R. and Isasi J.A., "Electron beam microanalysis", ASTM, special technical publication 506, 1972.

Bethe H.A., "Zur Theory des Durchgangs Schneller Korpuskularstrahlen durch Materie", Annalen der Physik (Leipzig), ANPYA, vol. 5, 1930, p. 325.

Bohm V.K., "Untersuchungen über die azimutale Intensitätsverteilung der Röntgenbremsstrahlung", Annalen der Physik, vol. 33, 1938, pp. 315 - 334.

Boyle M.J. and Ahlstrom H.G., "Imaging characteristics of an axisymmetric, grazing incidence x-ray microscope designed for laser fusion research", Rev. Sci. Instrum., vol. 49, part 6, 1978, pp. 746 - 751.

Castaing R., "Application of electron probes to local chemical and crystallographic analysis", Thesis, University of Paris, 1951.

Christofides S., "Development of Energy Dispersive X-ray Fluorescence Analysis for use in Forensic Science", 3rd year industrial training report, University of Aston in Birmingham, 1977.

Christofides S. and Mulvey T., "A high flux density single pole-

piece lens", Electron Microscopy, eds. Brederoo P. and Boom G. (7th Europ. Congr. on Electron Microscopy Foundation, Leiden, 1980), vol. 1, 1980, pp. 70 - 71.

Cleaver J.R.A., "The choice of polepiece shape and lens operating mode for magnetic objective lenses with saturated pole-pieces", OPTIK, vol. 57, No 1, 1980, pp. 9 -34.

Cosslett V.E., "Intensity limitations in a point source of x-rays", Proc. Phys. Soc., vol. 65B, pp. 782 - 785.

Cosslett V.E. and Nixon W.C., "The x-ray shadow microscope", J. Appl. Phys., 1953, pp. 1 - 8.

Cosslett V.E., "X-ray microscopy : a rival to electron microscopy?", Rapport Europees congres T.E.M., 1954, pp. 281 - 292.

Cosslett V.E. and Dyson N.A., "Measurement of spectral and angular distribution of x-rays from thin targets", X-ray microscopy and microradiography, Academic press Inc., Publishers, New York, 1957, pp. 405 - 413.

Cosslett V.E. and Thomas R.N., "Multiple scattering of 5 - 30 Kev electrons in evaporated metal films", Brit. J. Appl. Phys., vol. 15, 1964, pp. 1283 - 1300.

Dijkstra J.H. and Lantwaard L.J., "Holographic construction of open structure, dispersion transmission gratings", Optics Communications, vol. 15, No 2, 1975, pp. 300 - 305.

Dudley R.J., Howden C.R., Taylor T.J. and Smalldon K.W., "The discrimination and classification of small fragments of window and non-window glasses using energy-dispersive x-ray fluorescence spectrometry", X-ray Spectrometry, vol. 9, No. 3, 1980, pp. 119 - 122.

Duncumb P., "Improved resolution with the x-ray microanalyser", X-ray Microscopy and X-ray Microanalysis, proceedings of the second International symposium, Stockholm, 1960, pp. 365 - 371.

Ely R.V., "Microfocal radiography", ed. Ely R.V., Academic press, 1980.

Franks A., "X-ray Optics", Sci. Prog. Oxf., vol. 64, 1977, pp 371 - 422.

Gray C.C. "X-ray production cross-sections and their use in micro-analysis of thin specimens", Thesis, Glasgow University, 1981.

Gursky H. and Zehnpfennig T., "An image-forming slitless spectrometer for soft x-ray Astronomy", Applied Optics, vol. 5, No 5, 1966, pp. 875 - 876.

Haine M.E. and Linder D., "High brighness electron guns", Focusing of charged particles, vol. 1, ed. Septier A., Academic press, 1967.

Halpern G.M., Varon J., Leiner D.C. and Moore D.T., "Laser fusion microballoon wall-thickness measurements : A comparative study", J. Appl. Phys., vol. 48, No 3, 1977, pp. 1223 - 1228.

Harris P. and Mulvey T., "An experimental single-polepiece magnetic lens probe-forming system", Development in Electron Microscopy and Analysis, ed. Venables, J.A., Academic press, 1976, pp. 49 - 50.

Henderson T.M., Cielaszyk D.E. and Simms R.J., "Microradiographic characterization of laser fusion pellets", Rev. Sci. Instrum., vol. 48, No 7, 1977, pp. 835 - 840.

Howden C.R., Dudley R.J. and Smalldon K.W., "The analysis of small glass fragments using Energy dispersive X-ray Fluorescence Spectrometry", HOCRE report No 241, 1977.

Humphreys C.J. and Spence J.C.H., "Sub-Angstrom resolution transmission electron microscopy using a field emission gun", Inst. Phys. Conf. Ser. No 52, 1980, pp. 449 - 452.

Juma S.M. and Mulvey T., "The axial field distribution of single-polepiece lenses", Inst. Phys. Conf. Ser. No 52, chapter 1, 1980, pp. 59 - 60

Keeley R.H. and Christofides S., "Classification of small glass fragments by x-ray microanalysis with the SEM and a small sample XRF spectrometer", Scanning Electron Microscopy/ 1979/I, SEM inc., AMF O'Hare, IL. 60666, USA, pp. 459 - 464.

Long J.V.P. and Cosslett V.E., "Some methods of x-ray microchemical analysis", X-ray microscopy and microradiography, 1957, Academic press inc., publishers, New York, USA, pp. 435 - 442.

Long J.V.P., "X-ray absorption microanalysis with fine-focus tubes", J. Sci. Instrum., vol. 35, 1958, pp. 323 - 329.

Long J.V.P. and Rockert H.O.E., "X-ray fluorescence microanalysis and the determination of potassium in nerve cells", X-ray Optics and X-ray Microanalysis, 1963, Academic press inc., New York, pp. 513 - 521.

Marai F.Z., "Electron-Optical properties of single-pole magnetic elecrtron lenses", Thesis, The University of Aston in Birmingham, 1977.

Montecalvo F., "Problems encountered in x-ray fluorescence analysis of small glass particles", Crime Laboratory Digest, FBI, Issue 77-9, 1977, pp. 4 - 8.

Mulvey T., "A new microanalyser", Proceedings of 2nd International symposium of X-ray Microscopy and X-ray Microanalysis, Stockholm 1959, publ. 1961, eds. Engstrom, Cosslett, Pattee and Elsevier, pp. 372 - 378.

Mulvey T., "Electron Microprobes", Focusing of charged particles, vol. 1, ed. Septier A., Academic press, 1967.

Mulvey T. and Nasr H., "Limitations of the finite element method", Inst. Phys. Conf. Ser. No 52, chapter 1, 1980, pp. 53 - 54.

Mulvey T. and Nasr H., "An improved finite element program for calculating the field distibution in magnetic lenses", Electron Microscopy, eds. Brederoo P. and Boom G.(7th Europ. Congr. on Electron Microscopy Foundation, Leiden, 1980), vol. 1, 1980, pp. 64 - 65.

Mulvey T. and Nasr H., " An improved finite element method for calculating the magnetic field distribution in magnetic lenses and electromagnets", Proc. 1st Conf. on charged particle optics, Giessen, Germany, Sept., 1980, ed. Wollnik H., North Holland publishing Co., Amsterdam, 1981, pp. 201 - 208.

Mulvey T. and Al-Khashab M., Private communication , The University of Aston in Birmingham, 1981.

Munro E., "A set of computer programs for calculating the properties of electron lenses", Cambridge University Engineering Department Report, CUED/B-Elect. TR45, 1975.

Nasr H., "A critical assessment of the finite element method for calculating electric and magnetic fields", Thesis, The University of Aston in Birmingham, 1981.

Nicholson W.A.P., "The combination of x-ray fluorescence microanalytical and projection microradiographic techniques", Thesis, Cambridge, 1971.

Nixon W.C. and Baez A.V., "Lectures on the x-ray microscope", University of Redlands, Redlands, California, USA, 1956.

O'Dell M.A., "The determination of the spherical aberration for a single pole-piece magnetic electron lens", Final Year project report, The University of Aston in Birmingham, 1979.

Oosterkamp W.J., "The heat dissipation in the anode of an x-ray tube", Philips Res. Rep. 3, 1948, pp. 49 - 59, 161 - 173, 303 -317.

Pugh D.J and West P.D., "An electron source for a microfocus x-ray tube incorporating a single pole magnetic lens and a novel focusing system", Inst. Phys. Conf. Ser. No 36, chapter 1, 1977, pp. 29 - 32.

Reed S.J.B., "Spatial resolution in electron-probe microanalysis", X-ray Optics and Microanalysis, IV^{e} congres international sur l'optique des Rayons X et la Microanalyse, ORSAY, 1965, pp. 339 - 349.

Reeve V. and Keener T., "Programmed Energy Dispersive X-ray Analysis of Top coats of Automotive paint", J. Forensic Sci. vol. 21, No 4, 1976, pp. 883 - 907.

Rockett P. and Brundin C.L., Private communication , Oxford Instrum., 1980.

Singleton R.M., Weinstein B.W. and Hendricks C.D., "X-ray measurement of laser fusion targets using least squares fitting", Applied Optics, vol. 18, No 24, 1979, pp. 4116 - 4123.

Thomson W. (Lord Kelvin), "Reprints of papers on electrostatics and magnetism", Second edition, Publ. MacMillan and Co., 1884.

Venables J.A., "Design trends in scanning electron microscopy", Sixth European Congress on Electron Microscopy, Jerusalem, Electron Microscopy, vol. 1, 1976, pp. 67 -72.

Vine J. and Einstein P.A., "Heating effects of an electron beam impinging on a solid surface, allowing for penetration", Proc. IEE, vol. 111, No 5, 1964, pp. 921 - 930.

West J.C., "Examination of paint smears on clothing by x-ray fluorescence spectrometry", X-ray Spectrometry, Vol. 4, 1975, pp. 71 - 73.

Whitman R.L., Day R.H., Kruger R.P. and Stupin D.M., "Microradiographs of laser fusion targets : 2-D modeling and analysis", Applied Optics, vol. 18, 1979, pp. 1266 -1274.

Whitman R.L. and Day R.H., "X-ray micrographs of laser fusion targets : Improved image analysis techniques", Applied Optics, vol. 19, No 10, 1980, pp. 1718 - 1722.

Zehnpfennig T., "A functioning model of the soft x-ray slitless spectrometer", Applied Optics, vol. 5, No 11, 1966, pp. 1855 - 1856.

8 Appendices

Appendix A

X-ray fluorescence analysis and alternative primary excitation sources

A1 X-ray fluorescence

The type of x-ray spectrum obtained in fluorescence analysis is dependant on the method used to generate it, which is generally by illuminating the specimen with a primary x-ray beam or by bombarding it with charged particles (Cooper, 1977).

When a particle strikes the specimen, it can generate x-rays in two ways. The particle can loose energy by interacting with the atom, simultaneously radiating an x-ray of the same energy as that lost by the particle, which can be any energy upto the total energy of the incident particle. It can also loose energy by knocking one of the inner-shell electrons out of the atom. The vacancy in the shell is filled immediately by one of the outer-shell electrons, which radiates an x-ray of energy equal to the energy difference of the two shells. This energy difference is a fixed quantity which is different for the atom of each element, so that the x-ray has an energy characteristic of the type of atom. The x-ray spectrum generated by charged particle bombardment therefore, consists of a continuous spectrum extending in energy from the maximum particle energy, superimposed by the x-ray lines characteristic of the elements in the specimen.

When the spectrum is generated by an x-ray beam, only the characteristic lines are present, since the incident x-rays can only loose energy by the discrete amount required to eject an inner-shell electron. The probability of this process of photoelectric absorption taking place, is higher when the incident x-ray has just enough energy to remove the electron from its orbit, so that for x-rays of a lower energy than this, the specimen will have a much

lower mass absorption coefficient. An important consequence of this is that an element always has a relatively lower absorption coefficient for its own characteristic radiation, which must lie on the low energy side of the absorption edge.

A2 Alternative primary excitation sources

Primary excitation sources, for x-ray fluorescence analysis, ranging from high energy cyclotrons and linear accelerators to radioactive isotopes have been used in the past, are used today and are developed for the future (Duke, 1981; Laine and Tukia, 1973; Robertson, 1977; Johansson and Johansson, 1976; Cookson, 1979; Deconnick, et al, 1975; Birks, et al, 1966; Faulkner, et al, 1977; Raith, et al, 1977; Puumalainen, 1977; Porter, 1973; Gould and Healey, 1975). Each method of primary excitation was developed and used for a specific and particular field of study for which that particular method of excitation has a number of advantages over other methods of excitation. These advantages sometimes are of scientific nature, where the purpose of the instrument is purely scientific such as in trying to push the detection limits further than it was possible in the past. Mainly these advantages are ones of convenience and economy, where the purpose of the instrument is such as for routine everyday analysis (Valkovic, 1977; Kemp, et al, 1975; Cookson and Pilling, 1976; Dyson and Simpson, 1976; Blum and Res, 1975; Herbert and Street, 1974; Robertson, 1968).

It is impossible to compare all primary excitation methods with each other taking into account scientific, economic and convenience of use aspects, to come up with an overall best method of excitation, which can be used in many applications. Comparisons of this kind can only be done for a specific application. For example, if a portable light-weight instrument for use in fields

such as Geology, where the instrument can be of help in remode places such as down mines or desert regions, where a Geologist can use x-ray fluorescence analysis for screening purposes, then a radioactive isotope can be the best method of primary excitation. On the other hand if an instrument is required for every day x-ray fluorescence analysis in a laboratory where comparisons of samples is of importance, an x-ray beam primary excitation source may be of advantage. Such a system will give lower detection limits than a radioactive isotope and it will be more economic to run and more convenient than a cyclotron accelerator.

In the present work the primary excitation source for x-ray fluorescence microanalysis is a micro-x-ray source produced by focusing an electron beam on a transmission x-ray target.

In the past a large number of comparisons were made between x-ray beam excitation and charged particle excitation x-ray fluorescence analysis, where the x-ray beam primary excitation was produced by a conventional x-ray tube (Scheer, et al, 1977; Ahlberg and Adams, 1978; Goulding and Jaklevic, 1977; Gedcke, et al, 1977). These comparisons arrived at conclusions where one technique was slightly better than the other one or both techniques were complementary to each other.

The most important comparisons made, which are relevant to the present work, are those between electron beam and micro-x-ray beam primary excitation sources. The work of Zullinger and Stewart (1977) and the work of Linnemann and Reiner (1978) were both carried out on scanning electron microscopes. A thin x-ray transmission target was used to provide x-ray beam excitation of the specimen. When this target was removed from the path of the electron beam, then electron beam excitation could be used. The conclusions of both works are that an increase in the signal to background ratio by a factor of 2 to 50 can be obtained by using

x-ray beam excitation x-ray fluorescence analysis. Emphasis is also given to the usefullness of x-ray excitation fluorescence analysis for analytical work in an SEM which does not need high spatial resolution; for example, to determine the doping of semiconductors. In both works the x-ray target to specimen distance was relatively large and thus a trade-off between spatial resolution and counting time was a critical factor, achieved by the use of limiting apertures. The overall conclusion of both works was that the two methods of excitation were complementary to each other, with the provision that x-ray beam excitation x-ray fluorescence analysis can be improved further by placing the x-ray target closer to the specimen to be analysed.

A3 Fluorescence x-ray intensity reaching the detector when generated in a specimen by a parallel and a divergent x-ray beam primary excitation source

The production of x-rays by a beam of electrons striking a solid target, where the x-rays used are collected from the same side as the striking electrons, has been extensively studied, both theoretically and experimentally, by a lot of workers in the field of microprobe analysis and x-ray production, where such factors as direct and indirect ionisation and absorption have been taken into account. The same principles will apply, by analogy, for a transmission target, providing that the thickness of the target is around twice the range of electron penetration in the target. This will not be discussed in the present work. The reader is referred to the published literature.

The important fact that needs to be considered here, is the difference in x-ray flux produced by an ordinary x-ray generator using large electron spot sizes and that produced by a micro-x-ray source using very small electron spot sizes. X-ray production is

proportional to the number of electrons striking the target at a given moment of time and the energy of these electrons. Hence the current density in an electron spot is proportional to the production of x-rays in the target. A simple comparison can be made between an ordinary x-ray generator and a micro-x-ray source.

Consider an ordinary x-ray generator operating at 50 KV and supplying 60 mA to a 1 mm diameter electron spot on the target. This will provide a current density of 76.39 mA mm^{-2} on the target using a power of 3000 watts. A micro-x-ray source operating at 50 KV and supplying 50 μA to an electron spot of 5 μm diameter on the target, will provide a current density of 2546.48 mA mm^{-2}, using only 2.5 watts of power. Hence this micro-x-ray source can produce upto 30 times more x-rays and using a power 1200 times less than the x-ray generator descibed above.

A parallel beam of x-rays can be produced from an ordinary x-ray generator using collimation apertures. This parallel beam can then be used to excite a specimen for micro-x-ray fluorescence analysis. The beam of x-rays usually produced using a micro-x-ray source is a divergent one. The divergence of which depends on the beam defining aperture used.

The difference in x-ray fluorescence yield that can be produced by a parallel and a divergent beam on the same specimen and also the x-ray flux intensity arriving at the detector need to be investigated. Figure A1 a) shows schematically a parallel beam striking a specimen to produce x-ray fluorescence which is then collected by the detector. Figure A1 b) shows a divergent beam exciting a specimen to produce x-ray fluorescence.

For both cases Muller (1972) has derived equations that give the intensity of characteristic K_α fluorescent x-rays reaching the detector, when the specimen is excited by characteristic K_α radiation. For a parallel beam the intenity of the characteristic

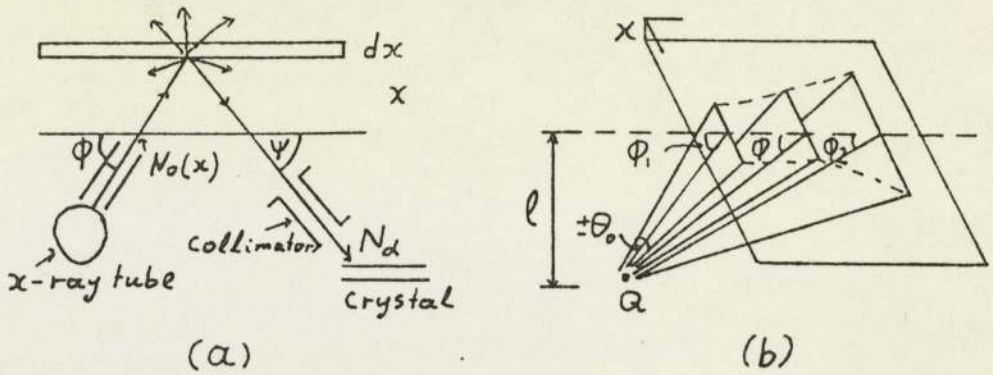

Figure A1 Schematic representation of a parallel a) and a divergent b) beam exciting a specimen for calculating the x-ray intensity reaching the detector.

fluorescent K_α x-rays reaching the detector is given by :

$$N_{K\alpha} = \frac{FgpE}{\sin\phi} \int_{\lambda_0}^{\lambda_K} N_0(\lambda)/\mu_\ell(\lambda)\, d\lambda \cdot \int_0^h dx \exp\left[-x\rho\left\{\frac{\mu_\ell(\lambda)}{\sin\phi} + \frac{\mu_\ell(\alpha)}{\sin\psi}\right\}\right] \quad ----A1$$

For a divergent beam the expresion becomes :

$$N_{K\alpha} = \frac{(\phi_2-\phi_1)2\theta_0\cos\theta' gpE}{\sin\phi} \int_{\lambda_0}^{\lambda_K} N_0(\lambda)/\mu_\ell(\lambda)\, d\lambda \cdot \int_0^h dx \exp\left[-x\rho\left\{\frac{\mu_\ell(\lambda)}{\sin\phi'\cos\theta'} + \frac{\mu_\ell(\alpha)}{\sin\psi}\right\}\right] \quad ---A2$$

(for the notations used above see Muller (1972)).

The difference in the two equations occur in the cross-sectional areas excited by the two beams and in the exponent of each equation. Namely these are :

$(\phi_2 - \phi_1)2\theta_0\cos\theta'$ instead of F

and

$\exp\left[\frac{\mu_\ell(\lambda)}{\sin\phi'\cos\theta'} + \frac{\mu_\ell(\alpha)}{\sin\psi}\right]$ instead of $\exp\left[\frac{\mu_\ell(\lambda)}{\sin\phi} + \frac{\mu_\ell(\alpha)}{\sin\psi}\right]$

Nothing changes in the basic structure of these equations, apart from these constant factors, which depend only on the aperture used to define the primary x-ray excitation beam. Hence in principle the equation for a parrallel beam may be used for a slightly divergent x-ray beam.

A4 References

Ahlberg M.S. and Adams F.C., "Experimental comparison of photon- and particle-induced x-ray emission analysis of air particulate matter", X-ray Spectrometry, vol. 7, No 2, 1978, pp. 73 - 80

Birks L.S., Labrie R.J. and Criss J.W., "Energy dispersion for quantitative x-ray spectrochemical analysis", Analytical Chemistry, vol. 38, No 6, 1966, pp. 699 - 707.

Blum F. and Res M.A., "Rapid quantitative analysis of some rare earth oxides in inorganic glasses by means of energy dispersive x-ray measurement in a scanning electron microscope", X-ray Spectrometry, vol. 4, 1975, pp. 48 - 51.

Cookson J.A. and Pilling F.D., "Proton microbeam analysis in air", Phys. Med. Biol., vol. 21, No 6, 1976, pp. 965 - 969.

Cookson J.A., "The production and use of a nuclear microprobe of ions at MeV energies", Nuclear instruments and methods, vol. 165, 1979, pp. 477 - 508.

Cooper J.A., "Interpretation of energy-dispersive x-ray spectra", International Laboratory, 1977, pp. 51 - 66.

Deconninck G and Demortier G. and Bodart F., "Applications of x-ray production by charged particles to elemental analysis", Atomic energy review, vol. 13, 1975, pp. 367 - 412.

Dyson N.A. and Simpson A.E., "Studies of normal and diseased human

liver tissue by proton-induced x-ray emission spectroscopy", Phys. Med. Biol., vol. 21, No 5, 1976, pp. 853 - 857.

Duke P.J., "X-ray microscopy : Resent developments and future prospects", Proc. RMS, vol. 16, No 3, 1981, pp. 186 -192.

Faulkner R.G., Hopkins T.C. and Norrgard K., "Improved spatial resolution microanalysis in a scanning transmission electron microscope", X-ray Spectrometry, vol. 6, No 2, 1977, pp. 73 - 79.

Gedcke D.A., Elad E. and Denee P.B., "An intercomparison of trace element excitation methods for energy-dispersive fluorescence analysers", X-ray Spectrometry, vol. 6, No 1, 1977, pp. 21 - 29.

Gould R.W. and Healey J.T., "Secondary fluorescent excitation in a scanning electron microscope : Improved sensitivity of energy dispersive analysis", Rev. Sci. Instrum., vol. 46, No 10, 1975, pp. 1427 - 1428.

Goulding F.S. and Jaklevic J.M., "XRF analysis - Some sensitive comparisons between charged-particle and photon excitation", Nuclear instruments and methods, vol. 142, 1977, pp. 323 - 332.

Hebert A.J. and Street K.Jr., "Nondispersive soft x-ray fluorescence spectrometer for quantitative analysis of the major elements in rocks and minerals", Analytical Chemistry, vol. 46, No 2, 1974, pp. 203 - 207.

Johansson S.A.V. and Johansson T.B., "Analytical application of particle induced x-ray emission", Nuclear Instruments and methods, vol. 137, 1976, pp. 473 - 516.

Kemp K., Palmergren Jensen F., Tscherning Moller J. and Gyrd-Hansen N., "Multi-element analysis of biological tissue by

proton-induced x-ray emission spectroscopy", Phys. Med. Biol., vol. 20, No 5, 1975, pp. 834 - 838.

Laine E. and Tukia L., "Isotope-excited x-ray fluorescence analysis of binary alloys using energy dispersion", X-ray Spectrometry, vol. 2, 1973, pp. 115 - 119.

Linnemann B. and Reiner L., "Comparison of x-ray elemental analysis by electron excitation and x-ray fluorescence", Scanning, vol. 1, 1978, pp. 109 - 117.

Muller R.O., "Spectrochemical analysis by x-ray fluorescence", Adam Higler Ltd, 1972.

Porter D.E., "High intensity excitation sources for energy spectrometry", X-ray Spectrometry, vol. 2, 1973, pp. 85 - 89.

Puumalainen P., "X-ray tube excited fluorescence method using critical absorbers", X-ray Spectrometry, vol. 6, No 2, 1977, pp. 80 - 82.

Raith B., Roth M., Gonsior B., Ostermann H. and Uhlhorn C.D., "Trace element analysis by ion induced x-ray emission spectroscopy", Nuclear instuments and methods, vol. 142, 1977, pp. 39 - 44.

Roberson J.A., "The electron probe microanalyser and its application in Medicine", Phys. Med. Biol., vol. 13, No 4, 1968, pp. 505 - 522.

Robertson R., "Energy dispersive soft x-ray fluorescence analysis by radioisotopic α-particle excitation", Nuclear instruments and methods, vol. 142, 1977, pp. 121 - 126.

Scheer J., Voet L., Watjen V., Koenig W., Richter F.W. and Steiner V., "Comparison of sensitivities in trace element analysis obtained by x-ray excited x-ray fluorescence and proton induced x-ray emission", Nuclear instruments and methods, vol. 142, 1977, pp. 333 - 338.

Valkovic V., "Proton-induced x-ray emission : Applications in Medicine", Nuclear Instruments and methods, vol. 142, 1977, pp. 151 - 158.

Zullinger H.R. and Steward W.D., "Bulk mode analyses in scanning electron microscopes", International Laboratory, 1977, pp. 35 - 42.

Appendix B

Optimum position of the x-ray detector

If a micro-x-ray source is to be used for micro-x-ray fluorescence analysis, then the optimum position of the solid state detector needs to be established, since this optimum position of the detector may influence the design of the objective lens of the probe forming system of such a micro-x-ray source.

In order to determine the optimum position of the x-ray detector the angular x-ray intensity distribution emitted from the target is required, since the x-ray detector must be placed in such a position so as to avoid detection of the direct primary x-ray beam. The x-ray detector should only record characteristic fluorescent x-rays emitted by the specimen, which is placed above the target and irradiated by the primary x-ray intensity.

For quantitative x-ray fluorescence analysis, the primary x-ray intensity should be monoenergetic, while for qualitative x-ray fluorescence analysis, the whole range of x-ray energy spectrum of the primary x-ray beam may be used. In the case of the monoenergetic (characteristic) primary x-ray beam, the angular x-ray intensity distribution is isotropic and the detector has no optimum position. For qualitative analysis using the whole primary x-ray spectrum generated in the x-ray target, the detector may have an optimum position due to the anisotropic nature of the Bremsstrahlung radiation present in the primary beam.

The ratio of the characteristic to Bremsstrahlung radiation will be a maximum at the optimum detector position.

The angular intensity of the Bremsstrahlung emitted from the target depends on the thickness and atomic number of the target material. It also depends on the electron accelerating voltage used.

For very thin target, which allow transmission of electrons

(Bohm, 1938), the angular x-ray intensity distribution is very anisotropic (figure B1 (a)) and the angles at which the maxima occur, increase with increasing accelerating voltage. The x-ray intensity in the forward direction is almost zero.

For x-ray targets thick enough to stop all the electrons within the target, the angular intensity distribution is less anisotropic (Cosslet and Dyson, 1957). The anisotropy is naturally less due to the increased scattering of electrons within the x-ray target (figure B1 (b)).

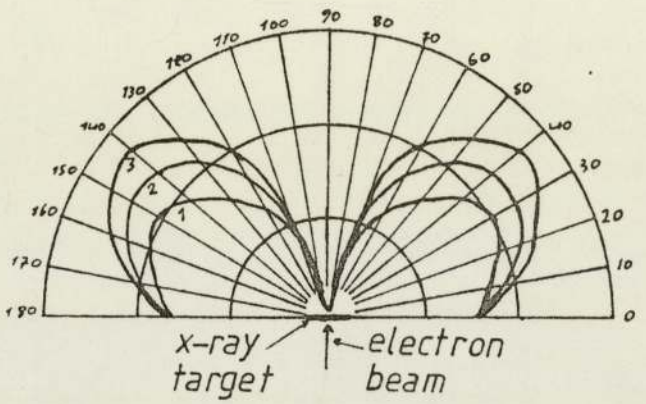

(a)

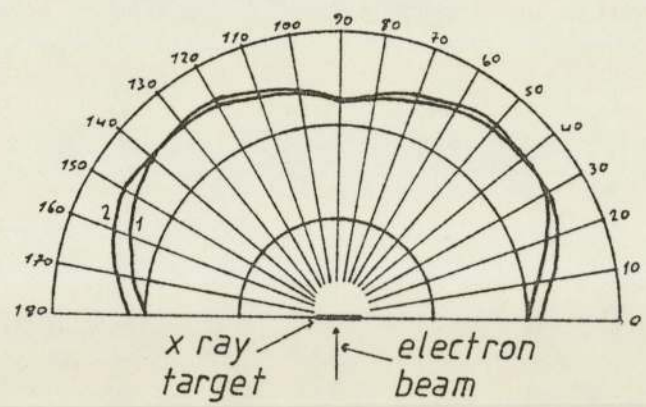

(b)

Figure B1 Angular x-ray intensity distributions of (a) a thin magnesium target of around 0.1 μm thick evaporated on a 0.1 μm thick celluloid film; 1 at 20 KV, 2 at 31 KV and 3 at 40 KV (Bohm, 1938). (b) a thin gold target of 0.209 μm thickness on a distrene film; 1 at 10.05 KV and 2 at 12.05 KV (Cosslett and Dyson, 1957).

There is a decrease in anisotropy with increasing target thickness for a given electron accelerating voltage and also a decrease in anisotropy with increasing atomic number of the target material.

From figure B1 it is evident that although the angular x-ray intensity distribution is weaker at angles close to the target plane, the detector will still record an amount of the primary x-ray intensity, wherever it is placed. In order to shield the detector from the primary x-ray intensity, it is necessary to collimate the primary x-ray beam. This is best achieved by the use of an aperture trap system used previously by Long and Rockert and by Nicholson (Long and Rockert, 1963; Nicholson, 1971). The x-ray aperture system used in the present work and shown in figure 4.29 (see chapter 4, sub-section 4.6) is also effective.

From figure 4.29 can be seen that the range of angles available for the correct positioning of the detector depends on the diameter of the x-ray aperture, its position above the target and the position of the specimen above the x-ray aperture. The range of detector angle can be as much as 80°. Although this angle can be that large, this angle may be limited by scattering of the primary x-ray beam from the specimen. Thus the optimum position of the detector within this large angle can only be determined by experiment.

From figure 4.29 can also be seen that a cross-sectional area of 6x15 mm is required around the polepiece tip of the objective lens in order to accommodate the electron aperture, x-ray target, x-ray aperture and the necessary shielding. Although it is possible to design an asymmetric conventional lens which will provide the required area around the polepiece, such a lens will still restrict easy access to the apertures and x-ray target.

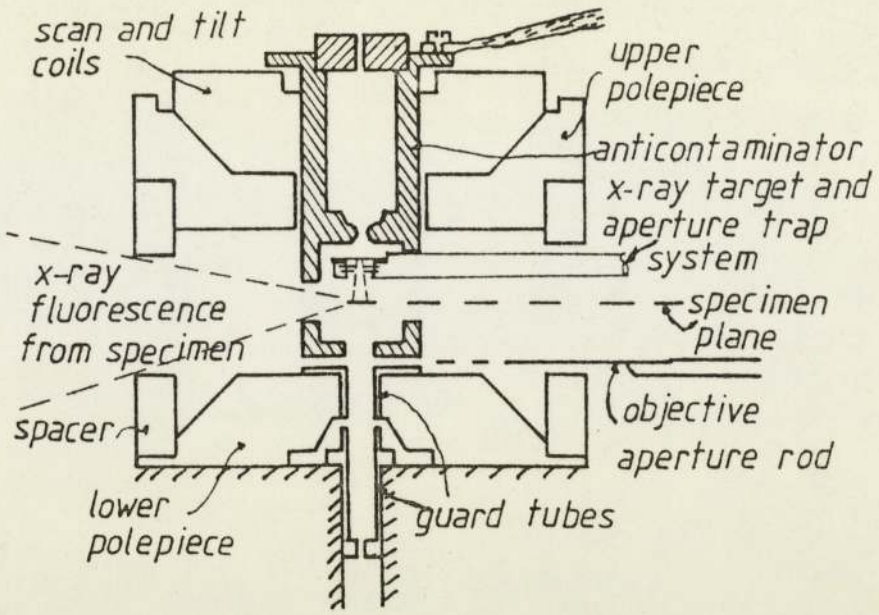

Figure B2 Modification of the specimen environment of a JEOL JEM 100C electron microscope for x-ray excited x-ray fluorescence analysis.

Therefore a single polepiece lens should offer more flexibility as an objective lens for the probe forming system of a micro-x-ray source than an asymmetric conventional lens.

With a micro-x-ray source of the above description, x-ray excited x-ray fluorescence analysis can be carried out in any atmosphere by making the target to seal the vacuum. If x-ray excited x-ray fluorescence analysis is to be performed routinely in vacuum, then it is possible to modify the specimen stage (environment) of a standard high resolution transmission electron microscope and thus avoiding the use of a micro-x-ray source (Gray, 1981). A possible modification of the specimen environment of a JEOL JEM 100C electron microscope is shown in figure B2.

The modifications shown in figure B2 are the same as used by Gray to perform electron excited x-ray fluorescence analysis. The additional modifications for x-ray excited x-ray fluorescence analysis, require the introduction of the x-ray target and the

x-ray aperture system, as shown in figure B2. For more detailed explanation of the modifications shown in figure B2, the reader is referred to the thesis of Gray (1981).

Appendix C

Computer programs

In designing the objective lens, three of Munro's programs (Munro, 1975), which use the finite element method, were used, namely the programs M12, M13 and M21. Also two of Nasr's (1981) programs were used, namely the programs BIOT and AREA. Below follows a brief description of these programs.

Program M12

Program M12 uses the finite element method to compute the vector potential and flux density distribution throughout the magnetic circuit and coil windings of any unsaturated rotationally symmetric lens. The magnetic circuit is assumed to have a constant (high) permeability.

The flux density is computed at points throughout the magnetic circuit. The results can be used to check that the magnetic circuit does not saturate in undesirable places.

Program M13

Program M13 performes the same functions as program M12, except that it deals with saturated magnetic lenses, in which the lens excitation is so high that the non-linear B/H curves of the magnetic materials must be taken into account. The program can handle composite magnetic circuits, constructed from up to five different magnetic materials. Any desired B/H curve can be specified for each magnetic material.

As in the case of program M12, the axial magnetic flux density distribution, the flux density values throughout the magnetic circuit and the vector potential throughout the two-dimensional mesh system within the boundary conditions are computed. The B/H curve used in conjuction with this program is given in table C1, which is that of soft iron, since the actual B/H curve of the

Table C1 The B/H curve of soft iron

H/A-t m^{-1}	B/tesla
50.0	0.400
100.0	0.680
150.0	0.880
200.0	1.020
344.0	1.224
560.0	1.282
807.7	1.325
1040.1	1.351
1344.1	1.377
2720.0	1.442
4716.6	1.500
8880.8	1.589
11124.9	1.623
15613.1	1.679
27509.9	1.790
44157.6	1.840
60940.5	1.866
77421.0	1.898
92469.1	1.919
106713.4	1.937
156847.3	2.000
236424.8	2.100
395579.8	2.300
634312.3	2.600
873044.8	2.900
1032199.8	3.100

magnetic material (Swedish iron)used to construct the lenses, was not available from the manufacturers.

Program M21

Program M21 computes the objective properties of any magnetic lens, whose axial magnetic flux density distribution has been computed previously by program M12 or M13.

The program can handle zero, finite or infinite magnification conditions (figure C1).

For a specified range of electron beam accelerating voltage, the program computes the excitation parameter, the objective plane or image plane, the objective principal plane, the objective focal length, the objective magnification, the spherical aberration

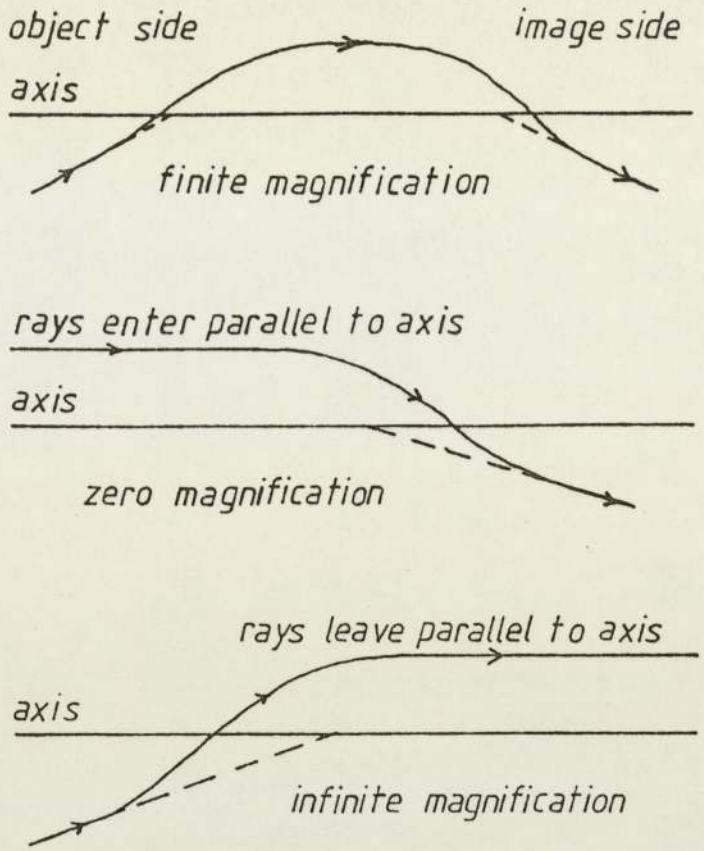

Figure C1 Ray diagram defining the magnification conditions, for which program M21, can compute the electron optical properties of a magnetic electron lens.

coefficient, the chromatic aberration coefficient and the magnetic flux density at the object or image plane as appropriate.

Program BIOT

Program BIOT computes the axial magnetic flux density distribution of any rotationally symmetric iron free magnetic electron lens, using the Biot-Savart law.

This program can be used to compute the coil axial magnetic flux density distribution of a lens for which the total axial magnetic flux density distribution ($B_{coil} + B_{iron}$) was previously computed by program M12 or M13. The difference between the two axial magnetic flux density distributions, give the contribution of the iron (B_{iron}) to the total axial magnetic flux density

distribution of the lens. This can be used as a check on the accuracy of the total axial magnetic flux density distribution (Mulvey and Nasr, 1980).

Program AREA

Munro's programs M12 and M13, were originally developed to compute the axial magnetic flux density distribution of conventional lenses in which the axial magnetic flux density distribution is completely immersed in the body of the lens. These programs require the vector potential to be zero at the boundary; this fact is built into the data required for the computations. For conventional lenses this condition is usually satisfied since the axial magnetic flux density distribution is surrounded by the magnetic circuit.

For a single polepiece lens this condition is satisfied only in the region which is surrounded by the magnetic circuit. This leaves one side of the lens "open" for which the vector potential is zero only at infinite. To satisfy the above condition, the boundary on this side of the single polepiece lens is set at a large distance from the lens.

The magnetic circuit of the lens and the area around it, inside the boundaries, are divided into meshes as required by the finite element method. The distance between the meshes should be as equal as possible through the entire boundary. The number of meshes one is able to use is restricted by the size of computer memory store available and hence an equal distance between the meshes may not be possible. Generally a high concentration of meshes is distributed around the polepiece which is the most important part of the single polepiece lens. These meshes then deviate from this high concentration as one approaches the boundaries. When a sharp change of the mesh size occurs, a discontinuity appears in the

axial magnetic flux density distribution. These discontinuities have a harmful effect on the calculation of the aberrations of the lens and they should be smoothed out before the electron optical properties of the lens are calculated by program M21. When the axial magnetic flux density distribution has been smoothed, the area under it may change. This area should of course equal the lens excitation, which is also required by program M21.

In order to ensure that the smoothing of the axial magnetic flux density distribution has been carried out correctly, the area under the smoothed distribution is computed by program AREA, which uses the trapezoidal rule. The area under the axial magnetic flux density distribution is given by :

$$\int H \, dz = \mu_o \, NI \quad - - - - - - - - - - - - - - - - - C1$$

where

NI is the lens excitation

μ_o is the permeability of free space

The correctly smoothed axial magnetic flux density distribution can then be used as the data for program M21.

Appendix D

The effect of coil position and polepiece shape

To visualise how the shape of the polepiece of a single polepiece lens should look like in order to take advantage of saturation effects, one, may start by considering an iron sphere in a uniform magnetic field, for which Lord Kelvin (Thomson, 1872; Alshwaikh and Mulvey, 1977) has calculated its magnetic potential.

Figure D1 shows the iron sphere in a uniform magnetic field and its axial magnetic flux density distribution, along the axial direction of the symmetry of the sphere. The magnetic flux inside the sphere is constant.

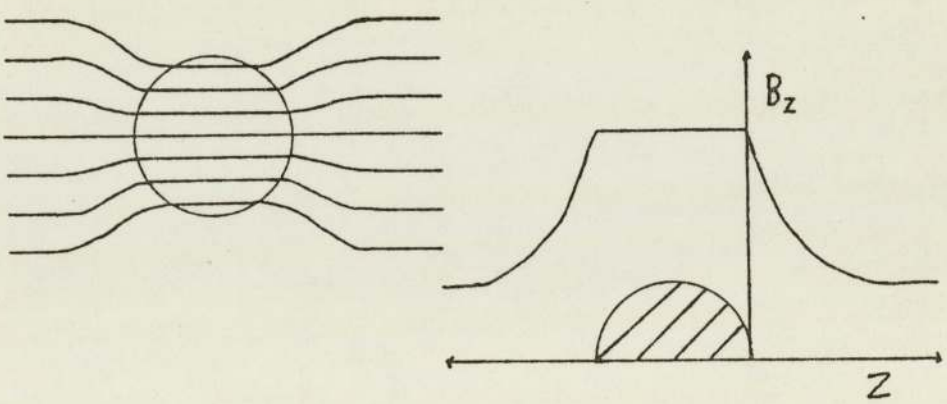

Figure D1 Schematic representation of an iron sphere in a uniform magnetic field and its axial magnetic flux density distribution.

Taking this idea further in using a single polepiece lens having a hemispherical polepiece, its axial magnetic flux density distribution can be expected to be similar to that shown in figure D2. The flux density inside the polepiece can be expected to be constant from the polepiece tip to the back plate of the lens and then drop sharply by the end of the lens. This can only be so provided that the shape and position of the coil is such that it will magnetise the hemispherical polepiece uniformly. The effect

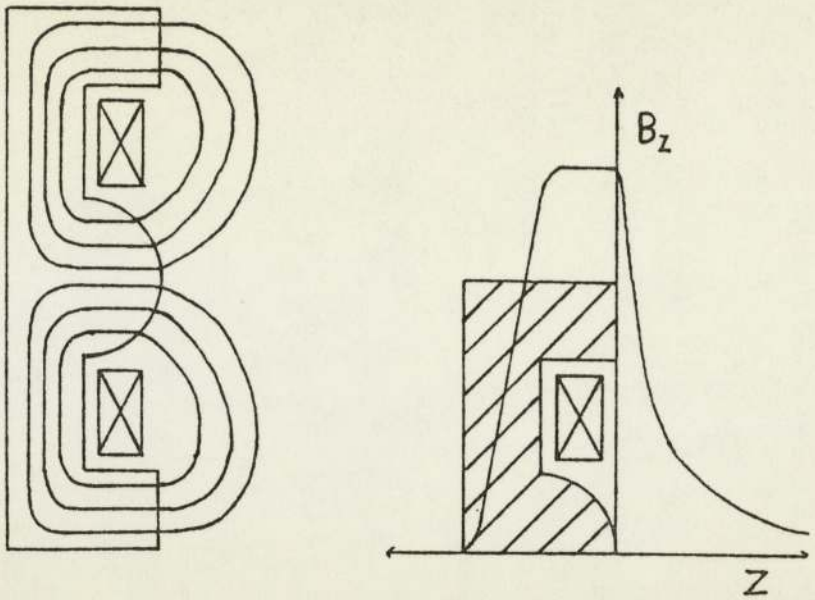

Figure D2 Schematic representation of a single polepiece lens with a hemispherical polepiece, without bore and its axial magnetic flux density distribution; provided that its coil magnetises its polepiece uniformly.

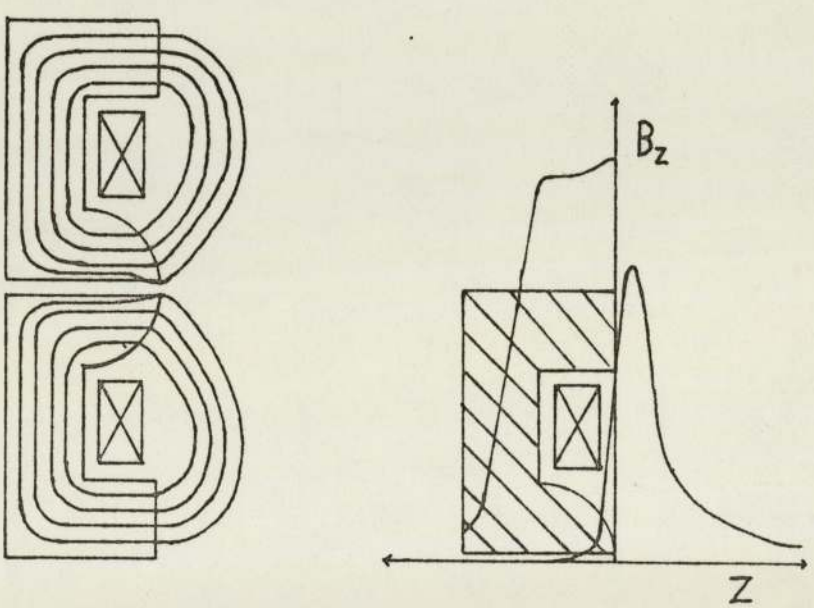

Figure D3 Schematic representation of a single polepiece lens, with a bore and its axial magnetic flux density distribution; provided its coil magnetises its polepiece uniformly.

of the coil position and shape will be considered later in this appendix.

A bore in the hemispherical polepiece will have the effect of

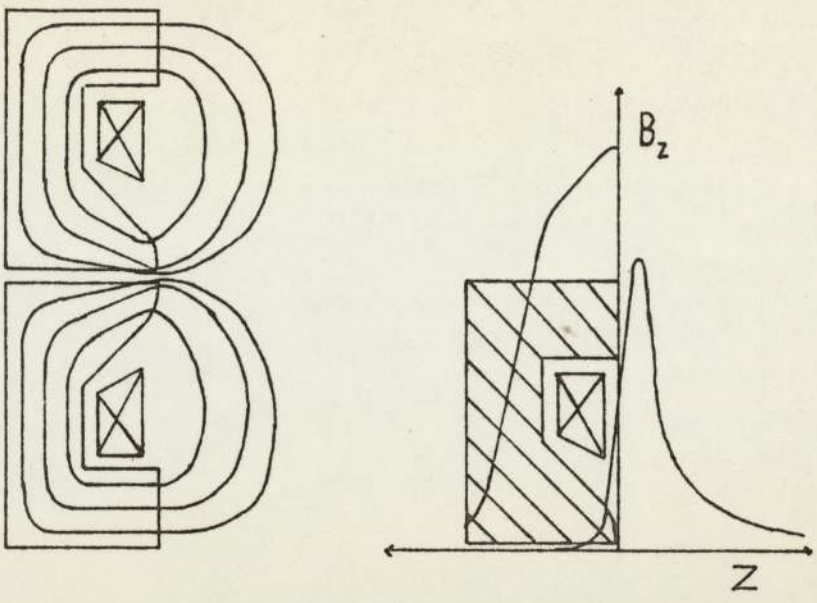

Figure D4 Schematic representation of a single polepiece lens with a conical polepiece and a spherical polepiece tip and its axial magnetic flux density distribution; provided its coil magnetises its polepiece tip uniformly.

raising the flux density inside the magnetic circuit at the tip of the polepiece, as shown in figure D3. The magnetic flux density inside the magnetic circuit, over the length of the polepiece, will not be constant. Initially it will drop gradually from the tip until a small distance inside the polepiece. From this point to the end of the polepiece, the magnetic flux density will have a constant value and then it will drop sharply by the end of the lens.

The ideal magnetic flux density inside the polepiece should be one that is falling gradually from the polepiece tip till the end of the polepiece region. To achieve this, extra magnetic material must be added at the back of the polepiece, where the cross-section of the extra magnetic material must form a tangent on the hemispherical polepiece, as shown in figure D4. If the cross-section of the extra material cuts the hemisphere, then saturation will occur more strongly in this position with the effect of a second peak of the magnetic flux density appearing at this region,

before the magnetic flux density begining to fall off.

For a lens to give optimum electron optical properties, over all lens excitations, the halfwidth of the lens must remain constant over all lens excitations. Also the position of the coil must be such that over all lens excitations the magnetic flux density in the magnetic circuit of the lens, must be highest at the lens polepiece tip.

For the halfwidth of a lens to remain constant over all lens excitations, the halfwidth of the axial magnetic flux density distribution of the coil, must be the same as the halfwidth of the magnetisation (B_{iron}) of lens polepiece tip.

Alshwaikh (1979) derived an expression which gives the magnetic flux density distribution of a uniformly magnetised sphere. He called this, the spherical field and is given by :

$$B_z = B_o(a/z)^3 \quad \text{- - - - - - - - - - - - - - - - - D1}$$

for $z \geq a$

where

B_o is the maximum flux density at the surface of the sphere

B_z is the magnetic flux density at a given distance z from the sphere

z is the distance in the axial direction measured from the centre of the sphere

a is the radius of the sphere

Alshwaikh also derived an expression for the halfwidth of the spherical field which is given by :

$$d_{hs} = 0.26\ a \quad \text{- - - - - - - - - - - - - - - - - - D2}$$

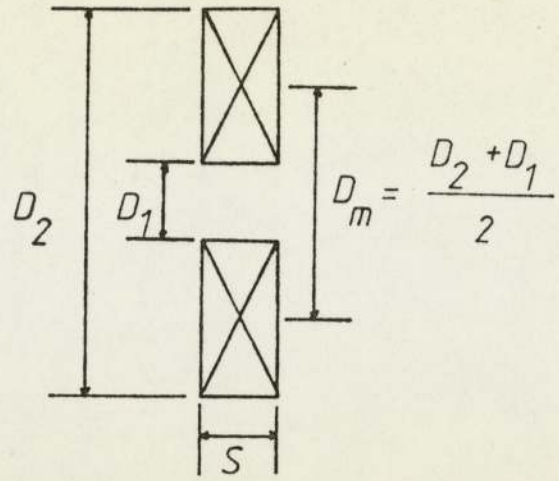

Figure D5 Diagram defining the parameters used by Marai to express the performance of iron free lenses.

According to the work of Marai (1977), on iron free lenses, the dimensions of a coil giving optimum electron optical properties, must be such that $S/D_m = 0.1$ and D_2/D_1 greater than 100, as illustrated by figure D5.

It is thus possible to combine analytically the axial magnetic flux density of a coil meeting Marai's criteria to the magnetisation of a sphere having a given radius, in such a way so that the halfwidth of the total axial magnetic flux density distribution will have a constant value for all lens excitations. Such a combination will yield an optimum objective lens for all lens excitations. To illustrate the above reasoning further, consider the following example :

A soft iron sphere of 10 mm radius, when fully magnetised by a uniform magnetic field, will have a maximum flux density at its surface of 1.8 Tesla and a halfwidth of 2.6 mm. If a coil with a halfwidth of 5.2 mm is positioned with its centre at the same plane as the surface of the sphere, so that it magnetises the tip of the sphere uniformly, then a magnetic lens with no bore will be

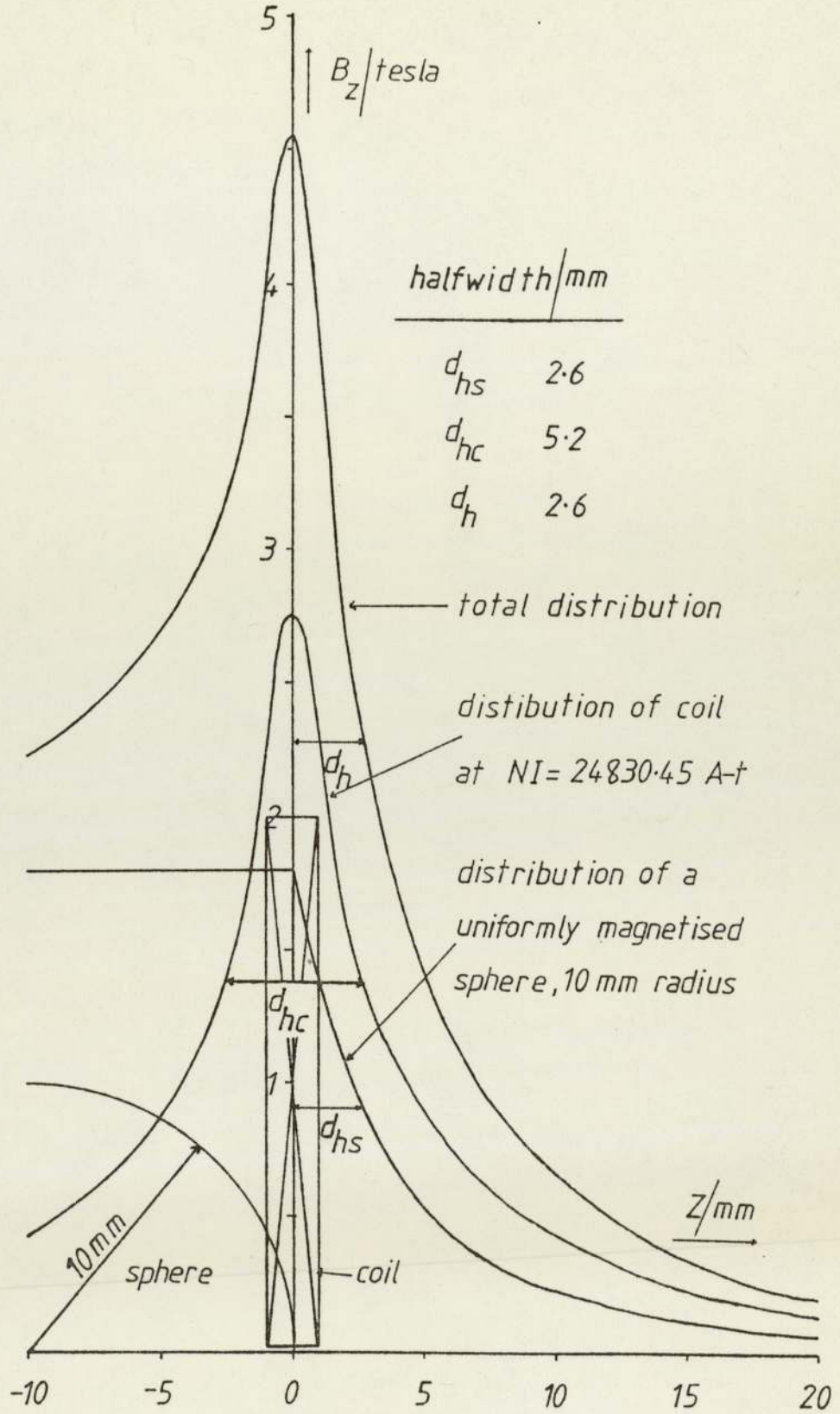

Figure D6 The combination of the axial magnetic flux density distribution of a coil meeting Marai's criteria and the magnetic flux density of a uniformly magnetised sphere having 10 mm radius.

produced, which will have an effective halfwidth d_h of 2.6 mm, for all lens excitations. Such a lens will be suitable for ray 1 beam orientation.

A coil meeting Marai's criteria and having a halfwidth of 5.2 mm, will have S = 2.0 mm, D_1 = 0.4 mm and D_2 = 40 mm. For this coil S/D_m = 0.099 and D_2/D_1 = 100.

Figure D6 shows the addition of the axial magnetic flux density distribution of this coil to the magnetisation of the soft iron sphere with 10 mm radius. In theory this combination produces an optimum magnetic electron objective lens, for all lens excitations. But such a coil will have to be immersed partly in the iron sphere, as shown in figure D6. This clearly suggests that such a combination brakes down.

Presently Mulvey and his collaborators (Mulvey and Al-Khashab, 1981), are trying to achieve an objective lens whose halfwidth remains constant over all lens excitations. They are using single polepiece lenses with spherical polepieces and coils that meet Marai's criteria. Their results look progressively encouraging, with the hope that in the near future a theoretical single polepiece lens will be available and meeting all the criteria of an optimum objective single polepiece lens, for all lens excitations.

In the present work for which a practical lens design is required, the coil shape and position are overlooked, with the knowledge that such lens designs, when operated under saturation conditions, will give optimum electron optical properties for only a specified range of lens excitations.

Appendix E

The effective halfwidth

In electron optics the peak value B_{max} and the halfwidth of the axial magnetic flux density distribution of a lens are related to the lens electron optical properties. The variation of these two parameters with lens excitation give a good indication of the performance of a lens before its electron optical properties are actually calculated.

In a probe forming system of a micro-x-ray source, the electron beam is brought to focus within the axial magnetic flux density distribution. Thus only a part of the axial magnetic flux density distribution is used to focus the electron beam. The electron optical properties of a lens in such an application, depend only on the shape and strength of the part of the axial magnetic flux density distribution which is used to focus the electron beam. The electron beam never "see" the remainder of the axial magnetic flux density distribution, which may be of any shape and strength; it will not make any difference to the focusing of the electron beam. Thus the variation of the halfwidth of the entire axial magnetic flux density distribution with lens excitation does not necessarily give an indication of the performance of the lens of a probe forming system of a micro-x-ray source.

A better parameter would be the effective halfwidth d_h, which is the halfwidth of the part of the axial magnetic flux density distribution, which is used to focus the electron beam. The effective halfwidth d_h would be different for each beam orientation.

From the work carried out on the BASIC lens it is evident that the optimum electron optical properties of a lens in ray 1 beam orientation are given by electron trajectories which come to focus very close to the polepiece tip of the lens (i.e. $z = 0$). In ray

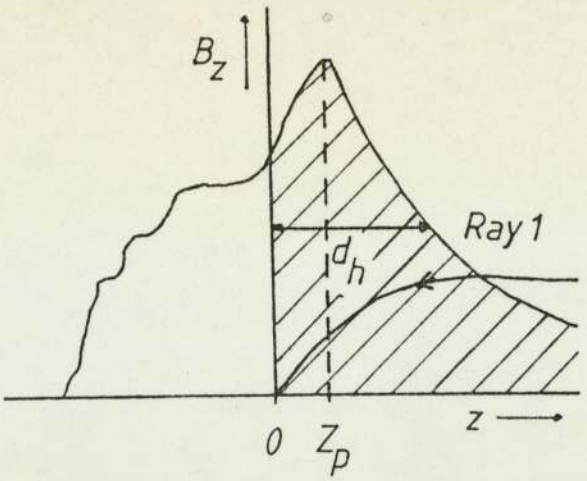

Figure E1 Diagram defining the effective halfwidth for ray 1 beam orientation.

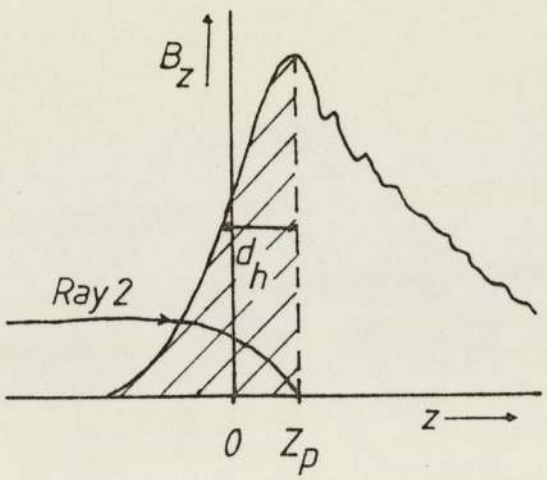

Figure E2 Diagram defining the effective halfwidth for ray 2 beam orientation.

2 beam orientation, the optimum electron optical properties of a lens are given by electron trajectories which come to focus very close to Z_p; the position of the peak value B_{max} of the axial magnetic flux density distribution.

In the present work the effective halfwidth for ray 1 beam orientation is defined as the halfwidth of the axial magnetic flux density distribution which is present in the positive z region (i.e. $z > 0$), as shown in figure E1. For ray 2 beam orientation the effective halfwidth d_h, is defined as the halfwidth of the

axial magnetic flux density distribution which is present in the z region smaller than Z_p (i.e. $z < Z_p$), as shown in figure E2.

Appendix F

Constructional details of lenses HERMES II and ZEUS

Figures F1 and F2 show the detailed cross-sectional diagrams of lenses HERMES II and ZEUS, respectively, as given to the Departmental workshop for construction.

The magnetic circuit of these lenses was constructed from Swedish iron. The percentage concentration of the constituent elements of Swedish iron are given in table F1, as supplied by the manufacturers.

The non-magnetic parts of the lenses, which are shown as shaded areas in figures F1 and F2, were constructed from brass.

The focusing coil of lens HERMES II was made of 450 turns of loosely wound 22 SWG enamelled copper wire. The total resistance of this coil was 2.10 ohms.

The focusing coil of lens ZEUS was made of 450 turns of loosely wound 19 SWG enamelled copper wire. The total resistance for this coil was 1.68 ohms.

Table F1 The constituent elements of Swedish iron

Element	Normal values (%)	Maximum values (%)
C	0.025	0.030
Si	0.030	0.050
Mn	0.160	0.180
P	0.005	0.010
S	0.015	0.020
Cr	0.020	0.050
Ni	0.040	0.080
Cu	0.030	0.050
Sn	0.002	0.010

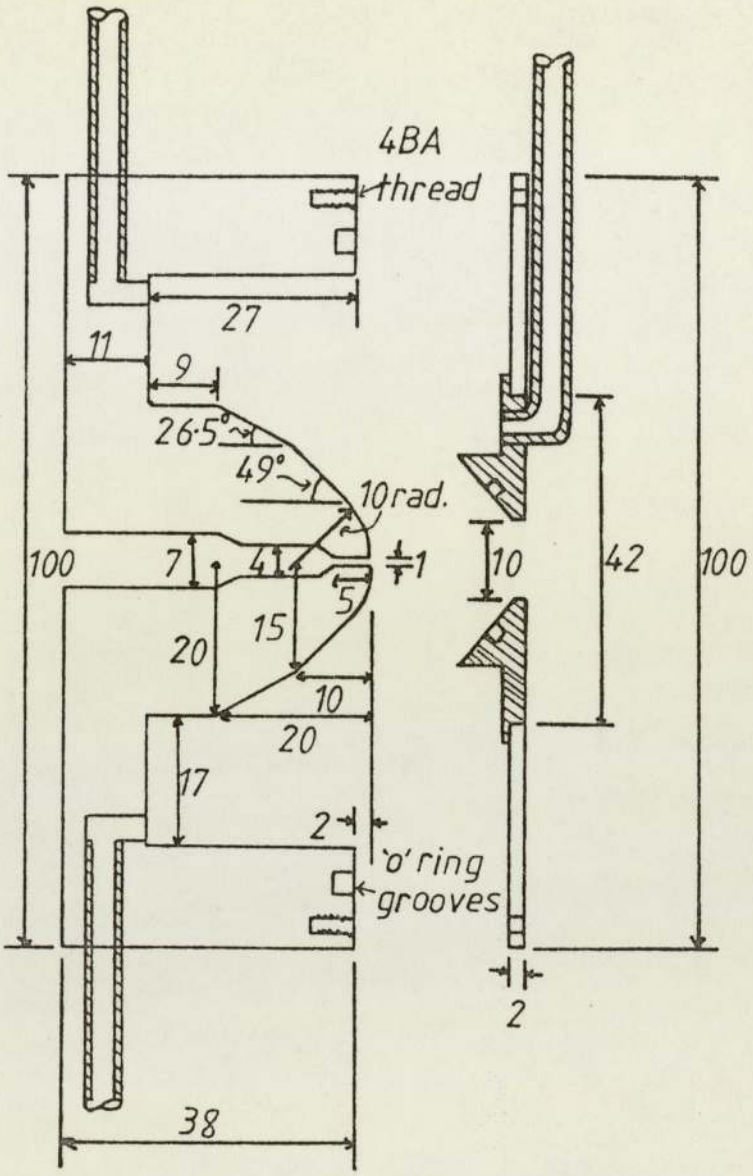

All dimensions are in mm

Scale 1:1

Material

open areas from Swedish iron

shaded areas from Brass

Figure F1 Detailed cross-sectional diagram of lens HERMES II

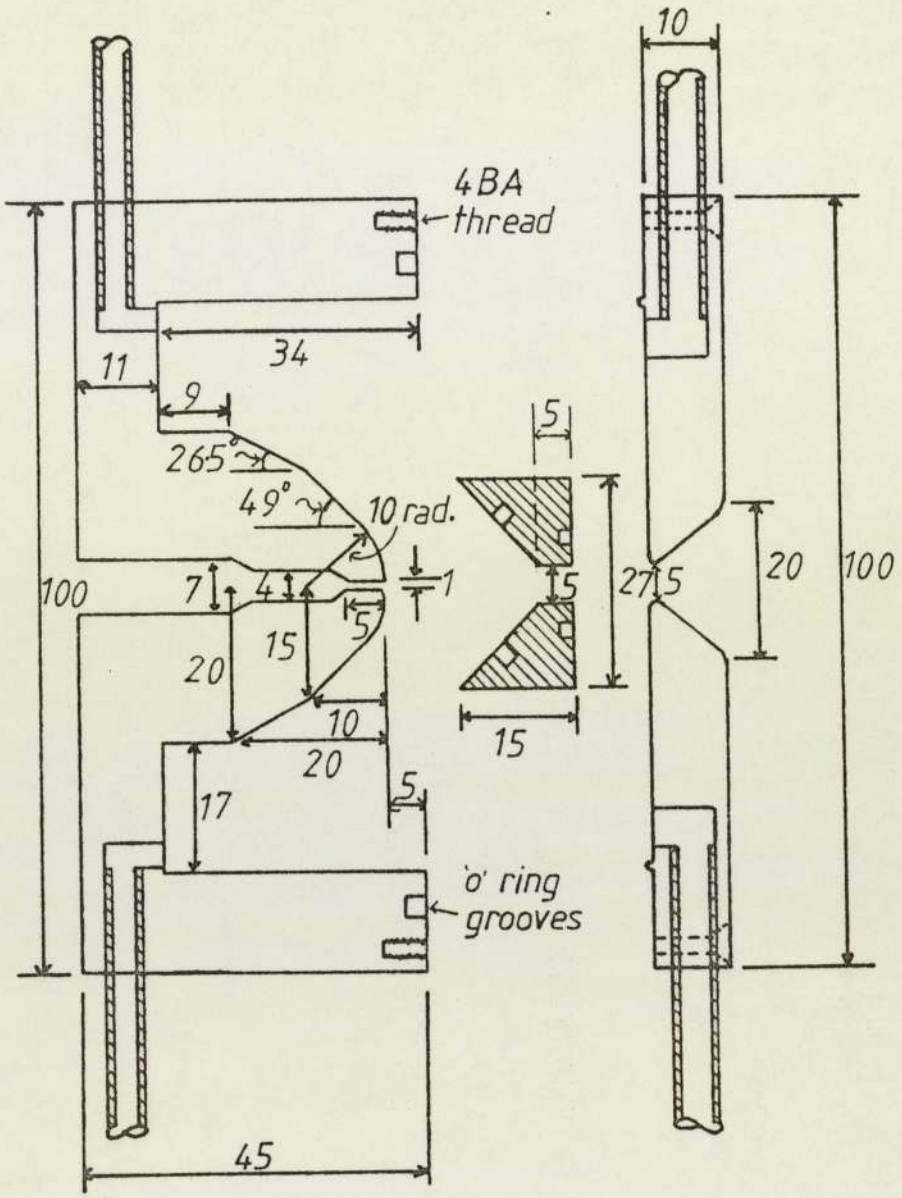

All dimensions are in mm

Scale 1:1

Materials

open areas from Swedish iron

shaded areas from Brass

Figure F2 Detailed cross-sectional diagram of lens ZEUS.

Appendix G

SCANNING ELECTRON MICROSCOPY/1979/I
SEM Inc., AMF O'Hare, IL 60666, USA

CLASSIFICATION OF SMALL GLASS FRAGMENTS BY X-RAY MICROANALYSIS WITH THE SEM AND A SMALL SAMPLE XRF SPECTROMETER

R. H. Keeley and S. Christofides*

Metropolitan Police Forensic Science Laboratory
109 Lambeth Road
London, SE1 7LP, U.K.

*Present Address
Department of Physics
University of Aston,
Birmingham, U.K.

Abstract

A method is described for classifying small glass samples into window and non-window types using X-ray microanalysis with the Scanning Electron Microscope (SEM) and a purpose built small sample X-ray fluorescence (XRF) system. The peak intensity of magnesium will assign most samples to window (high Mg) or non-window (low Mg) groups. Further discrimination can be obtained from iron and arsenic measurements from XRF spectra. The method is suitable for samples as small as 50 μg.

KEY WORDS: Glass, X-Ray Fluorescence (XRF), X-Ray Microanalysis, Forensic Applications

Introduction

Refractive index measurements are very useful in the forensic examination of glass fragments and large surveys have been made of the distribution of refractive indices in glasses from windows, containers and other sources. This information can be used to show how often a glass has occurred in the population sampled, as long as the type of glass can be identified. An important requirement of any method of glass analysis is to correctly identify the origin of the sample; in particular to distinguish between sheet glass and other types since glass from windows is by far the commonest type recovered in case-work.

Methods suitable for the forensic examination of glass should be able to cope with very small fragments (<100 μg), be sensitive (detection limit <10 ppm) and capable of rapid sample throughput. X-ray microanalysis in the SEM satisfies two of these requirements but lacks sensitivity. The lower limit of detection for most elements in a matrix is approximately 0.1% (1000 ppm), so that only major elements in glass can be detected. Andrasko and Maehly[1] have used analysis in the SEM for discriminating between window glasses but an additional analytical technique, emission spectrography, was needed to separate some samples. Howden et al[2] have developed a successful method for classifying 100-200 μg glass samples using XRF and Reeve et al[3] reported discrimination between all but two of 81 samples by XRF, though no indication of sample size was given and many of the samples could be separated by physical properties alone.

In this work we use the SEM and an XRF system designed for small samples. The instruments have been applied to the problem of classifying samples weighing about 50 μg and having refractive indices in the range 1.51-1.52.

Apparatus

The XRF system[4] was built around a 205 ev. solid state X-ray detector and a 256 channel multi-channel analyser formerly used on our SEM. It is designed to fit onto the camera slide of a Philips X-ray tube shield without interfering with cameras and a diffractometer on the other three ports. The sample chamber is hexagonal and made of $\frac{1}{4}$ inch mild steel; it has access ports on the sides and top and can be evacuated. X-rays enter through a 6 μm mylar window and pass down a 1 mm diameter copper collimator. (Figure 1). The sample is presented to the beam on the end of a fine perspex probe which fits into a simple specimen stage. The sample can be moved through approximately 1 cm with controls located outside of the chamber. There is a fibre optic light source and a simple microscope for observing and aligning the sample. The X-ray source is a 1.8 KW copper anode tube.

Sample Preparation and Analysis

Samples are analysed first by XRF; fragments weighing about 50 μg are attached to the end of the probe with dilute glue extracted from adhesive tape. The probe is inserted into the stage and the chamber evacuated with a rotary pump to 10^{-2} torr. The absorption of low energy photons by the tube window and the short air path between it and the chamber window mean that very few reach the sample; the reason for evacuating the chamber is to eliminate the large argon peak which would otherwise be seen in the spectrum. The sample is aligned in the beam using the microscope or more simply by observing the count rate on a rate meter. The height of the probe must be adjusted manually so that its tip is just inside the lower edge of the beam. Although the probe is only 0.5 mm in diameter it is large in comparison with the sample and if it protrudes too far, scattering of the beam causes excessive dead time and a large copper line in the spectrum. Adjustment of the probe is tedious but once aligned it can be removed and replaced without further adjustment.

Tube is run at 45 KV and the analyser preset to acquire 40 K counts in the highest channel (the centre channel of the Ca Ka peak). Spectra are recorded over the range 0-16.5 KeV. The analysis time for 50 μg samples under these conditions is about 15 minutes. The analyser used in this work has no integrating facilities and no teletype output; spectra were recorded on a strip chart recorder.

The sample is removed from the probe after analysis, washed in trichlor ethylene and embedded in conducting bakelite using a metallurgical mounting press. Small fragments are difficult to locate and identify in the finished block unless they are surrounded by a marker. Each sample is placed in the centre of a small brass nut (internal diameter 1 mm) after arranging the nuts around the circumference of the mould. 30 samples or more can easily be accommodated in a 2 cm diameter disc. The bakelite is ground in a mortar and pestle and sieved through a 50 μm mesh; fine powder flows around the samples ensuring that they do not fall out of the block during polishing. The discs are hand polished with 3 μm and 0.2 μm alumina on a soft lap, washed to remove abrasive and coated with carbon.

All analyses were performed under identical conditions. The stage tilt, sample to detector distance and working distance were all carefully measured. The beam current was adjusted before each analysis by setting the specimen current to 6×10^{-10} A on the exposed surface of the brass nut surrounding the sample. Net peak counts were obtained by measuring the background on either side of the peak; for lower atomic number elements where the peaks are close together the background was taken as the height at 900 eV.

Samples

Samples were taken from a large collection of glasses of all types maintained in the laboratory. The majority of the samples were chosen from the refractive index range 1.516-1.517, since this is the region of the maximum in the distribution of a large number of window glasses measured by Dabbs and Pearson[5]. A total of 160 samples of all types have been examined. The non-window types were from containers, drinking vessels and headlamps.

Results

Spectra of the same sample recorded by XRF and SEM are compared in Figure 2. The XRF system performs poorly below 3 KeV mainly because of absorption of low energy photons in the tube window and the air path, but is very sensitive at higher energies, especially for iron. By contrast, the electron excited spectrum shows good detection at the low energy end, but no elements above calcium are detected. Table 1 lists the elements detected in three window and three non-window glasses chosen at random. Although there are qualitative differences between samples in both

groups window glasses are generally of fairly uniform composition and quantitative analysis is necessary to discriminate between them.

Net peak counts of sodium, magnesium, aluminium, silicon, potassium and calcium were obtained from the SEM spectra. The values for each element were plotted against refractive index. There was considerable overlap between window and non-window glasses for all elements except magnesium. Two distinct populations can be seen in the magnesium plot; window glasses have high and non-window glasses low magnesium levels. A few of the samples were classified either between the two groups or in the wrong group altogether (Figure 3). Of the latter, two samples were of flat glass from speedometers and another was from a table top and so were correctly classified as sheet glass although they were not from windows. Some of the window samples which were incorrectly classified were from old buildings. Pre 1930 window glass is said to have low magnesium levels but has iron levels similar to modern glass [6]. A crude measure of iron levels was obtained by using the ratio of the heights of the iron and calcium peaks taken from the charts of XRF spectra. The ratios were plotted against magnesium (Figure 4). The samples which were wrongly classified now form a third population of glasses with low magnesium and high iron. The non-window samples with high magnesium are now correctly classified by their low iron content.

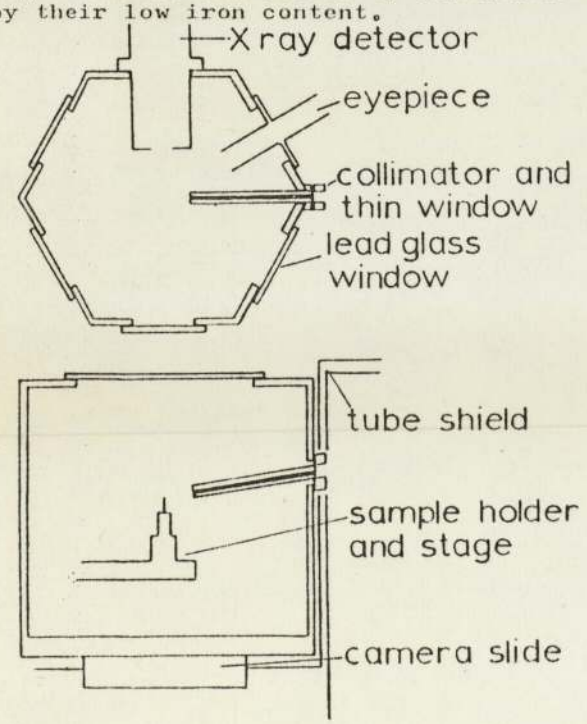

Figure 1 Small sample XRF system

1.5170	W	Ti			Mn	Fe			Sr	Zr
1.5170	W	Ti			Mn	Fe			Rb Sr	Zr
1.5167	W	Ti			Mn	Fe				Zr
1.5166	NW		Ba			Fe	As		Sr	Zr
1.5167	NW	Ti		Cr	Mn	Fe		Se	Sr	Zr
1.5167	NW	Ti		Cr	Mn	Fe	As		Rb Sr	Zr

Table 1. Elements detected by XRF in samples of window (W) and non-window (NW) glasses.

Discussion

The errors associated with measuring peak heights of energy dispersive spectra from charts are high, but in this study at least, the ratios were sufficiently accurate to distinguish between high and low iron content. However peak areas should be measured by integration if possible. Scattering and absorption of X-rays due to the irregular shapes of samples are also important sources of error [2,7], affecting the reproducibility of measurements. This is not very important when large differences between samples are being measured, but can be a severe limitation when differences are small. As the sample size decreases critical depth effects increase because higher atomic number elements are less efficiently excited than those of lower atomic number. The peak ratios to calcium change with sample size and it is important when comparing small fragments by XRF to ensure that they are of similar size and shape.

Analysis by XRF is slower than in the SEM, even with the additional time taken embedding and polishing. The method could be speeded up if samples were examined by SEM first and only those with low or intermediate magnesium examined by XRF. It is possible that a sufficiently accurate analysis might be obtained without embedding and polishing to enable a sample to be identified as high or low magnesium glass. Usable peak ratios have been obtained from uncoated and unpolished samples [1] and the problem of obtaining reproducible magnesium count measurements with a minimum of sample preparation merits further attention.

The results reported here show good discrimination between window and non-window types. The samples were chosen at random from those with the commonest refractive indices and should be reasonably representative of the majority of samples encountered in case-work.

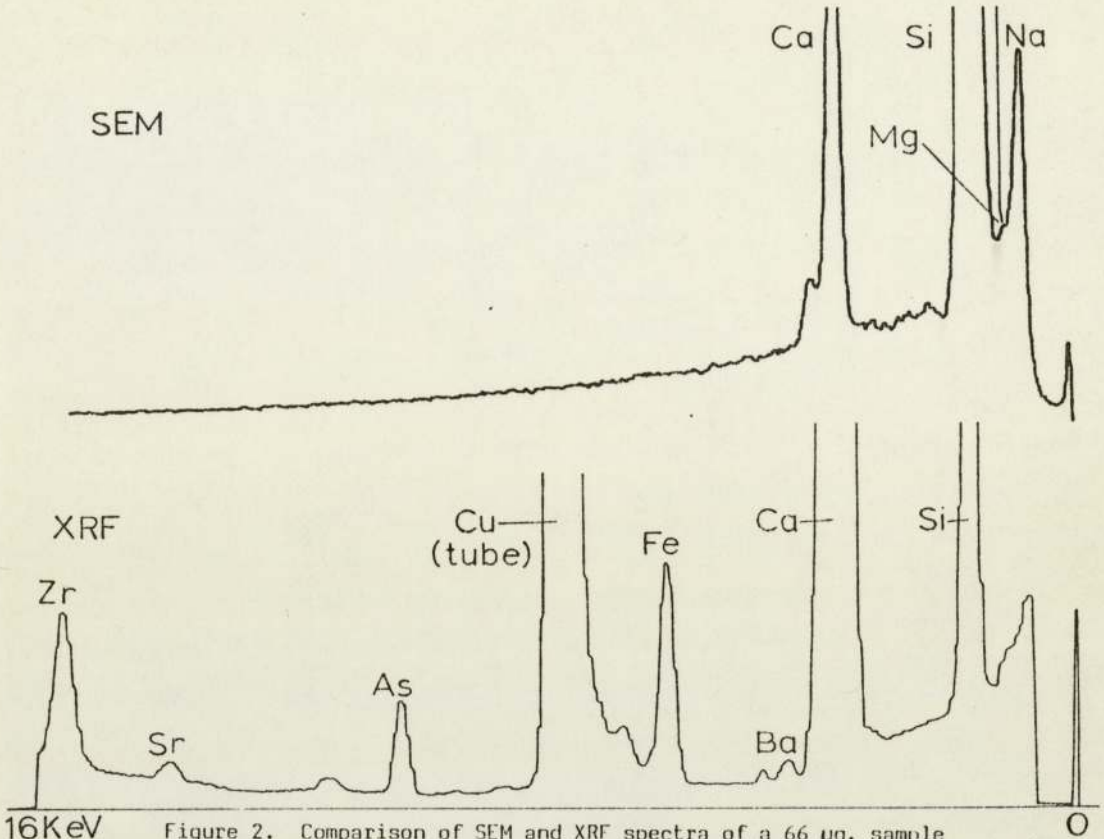

Figure 2. Comparison of SEM and XRF spectra of a 66 µg. sample of container glass (G3402). The same X-Ray detector (205 eV.) was used for both spectra.

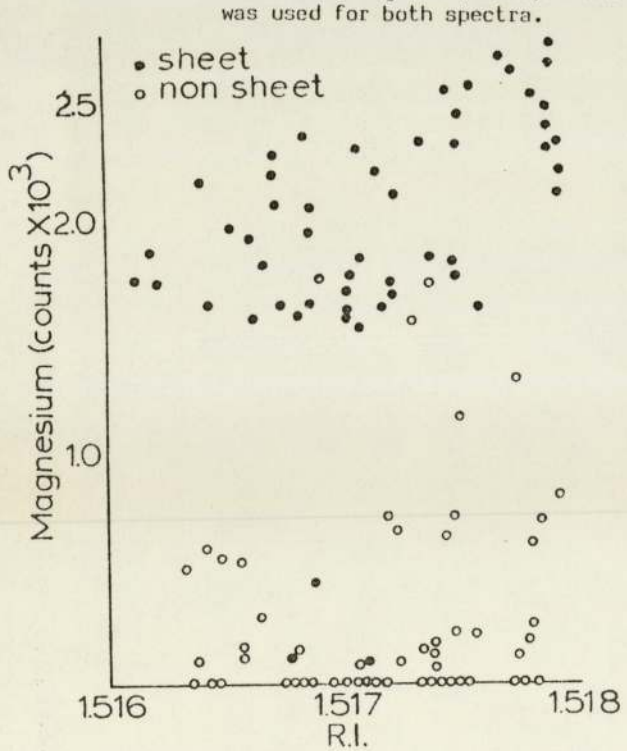

Figure 3. Magnesium levels (SEM) plotted against Refractive Index.

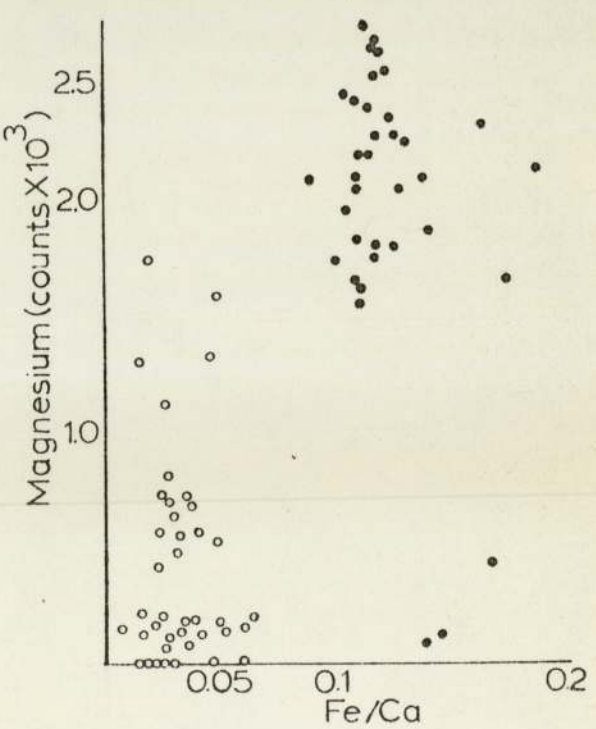

Figure 4. Magnesium levels (SEM) plotted against iron/calcium (XRF).

References

1. J. Andrasko and A. C. Maehly. The Discrimination Between Samples of Window Glass by Combined Physical and Chemical Techniques. J. For. Sciences, 23(2)1978 pp. 250-262.
2. C. R. Howden, R. J. Dudley and K. W. Smalldon. The Analysis of Small Glass Fragments Using ED/XRF. J. For. Sci. Soc 18(1-2) 1978 pp. 99-112.
3. V. Reeve, J. Mathieson and K. Fong. J. For. Sciences, 21(2) 1976 pp. 291-306.
4. R. H. Keeley and S. Christofides, A Simple XRF System. Metropolitan Police Laboratory SEM Report 4a, 1977. Available from the authors.
5. M. G. Dabbs and E. F. Pearson. Some Physical Properties of a Large Number of Window Glass Specimens. J. For. Sciences, 17(1) 1972 pp. 70-78.
6. C. R. Howden, B. German and K. W. Smalldon. The Determination of Iron and Magnesium in Small Glass Fragments Using Flameless AA. J. For. Sci. Soc. 17(2-3) 1977 pp. 153-159.
7. F. Montecalvo. Problems Encountered in XRF Analysis of Small Glass Particles Crime Laboratory Digest, Federal Bureau of Investigation. Issue 77-9, December 1977 pp. 4-8.

Discussion with Reviewers

J. M. Dubery; The 160 glass samples used in this survey show reasonable separation of the window and container glasses into high and low magnesium bands respectively. A survey of 550 glass samples from scenes of crime collected by my laboratory shows a considerably greater overlap. From these data it is my opinion that the magnesium and refractive index information is not sufficient to distinguish window and container glasses except in a few restricted regions of the Mg/RI plot. Can you explain this apparent discrepancy?

Authors; We believe that there is no discrepancy between your results and ours. Figure 3 shows that the window and non-window groups do have overlapping magnesium levels; as more samples are examined the size of the overlapping group will increase and the effect become more noticeable. We agree that magnesium content alone is not sufficient for reliable discrimination and for this reason have used iron measurements by XRF to improve discrimination.

L. F. Vassamillet; It is not explicitly stated in the paper that the combination of these two techniques is a definitive one. Have the authors established the probability that identification of a glass fragment, large enough so that measurement errors are negligible (100 µg?) is either window or non-window glass? Would that probability exceed 95%?

Authors: We cannot yet state that the combination of the two techniques is a definitive one nor can we say that the probability of correct identification exceeds 95%, although it almost certainly does for samples weighing more than 100 µg. All of the samples in this study were correctly classified, but 160 samples is a small population and we need to examine many more, particularly old and coloured glass, before we can form firm conclusions on the reliability of the method.

V.R. Matricardi: Are you now, or will you soon be using this XRF-SEM/ED combination on case-work? If so, do you plan to use it as a screening technique prior to density and/or refractive index determination?

Authors: The method has not yet been used on case-work samples. When introduced it will be used on samples with matching refractive indices.

J.M. Dubery: Previous work on XRF of small glass fragments has been published; does this work add anything new to the subject?

Authors: It has been noted[2] that XRF measurements become increasingly unreliable as the sample size falls below 100 µg and it is well known that X-ray excitation is much less sensitive for low atomic number elements than electron excitation. Reliable results for magnesium can be obtained for sample weights well below 50 µg with the SEM; the combination of the two techniques offsets the loss of precision in the XRF analysis of very small samples.

J.M. Dubery: The iron levels measured from the XRF plots are ratioed to calcium; is this not a rather dangerous practice with small irregular samples as the calcium intensity is very orientation dependent?

Authors: The peak intensities of all elements vary with changes in sample orientation. These variations can be minimized by measuring ratios between peaks close together in the spectrum; calcium was chosen because it is the largest peak close to iron.

L.F. Vassamillet: It can be seen that Figures 3 and 4 do not represent measurements on identical sample sets. Why weren't Fe/Ca ratios obtained on all 107 samples that were measured in the SEM?

Authors: Clusters of samples with very low iron and very low magnesium have been omitted from Figure 4 for the sake of clarity.

J.M. Dubery: Were all the samples of clear colourless glass?

Authors: The results plotted in Figure 3 and Figure 4 are all from colourless glass; very small fragments of green and brown bottle glass appear to be colourless and sometimes have intermediate or high magnesium and iron levels. These would be wrongly classified on the basis of magnesium and iron, but they also contain characteristic levels of barium and arsenic which can be used to assign them to the correct group.

V.R. Matricardi: Why was copper chosen as the X-ray tube? Was it to provide better sensitivity for iron? What tube current do you use?

Authors: The apparatus was designed for use on a tube shield with a Guinier camera and a diffractometer both of which use copper radiation. Copper radiation is ideal for exciting iron; in fact it is so efficient that care must be taken to shield the detector from fluorescence from the walls of the sample chamber. The tube is run at currents between 15 and 30 mA depending on sample size.

V.R. Matricardi: What is the composition of the sample holder?

Authors: The sample holder was machined from Plexiglass (methyl-methacrylate)

J.M. Dubery: The authors state the requirement that all small samples must be of similar size and shape for XRF analysis. Is this a realistic requirment for case-work samples?

Authors: There is generally plenty of control glass available in case-work and it is easy to select a fragment of approximately the same size and shape as the suspect.

Appendix H

A HIGH FLUX DENSITY SINGLE POLEPIECE OBJECTIVE LENS

S.Christofides and T.Mulvey

Department of Physics, The University of Aston in Birmingham
Birmingham B4 7ET (UK)

In an objective lens, the spherical and chromatic aberrations can be reduced by increasing the maximum flux density on the axis. In a single polepiece lens, axial flux densities of up to 2 Tesla can easily be achieved. In a well designed lens only the iron in the immediate vicinity of the poleface should reach saturation flux density. Such a lens is shown in Figure 1. It consists of a cylindrical iron block with an integral single polepiece having an optimised[1] bore of 1mm at the poleface. The coil is directly immersed in the cooling water and provides a maximum excitation of 15,000 A-t. An iron lid of large internal diameter (42mm) completes the magnetic circuit. The lens was primarily intended as a micro-x-ray source[2,3], but can also be used as a high resolution 200 KV objective lens. The specimen or x-ray target is placed at a distance Z_f from the poleface of about 1.5mm. For x-ray purposes, a parallel beam of electrons passing through the lens bore is brought to a focus at this point. In TEM, electrons scattered by the specimen would follow the same path but in the reverse direction. In a single polepiece lens this mode of operation leads to a low chromatic rather than low spherical aberration values. However at high values of the excitation parameter $NI/V_r^{\frac{1}{2}}$, acceptably low values of the spherical aberration coefficient C_s can also be obtained. Figure 1 shows the calculated[4] and experimentally measured axial magnetic flux density distribution at a lens excitation NI of 10,800 A-t. The peak axial flux density is 1.6 T, corresponding to a flux density of some 1.9 T at the poleface. This is close to the saturation value of the low carbon steel employed, so that one can expect the shape of the axial flux density distribution to change with excitation. However in this design, these effects are small. Thus at the maximum available excitation of 15,000 A-t the increase in 'half-width' of the distribution is less than 5%, and both the chromatic and the spherical aberration fall steadily with increasing lens excitation. This is an ideal situation for an x-ray source, as shown in Figure 2. Here the target position Z_f, the chromatic aberration coefficient C_c and the spherical aberration coefficient C_s, expressed as a fraction of the objective focal length F_{obj} are shown as a function of the lens excitation parameter $NI/V_r^{\frac{1}{2}}$, where V_r is the relativistically corrected accelerating voltage. The experimentally measured Z_f and C_s values are also indicated on the curve. Figure 2 shows that for $NI/V_r^{\frac{1}{2}} = 50$ this lens has excellent focal properties, $C_s = 1.1$mm, $C_c = 0.75$mm, and $F_{obj} = 0.9$mm. Since $Z_f = 1.52$mm there is just enough room (0.6mm) for a lens aperture. Similar remarks would apply to this lens used as a TEM objective. In x-ray mode the probe current $I_p = 2\beta d^{8/3} C_s^{-2/3}$ where β is the brightness, d the electron spot size. For a value of $\beta = 500{,}000$ A.cm^{-2} sterad^{-1} (50 KV), and a focussed spot of 1μm in diameter, the probe current increases linearly with excitation, from 20μA at 3000 A-t to 130μA at 15000 A-t. Because of the low values of C_c the corresponding tolerance for the stability dV/V of the accelerating voltage is of the order of 10^{-3}. As a TEM objective lens performance can be judged by the parameter $\delta_o = 0.707(C_s\lambda^3)^{\frac{1}{4}}$ representing the smallest separation that can be interpreted by direct observation. For this lens $\delta_o = 4.6$Å at 100 KV (10,800 A-t); for 200 KV (13,400 A-t) the corresponding resolution is 3.3Å. comparable with the best TEMs with conventional lenses; here the single polepiece lens offers a lower chromatic aberration

1. S.M Juma and T. Mulvey, Inst.Phys.Conf. Ser.No. 52,59-60,1980.
2. D.J. Pugh and P.D. West, Inst.Phys.Conf.Ser.No. 36,29-32,1977.
3. R.H. Keeley and S. Christofides, Scanning Electron Microscopy 1979/I, ed. O.Johari, 459-464, SEM Inc. AMF O'Hare, USA 1979.
4. E. Munro, Ph.d. Dissertation, Cambridge 1971.

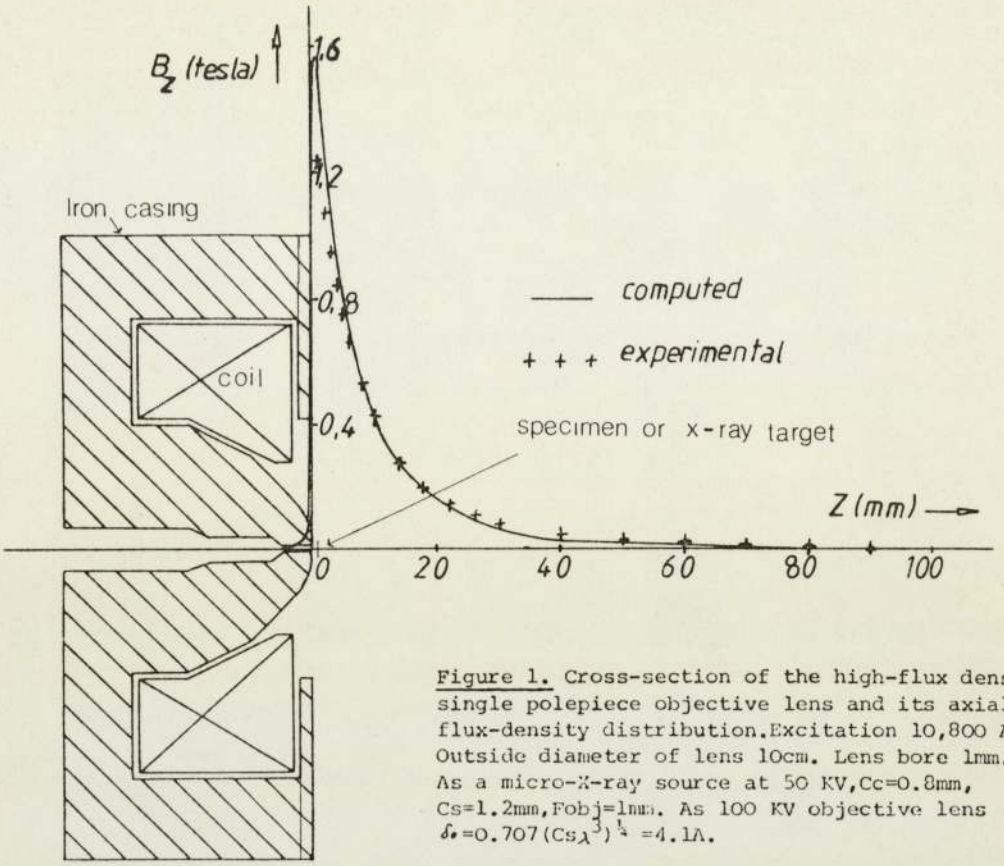

Figure 1. Cross-section of the high-flux density single polepiece objective lens and its axial flux-density distribution. Excitation 10,800 A-t. Outside diameter of lens 10cm. Lens bore 1mm. As a micro-X-ray source at 50 KV, Cc=0.8mm, Cs=1.2mm, Fobj=1mm. As 100 KV objective lens $\delta_o = 0.707 (Cs\lambda^3)^{\frac{1}{4}} = 4.1$Å.

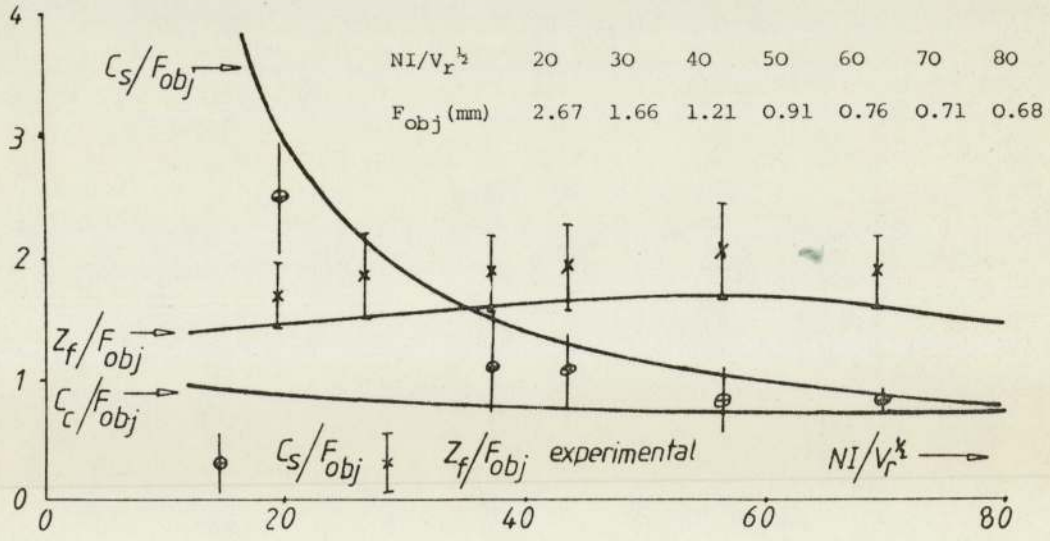

Figure 2. Calculated and experimentally measured relative focal properties of the high-flux density single polepiece objective lens as a function of the excitation parameter $NI/Vr^{\frac{1}{2}}$. Zf-distance from poleface to focal point, Cc-chromatic aberration coefficient, Cs-spherical aberration coefficient, Fobj-objective focal length. Solid line indicates computed values.